

**Study of non-equilibrium interactions between an air bubble and a hydrophilic/hydrophobic solid surface with the non-linearized Stokes-Reynolds-Young-Laplace model (NSRYL model)**

by

**Seyedehmansoureh Shahalami**

A thesis submitted in partial fulfillment of the requirements for the degree of

**Doctor of Philosophy**

in

**Chemical Engineering**

**Department of Chemical and Materials Engineering  
University of Alberta**

© Seyedehmansoureh Shahalami, 2014

## Abstract

The interaction between bubbles and solid surfaces is important to a broad range of industrial and biological processes. Various experimental techniques have been developed to measure the interactions of bubbles approaching solids in a liquid. In this thesis the consistency and accuracy of such measurement are tested against Stokes-Reynolds-Young-Laplace model in which the augmented Young Laplace equation is linearized within the interaction zone. The main focus of this thesis is to model thin liquid film drainage using the non-linearized Young Laplace equation in combination with the Stokes Reynolds equation. The scaled equations of the non-linearized SRYL model do not have a universal nature and depend on the physical parameters of system via capillary number. The numerical results show that in contrast to the linearized SRYL model, the hydrodynamic resistance force predicted from the non-linearized SRYL model strongly depends on the capillary number,  $Ca$ . The non-linearized SRYL model is compared with the linearized SRYL model at a broad range of capillary number from  $10^{-8}$  to  $10^{-3}$ . The numerical results show that at low  $Ca$  number of  $10^{-8}$  and smaller, both the non-linearized and linearized SRYL models lead to the same prediction for bubble deformation, time dependent force and hydrodynamic force. Therefore, over this range of  $Ca$  number both the non-linearized and linearized SRYL models can be confidently used to obtain the spatial and temporal evolutions of the film profile, once these models are shown to be able to give an accurate prediction of time dependent force profiles. For systems of  $Ca$  number larger than  $10^{-8}$ , the linearized SRYL model predicts a stronger hydrodynamic repulsive force, and the maximum difference in prediction between the two models occurs at the  $Ca$  number around  $\sim 3.4 \times 10^{-5}$ . The numerical results show that in comparison with the non-

linearized SRYL model at the same  $r_{max}$  (the boundary of the solution domain), the linearized SRYL model overestimates the hydrodynamic resistance force for the  $Ca$  numbers tested which in turn influences the prediction of bubble deformation and time dependent force profiles. However over this high  $Ca$  number range, both the non-linearized and linearized SRYL models can predict the same time dependent force profiles with different overlaps (different adjustable parameters), while there are differences in the prediction of bubble shape and hydrodynamic repulsive force. Therefore, even if the linearized SRYL model is shown to be able to give an accurate prediction for time variations of the interaction forces over this range of  $Ca$  numbers, we cannot confidently use the linearized SRYL model to predict the spatial and temporal evolutions of the shape of the film trapped between interacting interfaces. Validation of simulation results by thin film profile measurement using thin film force apparatus (TFFA), conclude that the non-linearized SRYL model is more accurate for high  $Ca$  number systems.

For a system of very high capillary numbers the non-linearized SRYL model predicts a solid-like bubble that does not deform in the approach phase. In contrast, the linearized SRYL model is unable to show the bubble rigidity at high capillary numbers. Furthermore the non-linearized SRYL model is able to predict the critical bubble approach velocity above which the bubble behaves like a solid sphere. This study shows that the non-linearized SRYL model is needed to study the effect of individual parameters of system such as bubble size, interfacial tension and liquid viscosity on the critical bubble approach velocity at which bubble behaves like a solid sphere.

The non-linearized SRYL model is used to model the measurements of the recently developed integrated thin film drainage apparatus (ITFDA) which has been used to measure the bubble-particle interactions over a wide range of hydrodynamic conditions. The excellent

agreement between the predicted and measured interaction forces between an air bubble and solid surface in three liquids of very distinct physicochemical properties demonstrates that the non-linearized SRYL model can be applied to the systems of a wider range of bubble approach velocity, liquid interfacial tension and viscosity. The excellent agreement suggests that the non-linearized SRYL model can be used to obtain quantitative information on film profiles during the bubble approach-retract cycle. The simulation results indicate that the minimum film thickness between an air bubble and hydrophilic solid surface in a liquid over a given approach period is thinner for the system of low bubble approach velocity, and/or low viscosity and high surface tension of the liquids.

In this thesis the non-linearized SRYL is further developed to account for the effect of solid surface hydrophobicity. The experimental data quantified with the integrated thin film drainage apparatus (ITFDA) and the thin film force apparatus (TFFA) was used to validate the extended non-linearized SRYL model. The hydrophobic force which was considered as the driving force for destabilizing water films on hydrophobic surface was evaluated with the best fit between the measured and predicted time evolution forces. The numerical results showed that the longer-range hydrophobic force with increasing the surface hydrophobicity was responsible for film rupture. The effect of surface hydrophobicity and bubble approach velocity on the drainage rate of intervening liquid film was studied. The results showed that the wetting films formed on hydrophobic glass sphere of increasing surface hydrophobicity, thin much faster. Film drainage resistance or force barrier are determined to reduce greatly with increasing the solid surface hydrophobicity. Moreover the film drainage resistance or force barrier is found to increase with increasing bubble approach velocity. Decreasing bubble approach velocity or/and increasing

surface hydrophobicity are found to decrease the film radius. As a result the film ruptures at locations closer to the center of the film.

The extended non-linearized SRYL model incorporating proper form of hydrophobic force is able to predict the critical film thickness where the film ruptures. The prediction of the critical film thickness is achieved by solving non-linear SRYL equations without simplifications. The simulation results indicate that the critical film thickness increases with increasing surface hydrophobicity and bubble approach velocity.

### **Key Words**

Bubble-particle interaction, film drainage dynamics, induction time, hydrodynamic force, hydrophobicity, force barrier, critical film thickness.

## Preface

1. Shahalami, S., Zhang, X., Masliyah, J., Xu, Z. “Study of non-equilibrium interactions between an air bubble and a solid surface using the linearized and non-linearized forms of the Stocks-Reynolds-Young-Laplace model” *manuscript in preparation*. All the experiments of this work were performed by Xurui Zhang.
2. Shahalami, S., Wang, L., Wu, C., Masliyah, J., Xu, Z., Chan, D. “ Measurement and modeling on hydrodynamic forces and deformation of an air bubble approaching a solid sphere in liquids with the integrated thin film drainage apparatus (ITFDA)” *manuscript submitted*. All the experiments of this work were performed by Louxiang Wang.
3. Shahalami, S., Wang, L., Zhang, X., Masliyah, J., Xu, Z. “Study the effect of hydrophobicity and bubble approach velocity on the stability of wetting films formed on the glass surfaces with the NSRYL model” *manuscript in preparation*. All the experiments of this work were performed by Louxiang Wang and Xurui Zhang.

## **Dedication**

To my parents for their endless love

To my dear husband, *Morteza Fougerdi* for his love and patient

and

To my lovely daughter *Katayoun Fougerdi*

## **Acknowledgments**

I would like to express my deepest appreciation to my supervisor, Dr. Zhenghe Xu and Dr. Jacob H. Masliyah for their support, encouragement, constructive criticism and for their great idea which became the basis of this thesis. I am grateful for the wonderful opportunities they provided me and for all their enthusiasm towards my work.

I would like to thank Dr. Derek Chan for his guidance in this collaborative research work. Many thanks also to Dr. Plamen Tchoukov for his assistance to review this thesis and for his consulting for the experiments. I acknowledge Ms. Lisa Carreiro for being accommodating and resourceful on every occasion. I am thankful for financial support from NSERC Industrial Research Chair in Oil Sands Engineering.

# Table of contents

Abstract . . . . .	ii
Preface . . . . .	vi
Dedication . . . . .	vii
Acknowledgments . . . . .	viii
List of Tables . . . . .	xiii
List of Figures . . . . .	xiv
Nomenclature . . . . .	xix
<b>Chapter 1</b>	
<b>Introduction</b>	
1.1 Background . . . . .	1
1.2. Main contribution . . . . .	4
1.3. Objectives of the study . . . . .	4
1.4. Organization of the thesis . . . . .	5
<b>Chapter 2</b>	
<b>Literature review</b>	
2.1. Thin liquid film . . . . .	6
2.1.1 Experimental studies . . . . .	7
2.1.2 Theoretical studies . . . . .	10
2.1.2.1 Bubble deformation . . . . .	11
2.1.2.1.1 Augmented Young-Laplace equation . . . . .	11
2.1.2.1.2 Solution of the augmented Young-Laplace equation . . . . .	14
2.1.2.2 Hydrodynamic . . . . .	15
2.1.2.2.1 Stokes–Reynolds lubrication theory . . . . .	16
2.1.2.2.2 Navier Slip model . . . . .	17
2.1.2.2.3 Manev-Tsekov-Radoev model . . . . .	18
2.1.2.2.4 Stokes–Reynolds–Young–Laplace model . . . . .	19
2.1.2.2.5 Stefan–Reynolds Flat Film model . . . . .	22
2.1.2.3 Disjoining pressure/surface force . . . . .	24
2.1.2.3.1 Electric double layer force . . . . .	25
2.1.2.3.2 Van der Waals force . . . . .	26

2.1.2.3.3 Hydrophobic force.....	27
2.2. Critical film thickness.....	31
2.3. Induction time .....	32

### Chapter 3

#### Study of non-equilibrium interactions between an air bubble and a solid surface using linearized and non-linearized forms of SRYL model

3.1. Introduction.....	37
3.2. Experimental method.....	40
3.2.1 Materials.....	40
3.2.2 Bubble generation and displacement control .....	41
3.2.3 Film thickness measurement .....	41
3.3. Augmented Young Laplace model.....	42
3.4. Formulation of the NSRYL model.....	43
3.4.1 Scaling of the governing equations.....	45
3.5. Formulation of the LSRYL model .....	47
3.6. The difference between the two model equations: NSRYL and LSRYL.....	48
3.7. Results.....	49
3.7.1 Comparison of the NSRYL model with the LSRYL model .....	51
3.7.1.1 Comparison at $Ca$ number of $10^{-8}$ .....	51
3.7.1.2 Comparison at $Ca$ number of $5.15 \times 10^{-6}$ .....	57
3.7.1.3 Comparison at $Ca$ number of $3.4 \times 10^{-5}$ .....	61
3.7.1.4 Comparison at $Ca$ number of $1.09 \times 10^{-4}$ .....	64
3.7.1.5 Comparison at $Ca$ number of $2.3 \times 10^{-3}$ .....	68
3.7.1.6 Wall impact on the approaching bubble.....	72
3.7.2 Validation of the NSRYL model .....	74
3.8. Discussion .....	77
3.9. Conclusions.....	81

### Chapter 4

#### Measurement and modeling on hydrodynamic forces and deformation of an air bubble approaching a solid sphere in liquids with the integrated thin film drainage apparatus (ITFDA)

4.1. Introduction.....	84
4.1.1 Background and motivations .....	84

4.1.2	Coverage and scope .....	87
4.2.	Dynamic experimental methods.....	88
4.2.1	Free bubble rise method.....	89
4.2.2	Bubble expansion methods.....	89
4.2.3	Surface forces apparatus.....	90
4.2.4	Atomic force microscope .....	91
4.2.5	An important but less explored domain .....	92
4.3.	Integrated thin film drainage apparatus (ITFDA) .....	93
4.3.1	Design features .....	94
4.3.2	Force sensing bimorph .....	94
4.3.3	The glass sphere.....	96
4.3.4	Bubble generation and displacement control .....	96
4.3.5	Force measurement protocol .....	97
4.3.6	Cantilever deflection.....	99
4.4.	Theoretical model.....	99
4.4.1	Governing equations .....	100
4.4.2	Scaling and universality of the governing equations .....	102
4.5.	Experiments with hydrophilic glass .....	104
4.5.1	Surface treatment .....	105
4.5.2	Interaction in aqueous electrolyte solutions .....	106
4.5.3	Interaction in ethanol and silicone oil .....	111
4.5.4	Scaling of experimental results.....	114
4.6.	Conclusions and future perspectives .....	116

## **Chapter 5**

### **Effect of hydrophobicity and bubble approach velocity on stability of wetting films between bubble and glass surfaces studied by Non-linearized SRYL (NSRYL) model**

5.1.	Introduction.....	118
5.2.	Formulation of the problem (model) .....	123
5.2.1	Scaling of governing equations .....	126
5.3.	Experimental methods .....	128
5.3.1	The glass sphere.....	129
5.3.2	Bubble generation and motion control.....	130

5.3.3	Force measurement .....	131
5.3.4	Bimorph cantilever.....	133
5.4.	Results.....	134
5.4.1	Evaluation of hydrophobic force .....	135
5.4.2	Contact angle of 52° .....	143
5.4.3	Contact angle of 38°, 84° and 103°.....	145
5.5.	Discussion .....	149
5.5.1	Effect of approach velocity .....	152
5.5.2	Effect of surface hydrophobicity .....	154
5.6.	Conclusion .....	156
<b>Chapter 6</b>		
<b>Conclusions and future perspectives</b>		
6.1.	Major conclusions .....	158
6.2.	Suggestions for future research.....	161
<b>References.....</b>		<b>163</b>
<b>Appendix .....</b>		<b>176</b>

## List of Tables

Table 3.1. Parameters used in the theoretical study .....	51
Table 3.2. Value of physical parameters used in the NSRYL model and LSRYL model calculations at $Ca$ number of $10^{-8}$ with scaled approach time of 180 .....	52
Table 3.3. Value of physical parameters used in the NSRYL model and LSRYL model calculations at $Ca$ number of $5.15 \times 10^{-6}$ with scaled approach time of 180 .....	60
Table 3.4. Value of physical parameters used in the NSRYL model and LSRYL model calculations at $Ca$ number of $3.4 \times 10^{-5}$ with scaled approach time of 180 .....	62
Table 3.5. Value of physical parameters used in the NSRYL model and LSRYL model calculations at $Ca$ number of $1.09 \times 10^{-4}$ with scaled approach time of 180 .....	67
Table 3.6. Value of physical parameters used in the NSRYL model and LSRYL model calculations at $Ca$ number of $2.3 \times 10^{-3}$ with scaled approach time of 180 .....	68
Table 3.7. Material constants and modified ITFDA parameters .....	75
Table 4.1 Material constants and ITFDA parameters .....	105
Table 5.1. Material constants used in the experiments with ITFDA .....	135
Table 5.2 The best fitted hydrophobic force constants of various models and air bubble surface boundary conditions .....	136
Table 5.3 The best fitted of hydrophobic force constant, $K_{132}$ (J), in eqn. 5.10 using immobile bubble surface boundary condition .....	149

## List of Figures

Fig. 2.1 Schematic of an axisymmetric residing drop/bubble of constant surface tension, $\gamma$ , on a substrate.....	12
Fig. 2.2 Schematic of the Stefan-Reynolds Flat Film model for a drop (or bubble) approaching a flat solid surface .....	23
Fig. 2.3 bimorph signal as a function of measurement time between an air bubble and a hydrophobic glass sphere ( $\theta_a = 38^\circ$ ) in 1 mM KCl solutions of pH 5.6.....	36
Fig. 3.1. A photograph of the bubble-glass sphere configuration of the thin film force apparatus (TFFA).....	42
Fig. 3.2. Schematic diagram of the geometry between an air bubble and a flat surface at two times of $\theta$ (a) and $t$ (b).....	50
Fig. 3.3. (a) Variation of scaled force with scaled time, (b) time dependent force profile, (c) variation of hydrodynamic force with thickness of aqueous film at the axis of symmetry, and (d) variation of film thickness with film radius in aqueous electrolyte (100 mM KCl, pH = 5.6) at a bubble approach velocity of 1 $\mu\text{m/s}$ ,.....	54
Fig. 3.4. (a) Variation of scaled force with scaled time, (b) variation of film thickness with film radius in aqueous electrolyte (100 mM KCl, pH = 5.6) at a bubble approach velocity of 1 $\mu\text{m/s}$ , corresponding to a capillary number of $1.4 \times 10^{-8}$ .....	56
Fig. 3.5. Variation of $\partial h / \partial r^2$ , in eqn. 3.3, as a function of $r_{\text{max}}$ in aqueous electrolyte solutions (100 mM KCl, pH = 5.6) at the bubble approach velocity of 1 $\mu\text{m/s}$ .....	57
Fig. 3.6. (a) Variation of scaled force with scaled time, (b) time evolution of force, (c) variation of hydrodynamic force with thickness of aqueous film at the axis of symmetry, and (d) variation of film thickness with film radius in aqueous electrolyte solutions (100 mM KCl, pH = 5.6) at a bubble approach velocity of 375 $\mu\text{m/s}$ ,.....	61
Fig. 3.7. (a) Variation of scaled force with scaled time, (b) time evolution of force, (c) variation of hydrodynamic force with thickness of aqueous film at the axis of symmetry, and (d) variation	

of film thickness with film radius in aqueous electrolyte solutions (100 mM KCl, pH = 5.6) at a bubble approach velocity of 2500 $\mu\text{m/s}$ .....	63
Fig. 3.8. (a) Variation of scaled force with scaled time, (b) time evolution of force, (c) variation of hydrodynamic force with thickness of aqueous film at the axis of symmetry, and (d) variation of film thickness with film radius in aqueous electrolyte solutions (100 mM KCl, pH = 5.6) at a bubble approach velocity of 8000 $\mu\text{m/s}$ .....	67
Fig. 3.9. (a) Variation of scaled force with scaled time and (b) variation of film thickness with film radius in aqueous electrolyte (100 mM KCl, pH = 5.6) at a bubble approach velocity of 165000 $\mu\text{m/s}$ , corresponding to a capillary number of $2.3 \times 10^{-3}$ .....	70
Fig. 3.10. Variation of the film drainage velocity with separation distance at a bubble approach velocity of 165000 $\mu\text{m/s}$ , corresponding to a capillary number of $2.3 \times 10^{-3}$ .....	72
Fig. 3.11. Variation of force with time (a), variation of film thickness with time (b), and variation of the difference between local film thickness at center and rim with time (c) in aqueous electrolyte solution (100 mM KCl, pH = 5.6) at bubble approach velocity of $\sim 155000 \mu\text{m/s}$ , corresponding to a capillary number of $2.18 \times 10^{-3}$ .....	73
Fig. 3.12. Profile of the aqueous film, $h(r,t)$ between the bubble and the flat glass surface at different measurement times during the holding phase (in which the bubble approach velocity is zero) predicted with (a) the NSRYL model and (b) the LSRYL model .....	76
Fig. 3.13. Variation of the scaled hydrodynamic force with the scaled film thickness at the axis of symmetry with (a) the NSRYL model and (b) the LSRYL model at a wide range of $Ca$ numbers .....	78
Fig. 3.14. Variation of the scaled force with the scaled time with the NSRYL model (a) and the LSRYL model (b) at a wide range of $Ca$ numbers .....	79
Fig. 3.15. Variation of the scaled film profile with the scaled bubble radius using the NSRYL model (a): film profile where bubble initially forms and c: film profile at the end of approach) and the LSRYL model (b): film profile where bubble initially forms and d: film profile at the end of approach) .....	81

Fig. 4.1 (a) Schematic diagram of the key components and characteristic parameters of the ITFDA .....	95
Fig. 4.2 (a) The measured (points) displacement of the capillary tube $\Delta X(t)$ and the corresponding polynomial fit (line); and (b) the instantaneous velocity $dX(t)/dt$ .....	98
Fig. 4.3 Variation of the force $F(t)$ – experiment (dashed line) and model (solid line), calculated central film thickness $h(0,t)$ and central pressure $p(0,t)$ as a function of measurement time for an air bubble approaching a solid sphere in aqueous electrolyte solution of 1 mM KCl and pH = 5.6 at nominal velocity of 33 $\mu\text{m/s}$ , .....	107
Fig. 4.4 Thickness of the aqueous film, $h(r,t)$ between the bubble and the glass sphere at different measurement times during (a) approach and (b) retraction; and the hydrodynamic pressure profile, $p(r,t)$ scaled by $(\gamma/R) = 64.5$ .....	109
Fig. 4.5 Variation of the force $F(t)$ – experiment (points) and model (line), calculated central film thickness $h(0,t)$ and central pressure $p(0,t)$ as a function of measurement time for an air bubble approaching a solid sphere in aqueous electrolyte (1 mM KCl, pH = 5.6) at nominal velocity of 134 $\mu\text{m/s}$ .....	110
Fig. 4.6 Variation of the force $F(t)$ – experiment (points) and model (line) along with the calculated central film thickness $h(0,t)$ and central pressure $p(0,t)$ as a function of measurement time of an air bubble approaching a solid sphere in ethanol at the nominal velocity of 33.4 $\mu\text{m/s}$ , .....	113
Fig. 4.7 Variation of the force $F(t)$ – experiment (points) and model (line) along with the calculated central film thickness $h(0,t)$ and central pressure $p(0,t)$ as a function of measurement time .....	114
Fig. 4.8 A comparison between the measured and the calculated contact diameter between the bubble and the glass sphere in water, ethanol and silicone oil. ....	115
Fig. 4.9 Correlation between the measured repulsive forces normalized by capillary pressure $(2\gamma/R_b)$ and the film area. ....	116
Fig. 5.1. A photograph of the bubble-glass sphere configuration in the ITFDA .....	129

Fig. 5.2 A representative capillary tube position (a) and bimorph signal (b) as a function of measurement time between an air bubble and a hydrophobic glass sphere ( $\theta_a=38^\circ$ ) in 1 mM KCl solutions of pH 5.6..... 133

Fig. 5.3 Variation of the force  $F(t)$  – experiment (dashed line) and model (solid line) for an air bubble approaching a hydrophobized solid sphere of  $\theta_a=52^\circ$ ..... 138

Fig. 5.4 Thickness of the aqueous film,  $h(r,t)$  between the bubble and hydrophobic glass sphere at different measurement times (a) and corresponding variation of the hydrodynamic resistance force (b)..... 139

Fig. 5.5 The film pressure (a), classical disjoining pressure (b), hydrodynamic (c) and hydrophobic pressures (d) scaled by  $(\gamma/R)$  in the water film. .... 141

Fig. 5.6 Thickness of the aqueous film,  $h(r,t)$  between the bubble and hydrophobic glass sphere at (a) bubble approach velocity of 24  $\mu\text{m/s}$ , which is the same as Figure 5.4a and (b) bubble approach velocity of 10  $\mu\text{m/s}$  (b)..... 142

Fig. 5.7 (a), (b) and (c): Variation of the – measured (dashed line) and predicted (solid line) – force  $F(t)$  and (d): the effect of bubble approach velocity on the induction time, for an air bubble approaching a hydrophobized solid sphere of  $\theta_a=52^\circ$  in aqueous electrolyte solution of 1 mM KCl and pH = 5.6 at bubble approach velocities of 24, 120 and 240  $\mu\text{m/s}$  ..... 144

Fig. 5.8 (a), (b) and (c): Variation of the – measured (dashed line) and predicted (solid line) – force  $F(t)$  and (d): the effect of bubble approach velocity on the induction time, for an air bubble approaching a hydrophobized solid sphere of  $\theta_a=38^\circ$  in aqueous electrolyte solution of 1 mM KCl and pH = 5.6 at bubble approach velocities of 48, 120 and 240  $\mu\text{m/s}$  ..... 146

Fig. 5.9 (a), (b) and (c): Variation of the – measured (dashed line) and predicted (solid line) – force  $F(t)$  and (d): the effect of bubble approach velocity on the induction time, for an air bubble approaching a hydrophobized solid sphere of  $\theta_a=84^\circ$  in aqueous electrolyte solution of 1 mM KCl and pH = 5.6 at bubble approach velocities of 120, 240 and 480  $\mu\text{m/s}$  ..... 147

Fig. 5.10 (a), (b) and (c): Variation of the – measured (dashed line) and predicted (solid line) – force  $F(t)$  and (d): the effect of bubble approach velocity on the induction time, for an air bubble

approaching a hydrophobized solid sphere of $\theta a=103^\circ$ in aqueous electrolyte solution of 1 mM KCl and pH = 5.6 at bubble approach velocities of 240, 480 and 4800 $\mu\text{m/s}$ .....	148
Fig. 5.11 Effect of bubble approach velocity on the force barrier (a), and induction time (b) for an air bubble to approach a hydrophobized solid sphere in aqueous electrolyte solution of 1 mM KCl and pH = 5.6.....	151
Fig. 5.12 Effects of bubble approach velocity and surface hydrophobicity on the predicted critical film thickness .....	152
Fig. 5.13 Thickness of the aqueous film, $h(r,t)$ between the bubble and hydrophobized glass sphere of $\theta a=38^\circ$ at point 1 where dimple starts to form and point 3 at the moment of film rupture for (a) bubble approach velocity of 48 $\mu\text{m/s}$ and (b) bubble approach velocity of 240 $\mu\text{m/s}$ . The corresponding hydrodynamic pressure profile, $phydrodynamic * (r, t)$ scaled by $(\gamma/R) = 125.9 \text{ Pa}$ for (c) bubble approach velocity of 48 $\mu\text{m/s}$ and (d) velocity of 240 $\mu\text{m/s}$ ....	154
Fig. 5.14 Thickness of the aqueous film, $h(r,t)$ between the bubble and the hydrophobized glass sphere with bubble approach velocity of 240 $\mu\text{m/s}$ at point 1 where dimple initially forms and point 3 where the film ruptures for (a) $\theta a=103^\circ$ and (b) $\theta a=38^\circ$ .....	156

# Nomenclature

## Symbols

- $A_{132}$  Hamaker constant of phase 1 and phase 2 through a medium 3, J
- $A_s$  Helmholtz surface free energy, J
- $Ca$  capillary number,  $Ca = \mu V / \gamma$
- $D$  Separation distance between two surfaces, m
- $e$  Charge of electron ( $=1.602 \times 10^{-19}$  C)
- $F$  Interaction force, N
- $F_{bar}$  Force barrier, N
- $G$  Gibbs free energy, J
- $h(r,t)$  Film profile or local film thickness, m
- $h_0$  Initial separation distance, m
- $h_c$  Critical film thickness, m
- $K$  Effective spring constant, N/m
- $k_B$  Boltzmann constant ( $=1.38 \times 10^{-23}$  J/K)
- $p(r,t)$  Hydrodynamic pressure in the film relative to the bulk pressure, N/m<sup>2</sup>
- $R$  Radius, m
- $R_b$  Bubble radius of curvature, m
- $R_g$  Radius of glass sphere, m
- $R_s$  Solid sphere radius, m
- $R_0$  Unperturbed radii of curvature, m
- $r_{max}$  Outer boundary condition, m
- $S(t)$  Deflection of bimorph end, m
- $T$  Absolute temperature, K
- $V$  Glass tube drive velocity, m/s
- $v$  Film drainage rate, m/s
- $X(t)$  Displacement of glass capillary, m
- $\psi$  Stern potential, V

$\rho$  Charge density, Kg/m<sup>3</sup>  
 $\varepsilon$  Relative permittivity of the solution  
 $\varepsilon_0$  Permittivity of vacuum ( $= 8.854 \times 10^{-12} \text{C}^2\text{m/J}$ )  
 $\lambda$  Debye length, m  
 $\mu$  Viscosity of solution, Pa s  
 $\theta$  Contact angle, degrees  
 $\theta_r, \theta_a$  Receding and advancing contact angle, degrees  
 $\gamma$  Liquid/vapor interfacial tension, N/m  
 $\Delta P$  Laplace pressure drop across interface, N/m<sup>2</sup>  
 $\Delta X_{max}$  Maximum glass tube displacement, m  
 $\Pi$  Disjoining pressure, N/m<sup>2</sup>

### **Abbreviations**

ITFDA Integrated thin film drainage apparatus  
TFFA Thin film force apparatus  
LSRYL Linearized Stokes-Reynolds-Young-Laplace model  
NSRYL Non-linearized Stokes-Reynolds-Young-Laplace model  
AFM Atomic force microscopy  
SFA Surface force apparatus  
CCD Charge-coupled device  
DLVO Derjaguin-Landau-Verwey-Overbeek  
KCl Potassium chloride  
TPC Three phase contact  
DDOA Dimethyldioctyl ammonium  
CTAB Cetyltrimethyl ammonium bromide  
TFB Thin film balance

# Chapter 1

## Introduction

### 1.1 Background

Flotation is the most widely used mineral separation process. This complex process depends on the surface properties of mineral particles in a dynamic system in which the hydrodynamic effects also have a crucial role for successful flotation. The combination of the micro processes involved in flotation leads to the separation of valuable mineral species. Within the micro processes of the flotation as a whole, the attachment between bubbles and solid particles is of great importance.

Early Studies of dynamic interactions involving deformable bubbles and solids were conducted by Derjaguin and Kussakov (Derjaguin and Kussakov Reprinted in Prog Surface Sci 1992). They studied the time-dependent behavior of a rising bubble towards a flat plate under buoyancy force. Subsequent dynamic studies aimed at understanding the drainage phenomena of the liquid film between deformable droplets/bubbles (Scheludko 1967). A number of different experimental techniques have been used to study film drainage and time dependent interactions between an air bubble and a solid surface immersed in a liquid (Chan et al. 2011). One of the earliest methods to study the dynamic film drainage involving deformable interfaces was based on the Scheludko cell (Platikanov 1964; Ivanov 1988; Blake and Kitchener 1972; Schulze 1975). This method allows the determination of time evolution of the liquid film thickness,  $h(t)$ , but it was not capable of measuring the interaction forces between an air bubble and a solid surface. The atomic force microscope (AFM), on the other hand, has been widely used to measure both

static and dynamic interaction forces of deformable bubbles (Ducker et al. 1994; Butt 1994; Fielden et al. 1996; Preuss and Butt 1998) approaching solid probe particles in aqueous solutions. Neither the thin liquid film apparatus nor the AFM colloid/bubble probe technique is able of determining simultaneously the deformation of air bubbles and dynamic interaction forces. Moreover, the experiments conducted by the thin liquid film apparatus and AFM probe technique are mostly in the low Reynolds number regime. To overcome some of these shortages, an integrated thin film drainage apparatus (ITFDA) was developed recently to measure the bubble-particle interactions over a wide range of dynamic conditions at bubble Reynolds number of 10 (Wang et al. 2012; Wang 2013). ITFDA is capable of measuring simultaneously the dynamic forces and the shape of the bubble interacting with solid particles. Since the bubble approach velocity can be as high as 5000  $\mu\text{m/s}$ , the ITFDA is an appropriate device to study the bubble-particle interactions under dynamic conditions (Wang et al. 2012; Wang 2013).

There are many attempts in the literature to model the thinning of intervening aqueous film between an air bubble and solid surface with varying degrees of technical complexity. One essential element to understand and predict dynamic interactions involving deformable bubble is choosing a proper hydrodynamic model which describes the time and position dependent hydrodynamic force arising from the film drainage. One approach to treat hydrodynamic interactions is to solve the complete Stokes flow equations using direct numerical simulations (Baldessari and Leal 2006; Yoon et al. 2007). Another element to understand dynamic interactions involving deformable bubble is to describe how drops/bubbles deform and characteristic geometries such as dimple. The augmented Young-Laplace equation (Yeh et al. 1999; Chan et al. 2001) can be used to describe the deformation of a drop/bubble due to the proximity of another drop/bubble or solid particle. Furthermore, knowledge about the nature of

surface/colloidal forces between interfaces in close proximity is the last essential element to determine collision stability or coalescence. There are previous efforts to assemble all these essential steps to form a coherent description of dynamic film drainage between deformable bubbles and solids (Ivanov et al. 1985; Chan et al. 2009; Baldessari and Leal 2006; Carnie et al. 2005; Lai and Bremond, N. and Stone, H. A. 2009). However due to the complexity of numerical solution of coupled equations, in the early studies the drop interfaces are assumed to be plane parallel and for instance, the Stefan–Reynolds flat film model used (Reynolds 1886; Stefan J. 1874) to model film drainage. This model gives rise to internal inconsistencies with even the simplest experiments which led to the introduction of subsequent corrections for the Stefan–Reynolds flat film model (Coons et al. 2003; Manev and Nguyen 2005; Tsekov 1998; Tsekov and Evstatieva 2004).

In 1973 it is stated (Burrill and Woods 1973) *‘The difficulty encountered in the design and operation of industrial equipment in which coalescence occurs is partly due to a lack of knowledge of coalescence’*. Though this statement is still true and there is a lack of understanding of liquid film rupture between droplets and/or bubbles and also between bubbles and solids. There have been efforts to measure and predict the dynamics of film drainage and time-dependent forces but still, few succeeded to elucidate the underpinning physics of coalescence phenomena. Since the thinning and rupture of intervening aqueous film between particle and bubble can be the rate determining step in flotation, therefore a better understanding of the process from both experimental and theoretical aspects, especially under dynamic conditions, remains to be established.

## 1.2. Main contribution

Improving our appreciation of thin liquid film drainage and rupture phenomena is of great importance as the thin liquid film drainage plays a crucial role in various industrial processes, most notably in froth flotation used in the separation of mineral particles. The Stokes–Reynolds–Young–Laplace (SRYL) model is proposed to describe a broad range of experimental studies of film drainage and dynamic interaction involving drops and bubbles. Because this model is a combination of Stokes–Reynolds equation with the linearized approximation of augmented Young–Laplace equation, in this thesis, it is named the linearized SRYL model (LSRYL). It is well established that the scaled equations of the LSRYL model do not depend on the capillary number ( $Ca \equiv \mu V/\gamma$ ) and behave nearly universal. Consequently all the scaled results about the dimple formation, time dependent force, spatial and temporal evolution of film thickness, film profiles and film drainage rates are almost the same at broad range of capillary numbers. In this thesis, we used the original non-linearized form of augmented Young Laplace equation which leads to the appearance of capillary number in the scaled equation. Hence, at various capillary numbers, the scaled results do not behave in a universal way and depend on the capillary number. The approach proposed here, is a step forward in reaching greater understanding about thin film drainage and rupture phenomena.

## 1.3. Objectives of the study

The objectives of this thesis are:

- 1) To compare the non-linearized SRYL model with the previously used linearized SRYL model at a broad range of capillary numbers. The aim of this part is to show that in contrast of previously used linearized SRYL model, the scaled results obtained using non-linearized SRYL model depend on the capillary number.

2) To study the dynamic interactions and bubble deformation of an air bubble approaching a hydrophilic solid sphere in liquid using non-linearized SRYL model and fit experimental data obtained with ITFDA. This part mainly focuses on the effect of surface tension, fluid viscosity and bubble approach velocity for bubble deformation and hydrodynamic forces.

3) To study the dynamic interactions and bubble deformation of an air bubble approaching a hydrophobic solid sphere in liquid with the non-linearized SRYL model, the experimental data quantified with the ITFDA. This part mainly focuses on the effect of hydrophobicity of the solid surface and bubble approach velocity on the film drainage rate. In this part, it is demonstrated that the SRYL model is able to numerically predict the critical film thickness where rupture occurs.

#### **1.4. Organization of the thesis**

The thesis is organized into six chapters and the details of the chapters are presented as follows:

**Chapter 1** presents the general background of this study and includes introduction, main contributions, objectives and outline of the thesis. **Chapter 2** provides a literature review of experimental and modeling studies on the aqueous film drainage between an air bubble and a solid surface. The detailed theoretical and experimental results for the objectives stated in Section 1.3 are analyzed and discussed in **Chapter 3**, **Chapter 4** and **Chapter 5** of this thesis, respectively. Conclusions were drawn based on our findings. Finally, the conclusion and summary of the entire research project and recommendations for future work are presented in **Chapter 6**. The Appendix at the end of the thesis provides more detailed information about the scaled form of non-linearized SRYL model.

# Chapter 2

## Literature review

Flotation is a most preferred method for the mineral separation process. This process is widely used in various industries such as mining industry for the recovery of valuable minerals, pulp and paper industries for separation of ink, toner, and other unwanted contaminants during waste paper recycle operations. Flotation also is used in Canadian oil sands operation, to recover bitumen from oil sands. The attachment between air bubbles and solid surfaces is one of the most critical sub-processes for the successful flotation. The attachment depends largely on drainage kinetics of thin liquid film between solid particles and air bubbles in a dynamic system. This thesis focuses on the theoretical study of thin liquid film drainage between an air bubble and a solid surface. So the literature reviews comprise of the following components: (1) overview on the thin liquid drainage between an air bubble and solid surface, from both experimental and theoretical point of view; (2) summary of the critical film thickness and (3) induction time studies.

### 2.1. Thin liquid film

Thin liquid films can be formed between bubbles and/or droplets and also between bubbles/droplets and/or solids in colloidal system. Many industrial processes and products rely on fundamental interfacial interactions which occur in these intervening liquid films. It is clear that a film is thin when its thickness is much smaller than its lateral dimension. However, from a physical aspect a liquid film formed between two macroscopic phases is thin when the energy of interaction between the two phases across the film is not negligible. Thin liquid film drainage

(TLF) between bubbles and solid surfaces is considered as an important key to interpret flotation (Frumkin 1933). Thinning and rupture of intervening aqueous film between particle and bubble can be the rate determining step in flotation. Therefore the quantitative understanding of the dynamics of thin liquid films is essential and thin film studies attracted lots of researchers for many years. A brief historical perspective of research works done in this area is given here.

### **2.1.1 Experimental studies**

The interactions between air bubbles and mineral particles in water are of special interest due to their importance for mineral flotation processes. First experimental studies of the dynamic interactions involving deformable bubbles and a flat plate were carried out by Derjaguin and Kussakov (Derjaguin and Kussakov 1992). In these experiments a bubble was allowed to rise against a horizontal glass plate or mica sheet under constant buoyancy force. The dynamic behavior of the intervening liquid film trapped between bubbles and flat plate was monitored using the optical interference technique. By observing the interference fringes Derjaguin and Kussakov concluded that the non-equilibrium film profile forms a dimple. However due to experimental limitations, they were not able to measure the film thickness. They pointed out that the barrier rim of the dimple has significant effect on the time required for the rising bubbles to reach the equilibrium state. This method has been used by other researchers to study the approach and attachment of an air bubble to a solid surface (Malysa et al. 2005; Krasowska and Malysa 2007). A major advance in colloidal science occurred when two groups of scientists, Derjaguin-Landau (Derjaguin and Landau 1941; Verwey and Overbeek 1948) and Verwey-Overbeek, (Derjaguin and Landau 1941; Verwey and Overbeek 1948) independently published a quantitative theoretical analysis of the problem of colloidal stability, known as DLVO theory. DLVO was able to explain the stability of suspensions of solid particles in terms of a balance surface forces

acting in thin films. DLVO theory led many researchers to develop experimental techniques to study the film drainage and interactions involving bubbles and drops. But despite of the study of Derjaguin and Kussakov and success of DLVO theory, many of the later studies ignored the importance of interfacial deformations. In these studies, the transient phenomena were generally considered using the Reynolds Flat Film model.

The most extensive experimental studies on film drainage have been carried out using Scheludko cell technique (Scheludko 1967). In this technique a captive bubble is pressed against a flat silica surface through a capillary tube, or by withdrawing the liquid between two approaching surfaces. The film thickness between the two surfaces is measured using the micro interferometric method based on multiple reflection and interference of a monochromatic light. Using this method, the time evolution of the central film thickness,  $h(0,t)$ , can be obtained rather than the detailed spatial variations of the position of the film interface. The experimental results from the Scheludko cell are mostly interpreted using the Stefan–Reynolds Flat Film model.

In contrast to the Scheludko cell technique that is concerned with film geometry, the Surface Force Apparatus (SFA) and Atomic Force Microscope (AFM) has made possible to measure the interaction forces between two approaching surfaces. The SFA technique was pioneered by Israelachvili et al. in the early 1970 (Israelachvili and Tabor 1972; Tabor and Winterton 1969). In this instrument two surfaces are carefully moved towards and retracted from one another, while a direct measurement of colloidal forces at the resolution of  $10^{-8}$  N is provided. This technique uses piezoelectric positioning elements and senses the separation between the surfaces by optical interferometry to a nanometer resolution. Although the SFA is able to measure the interaction forces with high precision, these measurements require the surfaces being transparent, which greatly limits its application to only a limited number of materials and systems. The

introduction of AFM by Binnig et al. in 1986 (Binnig et al. 1986), made possible to study almost any kind of surfaces (Ducker et al. 1991). In this technique, also called colloidal probe technique, a spherical probe particle is attached to the cantilever of the AFM and the lower surface is moved up and down using a piezoelectric transducer. The interaction forces are measured by monitoring the deflection of cantilever. The AFM probe technique was first applied to study the aqueous intervening film between the air bubble and particle by Ducker et al. (Ducker et al. 1994), Butt (Butt 1994) and Fielden et al. (Fielden et al. 1996). In their experiments a small bubble ( $\sim 500 \mu\text{m}$ ) is placed on a hydrophobic substrate and a spherical probe particle is attached to the cantilever of the AFM. In most of the measurements, the air bubble is moved up and down through a piezoelectric transducer to approach to and retract from the probe particle. In some cases, the cantilever is driven to approach and retract from the lower air bubble/droplet surface. AFM has also been employed to measure forces between a deformable liquid droplet and solid particle or between two oil droplets in aqueous solutions (Dagastine et al. 2004; Gunning et al. 2004; Mulvaney et al. 1996; Snyder et al. 1997). Although the colloidal probe technique AFM can provide sufficient information to model the time-dependent force, information about bubble deformations is not directly accessible. Despite some successes of the SFA and AFM techniques to directly measure the interaction forces between approaching interfaces, a major shortcoming of these techniques is that the experiments are conducted at low approach velocities (low Reynolds numbers). To overcome this limitation a new Integrated Thin Film Drainage Apparatus (ITFDA) was recently designed and constructed to directly and simultaneously measure the drainage and interaction forces between two approaching interfaces under a wide range of bubble approach velocities (Wang 2013). In this technique an air bubble which is generated at the end of a glass capillary tube is moved to approach or retract from the glass sphere. This lower surface is

clamped at the free end of a bimorph sensor which is used as a cantilever to measure very small forces. In this device the displacement of the glass tube holding the bubble is independently measured using a displacement sensor with a sensitivity of 5  $\mu\text{m}$ . As ITFDA is more suitable for the real system, the results obtained with ITFDA will be used in this study.

### **2.1.2 Theoretical studies**

In a suspending medium, drops move together and this approaching movement leads to generate the hydrodynamic interactions that resist the film thinning. At close proximity of droplet interfaces, the surface forces also play a role in the film drainage and attachment process. The presence of these interaction forces in intervening liquid film cause the interfaces to deform. Thus to model time-dependent interactions in the thin film, three key elements must be considered as following:

- (i) A description of how drops/bubbles deform under the influence of stresses arising from hydrodynamic flow and surface forces.
- (ii) A description of the hydrodynamic interactions arising from film drainage.
- (iii) A description of the surface or colloidal forces.

There are many attempts in the literature to assemble all these elements to provide a coherent description for film thinning. All these elements affect the collision stability or coalescence and must be treated in a consistent way. For example, the deformed interfaces of the drops or bubbles determine the boundaries of the thin film where the intervening fluid must flow during interaction. As a result, this flow will generate the pressure profiles within the film which in turn has an effect on the thin film stability and also characterize the shape of the interfaces. Some models such as the Stefan–Reynolds Flat Film model ignore the bubble deformation and as

a result gives rise to internal inconsistencies that require subsequent correction. This section will concentrate on some fundamental aspects of drop deformation, hydrodynamic interactions and the established theories for surface forces.

### **2.1.2.1 Bubble deformation**

From the beginning of thin liquid film studies, it was recognized that the forces involved in film drainage influenced the shapes of drops and bubbles approaching solid surfaces. The British physician Thomas Young in 1805 (Young 1805) was the first one who analyzed the shape of a deformable interface under the action of capillary forces without using any equations. Another approach for the shape of deformable interface was suggested in terms of the principle of minimization of interfacial area under the action of interfacial tension or energy (Gauss 1830). All these analyses were under equilibrium conditions. In case of non-equilibrium conditions, when both hydrodynamic interactions and surface forces are important, it is assumed that a drop can adjust its shape instantaneously to accommodate changes in the hydrodynamic pressure and surface forces.

#### **2.1.2.1.1 Augmented Young-Laplace equation**

The augmented Young-Laplace equation was first introduced by both Frumkin and Deryagin (Deryagin and Khim 1940; Derjaguin 1955; Frumkin and Khim 1938). Later the deformation of droplets were studied in more detail by other researchers (De Gennes 1985; Brochard-Wyart et al. 1991). However, in these theoretical studies a little attention was paid to the thermodynamic analysis (Yeh et al. 1999) introduced for a drop or bubble immersed in a continuous phase and residing on a solid surface, **Figure 2.1**. They demonstrated that the bubble deformation can be obtained by minimizing the Helmholtz surface energy of the system.

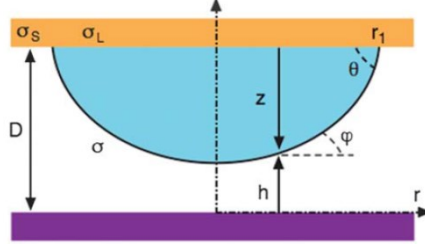


**Fig. 2.1** Schematic of an axisymmetric residing drop/bubble of constant surface tension,  $\gamma$ , on a substrate in which the interaction with a flat surface is concentrated within a small interaction zone around the apex (Chan et al. 2011).

The Helmholtz surface energy in terms of the drop/bubble height,  $z(r,t)$ , can be written as follow:

$$A_s = 2\pi \int_0^{r_1} \left[ \gamma \sqrt{1 + z_r^2} + \gamma_{SL} + \gamma_{SG} + E(h) - p_c z \right] r dr \quad (2.1)$$

where  $z_r \equiv \frac{\partial z}{\partial r}$ .  $\gamma_{SL}$  and  $\gamma_{SG}$  denote the surface tension of the solid-liquid and solid-gas interfaces.  $\gamma$  is the surface tension of liquid-gas or surface energy per unit area. The potential energy of interaction per unit area between approaching interfaces in thin liquid film is given by  $E(h)$ , which is related with the disjoining pressure  $\Pi(h) = -\frac{dE(h)}{dh}$  (Butt et al. 2013). The potential energy of interaction,  $E(h)$  only affects the apex region of the drop.  $p_c = 2\gamma/R_L$  is the capillary pressure and  $R_L$  is the Laplace radius of the drop/bubble. Here the gravitational contribution to the free energy has been omitted due to very small drop size, which is in the range of millimeter or smaller. Because the surface forces between interacting interfaces are functions only of  $h$ , then from **Figure 2.1**,  $h(r,t)$  can be written as:

$$z(r, t) = D(t) - h(r, t) \quad (2.2)$$

The perturbation  $h(r, t) \rightarrow h(r, t) + \delta h(r, t)$  is used in **eqn 2.1**. To minimize the Helmholtz surface energy,  $A_s$ , the first order of its variation,  $\delta A_s$ , considered as zero which yields the classic augmented Young-Laplace differential equation:

$$\gamma(\delta_1 + \delta_2) = \frac{\gamma}{r} \frac{\partial}{\partial r} \left( \frac{r h_r}{(1 + h_r^2)^{1/2}} \right) = p_c + \frac{dE}{dh} = \frac{2\gamma}{R_L} - \Pi(h) \quad (2.3)$$

$\delta_1$  and  $\delta_2$  show the curvatures in the plane and the axisymmetric drop surfaces, respectively. A repulsive interaction,  $\Pi(h) > 0$ , will reduce or flatten the curvature of the drop at the apex. The augmented Young-Laplace equation describes droplet shape at equilibrium. For the dynamic case, as it already mentioned, it is assumed that the drop can adjust its shape immediately to accommodate changes in hydrodynamic and disjoining pressures. This is a reasonable assumption as long as changes in velocities of these disturbances are much slower than the speed of propagation of interfacial perturbations around the drop. Consequently, the non-equilibrium augmented Young-Laplace equation can be obtained by adding the hydrodynamic pressure,  $p$ , to the right hand side of **eqn 2.3**:

$$\gamma(\delta_1 + \delta_2) = \frac{\gamma}{r} \frac{\partial}{\partial r} \left( \frac{r h_r}{(1 + h_r^2)^{1/2}} \right) = \frac{\gamma}{r} \frac{\partial}{\partial r} (r \sin \varphi) = \frac{2\gamma}{R_L} - \Pi(h(r, t)) - p(r, t) \quad (2.4)$$

In this equation, the curvature is expressed in terms of the tangent angle,  $\varphi$ , where  $h_r \equiv \partial h / \partial r \equiv \tan \varphi$ , see **Figure 2.1**. The repulsive hydrodynamic pressure ( $p > 0$ ), like repulsive disjoining pressure will flatten the interacting zone around the drop apex. The first integral of **eqn 2.4** with respect to  $r$  gives:

$$r \sin \varphi = \frac{r^2}{R_L} - \frac{1}{2\pi\gamma} \Phi(r, t) \quad (2.5)$$

$$\Phi(r, t) \equiv 2\pi \int_0^r [p(r, t) + \Pi(r, t)] r dr \quad (2.6)$$

Some important results regarding to drop deformation can be explained by using **eqn. 2.5** and **2.6** (Chan et al. 2011; Chan et al. 2011). As expected from the assumption of axial symmetry, the drop always has zero slope at the apex, i.e., at  $r=0$  (see **Figure 2.1**). When  $\Phi(r, t) = 0$ , from **eqn. 2.5**,  $\sin\varphi$  is positive and the shape of drop will be always concave, see **Figure 2.1**. Furthermore, outside of interaction zone, corresponds to  $r \gg r_{rim}$  ( $r_{rim}$  is film radius), due to negligible value of interaction forces, the curvature of the drop shape must be concave.

#### 2.1.2.1.2 Solution of the augmented Young-Laplace equation

A brief summary about the solutions of the augmented Young Laplace equation for two different cases are given here and more details can be find in the literature (Chan et al. 2011; Chan et al. 2011).

- i. Between a drop/bubble and a flat wall
- ii. Between a drop/bubble and a spherical solid particle

##### (i) Drop/bubble against flat wall

In the finite domain defined from  $r=0$  to  $r = r_{rim}$ , the drop interface is approximately flat compare to the drop size. Consequently with the assumption of  $h_r = \frac{\partial h}{\partial r} \ll 1$ , the augmented Young Laplace equation, **eqn. 2.4**, can be linearised to give:

$$\frac{\gamma}{r} \frac{\partial}{\partial r} \left( r \frac{\partial h}{\partial r} \right) = \frac{2\gamma}{R_L} - \Pi - p \quad (2.7)$$

The film thickness in the interaction zone,  $h$ , can be derived by numerically integrating of **eqn. 2.7**.  $R_L$  is the Laplace radius and is of the order of the unperturbed drop/bubble radius,  $R_b$  (Chan et al. 2011; Chan et al. 2011).

### (ii) Drop/bubble against a spherical particle

For the interaction between drop or bubble with a solid sphere of radius  $R_s$ , the film thickness,  $h$ , has to account for variations in the shape of sphere. Using the **eqn. 2.4** and consider the linearisation in the inner region where  $\frac{\partial h}{\partial r} \ll 1$ , the augmented Young-Laplace equation can be obtained as:

$$\frac{\gamma}{r} \frac{\partial}{\partial r} \left( r \frac{\partial h}{\partial r} \right) = \frac{2\gamma}{R_0} - \Pi - p \quad (2.8)$$

where  $R_0 \equiv (1/R_b + 1/R_s)^{-1}$ . The film thickness in the inner region,  $h$ , can be obtained by numerically integrating of the **eqn. 2.8** (Chan et al. 2011; Chan et al. 2011).

#### 2.1.2.2 Hydrodynamic

Frumkin is the first one who paid particular attention to the thinning kinetics of liquid film between an air bubble and a solid surface (Frumkin 1933). He linked thinning kinetic to the mechanism of froth flotation. The film rupture and attachment process is controlled by both surface forces and hydrodynamic forces. In force measurement experiments, the approaching movement of interacting interfaces leads to hydrodynamic interactions that resist the film thinning. In this section a particular focus is placed on the film thinning equations and hydrodynamic resistance forces between the particle and bubble surfaces.

### 2.1.2.2.1 Stokes–Reynolds lubrication theory

To formulate the thin film drainage of deformable interfaces in the low Reynolds number regime, Stokes flow is appropriate. In most of experiments, it is observed that the continuous aqueous phase behaves as a Newtonian fluid with constant shear viscosity  $\mu$ . Since the film thickness is very small compared to the radial extent of the film, the Reynolds lubrication theory can be applied to describe the dynamic drainage between deformable interfaces. Using these assumptions, the Naveir-Stokes and continuity equations are as following (Chan et al. 2011; Chan et al. 2011):

$$\frac{\partial P}{\partial r} = \mu \frac{\partial^2 u_r}{\partial z^2} \quad (2.9)$$

$$\frac{1}{r} \frac{\partial}{\partial r} (r u_r) + \frac{\partial u_z}{\partial z} = 0 \quad (2.10)$$

As it can be seen from **eqn. 2.9**, within the axisymmetric film of **Figure 2.1**, the dominant velocity component,  $u(r,z,t)$  is in the radial  $r$ -direction and the pressure,  $p$  only varies in the  $r$ -direction. Integrating continuity **eqn. 2.10**, from  $z=0$  to  $h(r,t)$  gives the general evolution equation of the film thickness:

$$\frac{dh(r,t)}{dt} = -\frac{1}{r} \frac{\partial}{\partial r} \left( r \int_0^{h(r,t)} u_r dz \right) \quad (2.11)$$

$u_r$  can be calculated by the integration of the Naveir-Stokes equation with respect to  $z$ . This solution depend on the defined hydrodynamic boundary conditions at the film surface, i.e., at  $z=0$  and  $z=h(r,t)$ . By replacing this solution into **eqn. 2.11**, provides an equation that relates  $h(r,t)$  and  $p(r,t)$  together. Suitable boundary conditions were selected by considering the experimental conditions. For example the assumption of no-slip boundary condition is

appropriate when there are surface-active species or contaminations in the system. For axisymmetric flow in the radial direction in a film with tangentially immobile boundaries,  $u_r|_{z=0} = 0$  and  $u_r|_{z=h} = 0$ , the  $u_r$  has obtained as following:

$$u_r = \frac{(z^2 - hz)}{2\mu} \left( \frac{\partial P}{\partial r} \right) \quad (2.12)$$

Substituting **eqn. 2.12** into **eqn. 2.11**, we now obtain Stokes–Reynolds equation for the film thickness, that relates  $h(r,t)$  and  $p(r,t)$  together:

$$\frac{dh}{dt} = \frac{1}{12\mu} \frac{1}{r} \frac{\partial}{\partial r} \left[ rh^3 \left( \frac{\partial P}{\partial r} \right) \right] \quad (2.13)$$

The fully mobile boundary condition is used for clean system. In this case, the boundary condition at the air/water interface is  $\frac{\partial u_r}{\partial z} = 0$  which lead to:

$$u_r = \frac{(z^2 - 2hz)}{2\mu} \left( \frac{\partial P}{\partial r} \right) \quad (2.14)$$

Substituting **eqn. 2.14** into **eqn. 2.11**, the Stokes–Reynolds equation for full mobile boundary condition obtained as (Chan et al. 2011; Chan et al. 2011):

$$\frac{dh}{dt} = \frac{1}{3\mu} \frac{1}{r} \frac{\partial}{\partial r} \left[ rh^3 \left( \frac{\partial P}{\partial r} \right) \right] \quad (2.15)$$

#### 2.1.2.2.2 Navier Slip model

In this model, it is assumed that the variations of the air/water interface mobility are between the two limits of no-slip and full-slip boundary conditions. These variations in the interface mobility can be modeled by the Navier Slip model characterized by a constant slip length  $b$  which relates fluid velocity at the interface to the bulk shear stress (Vinogradova 1996):

$$u_r = b \frac{\partial u_b}{\partial z} \quad (2.16)$$

where  $u_b$  is the liquid bulk flow rate,  $z$  is the axis perpendicular to the interface. If the viscosity of the near-to-interface layer is characterized by average value  $\mu_r$ , the order of magnitude  $b$  can be estimated as:

$$b = \delta \left( \frac{\mu_b}{\mu_r} - 1 \right) \quad (2.17)$$

where  $\delta$  is the thickness of the boundary layer and  $\mu_b$  is the bulk viscosity. At,  $b \rightarrow 0$ ,  $u_r = 0$ , which corresponds to the conventional no-slip or tangentially immobile condition at the liquid-solid interface. It was proposed that the Navier slip model is appropriate for hydrophobic surfaces (Vinogradova 1995). The film drainage equation between two solid surfaces that obeys the Navier slip boundary condition with the possibility of different slip lengths  $b_0$  at  $z=0$  and  $b_h$  at  $z=h$  has the following form (Vinogradova 1995):

$$\frac{dh}{dt} = \frac{1}{12\mu} \frac{1}{r} \frac{\partial}{\partial r} \left[ r h^3 \left( \frac{\partial P}{\partial r} \right) \right] + \frac{1}{4\mu r} \frac{\partial}{\partial r} \left[ r \left( \frac{(b_0 + b_h)h^3 + 4b_0b_h h^2}{h + b_0 + b_h} \right) \frac{\partial P}{\partial r} \right] \quad (2.18)$$

Compare to the tangentially immobile model of **eqn. 2.13** there is an additional term in the film drainage equation of Navier slip model of **eqn. 2.18**. The classical no-slip or immobile condition will be obtained by setting both slip lengths to zero.

### 2.1.2.2.3 Manev-Tsekov-Radoev model

The shortcomings of the original Reynolds Flat Film model led to develop a complex corrections for film drainage rate, such as Tsekov-Manev-Radoev expression. The assumption of Flat Film model was first challenged when light scattering experiments indicated that the film interfaces are corrugated (Radoev et al. 1983; Manev et al. 1997; Tsekov 1998). The flexibility

of the interfaces complicated the problem substantially. Radoev et al.(Radoev et al. 1983) and Manev and Pugh (Manev and Pugh 1997) reported thinning velocities of the foam films over a wide rang of film radii and demonstarted that there are discrepancies from Reynolds Flat Film model. Manev (Manev et al. 1997) and Tsekov (Tsekov 1998) used the experimental data of Radoev et al.(Radoev et al. 1983) and proposed that the film pressure increases due to the presence of hydrodynamic corrugations. Their work lead to the following expression for thinning velocity:

$$v = \frac{1}{6\mu} \left( \frac{C^3}{4} \right)^{1/5} \left[ \frac{h^{12} \Delta P^8}{\gamma^3 R^4} \right]^{1/5} \quad (2.19)$$

In the Tsekov's velocity experssion, the constant C is unity:

$$v_{Tsekov} = \frac{1}{6\mu} \left[ \frac{h^{12} \Delta P^8}{4\gamma^3 R^4} \right]^{1/5} \quad (2.20)$$

Compared to the Reynolds equation for the thinning velocity, the Tsekov's experssion is less dependent on the film radius. And the prediction of Teskov equation for drainage rate is higher than Reynolds model. However, these expressions were not capable of giving quantitative agreement with experimental data. The failure of original Reynolds Flat Film model and its modifications to predict experimental data, led to the idea to combine the film hydrodynamics with bubble/drop interfacial deformations or Stokes–Reynolds–Young–Laplace model.

#### **2.1.2.2.4 Stokes–Reynolds–Young–Laplace model**

The governing equations of SRYL model were formulated by Ivanov et al.(Ivanov et al. 1985) to describe the shape of the trapped film between two bubbles. In this model, the Stoke-Reynolds equation (**eqn. 2.13**) for tangentially immobile interfaces and proper augmentaed

Young-Laplace equation given by **eqn. 2.7** or **2.8** are combined and provided a set of coupled partial differential equations. These equations cannot be solved analytically even by considering perturbation solutions for weak interactions (Chan et al. 2009; Lai and Bremond, N. and Stone, H. A. 2009). The resulting system of these coupled partial differential equations can only be solved numerically when the form of the disjoining pressure  $\Pi(h)$  is specified. For numerical solution of these equations very significant computational effort is required due to the widely different length scales of the problem. In 2005, Carnie et al. (Carnie et al. 2005) has developed a new approach that combined boundary conditions specific to experimental setups together with a rapid and robust numerical algorithm to solve the SRYL equations. By imposing appropriate initial conditions, they solved these equations in the finite domain  $0 < r < r_{max}$  together with boundary conditions at  $r = 0$  and  $r_{max}$ . At  $r = 0$ , these boundary conditions are  $\frac{\partial h}{\partial r} = 0$ ,  $\frac{\partial p}{\partial r} = 0$ , because of axisymmetry. At  $r = r_{max}$ , the boundary condition for pressure is  $r \left( \frac{\partial p}{\partial r} \right) + 4p = 0$ . The drops at the initial separation of closest approach,  $h_0$ , are undeformed, thus a locally quadratic drop shape with the initial film thickness will be in the form (Chan et al. 2011; Chan et al. 2011):

$$h(r, t) = \begin{cases} h_0 + \frac{r^2}{2R_d} & \text{drop - wall} \\ h_0 + \frac{r^2}{2} \left( \frac{1}{R_d} + \frac{1}{R_s} \right) & \text{drop - particle} \end{cases} \quad (2.21)$$

The final boundary condition at  $r=r_{max}$  specifies how the drops are moved and is given by:

$$\frac{\partial h(r_{max}, t)}{\partial t} = \frac{dD(t)}{dt} - \frac{1}{2\pi\gamma} \frac{dF(t)}{dt} \left\{ \log \left( \frac{r_{max}}{2R_0} \right) + B(\theta_0) \right\} \quad (2.22)$$

In the force measurement experiments using the atomic force microscope, it is also essential to consider the deflection of the force sensing cantilever given by  $S = F/K$ , where  $K$  is the spring

constant of the cantilever. Therefore the last boundary condition, **eqn. 2.22**, will change to the following equation for the drop–wall or drop–particle interaction in AFM experiments (Chan et al. 2011; Chan et al. 2011):

$$\frac{\partial h(r_{max}, t)}{\partial t} = \frac{dX(t)}{dt} - \frac{1}{2\pi\gamma} \frac{dF(t)}{dt} \left\{ \log \left( \frac{r_{max}}{2R_0} \right) + B(\theta_0) - \frac{2\pi\gamma}{K} \right\} \quad (2.23)$$

where  $X$  is the position of the cantilever which can be controlled independently in the atomic force microscope. **Eqns. 2.22** and **2.23** are conditions to be imposed at the boundary of the solution domain at  $r = r_{max}$ . The Stokes–Reynolds–Young–Laplace equations together with the given boundary conditions provide a set of coupled non-linear partial differential equations. This differential algebraic equation system can be solved numerically by the “method of lines” using standard software packages (Carnie et al. 2005). Since the domain  $r_{max}$  may be up to millimeter range while the film thickness may be down in the nanometer range, appropriate scaling of the equations is required for numerical robustness. There are several attempts to compare solution of SRYL equations and data obtained in different type of experiments that measure deformations and forces (Manica et al. 2008; Manica et al. 2007; Klaseboer et al. 2000). This comparison indicate good agreements in both spatial and temporal variations of the fringe pattern or the film thickness,  $h(r, t)$ , without any adjustable parameters. This excellent agreement confirms that the Stokes–Reynolds–Young–Laplace (SRYL) equations with the assumption of tangentially immobile boundary conditions at the drop interfaces and also boundary conditions related to the experimental situation has captured the physical behaviour of the system. There are other solutions for the Stokes–Reynolds–Young–Laplace equations beginning with the classical Stefan-Reynolds model which will be discussed in more details in the next section.

### 2.1.2.2.5 Stefan–Reynolds Flat Film model

As it was already mentioned, the SRYL model cannot be solved analytically even for simple axisymmetric flow and by considering perturbation solutions in the limit of weak interactions. This apparent complexity of the SRYL model led to a number of approximate models aimed to describe film drainage process. One of these approximate solutions for the SRYL equations is based on the Stefan-Reynolds Flat Film model. The Stefan-Reynolds model has been developed with varying degrees of complexity and varying numbers of additional assumptions and parameters (Coons et al. 2003; Manev and Nguyen 2005). To illustrate this model, we will consider a drop/bubble approaching to a flat solid surface in a continuous liquid phase under the action of an external force,  $F_{ext}$ , **Figure 2.2**. In this model, the deformation is assumed to have the shape of a circular flat disc with the radius of  $a$ , which is parallel to solid surface. Solving the Navier-Stokes and continuity equations, **eqns. 2.11** and **2.12**, gives the pressure profile due to viscous flow in the film (  $p_0$  at  $r \geq a$  ):

$$P(r, t) - P_0 = \frac{3\mu}{h^3} \left( -\frac{dh}{dt} \right) (a^2 - r^2) \quad (2.24)$$

In the presence of surface forces acting across the film of area  $\pi a^2$ , the film drainage dynamics is found by a quasi-static force balance in the  $z$  direction:

$$-F_{ext} + F_{hydro} + (\pi a^2)\Pi(h) = 0 \quad (2.25)$$

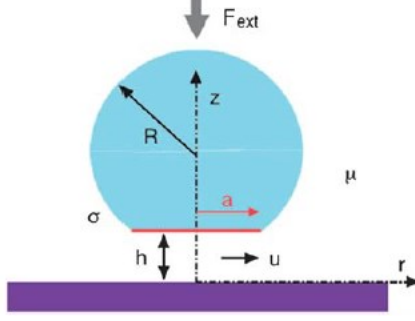


**Fig. 2.2** Schematic of the Stefan-Reynolds Flat Film model for a drop (or bubble) approaching a flat solid surface (Chan et al. 2011).

where the hydrodynamic force is derived from **eqn. 2.24**, given by:

$$F_{hydro} = 2\pi \int_0^a (p - p_0)rdr = -\frac{3\pi\mu a^4}{2h^3} \left(\frac{dh}{dt}\right) \quad (2.26)$$

If the disjoining pressure has the van der Waals form:  $\Pi(h) = -A/(6\pi h^3)$ , where  $A$  is the Hamaker constant, then the combination of **eqns. 2.25** and **2.26** gives:

$$F_{ext} + \int_0^a \frac{3\pi\mu a^4}{2h^3} \left(\frac{dh}{dt}\right) + (\pi a^2) \frac{A}{6\pi h^3} = 0 \quad (2.27)$$

By considering both the external force  $F_{ext}$  and the film radius  $a$  are independent of time, **eqn. 2.27** can be integrated to give the coalescence time,  $t$ :

$$t = \frac{\tau}{6\alpha^2} \left\{ \log \left[ \left( \frac{1+\alpha}{H+\alpha} \right)^3 \left( \frac{H^3+\alpha^3}{1+\alpha^3} \right) \right] + \sqrt{12} \left[ \arctan \left( \frac{2-\alpha}{\sqrt{3}\alpha} \right) - \arctan \left( \frac{2H-\alpha}{\sqrt{3}\alpha} \right) \right] \right\} \quad (2.28)$$

where  $H(t) \equiv h(t)/h_0$  is the scaled film thickness by the initial thickness of  $h_0$  and  $\alpha \equiv$

$\left( \frac{a^2 A}{6h_0^3 F_{ext}} \right)^{1/3}$  and  $\tau \equiv \left( \frac{3\pi\mu a^4}{2h_0^2 F_{ext}} \right)$ . Then the coalescence time or the final equilibrium thickness can

be derived from **eqn. 2.28**.

The analytical results of Stefan-Reynolds Flat Film model are limited to the special case where the external force is a known constant such as interaction under bouncy forces. However the film radius  $a$  is not known, which limits the predictive capabilities of the model. There are further developments of this model but the physical meaning of these modifications are not always well justified. In summary, in spite of increasing complexity of corrections to Stefan-Reynolds Flat Film model, it cannot achieve good quantitative agreement with experimental data (Ivanov et al. 1985; Manev and Nguyen 2005; Manev et al. 1997; Coons et al. 2003).

### 2.1.2.3 Disjoining pressure/surface force

The term disjoining pressure was historically introduced to explain experiments on the free films between air bubbles or between an air bubble and a solid surface, which were performed by Derjaguin and co-workers (Derjaguin et al. 1939). In fact, the presence of an additional pressure is essential to balance the external forces exerted on the interfaces. A positive disjoining pressure is assumed to push the two interfaces apart, “disjoin” the interfaces, and resist the film thinning. While a negative disjoining pressure pulls film interfaces together. The disjoining pressure alternatively has been defined in terms of thermodynamic variables (Eriksson and Toshev 1982). The disjoining pressure is determined by the variation in the Gibbs free energy,  $G$ , of the system with the film thickness  $h$  as (at constant chemical potential,  $\mu$ , temperature,  $T$  and surface area,  $A$ ):

$$\Pi(h) = -\left(\frac{\partial G}{\partial h}\right)_{\mu, A, T} \quad (2.29)$$

Indirect method of calculating the double layer components of the disjoining pressure is often simpler and more effective. In the colloidal stability theory, it is assumed that the net disjoining pressure can be divided into independent and additive components having different

origins. DLVO theory named after Derjaguin-Landau-Verwey-Overbeek (Derjaguin and Landau 1941; Verwey and Overbeek 1948) considers two main contributions to disjoining pressure due to van der Waals and electrostatic double layer interaction. The non-DLVO forces which are significant to bubble-particle attachment can be steric forces, hydration forces and hydrophobic forces. Assuming that the different DLVO and non-DLVO contributions are additive the disjoining pressure can be presented as:

$$\Pi_{\text{Total}}(h) = \Pi_{\text{Electrostatic}}(h) + \Pi_{\text{Van-der-Waals}}(h) + \Pi_{\text{Steric}}(h) + \Pi_{\text{Hydration}}(h) + \Pi_{\text{Hydrophobic}}(h) \quad (2.30)$$

Israelachvili (Israelachvili. J. 1991) provides a comprehensive review of various interaction forces involved in thin films.

#### 2.1.2.3.1 Electric double layer force

In general, the electrostatic forces between the charged surfaces or interfaces have received extensive attention for colloids and foams. Ionic surfactants or other dissociated species assemble at the interface, resulting in a buildup of surface charge. This in turn, creates a diffuse layer of counter-ions next to the charged surface which lead to preserve charge neutrality. This diffuse layer is partially responsible for the interaction between the charged surfaces. For a thin film by assuming a symmetric z-z electrolyte, the contribution of the electrostatic interactions can be calculated from the following equation (Newman 1991):

$$\Pi_{EL} = 2\rho_{\infty}k_B T \left[ \cosh\left(\frac{ze\Psi_m}{k_B T}\right) - 1 \right] \quad (2.31)$$

in which  $e$ ,  $\rho_{\infty}$ ,  $\Psi_m$ ,  $k_B$  and  $T$  are the unit of charge, the bulk density of ions in the system, the electrostatic potential, Boltzmann constant and absolute temperature, respectively. For relatively

low electrostatic potentials, the hyperbolic cosine can be extended and by keeping only the lowest order terms, the electrostatic interaction can be given by:

$$\Pi_{EL} = \rho_{\infty} k_B T q^2 \tanh\left(\frac{\Psi_0}{4}\right) \exp(-h\kappa) \quad (2.32)$$

where  $q$  is the charge density,  $\kappa$  is the inverse of Debye length and  $\Psi_0$  is the potential at the surface. The Debye length is the characteristic separation at which the double layers of each interface overlap and begin to interact, and defined as:

$$\kappa^{-1} = \sqrt{\frac{e^2}{\epsilon k_B T} \sum_i z_i^2 \rho_{i\infty}} \quad (2.33)$$

where  $\epsilon$  is the relative permittivity. A complete discussion of electrostatic forces in thin liquid films may be found in Ivanov (Ivanov 1988).

### 2.1.2.3.2 Van der Waals force

One of the most basic forces, present in all system are the van der Waals forces. The van der Waals interaction can be calculated using the microscopic approach proposed by Hamaker or the macroscopic approach of Lifshitz. In the microscopic approach the interaction force between two macroscopic bodies is calculated by a pairwise summation of all the relevant microscopic interactions, which are assumed to be additive. The Lifshitz approach treats each interacting material as a continuum with certain macroscopic electrodynamic properties. In this approach the London-van der Waals interaction is derived by considering the interaction of fluctuating electromagnetic fields between the two interacting materials (Mahanty, J. and Ninham, B. 1977). The Hamaker theory gives:

$$\Pi_{vdw} = -\frac{A_{123}}{6\pi h^3} \quad (2.34)$$

in which  $A_{123}$  is the Hamaker constant for the interaction between two interfaces immersed in the same solution. It is important to note that for bubble-particle interactions the Hamaker constant is always negative, and thus the van der Waals interactions are repulsive. The investigations shows that the results of the Hamaker theory are not significantly different when an experimentally determined Hamaker constant based on the Lifshitz theory is used (Nguyen and Schulze 2004).

### 2.1.2.3.3 Hydrophobic force

It is believed that the hydrophobic forces may be responsible for the film rupture. Hydrophobic forces between macroscopic hydrophobic surfaces increase with the hydrophobicity of surfaces, as defined by the contact angle of water on these surfaces (Ferrari et al. 2012). These forces have been found to be much stronger than the repulsive hydration force between hydrophilic surfaces and those predicted on the basis of van der Waals interactions (Ferrari et al. 2012). Firstly Israelachvili (Israelachvili and Pashley 1984; Israelachvili and Pashley 1982), experimentally determined the hydrophobic attractive forces between mica surfaces immersed in cetyltrimethylammonium bromide (CTAB) solutions using surface force apparatus. The mica surfaces were rendered moderately hydrophobic by the adsorption of a monolayer of this cationic surfactant, giving an advancing water contact angle of 60°. The difference between the experimental data and the DLVO forces attributed to the hydrophobic attractive force and can be best fitted by a single exponential function (Kékicheff et al. 1989; Herder 1990; Pashley et al. 1985):

$$\frac{F}{R} = K \exp(-h/\lambda) \quad (2.35)$$

in which  $\lambda$  is the decay length and  $K$  is a negative constant.  $R$  is the radius of curvature of the mica surfaces. In 1988, Claesson (Claesson and Christenson 1988) carried out experiments with uncharged Langmuir-Blodgett films of hydrocarbon and fluorocarbon surfactants. The results were quite surprising and proved the existence of hydrophobic attractive forces even at separation of 90 nm. For these experiments, the hydrophobic force was again fitted by a double exponential function with the short-range decay length from 2-3 nm for both surfaces. While the long-range decay length was 13 nm for dimethyldioctylammonium (DDOA<sup>+</sup>) ions and 16 nm for fluorocarbon surfaces. Some researchers (Yoon et al. 1997) used a power law to represent hydrophobic forces (Yoon et al. 1997; Claesson et al. 1986):

$$\frac{F}{R} = \frac{K}{6h^2} \quad (2.37)$$

This equation has the same form as the van der Waals-dispersion force, with  $K$  being the only adjustable parameter. The pioneering efforts to emphasize that the hydrophobic force plays an important role in the spontaneous rupture of the thin films between air bubbles in aqueous solution were conducted by Tchaliowska, et al. (Tchaliowska et al. 1994) and Pugh et al. (Pugh and Yoon 1994). Tchaliowska measured the thickness of thin flat film in aqueous dodecylammonium chloride (RNH<sub>3</sub>Cl) solutions using the thin film balance (TFB). The results were analyzed using the DLVO theory (which considers only electrostatic and dispersion forces) in order to estimate the interfacial potential of the liquid-air interface. Then the interfacial potential was calculated using the Gibbs adsorption isotherm based on the surface tension data (Motomura et al. 1981). It was found that the interfacial potential calculated using DLVO theory were significantly lower than those obtained by considering the Gibbs adsorption theory. The discrepancy was attributed to an additional attractive force. Pugh and Yoon (Pugh and Yoon 1994) measured the critical

film thickness in the presence of nonionic surfactants. Using these experimental results, they evaluated the magnitude of the hydrophobic forces using a single exponential force law. With the invention of AFM, direct measurement of the interaction forces between a bubble and a solid surface became possible (Binnig et al. 1986). Ducker et al. observed an attractive force between hydrophilic particles and bubbles probably due to the hydrophobic contamination in the system (Ducker et al. 1994; Fielden et al. 1996). The origin of the strong and often long-range attraction between hydrophobic surfaces has been the focus of many investigations. Different theories have been proposed to explain the origin of hydrophobic forces, involving entropic effects due to configurationally orientation and rearrangement of water molecules when two hydrophobic surfaces approach each other and correlation of dipoles on hydrophobic domains (Chandler 2005; Pashley et al. 1985; Ashbaugh et al. 1999; Cheng Y.K. and Rosicky 1998). However it is difficult to consider the hydrophobic force as a structural force because the molecular dynamic simulations showed that restructuring of water is limited to only a few layers of solvent molecules, while the long-range attractions are observed in experiment even at  $h \approx 80$  nm. In summary, there is no a single theory that can account for the diversity of phenomenon observed with hydrophobic surfaces. The initial hydrophobic force measurements were followed by a large number of studies using SFA and AFM colloidal probe technique. Based on the reported data in the literature, the vast majority of interactions measured between hydrophobic surfaces can be divided into three categories (Christenson and Claesson 2001). The first category is strongly attractive and short range occurs between apparently stable surfaces. The water contact angle on these surfaces is well over  $90^\circ$ , with relatively small hysteresis. These hydrophobic forces range up to 20 nm and are not significantly affected by electrolytes. There is no evidence about the effects of temperature or pressure on the measured interactions (Parker et al. 1994). In

the second type, there is a sharp onset of strongly attractive forces at a distance range from 25 to 250 nm, due to the presence of submicroscopic bubbles. Such forces have been found with glass and silica surfaces rendered hydrophobic by a silanation process in the gas phase. The surfaces of this type of behavior showed high contact angles of water usually above 90°. In the last category, a long-range, exponentially decaying attraction forces has been observed. These forces were measured between many surfaces rendered hydrophobic by surfactant in situ from aqueous (Herder 1990; Yoon and Ravishankar 1996) or cyclohexane solutions (Tsao et al. 1993; Tsao et al. 1993). The decay length was found to be in the range of 5 to 50 nm.

Pan et al. (2011), developed a methodology to calculate disjoining pressure from spatial and temporal profiles of wetting films. Their results indicated that the wetting films formed on a hydrophobic gold, drain much faster when the receding contact angle increases, due to the presence of negative  $\Pi(h)$  in the film. They used a double-exponential function to represent the hydrophobic force and the Frumkin–Derjaguin isotherm to analysis the experimental data and explain film rupture. They suggested that the short-range hydrophobic force is responsible for the rupture of wetting films formed on the hydrophobic surface, while the long-range hydrophobic force is responsible for the accelerated film thinning. More recently, Wang et al. (2013) used a custom-built integrated thin film drainage apparatus (ITFDA) to measure the dynamic interactions between a hydrophobic spherical glass surface and an air bubble under a wide range of air bubble approach velocities. Their observations indicated that by increasing the contact angle which represents surface hydrophobicity, the film drainage accelerates. In other words the surface hydrophobicity can control the thin film draniage between approaching surfaces. In spite of the extensive progress and innovations in surface force measurements, it is still a challenge to directly measure negative disjoining pressure. There are several reasons that make these

measurements difficult, including fast kinetics of film thinning, deformation of air/water interface, and complex interactions between hydrodynamic and surface forces.

## **2.2. Critical film thickness**

The critical film thickness, where the spontaneous self-destruction of the film occurs, has been the subject of several theoretical and experimental investigations during the past four decades (Vrij 1966; Radoev et al. 1983; Valkovska et al. 2002; Scheludko and Manev 1968; Ivanov et al. 1970; Manev et al. 1974; Sharma and Ruckenstein 1987; Angarska and Manev 2001; Coons et al. 2003). It has been demonstrated that thin aqueous films are not homogenous in thickness. It is assumed by photometric measurements the thinnest part of film is responsible for film destruction (Radoev et al. 1983). Vrij (1966) proposed that thin liquid films become unstable when long range van der Waals forces induce the growth of capillary waves on the film interfaces. However, Vrij derived an approximate equation to predict the critical film thickness but this approximate equation is valid where either the Plateau border capillary pressure drops or disjoining pressure dominates and controls film drainage. Thus, this approximate equation is not applicable for the most general case when both the Plateau pressure and disjoining pressure are significant. In fact, Vrij's theoretical approach predicts much larger values for the critical thickness than the experimental results. Ivanov et al. (Ivanov et al. 1970) again used the corrugations growth rate expressions. This rupture criterion increases the predicted critical film thickness by 15 to 20% in comparison to Vrij's approach (Coons et al. 2003). Several efforts have been made to validate these approximate equations obtained from linear stability analysis with the experimental measurements of critical thickness (Sharma and Ruckenstein 1987; Radoev et al. 1983). Both Sharma et al. and Radoev et al. developed a theoretical correlation between the critical film thickness and thinning velocity with different assumption on

corrugation growth expression. These theoretical developments referred to the average film thickness, while the results were shown to agree closely with the minimum film thickness obtained by accounting for the hydrodynamic corrugations along the film interface. The main reason for the observed discrepancy between predicted and measured critical thickness is the absence of a general theory for the prediction of the hydrodynamic corrugation amplitude and accurate data for thinning velocities. As mentioned in free liquid film, the film thickness is not homogenous and the dimple forms as thinning proceeds (Manev et al. 1997; Radoev et al. 1983; Ivanov 1988). But the drainage theories used to predict the critical film thickness, for instance the film drainage equation proposed by Manev et al. (Tsekov 1998; Manev et al. 1997), assume that the local film thickness is a homogeneous function of the average film thickness. Reynolds model underestimates thinning velocities and the theoretical Manev-Tsekov-Radoev (MTsR) equation consistently overestimates thinning velocities (Coons et al. 2005). Consequently, errors associated with the drainage theory and the prediction of thinning velocity impress on the prediction of the critical film thickness. Despite the numerous efforts, there are significant confusions and uncertainties to predict critical film thickness from physiochemical properties of the system.

### **2.3. Induction time**

The attachment between air bubbles and mineral particles occurs if there is enough bubble-particle contact time for air bubbles to displace water from mineral surfaces (Wills 1988). Three fundamental stages in bubble attachment were proposed by Nguyen et al. (Nguyen et al. 1997): (i) aqueous films thin from the initial thickness to a critical thickness, (ii) aqueous films rupture and form a three phase contact (TPC) line, and (iii) the expansion of the three phase contact line from a critical radius to a minimum radius for a stable attachment. The induction time is defined

by sum of these individual times required to complete the bubble-particle attachment processes, given by:  $t_{in} = t_t + t_r + t_e$ .

Where  $t_{in}$ ,  $t_t$ ,  $t_r$  and  $t_e$  are induction time, thinning time, rupture time and expansion time, respectively. Due to difficulties of measuring each of these times, they have been measured collectively and considered as induction time.

Early studies for the attachment of an air bubble to a mineral surface or induction time was conducted by Sven-Nilsson (Sven-Nilsson 1934) who measured attachment time by periodically oscillating a captive air bubble against a flat mineral surface. By using this technique the induction time, which is considered being the minimum time required for the aqueous film between an air bubble and a solid surface to drain to a critical thickness and rupture, was measured. This technique was developed by Glembotsky (Glembotsky 1953) in which the flat mineral surface replaced by a bed of small mineral particles. This technique has been successfully used by Eigeles and Volova (Eigeles and Volova 1960) which led to recognize the key role of induction time for flotation. They measured the induction time by moving a bed of small mineral particles toward and then away from a fixed captive bubble in an aqueous medium. Their study revealed that (1) the induction time increases linearly with increasing particle size and (2) induction time decreases exponentially with increasing temperature. Research has been conducted to understand the effect of water chemistry and particle characteristics on bubble-particle attachment. Laskowski and Iskra (Laskowski and Iskra ) showed the induction time decreases with increasing salt (KCl) concentration due to double layer suppression . The effect of pH on induction time was studied by Schulze (Schulze 1984) in a quartz-dodecyl amine system. He showed that the induction time decreases with increasing pH and reach to a minimum at pH 6.5 and a small increase until pH 8, before more decreasing for higher pH value. Despite of the

important role of air bubble-particle attachment in flotation, the research of the floatability in term of induction time measurement has received moderate attention due to both experimental and theoretical difficulties (Ye and Miller 1988).

The major improvement to measure induction time was achieved by replacing visual observations with optical interferometry to accurately determine the critical moment for two phase attachment. In this case the air bubble was driven toward the fixed particles bed and kept in contact with the particles bed for a given time and then the bubble was retracted and the occurrence of attachment was observed visually (Ye and Miller 1988; Yoon and Yordan 1991; Ye et al. 1989). If the attachment has occurred, the induction time is less or equal to, the contact time otherwise the induction time should be greater than the contact time. By using these advances in experimental techniques it was found the induction time strongly depends on the water chemistry of flotation system and the size of both air bubble and mineral particle. Yoon and Yordan (Yoon and Yordan 1991) and Ye and Miller (Ye et al. 1989) showed that the induction time increases linearly by increasing particle size, which was attributed to the longer time needed to displace the aqueous intervening film from a larger particle. Gu et al. (Gu et al. 2004) has developed the induction timer to accurately determine the induction time by employing a video-assisted system to monitor the contact process and a high-speed data-processing system to precisely control the contact time. In this induction timer, certain physical and mechanical parameters associated with the measurement were easily controlled and the influence of these parameters on the measured induction time investigated rigorously. Characterizing the influence of geometrical parameters on the measured induction time elucidates the trends of induction time with respect to the given controllable parameters. This information enables us to identify the regions in which the variation of induction time with those

parameters is minimal. Therefore, it provides a basis for optimizing the induction time. Unfortunately, in the research of Gu, the geometric complexity of the system, precluded any such theoretical prediction of the results. The results indicated that the induction time decreases with increasing the temperature and decreasing of bubble size (Gu et al. 2004; Gu et al. 2003). The recently introduced integrated thin film drainage apparatus (ITFDA) (Wang et al. 2012; Wang et al. 2013) create a possibility to study the thin liquid films confined between an air bubble and a hydrophobized glass sphere under wide range of hydrodynamic conditions. This technique is able to record the non-equilibrium force applied between two interfaces during the measurement and the induction time is measured from the force profiles. From force profiles, the induction time is measured as the time from point B to point D ( $t_{in} = t_D - t_B$ ), see **Figure 2.3**. Point B presents the moment where the interaction force between two interfaces becomes detectable and at point D the interfacial tension force at the TPC line pulls the glass sphere up, exhibits a “jump in” of the glass sphere which leads to the film rupture. The results illustrate that the liquid film drainage can be greatly controlled by controlling the solid surface hydrophobicity. However it is observed an increase in the induction time with increasing bubble drive velocity, but after a critical velocity the induction time remains constant (Wang 2013).

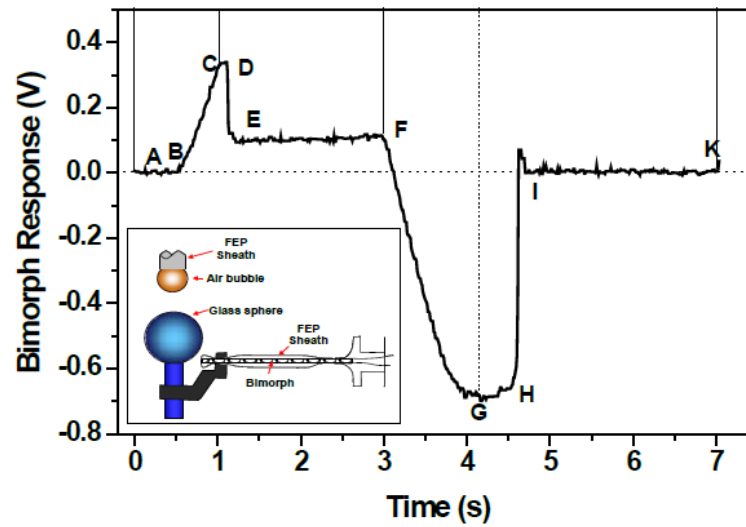


**Fig. 2.3** bimorph signal as a function of measurement time between an air bubble and a hydrophobic glass sphere ( $\theta_a = 38^\circ$ ) in 1 mM KCl solutions of pH 5.6. The bubble drive velocity was set at 240  $\mu\text{m/s}$ . Inset graph shows a schematic configuration of the integrated thin film drainage apparatus (ITFDA) (Wang 2013).

# Chapter 3

## Study of non-equilibrium interactions between an air bubble and a solid surface using linearized and non-linearized forms of

### SRYL model

#### 3.1. Introduction

Thin liquid films form between the dispersed phases in multiphase systems. An improved understanding of liquid film stability will benefit numerous industries relying on foam or emulsion products (Ivanov 1988; Fuerstenau and Herrera-Urbina *Surfactant Science Series* 1989; Ødegaard 2001). Thin films drain as a consequence of the pressure drop between the film interior and the plateau border at its perimeter (Coons et al. 2003; Ivanov 1988). As the film thickness decreases, the film pressure increases, which leads to deformation of the flexible interfaces. At smaller film thicknesses, the interfaces become more corrugated and form dimples or pimples which can lead to film rupture. Film drainage plays an important role in creating the conditions required to either maintain a stable film or destabilize the systems.

There are a number of experimental techniques to measure the non-equilibrium or dynamic interaction forces between an air bubble and a solid surface (Chan et al. 2011). The Scheludko cell was one of the earliest experimental systems designed to study thin liquid film drainage, in which a captive air bubble is pressed against a flat silica surface through a capillary tube (Platikanov 1964; Ivanov 1988; Blake and Kitchener 1972; Schulze ), or by withdrawing the liquid between the two approaching surfaces (Pan and Yoon 2010). This technique can provide the time evolution of the central film thickness, but cannot measure directly the interaction force

between an air bubble and a solid surface. The atomic force microscope (AFM) has been widely used to measure dynamic interactions between particles and air bubbles (Butt 1994; Butt et al. 1995; Ducker et al. 1994). However, the AFM method is not capable of measuring the bubble deformation. In experiments using the atomic force microscope (AFM) or the thin liquid film apparatus, the typical drive velocities span a range of 1–50  $\mu\text{m/s}$ , covering a small range of hydrodynamic condition in the intervening liquid film and low bubble Reynolds number. In most practical systems such as bubble-particle collision in flotation, the bubble-particle approach velocities are much higher, leading to significant hydrodynamic resistance between two approaching interfaces. The integrated thin film drainage apparatus (ITFDA) has recently been developed to directly and simultaneously measure the drainage time of intervening liquid films and corresponding force barrier under a wide range of bubble approach velocity or hydrodynamic conditions (Wang et al. 2013). In this device, the bubble approach velocity can be as high as 5000  $\mu\text{m/s}$ , approaching to a bubble Reynolds number of 10, which makes the ITFDA an appropriate device to study the bubble-solid interactions under dynamic conditions encountered in practical systems.

There are various theoretical approaches to estimate the hydrodynamic interactions between deformable drops and bubbles, driven by applied external forces. One of such approaches, which have received widespread attention in recent years, is the linearized SRYL (LSRYL) model. The governing equations of this model were formulated first by Ivanov et. al to describe the shape of the trapped liquid film between two bubbles (Ivanov et al. 1985). The LSRYL model was further developed by considering a new boundary condition, obtained by matched asymptotic expansions, to incorporate the weak deformation at the drop scale into the thin film scale (Dagastine et al. 2004). The comparison of the model predictions with available experimental

data (mostly at low  $Ca$  numbers) showed that the early LSRYL model is able to make accurate predictions of the shape of deformable films trapped between drops or bubbles as they undergo non-equilibrium interactions with solid surfaces or with other drops (Klaseboer et al. 2000; Manica and Chan 2011; Manica et al. 2007; Manica et al. 2008; Manica et al. 2008). Moreover, good agreements have been reported between the measured non-equilibrium forces involving drops and bubbles using the atomic force microscope (AFM) and predictions of the early LSRYL model at low  $Ca$  numbers (Vakarelski et al. 2010; Webber et al. 2008; Dagastine et al. 2006; Manor et al. 2008; Manor et al. 2008; Webber et al. 2008; Dagastine et al. 2004; Dagastine et al. 2005). One of the limitations of the experimental measurements using the AFM is that the film profile between interacting drops cannot be measured directly. Therefore the LSRYL model has been used to infer the spatial and temporal evolutions of the shape of the film between interacting drops and bubbles without experimental validation, after the LSRYL model was shown to be able to give an accurate prediction of nonequilibrium forces. Furthermore all these experiments and predictions were conducted for systems of low approach velocity or low capillary number ( $Ca = \mu V / \gamma$ , in which  $\mu$ ,  $\gamma$  and  $V$  are viscosity, interfacial tension and bubble approach velocity, respectively). The applicability of the existing LSRYL model to the systems of moderate to high capillary numbers remains to be determined. In this chapter the non-linearized SRYL (NSRYL) model is formulated and used to predict the dynamic interaction forces between deformable interfaces. In the non-linearized SRYL model, the augmented Young Laplace equation is not linearized within the interaction zone, which leads to appearance of  $Ca$  number in the scaled Young Laplace equation. Consequently the simulation results of NSRYL model are dependent on the  $Ca$  number.

The objective of this study is to compare the numerical results of the NSRYL model with the LSRYL model to determine the capillary number range where the LSRYL model is applicable. This study attempts to answer the question whether the existing LSRYL model can be confidently used to predict the shape of the film between interacting drops and bubbles, even though the existing LSRYL model has been proven to be able to predict the time dependent force profiles. By identifying the models that can precisely predict the film drainage, it is possible to determine whether the film drainage will lead to instability and rupture or not (Coons et al. 2005; Coons et al. 2005; Coons et al. 2003)

## **3.2. Experimental method**

### **3.2.1 Materials**

The glass surface used in this study was obtained by melting a  $1.5 \pm 0.1$  mm diameter Pyrex rod under a butane-oxygen flame. The glass surface prepared as such was found to be molecularly smooth with a peak-to-peak roughness determined by AFM imaging to be less than 1.2 nm. The capillary tube and the glass surface were treated in freshly prepared piranha solutions (3 H<sub>2</sub>SO<sub>4</sub>:1 H<sub>2</sub>O<sub>2</sub>, by volume) at 80-90°C for 30 min, rinsed thoroughly with Milli-Q water and blow-dried using an ultra-pure nitrogen stream. The surfaces prepared in this manner were free of contamination and completely water wettable. The sample chamber was cleaned in anhydrous ethyl alcohol (Commercial Alcohols Inc.) under ultrasonication for half an hour, rinsed with de-ionized water and then blow-dried with ultrapure nitrogen. The chamber was then filled with test solutions and placed on a three-dimensional translation stage. The capillary tube was filled with fresh air before being immersed into the solution. After generation of the bubble, the system was then left for two hours to equilibrate the interfaces.

### 3.2.2 Bubble generation and displacement control

The glass capillary tube has an inner diameter of  $1.1 \pm 0.05$  mm (Fisher Sci.). One end of the glass tube was placed under a butane flame to create a smooth end appropriate for bubble generation and film thickness measurements between air bubble and solid surfaces. Extreme caution was taken to avoid overheating which would result in a non-symmetric end of the glass tube. The bubble generation process and bubble size were monitored by real-time video observations. This arrangement allowed reproducible generation of bubbles with desired diameters of  $1.46 \pm 0.01$  mm. The other end of the capillary tube was attached to the diaphragm of a speaker that was used to control the vertical displacement of the capillary tube. A computer-generated waveform was used to control the patterns of the diaphragm displacement that in turn drove the attached air bubble towards or away from the lower glass surface in the desired manner.

### 3.2.3 Film thickness measurement

For film thickness measurements, a fresh air bubble was generated at the end of the glass tube, which is shown schematically in **Figure 3.1**. The bubble size as well as the gap between the bubble and glass surface were precisely controlled with the aid of two CCD cameras positioned perpendicular to each other in a horizontal plane near the chamber. These two cameras were also used to align the air bubble and the glass surface to geometrical symmetry. The air bubble was then driven by the speaker diaphragm through the glass tube towards the lower flat glass surface. Initially, the film thickness was reduced by moving the air bubble towards the flat glass surface by displacement of the capillary tube. Once interference patterns (Newton rings) appeared in the microscopic field of view, the film was allowed to thin spontaneously. The images were recorded by a high-speed CCD camera at a speed of 60 frames

per second. The interference patterns recorded were used to obtain time dependent film thickness profiles of the intervening liquid films trapped between the air bubble and flat glass surface. The film thicknesses were calculated using the algorithms described by Nedyalkov et al. (Nedyalkov et al. 2007). All the experiments described in this chapter were conducted by Xurui Zhang.

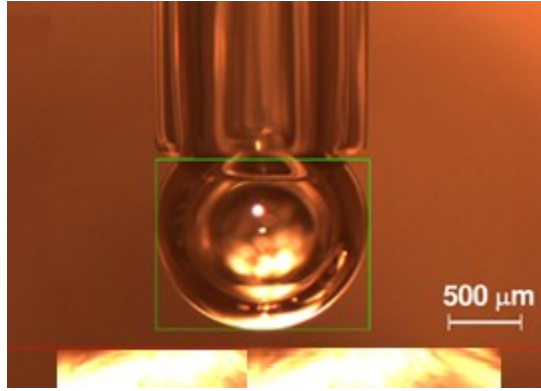


**Fig. 3.1.** A photograph of the bubble-glass sphere configuration of the thin film force apparatus (TFFA). The red line and green square are drawn to ensure the symmetry of the bubble.

### 3.3. Augmented Young Laplace model

The augmented Young-Laplace equation was firstly introduced by both Frumkin and Deryagin (Frumkin and Khim 1938; Deryagin and Khim 1940; Derjaguin 1955). In continuation of their researches, the deformation of droplets was studied in more detail by other investigators (De Gennes 1985; Brochard-Wyart et al. 1991). Yeh et al. (1999) introduced a thermodynamic analysis for a drop or bubble residing on a solid surface immersed in a continuous phase. The efforts led to the following dynamic augmented Young-Laplace equation:

$$\frac{\gamma}{r} \frac{\partial}{\partial r} \left( \frac{r h_r}{(1 + h_r^2)^{1/2}} \right) = \frac{\gamma}{r} \frac{\partial}{\partial r} (r \sin \varphi) = \frac{2\gamma}{R_L} - \Pi(h(r, t)) - p(r, t) \quad (3.1)$$

In this equation, the curvature is expressed in terms of the tangent of angle  $\varphi$ , where

$h_r \equiv \partial h / \partial r \equiv \tan \varphi$ , see **Figure 2.1**. Similar to repulsive disjoining pressure, the repulsive hydrodynamic pressure ( $p > 0$ ) will flatten the interacting zone around the drop apex. The solutions of the augmented Young Laplace equation in the interaction zone serve as a basis to define bubble deformation (Chan et al. 2011; Chan et al. 2011).

### 3.4. Formulation of the NSRYL model

The relative motion between interacting drops or between a drop and a solid particle will generate hydrodynamic interactions that arise from the flow of the continuous phase. Under Stokes flow, liquid film thinning can be described by the Reynolds lubrication theory (Batchelor 1968; Leal 2007). This theory relates the evolution of the position- and time-dependent separation,  $h(r, t)$  to the hydrodynamic pressure  $p(r, t)$ . The Stokes-Reynolds equation for film thinning is given by:

$$\frac{\partial h}{\partial t} = \frac{1}{12\mu} \frac{1}{r} \frac{\partial}{\partial r} \left[ r h^3 \left( \frac{\partial P}{\partial r} \right) \right] \quad (3.2)$$

where  $\mu$  is the shear viscosity of the Newtonian liquid. Implicit in **eqn. 3.2** is that the hydrodynamic boundary condition at the bubble surface is the same as a tangentially immobile boundary condition that holds at the glass surface. Trace surface impurities are suggested as being responsible for the observed immobile boundary condition at the bubble surface.

The liquid-air interface of the film deforms according to the Young-Laplace equation (**eqn. 3.1**) as a result of the hydrodynamic and disjoining pressures in the film and the film thickness evolution obeys the equation:

$$\frac{\gamma}{r} \frac{\partial}{\partial r} \left( \frac{r \partial h / \partial r}{(1 + (\partial h / \partial r)^2)^{1/2}} \right) = \frac{\gamma}{r} \left[ \frac{\partial h / \partial r + r \partial^2 h / \partial r^2 + (\partial h / \partial r)^3}{(1 + (\partial h / \partial r)^2)^{3/2}} \right] \quad (3.3)$$

$$= \frac{2\gamma}{R} - \Pi(h(r, t)) - p(r, t)$$

where  $\gamma$  is the surface tension of liquid.<sup>1</sup> The initial parabolic profile of the bubble is given by:

$$h(r, t) = h_0 + \frac{r^2}{2R} \quad (3.4)$$

By imposing appropriate initial conditions, **eqns. 3.2** and **3.3** are solved in the finite domain  $0 \leq r \leq r_{max}$  together with boundary conditions at  $r = 0$  and  $r_{max}$ . Because of axisymmetry, the boundary conditions become: at  $r = 0$   $\frac{\partial h}{\partial r} = 0$  and  $\frac{\partial p}{\partial r} = 0$ . For the pressure at  $r = r_{max}$ , the boundary condition is:  $r \left( \frac{\partial p}{\partial r} \right) + 4p = 0$ . The final boundary condition at  $r = r_{max}$ , which takes into account the drop deformation during the approach, is:

$$\frac{\partial h(r_{max}, t)}{\partial t} = V \frac{1}{2\pi\gamma} \frac{dF(t)}{dt} \left\{ \log \left( \frac{r_{max}}{2R} \right) + B(\theta) \right\} \quad (3.5)$$

$$B(\theta) = 1 + \frac{1}{2} \log \left( \frac{1 + \cos\theta}{1 - \cos\theta} \right) \quad (3.6)$$

and the force  $F(t)$  is given by

$$F(t) = F_{Hydrodynamic} + F_{Surface} = 2\pi \int_0^\infty p(r', t) r' dr' + 2\pi \int_0^\infty \Pi(h(r', t)) r' dr' \quad (3.7)$$

in which the hydrodynamic ( $F_{Hydrodynamic}$ ) and surface forces ( $F_{Surface}$ ) are calculated by:

---

<sup>1</sup> More information for **eqn. 3.3** is given in the Appendix A.

$$F_{Hydrodynamic} = 2\pi \int_0^{\infty} p(r',t) r' dr' \quad (3.7a)$$

$$F_{Surface} = 2\pi \int_0^{\infty} \Pi(h(r',t)) r' dr' \quad (3.7b)$$

In **eqn. 3.7** the the total force acting on the bubble can be calculated by considering hydrodynamic and disjoining pressures,  $p$  and  $\Pi$ , respectively. In this study only contribution from van der Waals and electrical double layer interactions are considered in the disjoining pressure in the DLVO theory (Verwey and Overbeek 1955).

Van der Waals interaction force between an air bubble and the glass surface is calculated using Lifshitz theory (Israelachvili. J. 1991) and the electrical double layer force is calculated by a numerical solution of the nonlinear Poisson-Boltzmann equation using the algorithm of Chan et al (Chan 2002; McCormack et al. 1995).

### 3.4.1 Scaling of the governing equations

The NSRYL equations can be non-dimensionalized with the following scaling parameters in which the dimensionless variables are denoted by asterisks (Klaseboer et al. 2001):

$$\begin{aligned} \text{film thickness: } h &\equiv [Ca^{1/2}R] h^* \\ \text{radial coordinate: } r &\equiv [Ca^{1/4}R] r^* \\ \text{time: } t &\equiv [Ca^{1/2}R/V] t^* \\ \text{pressure: } p &\equiv [\gamma/R] p^* \\ \text{disjoining pressure: } \Pi &\equiv [\gamma/R] \Pi^* \\ \text{force: } F &\equiv [(\gamma/R) (Ca^{1/4}R)^2] F^* \equiv [Ca^{1/2} \gamma R] F^*. \end{aligned} \quad (3.8)$$

where  $V \sim dX(t)/dt$  is displacement velocity and  $Ca \equiv \mu V / \gamma$  is the capillary number that is

the ratio of viscous forces to capillary forces. In terms of the scaled variables, the Stokes-Reynolds equation that describes film drainage between a bubble and a solid sphere, **eqn. 3.2**, becomes:

$$\frac{\partial h^*}{\partial t^*} = \frac{1}{12r^*} \frac{\partial}{\partial r^*} \left( r^* h^{*3} \frac{\partial p^*}{\partial r^*} \right) \quad (3.9)$$

and **eqn. 3.3** for film thickness becomes

$$\frac{1}{r^*} \left[ \frac{\partial h^*/\partial r^* + r^* \partial^2 h^*/\partial r^{*2} + Ca^{0.5} (\partial h^*/\partial r^*)^3}{(1 + Ca^{0.5} (\partial h^*/\partial r^*)^2)^{\frac{3}{2}}} \right] = 2 - p^* - \Pi^{**} h_0 + \frac{r^2}{2R} \quad (3.10)$$

The initial condition, **eqn. 3.4** now has the form

$$h^*(r^*, 0) = h_o^* + \frac{(r^*)^2}{2} \quad (3.11)$$

A remarkable observation of these equations is that the scaled Young Laplace equation contains the capillary number. Therefore, in spite of the LSRYL model, the governing equations (**eqns. 3.9** and **3.10**) of the NSRYL model depend on the physical parameters of the system via capillary number. Moreover the boundary condition at  $r^*_{max}$  (**eqn. 3.5**) has a weak logarithmic dependence on the capillary number  $Ca$

$$\frac{\partial h^*(r^*_{max}, t^*)}{\partial t^*} = -1 + \frac{1}{2\pi} \frac{dF^*}{dt^*} \left\{ \frac{2\pi\gamma}{K} - \log\left(\frac{1}{2} Ca^{1/4} r^*_{max}\right) - B(\theta) \right\} \quad (3.12)$$

The left hand side of **eqn. 3.10** is the small deformation approximation of mean curvature of  $h^*$ . If the disjoining pressure is negligible, that is  $\Pi^* \ll (\gamma/R)$ , then this curvature changes sign when the scaled pressure  $p^* \equiv (R/\gamma) p$  has the numerical value of 2. Further to solve the governing equations of the NSRYL model, the  $r^*_{max}$  is selected as its

maximum value and this is a criterion to solve this model. Using  $r_{max}^*$  as its maximum value (especially when this maximum is large compared to the bubble radius) is in contrast with the lubrication theory, in which the liquid only assumed to flow in the radial direction. But the presence of continuity equation (in which the liquid assumed to flow in both radial and vertical directions) in the Stokes-Reynolds equation, makes it reasonable to use  $r_{max}^*$  as its maximum value in the NSRYL model.

### 3.5. Formulation of the LSRYL model

The Stokes-Reynolds equation by considering the tangentially immobile boundary condition at the bubble surface is given by **eqn. 3.2**. Within the interaction zone or the inner region defined by the interval  $r=0$  to  $r=r_{rim}$ , the drop interface is relatively flat on the scale of the drop size. Considering a good approximation of  $\tan\varphi = \partial h/\partial r \ll 1$ , the augmented Young–Laplace equation (**eqn. 3.1**) can be linearized to give:

$$\frac{\gamma}{r} \frac{\partial}{\partial r} \left( r \frac{\partial h}{\partial r} \right) = \frac{2\gamma}{R} - \Pi - p \quad (3.13)$$

The other conditions including the initial and boundary conditions are the same as in the NSRYL model, which are described in Section 3.4. The linearized Stokes-Reynolds-Young-Laplace equations can be cast into a universal form using the scaling parameters given with **eqn. 3.8**. In terms of the scaled variables, the Stokes-Reynolds equation (**eqn 3.2**) becomes

$$\frac{\partial h^*}{\partial t^*} = \frac{1}{12r^*} \frac{\partial}{\partial r^*} \left( r^* h^{*3} \frac{\partial p^*}{\partial r^*} \right) \quad (3.14)$$

and **eqn. 3.13** for film thickness becomes

$$\frac{1}{r^*} \frac{\partial}{\partial r^*} \left( r^* \frac{\partial h^*}{\partial r^*} \right) = 2 - p^* - \Pi^* \quad (3.15)$$

Non-dimensional form of the initial and boundary conditions are the same as in the NSRYL model and given by **eqns. 3.11** and **3.12**. The LSRYL model is well established and readers are referred to the literature for more details (Chan et al. 2011; Chan et al. 2011). An important feature of governing **eqns. 3.14** and **3.15** is their universal nature, i.e., these scaled equations contain no other physical parameters except for the scaled disjoining pressure in **eqn. 3.15**. Indeed, the linearized SRYL model has a weak dependency to capillary number  $Ca$ , only via the boundary condition at  $r^*_{max}$ , **eqn. 3.12**. However, it was justified that using this boundary condition (**eqn. 3.12**) the predicted force curves are independent of  $r^*_{max}$  for  $r^*_{max} > 15$  (Carnie et al. 2005), in this chapter  $r^*_{max}$  is considered as 26 to solve the governing equations of the LSRYL model. Similar to the NSRYL model, due to presence of continuity equation in the Stokes-Reynolds equation, it is reasonable to use  $r^*_{max}$  as 26 in the LSRYL model.

### 3.6. The difference between the two model equations: NSRYL and LSRYL

Comparison between the equations of two models reveals that the only difference between the non-linearized and linearized SRYL model is the Young Laplace equation. In the scaled Young Laplace equation used in the NSRYL model, **eqn. 3.10**, the scaled hydrodynamic repulsive force can be obtained by the following equation:

$$p^* = 2 - \frac{1}{r^*} \left[ \frac{\partial h^* / \partial r^* + r^* \partial^2 h^* / \partial r^{*2} + Ca^{0.5} (\partial h^* / \partial r^*)^3}{(1 + Ca^{0.5} (\partial h^* / \partial r^*)^2)^{\frac{3}{2}}} \right] - \Pi^* \quad (3.16)$$

In the LSRYL model the scaled hydrodynamic force of **eqn. 3.15**, becomes:

$$p^* = 2 - \frac{1}{r^*} (\partial h^* / \partial r^* + r^* \partial^2 h^* / \partial r^{*2}) - \Pi^* \quad (3.17)$$

This comparison demonstrates that the estimation of two models for the scaled hydrodynamic force is different. This comparison also shows that the scaled hydrodynamic force predicted by the NSRYL model depends on the  $Ca$  number. Therefore it is expected that the estimation of the non-equilibrium interaction forces and film profiles by these two models would be different as discussed in Section 3.7.

### 3.7. Results

In this section, the dynamic interactions between an air bubble and a hydrophilic flat surface are theoretically studied using both the LSRYL and NSRYL models. The numerical results of the NSRYL model and LSRYL model are then compared with the experimental data obtained by Xurui Zhang. For the theoretical comparison, an air bubble is formed in a liquid at the end of a glass capillary tube. The bubble moves towards and then backs from the solid surface, **Figure 3.2**. This schematic diagram is similar to the Integrated Thin Film Drainage Apparatus (Wang 2013), which is a combination of induction time instrument (Gu et al. 2003) and Measurement and Analysis of Surface Interactions and Forces device (Parker 1992; Parker and Attard 1992), except that in the ITFDA a glass sphere instead of flat surface was used as solid surface.

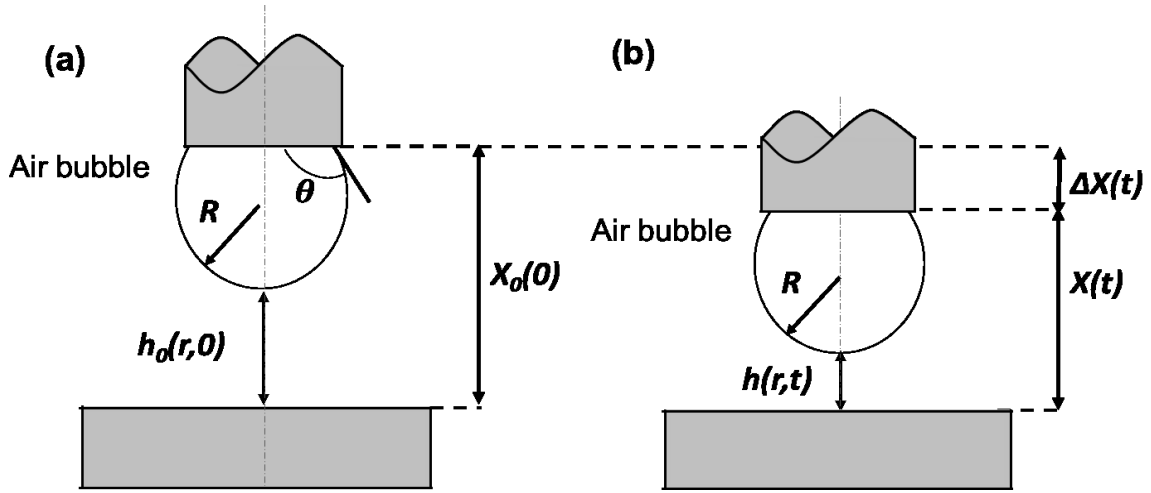


**Fig. 3.2.** Schematic diagram of the geometry between an air bubble and a flat surface at two times of  $\theta$  (a) and  $t$  (b).  $X(t)$  measures the distance between the position of the glass capillary tube and the reference point of the flat solid surface.  $R$  is bubble radius and  $h(r, t)$  is the film thickness.  $\theta$  is unperturbed angle of the bubble on the bottom of the capillary tube. The capillary tube displacement considered as  $\Delta X(t) = X(t) - X_0(\theta)$ .

Water is considered as the bulk fluid with viscosity and surface tension being 0.001 Pa.s and 0.072 N/m, respectively. The effect of different bubble driving velocities ranging from 1  $\mu\text{m/s}$  to 150000  $\mu\text{m/s}$  (corresponding to a capillary number range from  $1.4 \times 10^{-8}$  to  $2.06 \times 10^{-3}$ ) on the non-equilibrium interaction forces, the hydrodynamic repulsive force and the film profile is studied. To minimize the effect of the disjoining pressure,  $\Pi(h(r, t))$ , due to the surface forces, the electrical double layer is suppressed by considering high electrolyte concentration of 100mM KCl in the current study. By increasing the salt concentration, the double layer repulsive force is anticipated to be decreased. As a result, the equilibrium film will be thinner and the dimple will take longer to drain (Manica and Chan 2011). Therefore this work is mostly a fundamental study on the applicability of the NSRYL model and LSRYL model to predict the hydrodynamic repulsive force between two approaching interfaces. In this section, we show the simulation results of both the NSRYL and LSRYL models for the interactions between an air bubble and a

solid surface over a wide range of  $Ca$  numbers from  $10^{-8}$  to  $10^{-3}$ . Identical bubble radius of  $750\ \mu\text{m}$  is used in all of the studies reported in this chapter. The parameters used in the theoretical study are summarized in **Table 3.1**.

**Table 3.1.** Parameters used in the theoretical study.

Bubble radius, $R_b$	$750\ \mu\text{m}$
Surface tension, $\gamma$	$72.8\ \text{mN/m}$
Viscosity, $\mu$	$1\ \text{mPa s}$
KCl	$100\ \text{mM}$
pH	$5.6$
Scaled initial separation, $h(0,0)$	$150$
Scaled approach time	$180$
Zeta potential of air bubble	$-5\ \text{mV}$
Zeta potential of glass surface	$-5\ \text{mV}$
Hamaker constant	$-8 \times 10^{-21}\ \text{J}$

### 3.7.1 Comparison of the NSRYL model with the LSRYL model

#### 3.7.1.1 Comparison at $Ca$ number of $10^{-8}$

We now present results of the LSRYL model and NSRYL model applied to an aqueous thin film between a bubble and a hydrophilic flat surface. The results in **Figure 3.3** are for an initial separation of  $13.37\ \mu\text{m}$  of bubble from the solid surface, which is equal to the scaled initial separation of  $h_0^*=150$ . The bubble is first driven towards the solid surface at bubble approach velocity of  $1\ \mu\text{m/s}$  for  $16.05\ \text{s}$ , which corresponds to the scaled approach time of  $t^*=180$ , and then it is retracted away from the solid surface at the same velocity. This approach time is equivalent to a total glass tube displacement of  $16.05\ \mu\text{m}$ . The physical parameters used in the NSRYL and LSRYL models calculations are given in **Table 3.2**. At this capillary number the  $r_{max}^*$  is considered as 26 (correspond to  $r_{max}$  of  $\sim 213\ \mu\text{m}$ ) to solve both the LSRYL and NSRYL

models. Compare to the bubble radius ( $750 \mu\text{m}$ ) the selected  $r_{max}$  is  $\sim (0.3R_{\text{bubble}})$ . In this table, the overlap determines the extent that the bubble has been pushed to the solid surface, i.e., the extent of bubble deformation. The overlap is calculated as the difference between the glass tube displacement and the initial separation,  $(\Delta X - h_0)$ .

**Table 3.2.** Value of physical parameters used in the NSRYL model and LSRYL model calculations at  $Ca$  number of  $10^{-8}$  with scaled approach time of 180.

	Initial separation [ $\mu\text{m}$ ] $h_0$	Scaled initial separation $h_0^*$	Glass capillary tube displacement [ $\mu\text{m}$ ] $\Delta X$	Overlap [ $\mu\text{m}$ ] $\Delta X - h_0$
LSRYL	13.37	150	16.05	2.674
NSRYL	13.37	150	16.05	2.674

**Figure 3.3a** shows the results of time evolution of the scaled interaction force in approach-retract cycle, while **Figure 3.3b** shows the non-scaled form of the results. These figures confirm that the time dependent force predicted using the NSRYL model matches well with that predicted using the LSRYL model. Due to negligible disjoining pressure in the calculations, the increasing repulsive force towards the force maximum during the approach phase is solely due to hydrodynamic repulsion. The repulsive force then decreases steadily during the retract phase. The attractive (negative) force minimum in the retract phase is attributed to the hydrodynamic suction as the bubble separates from the solid surface. Similar hydrodynamic attractive force during separation of two surfaces in contact is well recognized (Chan et al. 2011).

The variation of hydrodynamic repulsive force with the central film thickness during the approach of the air bubble towards the solid surface is given in **Figure 3.3c**. The hydrodynamic repulsive force is calculated using **eqn. 3.7a**. This figure shows that the hydrodynamic force becomes significantly more repulsive with decreasing film thickness, as water has to be

displaced from the intervening aqueous film trapped between the approaching interfaces. The results in **Figure 3.3c** confirm that at low  $Ca$  number, both models predict the same variation of hydrodynamic repulsive force as a function of film thickness. The inset of **Figure 3.3c** shows the normalized variation of hydrodynamic repulsive force with the film thickness. In **Figure 3.3d**, we show the predicted film profiles with both models during the approach of the air bubble towards the solid surface in aqueous electrolyte solutions. Profiles  $E_1$  and  $E_2$  present the film profile when the dimple starts to form under the condition that the pressure drop across the liquid/air interface becomes zero or the scaled film pressure at the center, i.e.  $p_{film}^*(0, t)$ , reaches 2 as shown by **eqn. 3.18**.

$$\Delta p(r, t) = p_c(2 - p_{film}^*(r, t)) = p_c[2 - p_{hydrodynamic}^*(r, t) - \Pi_{classical}^*(r, t) - p_{hydrophobic}^*(r, t)] \quad (3.18)$$

in which  $p_c = \gamma/R$  is Laplace pressure of bubble. After profiles  $E_1$  and  $E_2$ , the large and repulsive hydrodynamic force and small disjoining pressure lead to an inversion in the curvature and after the approaching time of 16.05 s ( $t^*=180$ ) the bubble reaches profiles  $F_1$  and  $F_2$  at the end of approach phase. Profiles  $E_1$  and  $F_1$  represent the results of the LSRYL model and profiles  $E_2$  and  $F_2$  represent the results of the NSRYL model. **Figure 3.3d** indicates that both the LSRYL and NSRYL models led to the same prediction of spatial evolution of film profile. From profiles  $E_1$  and  $E_2$ , the dimple forms at the central film thickness about  $\sim 48$  nm. The minimum film thickness reached during the approach cycle is about  $\sim 33$  nm, profiles  $F_1$  and  $F_2$ . The large minimum film thickness at the end of approach phase confirms that the long-range hydrodynamic pressure rather than the disjoining pressure is responsible for the formation of the

dimple and its development. The inset of **Figure 3.3d** shows the normalized results for the variation of film profiles with the film radius.

It is known that the experimental techniques based on the AFM can measure the interaction force but are incapable of measuring the bubble deformation. The experiments conducted by AFM are under low velocity, which mostly give capillary number in the range of  $10^{-8}$  (Nguyen et al. 2003; Chan et al. 2011). The results in **Figure 3.3** show that at  $Ca$  number of  $10^{-8}$  both the NSRYL and LSRYL models can be confidently used to predict the spatial and temporal evolutions of the film profiles once these two models are shown to be able to predict the non-equilibrium forces measured by AFM.

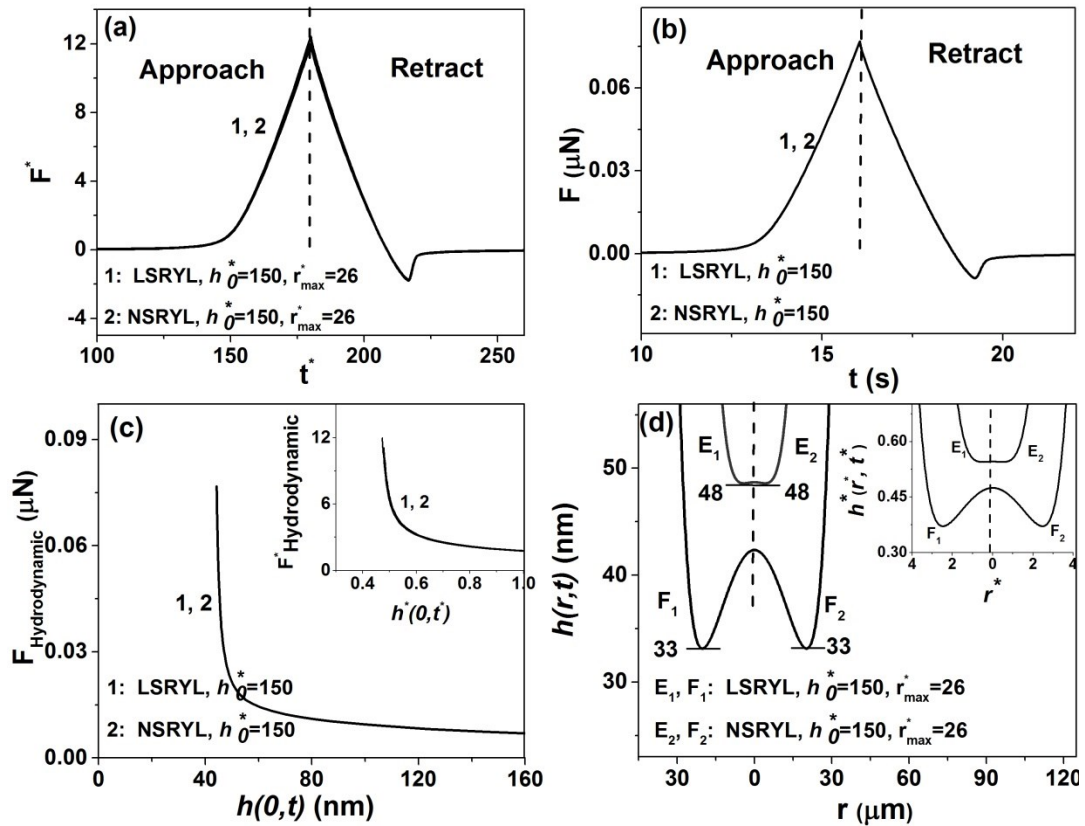


**Fig. 3.3.** (a) Variation of scaled force with scaled time, (b) time dependent force profile, (c) variation of hydrodynamic force with thickness of aqueous film at the axis of symmetry, and (d) variation of film thickness with film radius in aqueous electrolyte (100 mM KCl, pH = 5.6) at a

bubble approach velocity of  $1 \mu\text{m/s}$ , corresponding to a capillary number of  $1.4 \times 10^{-8}$ - the LSRYL model results are denoted with 1 and the NSRYL model results are denoted with 2. Insets: (c) Variation of scaled hydrodynamic force with scaled film thickness at the axis of symmetry, and (d) variation of scaled film thickness with scaled film radius. The immobile boundary condition at bubble surface was used in the two models.

Although **Figure 3.3** shows the simulation results of two models with the  $r_{max}^*$  of 26 (correspond to  $r_{max}$  of  $\sim 213 \mu\text{m}$ ), but the maximum  $r_{max}^*$  to solve the NSRYL model is  $\sim 88$  (correspond to  $r_{max}$  of  $\sim 720 \mu\text{m}$ ). The comparison of both models with the same  $r_{max}^*$  of 88 is shown in **Figure 3.4**. This figure demonstrates that even for the  $Ca$  number in the range of  $10^{-8}$ , when the two models are solved with the  $r_{max}$  close to the bubble radius, the difference between the prediction of two models for time dependent force profile is remarkable. The difference between the predicted force with two models can be important especially when the force is very small in the range of nano Newton (nN), but it is not significant for larger force in the range of  $\mu\text{N}$  (due to the very small  $Ca$  number). The inset of **Figure 3.4a** shows that the LSRYL model overestimates the hydrodynamic repulsive force. There is also difference in the prediction of film profiles with two models, but this difference is negligible, **Figure 3.4b**. Approximately we can say that for  $Ca$  number in the range of  $10^{-8}$ , the prediction of two models for time dependent force profile and film profile is the same, especially when the interaction force is in the range of  $\mu\text{N}$ .

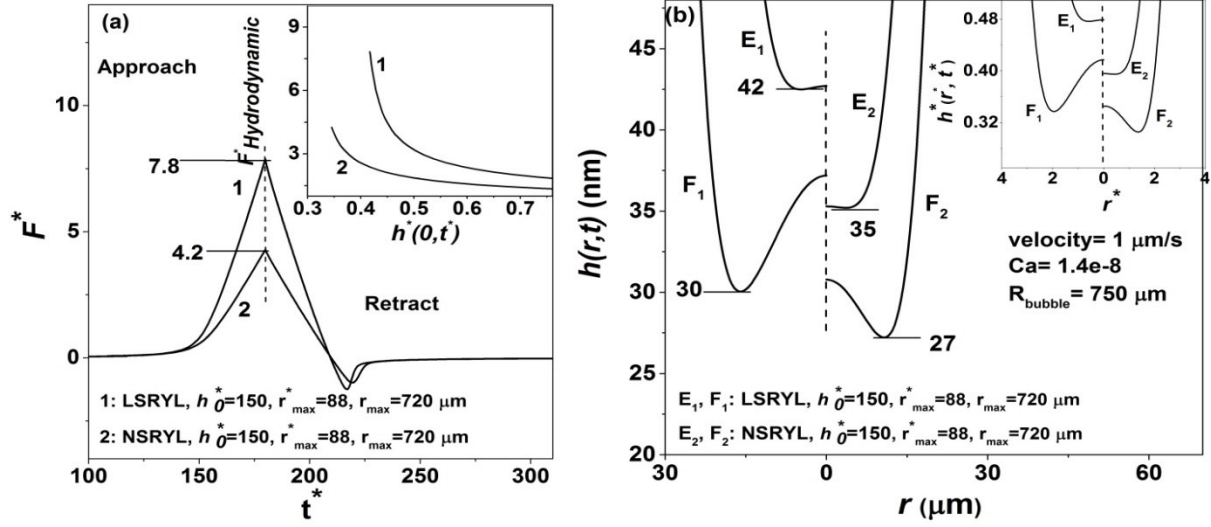


**Fig. 3.4.** (a) Variation of scaled force with scaled time, (b) variation of film thickness with film radius in aqueous electrolyte (100 mM KCl, pH = 5.6) at a bubble approach velocity of 1  $\mu\text{m/s}$ , corresponding to a capillary number of  $1.4 \times 10^{-8}$ - the LSRYL model results are denoted with 1 and the NSRYL model results are denoted with 2. Insets: (a) Variation of scaled hydrodynamic force with scaled film thickness at the axis of symmetry, and (b) variation of scaled film thickness with scaled film radius. In this run, the  $r_{max}^*$  is 88 (correspond to  $r_{max}$  of 720  $\mu\text{m}$ ). The physical parameters used in the NSRYL and LSRYL models summarized in Table 3.1 and **Table 3.2**. The immobile boundary condition at bubble surface was used in the two models.

As mentioned, there is limitation to choose the  $r_{max}$  with the NSRYL model and the maximum  $r_{max}$  that the NSRYL model can be solved with that, is around the bubble radius. Actually choosing of  $r_{max}$  is very important due to the term  $\left(\frac{\partial h}{\partial r}\right)^2$ , which is kept in the non-linear Young-Laplace equation (**eqn. 3.3**) of the NSRYL model. The simulation results of the NSRYL model shows that the importance of this term  $\left(\frac{\partial h}{\partial r}\right)^2$ , is around the edge of bubble, **Figure 3.5**. The magnitude of this term is negligible in proximity of the center but its magnitude significantly increases around the edge of bubble. As a result the choosing of  $r_{max}$  is very important and should

be around the bubble radius. In the LSRYL model, this term is ignored as compared to unity (in **eqn. 3.3**) at all the  $r_{max}$  tested.

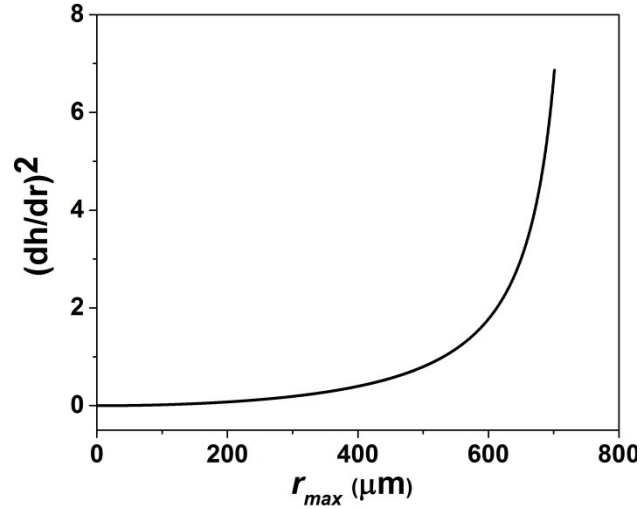


**Fig. 3.5.** Variation of  $\left(\frac{\partial h}{\partial r}\right)^2$ , in eqn. 3.3, as a function of  $r_{max}$  in aqueous electrolyte solutions (100 mM KCl, pH = 5.6) at the bubble approach velocity of  $1 \mu\text{m/s}$ , corresponding to a capillary number of  $1.4 \times 10^{-8}$ . The physical parameters used in the NSRYL are the same as in **Table 3.1** and **Table 3.2**.

### 3.7.1.2 Comparison at $Ca$ number of $5.15 \times 10^{-6}$

In **Figure 3.6** we compare the results of the NSRYL model with the predictions of the LSRYL model for film drainage between a bubble and a hydrophilic solid surface at bubble approach velocity of  $375 \mu\text{m/s}$ . At this capillary number the  $r_{max}^*$  is considered as 26 and 20 (correspond to  $r_{max}$  of  $\sim 935 \mu\text{m}$  and  $\sim 719 \mu\text{m}$ ) to solve the LSRYL and NSRYL models, respectively. The comparison of both models with the same  $r_{max}^*$  of 20 ( $r_{max}$  of  $\sim 719 \mu\text{m}$ ) can be found in Appendix B1. This approach velocity is higher than the approach velocity used in the experiments conducted by AFM. Firstly, the bubble is kept at the initial separation of  $255.33 \mu\text{m}$  which corresponds to a scaled initial thickness of  $h_0^* = 150$ . The bubble moves towards the surface for  $\sim 0.82 \text{ s}$  ( $t^* = 180$ ) and then away from the surface at the same speed. This approaching time is

equivalent to a glass tube displacement of 306.39  $\mu\text{m}$ , **Table 3.3**. A typical approach-retract cycle that shows variations of the interaction force with time is shown in **Figures 3.4a**. This force is mainly from hydrodynamic repulsive force. The results in this figure indicate that the predicted force maximum during the approach phase with the NSRYL model is smaller than that predicted from the LSRYL model. In other words, the LSRYL model predicts a higher hydrodynamic repulsive force for a  $Ca$  number of  $5.15 \times 10^{-6}$ . The variation of hydrodynamic repulsive force with the central film thickness in approach phase is shown in **Figure 3.6c**. Again the results in this figure confirm that for a  $Ca$  of  $5.15 \times 10^{-6}$  the LSRYL model predicts higher hydrodynamic repulsive force compared to the NSRYL model. In **Figure 3.6d**, we compare the prediction of two models for the spatial evolution of the film profiles when the bubble is driven towards the solid surface with the scaled initial thickness of  $h_0^*=150$ . Profiles  $E_1$  and  $E_2$  (predicted from the LSRYL model and NSRYL model, respectively) show where the dimple starts to form. From profiles  $E_1$  and  $E_2$ , the LSRYL model appears to predict the initial formation of dimple at larger film thickness than the NSRYL model. The NSRYL model predicts that the dimple initially forms at  $\sim 890$  nm, while using the LSRYL model dimple appears at  $\sim 961$  nm. Furthermore the higher hydrodynamic force predicted with the LSRYL model influences on the minimum film thickness reached during the approach cycle. Profiles  $F_1$  and  $F_2$  (predicted with the LSRYL model and NSRYL model, respectively) of **Figure 3.6d** show that the minimum film thickness reached in the approach phase with the NSRYL model is  $\sim 598$  nm which is smaller than  $\sim 635$  nm predicted with the LSRYL model. As we know, the drop deformation (either initial formation of dimple or its development) during interaction is determined by the balance among the hydrodynamic pressure, disjoining pressure and capillary pressure (Chan et al. 2011).

The observed differences in bubble deformation arise from larger hydrodynamic repulsive force predicted by the LSRYL model than that predicted by the NSRYL model.

Again we solve the system with the LSRYL model by just increasing the initial separation to 262.99  $\mu\text{m}$ , corresponding to the scaled initial thickness of 154.5. The bubble is driven to solid surface for  $\sim 0.82$  s ( $t^*=180$ ) and then retracts. As shown in **Table 3.3**, the glass tube displacement is the same as 306.39  $\mu\text{m}$ . Therefore at the same glass tube displacement, the higher initial separation leads to a lower overlap which means a smaller extent that the bubble and solid surface are pushed together. **Figure 3.6b** shows that by increasing the initial thickness the interaction force profile predicted with the LSRYL model ( $h_0^*=154.5$ , denoted with 3) is in good agreement with that predicted by the NSRYL model ( $h_0^*=150$ , denoted with 2). However by increasing the initial separation to  $h_0^*=154.5$ , the force profile predicted by the LSRYL model reaches a smaller force maximum during the approach phase, but the predicted hydrodynamic repulsive force with the LSRYL model remains higher than that predicted by the NSRYL model, line 3 in **Figure 3.6c**. The results of the spatial evolution of film profiles using the LSRYL model with increasing the scaled initial thickness to  $h_0^*=154.5$  are given by profiles  $E_3$  and  $F_3$  in **Figure 3.6d**. Profile  $E_3$  which is coincident with profile  $E_1$ , indicates the formation of dimple at  $\sim 961$  nm which is larger than prediction of the NSRYL model. Profile  $F_3$  shows that contrary to the good agreement for the force profile, the difference between the LSRYL model and NSRYL model for spatial evolution of film profile increases and the minimum film thickness in the approach phase predicted by the LSRYL model increases to  $\sim 678$  nm. In other words at this  $Ca$  number, even though the LSRYL model is shown to give an accurate account of time dependent force profile, we cannot confidently use the LSRYL model to predict the spatial and temporal evolutions of the shape of the film trapped between the interacting interfaces. The comparison of

both models at  $Ca$  of  $5.15 \times 10^{-6}$  with the same  $r_{max}^*$  of 20 ( $r_{max}$  of  $\sim 719 \mu\text{m}$ ) in the Appendix B1 shows that there is even more difference between two models compare to **Figure 3.6**.

**Table 3.3.** Value of physical parameters used in the NSRYL model and LSRYL model calculations at  $Ca$  number of  $5.15 \times 10^{-6}$  with scaled approach time of 180.

	Initial separation [ $\mu\text{m}$ ] $h_0$	Scaled initial separation $h_0^*$	Glass capillary tube displacement [ $\mu\text{m}$ ] $\Delta X$	Overlap [ $\mu\text{m}$ ] $\Delta X - h_0$
LSRYL	255.33	150	306.39	51.06
LSRYL	262.99	154.5	306.39	43.40
NSRYL	255.33	150	306.39	51.06

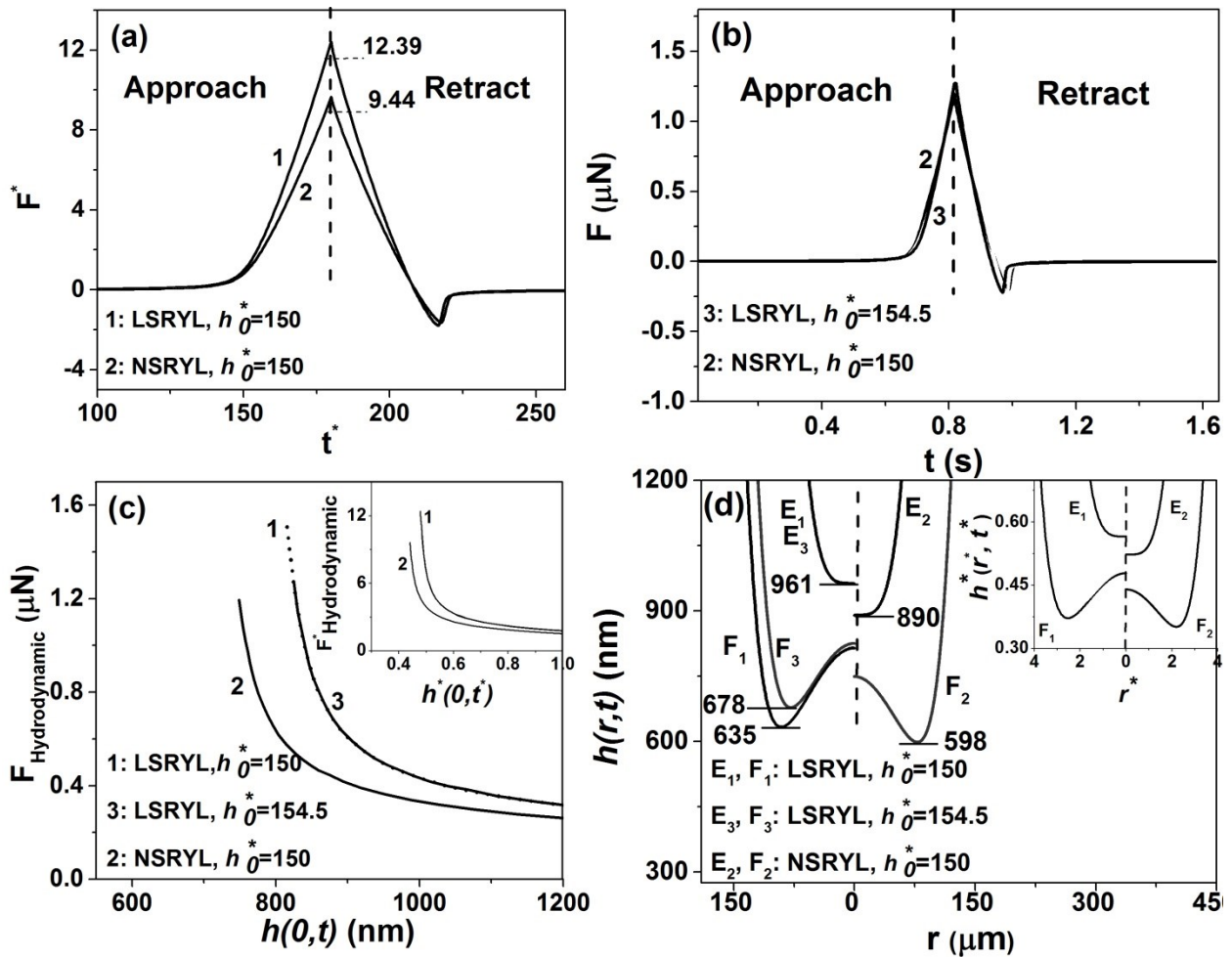


**Fig. 3.6.** (a) Variation of scaled force with scaled time, (b) time evolution of force, (c) variation of hydrodynamic force with thickness of aqueous film at the axis of symmetry, and (d) variation of film thickness with film radius in aqueous electrolyte solutions (100 mM KCl, pH = 5.6) at a bubble approach velocity of 375  $\mu\text{m/s}$ , corresponding to a capillary number of  $5.15 \times 10^{-6}$ . The NSRYL model results are denoted with 2 and the LSRYL model results are denoted with 1 and 3. Insets: (c) Variation of scaled hydrodynamic force with scaled film thickness at the axis of symmetry, and (d) variation of scaled film thickness with scaled film radius. The immobile boundary condition at bubble surface was used in the two models.

### 3.7.1.3 Comparison at $Ca$ number of $3.4 \times 10^{-5}$

In **Figure 3.7** we compare the results for the NSRYL model and LSRYL model at  $Ca=3.4 \times 10^{-5}$ , corresponding to a bubble approach velocity of 2500  $\mu\text{m/s}$ . At this capillary number the  $r_{max}^*$  is considered as 26 and 12.9 (correspond to  $r_{max}$  of  $\sim 1503 \mu\text{m}$  and  $\sim 745 \mu\text{m}$ ) to solve the LSRYL and NSRYL models, respectively. The maximum  $r_{max}$  that the NSRYL model can solve with that, is around the bubble radius (750  $\mu\text{m}$ ). The comparison of both models with the same  $r_{max}^*$  of 12.9 ( $r_{max}$  of  $\sim 745 \mu\text{m}$ ) can be found in Appendix B2. The time-dependent force profile between an air bubble and a hydrophilic solid surface, in 100 mM KCl aqueous electrolyte solutions, predicted with both models is shown in **Figure 3.7a**. The bubble is initially kept at the separation of 659.26  $\mu\text{m}$  ( $h_0^*=150$ ) from the solid surface. The bubble is driven towards the solid surface by moving the capillary tube for  $\sim 0.32 \text{ s}$  ( $t^*=180$ ) and then retracted at the same speed. The approaching time is equivalent to capillary tube displacement of  $\sim 791 \mu\text{m}$  or overlap of  $\sim 132 \mu\text{m}$ , **Table 3.4**. **Figure 3.7a** shows that the LSRYL model predicted a much larger force maximum of  $\sim 12.39$  during approach phase as compared to the NSRYL model which predicts a force maximum of  $\sim 5.01$ . As already mentioned, this force is solely due the hydrodynamic repulsion. It is therefore evident that at the  $Ca$  number of  $3.4 \times 10^{-5}$  the hydrodynamic repulsive force predicted by the LSRYL model

is significantly higher than that predicted by the NSRYL model.

The variation of hydrodynamic repulsive force with the central film thickness in approach phase is shown in **Figure 3.7c**. The results in this figure confirms that the hydrodynamic force calculated with the LSRYL model is significantly higher than that calculated by the NSRYL model. The spatial evolution of the film profiles predicted by the two models is shown in **Figure 3.7d**. Profiles  $E_1$  and  $E_2$  of **Figure 3.7d** show that the LSRYL model predicts the formation of the dimple at  $\sim 2481$  nm which is much higher than the value of  $\sim 1828$  nm predicted by the NSRYL model. From profile  $F_1$  in **Figure 3.7d**, the LSRYL model predicts a minimum film thickness of  $\sim 1636$  nm reached during the approach. This minimum film thickness is much thicker than  $\sim 1407$  nm predicted by the NSRYL model, profile  $F_2$ . As mentioned earlier, the drop deformation is determined by the balance between hydrodynamic pressure, disjoining pressure and capillary pressure (Chan et al. 2011). The observed differences can be attributed to different predictions of hydrodynamic repulsive force with these two models. The comparison of both models at  $Ca$  of  $3.4 \times 10^{-5}$  with the same  $r_{max}^*$  of 12.9 ( $r_{max}$  of  $\sim 745$   $\mu\text{m}$ ) in Appendix B2 shows that there is much more difference between the two models as compared with the results in **Figure 3.7**.

**Table 3.4.** Value of physical parameters used in the NSRYL model and LSRYL model calculations at  $Ca$  number of  $3.4 \times 10^{-5}$  with scaled approach time of 180

	Initial separation [ $\mu\text{m}$ ] $h_0$	Scaled initial separation $h_0^*$	Glass capillary tube displacement [ $\mu\text{m}$ ] $\Delta X$	Overlap [ $\mu\text{m}$ ] $\Delta X - h_0$
LSRYL	659.26	150	791.11	131.85
LSRYL	684.26	155.7	791.11	106.85
NSRYL	659.26	150	791.11	131.85

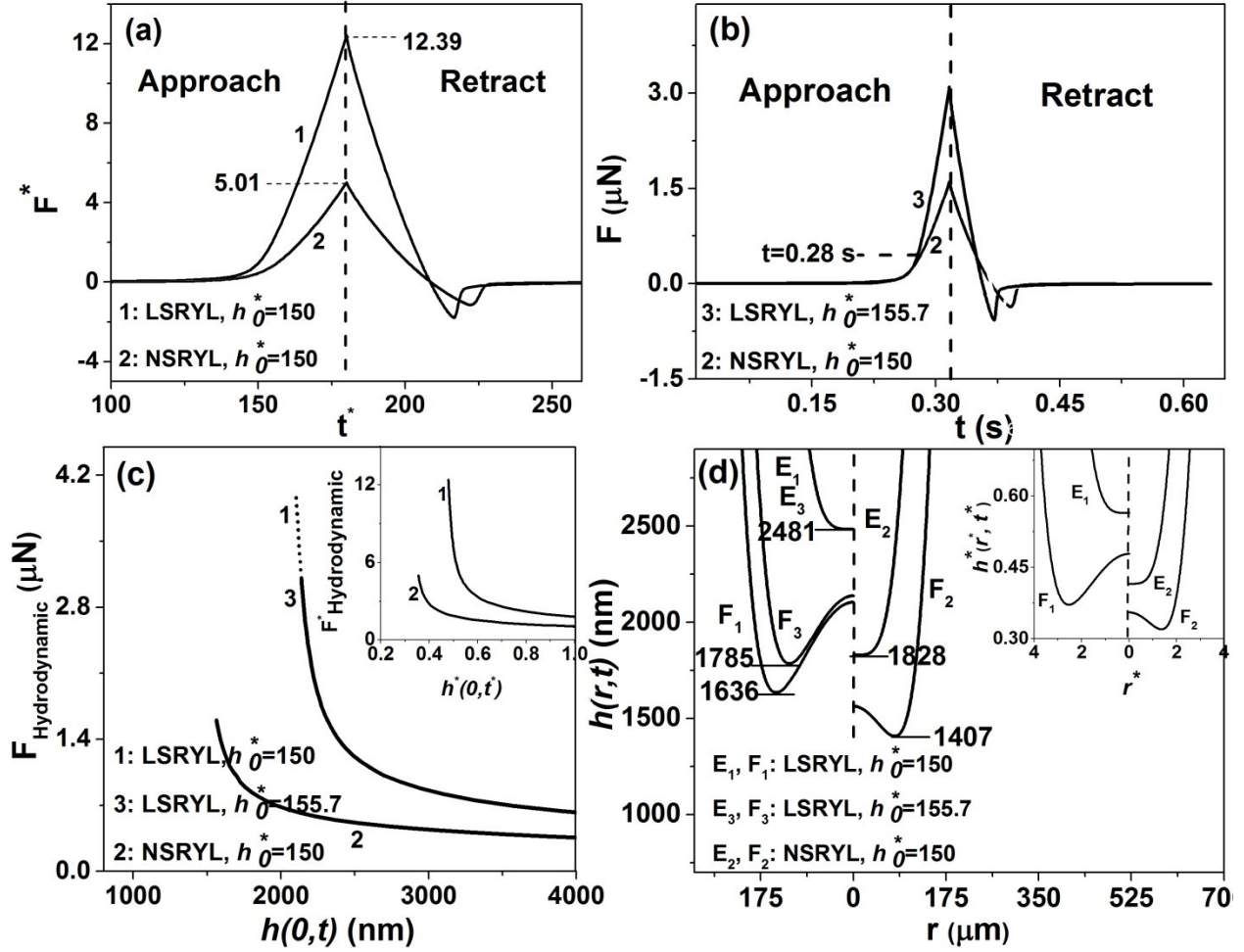


**Fig. 3.7.** (a) Variation of scaled force with scaled time, (b) time evolution of force, (c) variation of hydrodynamic force with thickness of aqueous film at the axis of symmetry, and (d) variation of film thickness with film radius in aqueous electrolyte solutions (100 mM KCl, pH = 5.6) at a bubble approach velocity of  $2500 \mu\text{m/s}$ , corresponding to a capillary number of  $3.4 \times 10^{-5}$ . The NSRYL model results are denoted with 2 and the LSRYL model results are denoted with 1 and 3. Insets: (c) Variation of scaled hydrodynamic force with scaled film thickness at the axis of symmetry, and (d) variation of scaled film thickness with scaled film radius. The immobile boundary condition at bubble surface was used in the two models.

Again we solve the system with the LSRYL model by just increasing the initial separation to  $684.26 \mu\text{m}$  corresponding to the scaled initial thickness of 155.7, **Table 3.4**. The bubble moves towards the solid surface for  $\sim 0.32$  s ( $t^* = 180$ ) and then it retracts. The approaching time is

equivalent to glass tube displacement of  $\sim 791 \mu\text{m}$  or overlap of  $\sim 107 \mu\text{m}$ . **Figure 3.7b** indicates even by changing the initial film thickness, the interaction force profile predicted with the LSRYL model ( $h_0^*=155.7$ , denoted with 3) cannot match with that given by the NSRYL model ( $h_0^*=150$ , denoted with 2). However this figure indicates that for approaching time of  $\sim 0.28\text{s}$  ( $t^*=160$ ), we can reach an acceptable agreement for the time dependent force profile with both models. Profiles  $E_3$  and  $F_3$  in **Figure 3.7d** show the film profiles predicted with the LSRYL model using the scaled initial film thickness of  $h_0^*=155.7$ . Profile  $E_3$  which is coincident with profile  $E_1$ , indicates the dimple first appears at  $\sim 2481 \text{ nm}$  which is larger than the prediction of NSRYL model for dimple formation. Profile  $F_3$  shows that by increasing the initial film thickness, the difference between the two models increases and the minimum film thickness in the approach phase reaches  $\sim 1785 \text{ nm}$  which is larger than  $\sim 1407 \text{ nm}$  predicted by the NSRYL model. As shown in Section 3.8, the maximum deviation between the two models for prediction of the hydrodynamic repulsive force is about a capillary number of  $\sim 3.4 \times 10^{-5}$ .

#### 3.7.1.4 Comparison at $Ca$ number of $1.09 \times 10^{-4}$

**Figure 3.8** shows the comparison of the NSRYL model with the LSRYL model at a nominal speed of  $8000 \mu\text{m/s}$  corresponding to a  $Ca$  number of  $1.09 \times 10^{-4}$ . At this capillary number the  $r_{max}^*$  is considered as 26 and 9.4 (correspond to  $r_{max}$  of  $\sim 2010 \mu\text{m}$  and  $\sim 727 \mu\text{m}$ ) to solve the LSRYL and NSRYL models, respectively. The maximum  $r_{max}$  that the NSRYL model can be solved with is around the bubble radius ( $750 \mu\text{m}$ ). The comparison of both models with the same  $r_{max}^*$  of 9.4 ( $r_{max}$  of  $\sim 727 \mu\text{m}$ ) can be found in Appendix B3. The bubble is first at a distance of  $1179.32 \mu\text{m}$  ( $h_0^*=150$ ) from the solid surface. The air bubble is driven towards the solid surface by moving the capillary tube for  $\sim 0.17 \text{ s}$  ( $t^*=180$ ) and then it is retracted at the same bubble approach velocity. From **Table 3.5** this approaching time is

equivalent to capillary tube displacement of  $\sim 1415 \mu\text{m}$  correspond to overlap of  $\sim 236 \mu\text{m}$ . **Figure 3.8a** shows the time-dependent force profile between an air bubble and a hydrophilic solid surface. From this figure, the force maximum predicted with the NSRYL model is  $\sim 9.91$ . This value is smaller than  $\sim 12.39$  predicted with the LSRYL model. As mentioned the hydrodynamic resistance force is responsible for this difference. As shown in **Figure 3.8c**, the hydrodynamic force predicted with the LSRYL model is larger than that predicted by the NSRYL model. The spatial evolution of the film profiles predicted with two models have been shown in **Figure 3.8d**. Profiles  $E_1$  and  $E_2$  of this figure show that dimple initially formed at  $\sim 4440 \text{ nm}$  with the LSRYL model which is higher than  $\sim 3794 \text{ nm}$  predicted with the NSRYL model. Meanwhile profiles  $F_1$  and  $F_2$  in **Figure 3.8d** show that the minimum film thickness reached during the approach phase with the NSRYL model is  $\sim 2840 \text{ nm}$  which is smaller than  $\sim 2930 \text{ nm}$  predicted with the LSRYL model. As mentioned earlier, drop deformation during interaction is determined by hydrodynamic pressure, disjoining pressure and capillary pressure (Chan et al. 2011). Consequently, the different prediction for hydrodynamic repulsive force with both models is responsible for the different film profiles. Comparison of **Figures 3.8a** and **3.7a** shows that the difference between the force maximum predicted with both models at the  $Ca$  number of  $1.09 \times 10^{-4}$  is less than that predicted with the  $Ca$  number of  $3.4 \times 10^{-5}$ . Furthermore, the difference between hydrodynamic force predicted with these two models at  $Ca$  number of  $1.09 \times 10^{-4}$  is less than that predicted at the capillary number of  $3.4 \times 10^{-5}$ , **Figures 3.8c** and **3.7c**. This observation indicates that the capillary number of  $\sim 3.4 \times 10^{-5}$  can be considered as the capillary number in which the difference between the hydrodynamic forces predicted with both models has its maximum values.

Again we solve the above mentioned system with the LSRYL model by just increasing

the initial separation to 1203.32  $\mu\text{m}$  corresponding to a scaled initial thickness of 153, **Table 3.5**. The air bubble driven towards the solid surface for  $\sim 0.17$  s ( $t^* = 180$ ) and then retracts.

From **Table 3.5** this approach time is equivalent to a capillary tube displacement of  $\sim 1415$   $\mu\text{m}$  corresponding to an overlap of  $\sim 212$   $\mu\text{m}$ . **Figure 3.8b** demonstrates that there is a good agreement in the time dependent force profiles predicted with the LSRYL model ( $h_0^* = 153$ ,

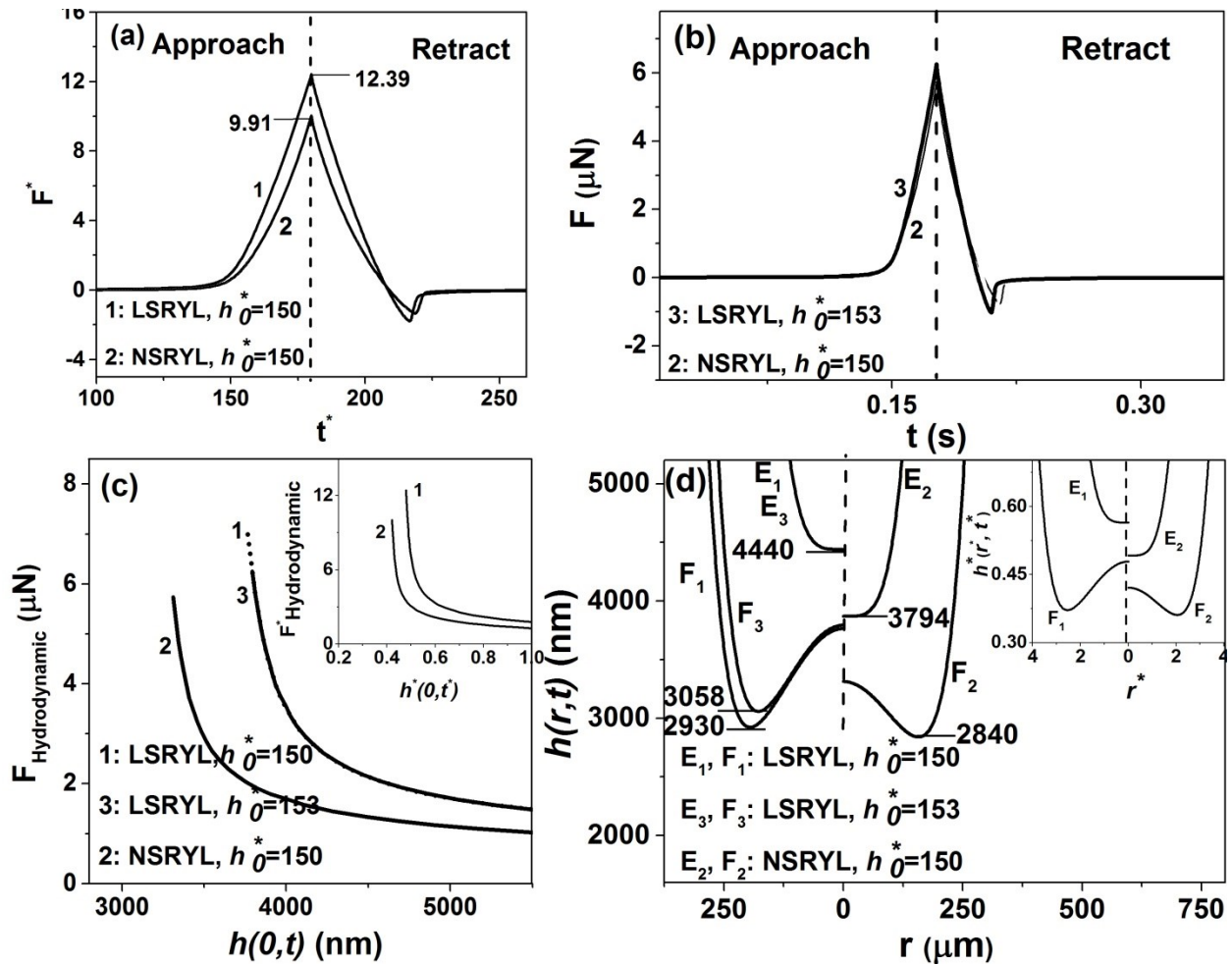


**Fig. 3.8.** (a) Variation of scaled force with scaled time, (b) time evolution of force, (c) variation of hydrodynamic force with thickness of aqueous film at the axis of symmetry, and (d) variation of film thickness with film radius in aqueous electrolyte solutions (100 mM KCl, pH = 5.6) at a bubble approach velocity of 8000  $\mu\text{m/s}$ , corresponding to a capillary number of  $1.09 \times 10^{-4}$ - the NSRYL model results are denoted with 2 and the LSRYL model results are denoted with 1 and 3. Insets: (c) Variation of scaled hydrodynamic force with scaled film thickness at the axis of symmetry, and (d) variation of scaled film thickness with scaled film radius. The immobile boundary condition at bubble surface was used in the two models.

**Table 3.5.** Value of physical parameters used in the NSRYL model and LSRYL model calculations at  $Ca$  number of  $1.09 \times 10^{-4}$  with scaled approach time of 180.

	Initial separation [ $\mu\text{m}$ ] $h_0$	Scaled initial separation $h_0^*$	Glass capillary tube displacement [ $\mu\text{m}$ ] $\Delta X$	Overlap [ $\mu\text{m}$ ] $\Delta X - h_0$
LSRYL	1179.32	150	1415.18	235.86
LSRYL	1203.32	153.052	1415.18	211.86
NSRYL	1179.32	150	1415.18	235.86

denoted with 3) and the NSRYL model ( $h_0^* = 150$ , denoted with 2). The profiles  $E_3$  and  $F_3$  in **Figure 3.8d** show the film profiles predicted with the LSRYL model using the scaled initial thickness of  $h_0^*=153$ . Profile  $E_3$  which is coincident with profile  $E_1$ , indicates the dimple first appears at  $\sim 4440$  nm which is larger than the prediction of the NSRYL model for dimple formation. Contrary to good agreement in the time dependent force, profile  $F_3$  shows that the difference between the two models to predict the minimum film thickness during the approach phase increases. From this figure, the minimum film thickness with the LSRYL model ( $h_0^*=153$ ) increases to  $\sim 3058$  nm which is larger than  $\sim 2840$  nm predicted with the NSRYL model. Again aforementioned observations confirm even if the LSRYL model gives an accurate prediction for time dependent force profile, this theoretical framework (LSRYL)

cannot be used confidently to predict the spatial and temporal evolutions of the shape of intervening liquid film. The comparison of both models at  $Ca$  of  $1.09 \times 10^{-4}$  with the same  $r_{max}^*$  of 9.4 ( $r_{max}$  of  $\sim 727 \mu\text{m}$ ) in Appendix B3 shows that there is much larger difference between the two models as compared with the results in **Figure 3.8**. The results show that by decreasing the  $r_{max}^*$  the overestimation of the hydrodynamic repulsive force predicted with the LSRYL model increase which in turn influences the prediction of film profiles.

### 3.7.1.5 Comparison at $Ca$ number of $2.3 \times 10^{-3}$

In **Figure 3.9** we compare the NSRYL and LSRYL models at  $Ca=2.3 \times 10^{-3}$ , corresponding to a bubble approach velocity of  $165000 \mu\text{m/s}$ . At this capillary number the  $r_{max}^*$  is considered as 26 and 4.54 (correspond to  $r_{max}$  of  $\sim 4285 \mu\text{m}$  and  $\sim 750 \mu\text{m}$ ) to solve the LSRYL and NSRYL models, respectively. The maximum  $r_{max}$  that the NSRYL model can be solved with is around the bubble radius ( $750 \mu\text{m}$ ). The comparison of both models with closer  $r_{max}^*$  can be found in Appendix B4. The bubble is initially kept at a separation distance of  $\sim 5431 \mu\text{m}$  ( $h_0^*=150$ ) from the solid surface. The bubble is driven towards the solid surface by moving the capillary tube for  $\sim 0.0395 \text{ s}$  ( $t^*=180$ ) and then it is retracted away at the same bubble approach velocity. This approach time is equivalent to capillary tube displacement of  $\sim 6517 \mu\text{m}$  or overlap of  $\sim 1086 \mu\text{m}$ , **Table 3.6**.

**Table 3.6.** Value of physical parameters used in the NSRYL model and LSRYL model calculations at  $Ca$  number of  $2.3 \times 10^{-3}$  with scaled approach time of 180

	Initial separation [ $\mu\text{m}$ ] $h_0$	Scaled initial separation $h_0^*$	Glass capillary tube displacement [ $\mu\text{m}$ ] $\Delta X$	Overlap [ $\mu\text{m}$ ] $\Delta X - h_0$
LSRYL	5431	150	6517	1086
NSRYL	5431	150	6517	1086

The time-dependent force profiles between an air bubble and a hydrophilic solid surface, in 100 mM KCl aqueous electrolyte solutions, predicted with these two models are shown in **Figure 3.9a**. This figure shows that the predicted force maximum during approach phase with the NSRYL model sharply increases to  $\sim 29$  compare to  $\sim 12.39$  as predicted with the LSRYL model. This force is solely due the hydrodynamic repulsion. Line 2 in the inset of **Figure 3.9a** indicates that when the bubble is still far from the solid surface ( $h^*=1$  corresponds to  $h=36.2\mu\text{m}$ ), the predicted hydrodynamic repulsive force with the NSRYL model is lower than that predicted with the LSRYL model. But in close proximity to solid surface the hydrodynamic repulsive force dramatically increases with the NSRYL model. It is very interesting to note that the sudden jump in the hydrodynamic repulsive force with the NSRYL model, prevents the bubble from driving to the solid surface. For example, line 2 of **Figure 3.9a** shows that the bubble just can approach the solid surface until proximity of point “A” corresponding to a scaled approach time of  $\sim 170$  (time of  $\sim 0.0373$  s and overlap of  $\sim 724 \mu\text{m}$ ) with the NSRYL model. After point A, the force begins to decrease indicating that the proximity of point A can be considered as the position where the bubble bounces back from the solid surface. More investigation is needed for the bubble behavior in proximity of point “A”. The LSRYL model is not capable to predict point “A” or the position where the force begins to decrease. As a result the LSRYL model is not able to predict the bouncing phenomenon.

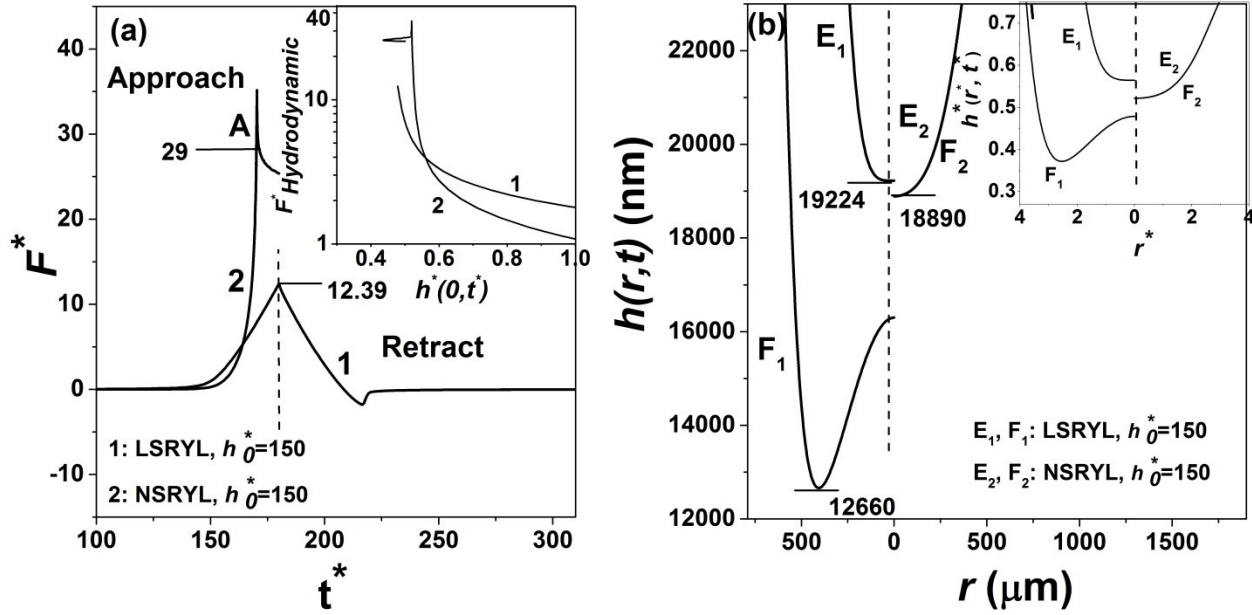


**Fig. 3.9.** (a) Variation of scaled force with scaled time and (b) variation of film thickness with film radius in aqueous electrolyte (100 mM KCl, pH = 5.6) at a bubble approach velocity of  $165000 \mu\text{m/s}$ , corresponding to a capillary number of  $2.3 \times 10^{-3}$ - the NSRYL model results are denoted with 2 and the LSRYL model results are denoted with 1. Insets: (a) Variation of scaled hydrodynamic force with scaled film thickness at the axis of symmetry and (b) variation of scaled film thickness with scaled film radius. The immobile boundary condition at bubble surface was used in the two models.

The spatial evolution of the film profiles predicted with the two models has been shown in **Figure 3.9b**. Profiles E<sub>1</sub> and E<sub>2</sub> show that the dimple initially forms at  $\sim 19224$  nm with the LSRYL model which is much larger than  $\sim 18890$  nm predicted with the NSRYL model. From **Figure 3.9b**, profile E<sub>1</sub> develops more and finally reaches to profile F<sub>1</sub> at the end of approach phase with the LSRYL model. The minimum film thickness during the approach using the LSRYL is  $\sim 12660$  nm. Furthermore, the above mentioned figure shows that the profile E<sub>2</sub> does not develop and coincides well with the profile F<sub>2</sub> using the NSRYL model. In other words, profile E<sub>2</sub> can be considered the end of approach phase with the NSRYL model. Both profiles E<sub>2</sub> and F<sub>2</sub> represent the same position (film profile) in proximity of point A. In

summary, with the NSRYL model bubble does not deform in the approach phase and in the proximity of point “A” bubble bounces back from the surface and bubble deformation happens in the retract phase, i.e., when bubble bounces back from the surface. The comparison of both models at  $Ca$  of  $2.3 \times 10^{-3}$  with the more closer  $r_{\max}^*$  in Appendix B4 shows that by decreasing the  $r_{\max}^*$  the LSRYL model significantly overestimates the hydrodynamic repulsive force which in turn influences the prediction of film profiles. Due to the large overestimation in the hydrodynamic repulsive force with the LSRYL model, recently (Manica et. al, 2013) for very high  $Ca$  numbers, the full mobile boundary condition at the bubble surface is suggested instead of the immobile boundary condition. The good agreement between the LSRYL model and experiment at very high  $Ca$  number with full mobile boundary condition (Manica et. al, 2013) is attributed to the lower hydrodynamic resistance force which arising from the full mobile condition at the bubble surface (Manor et. al, 2008).

Clearly in contrast to the LSRYL model which predicts bubble deformation at all range of capillary numbers, the NSRYL model predicts that above a critical capillary number, the bubble does not deform and behaves like a solid sphere. In other words, we can say that for a specific bulk solution, the NSRYL model is able to numerically predict the critical bubble approach velocity where a bubble behaves like a solid sphere. This critical bubble approach velocity depends on the size of bubble. In the next section, the critical bubble approach velocity for the bubble with a radius of 750  $\mu\text{m}$  in water as bulk solution is predicted with the NSRYL model.

In the current system, the Reynolds number based on the bubble diameter ( $d_b$ ) and bubble approach velocity,  $Re$  ( $= \rho v d_b / \mu$ ), is in the order of  $10^2$ , where  $\rho$  ( $=$

$1000 \text{ kg m}^{-3}$ ) and  $\mu (= 0.001 \text{ Pa s})$  are the density and dynamic viscosity of water, respectively. Although the Reynolds number that characterizes bubble movement is high (in the order of  $10^2$ ), the Reynolds number that characterizes film deformation and drainage is small,  $Re_{\text{film}} < 1$ . For the above mentioned system for example, **Figure 3.10** shows that at the film thickness of  $\sim 20 \text{ }\mu\text{m}$ , the film drainage velocity is only  $\sim 0.0001 \text{ m/s}$ , corresponding to a film Reynolds number ( $Re_{\text{film}} = \rho v h / \mu$ ) of  $\sim 10^{-2} < 1$ . Therefore, the Stokes-Reynolds-Young Laplace model based on the lubrication theory can provide a quantitative account of bubble deformation and film drainage dynamics (Manica et al. 2013).

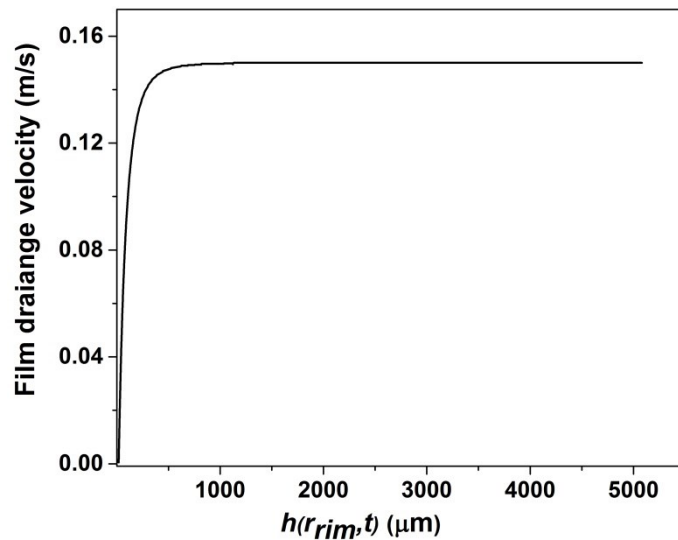


**Fig. 3.10.** Variation of the film drainage velocity with separation distance at a bubble approach velocity of  $165000 \text{ }\mu\text{m/s}$ , corresponding to a capillary number of  $2.3 \times 10^{-3}$ - for this figure the NSRYL model is solved using the initial film thickness and bubble overlap values summarized in **Table 3.6**.

### 3.7.1.6 Wall impact on the approaching bubble

In a surface force apparatus such as ITFDA the bubble is driven towards a solid surface with the aid of glass capillary tube. In the force measurement, a bubble moves with an approximately constant bubble approach velocity while it is subjected to time variable forces. Let us consider

an air bubble of 750  $\mu\text{m}$  in radius. The bubble moves towards the solid surface with constant bubble approach velocity.

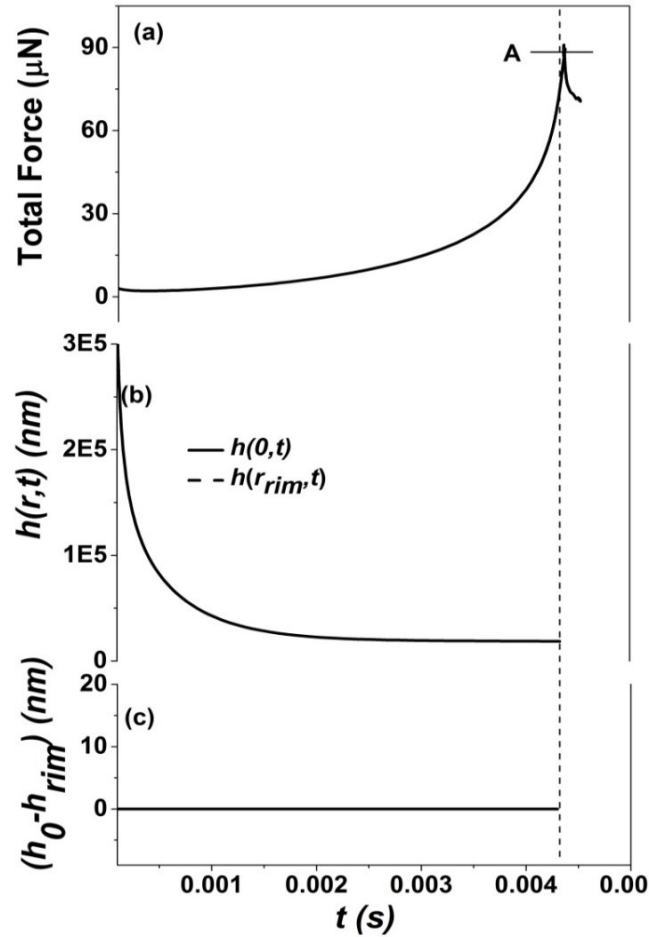


**Fig. 3.11.** Variation of force with time (a), variation of film thickness with time (b), and variation of the difference between local film thickness at center and rim with time (c) in aqueous electrolyte solution (100 mM KCl, pH = 5.6) at bubble approach velocity of  $\sim 155000 \mu\text{m/s}$ , corresponding to a capillary number of  $2.18 \times 10^{-3}$ . The immobile boundary condition at bubble surface was used in the NSRYL model.

**Figure 3.11** demonstrates that the critical bubble approach velocity predicted with the NSRYL model for the air bubble of 750  $\mu\text{m}$  radius in water is  $\sim 155000 \mu\text{m/s}$  ( $\sim 15.5 \text{ cm/s}$ ). It is necessary to mention to solve the NSRYL model, the  $r_{max}$  is the same with the bubble radius ( $\sim 750 \mu\text{m}$ ). **Figures 3.11b** and **c** confirm that the bubble behaves like a solid sphere in the entire

approaching process. This prediction for critical bubble approach velocity using the NSRYL model is comparable with the data reported in the literature and the Schiller–Naumann formula (Clift et al. 1978). For example for an air bubble with a diameter of 1.5 mm the measured critical velocity in tap water is  $\sim 15$  mm/s (Haberman et al. 1953) and for an air bubble with a radius of 625  $\mu\text{m}$ , the predicted critical velocity using Schiller–Naumann formula is  $\sim 13.5$  cm/s (Clift et al. 1978).

The NSRYL model provides a new opportunity to study the effect of individual physical parameters on the critical bubble approach velocity. This new approach is worth further investigation, as we can take into account the bubble deformation and all the physical parameters of a system for this prediction. Moreover the NSRYL model can be developed for rising bubble to numerically predict the bubble terminal velocity.

### 3.7.2 Validation of the NSRYL model

The thickness of intervening liquid film between an air bubble and a flat hydrophilic glass surface at bubble approach velocity of 1000  $\mu\text{m/s}$  in 100 mM KCl solution were measured by Xurui Zhang using the thin film force apparatus (TFFA), explained in Section 3.2. The experimental parameters used in this study are summarized in **Table 3.7**. The radius of bubble at the end of the glass tube has an undistorted curvature of 1200  $\mu\text{m}$ . The initial separation,  $h_0$ , between the bubble and the hydrophilic glass surface was adjusted to 300  $\mu\text{m}$  with the aid of the CCD camera. The maximum glass tube displacement,  $X_{max}$ , was set at 400  $\mu\text{m}$ . In their experiment, the bubble first approached with speed of 1000  $\mu\text{m/s}$  towards the flat glass surface with a capillary tube displacement of 400  $\mu\text{m}$ . Then the air bubble is held in contact with the flat glass surface for 21 minutes (holding phase). The images of interference patterns (Newton rings)

recorded by a high-speed CCD camera were used to obtain time dependent film thickness profiles of the intervening liquid film trapped between the air bubble and glass surface.

**Table 3.7.** Material constants and modified ITFDA parameters.

Bubble radius, $R_b$	1200 $\mu\text{m}$
Surface tension, $\gamma$	72.8 mN/m
Viscosity, $\mu$	1 mPa s
KCl	100 mM
pH	5.6
Zeta potential of air bubble	-5 mV
Zeta potential of glass surface	-5 mV
Bubble driving velocity	1000 $\mu\text{m/s}$
Initial separation, $h(0,0)$	300 $\mu\text{m}$
Maximum displacement, $\Delta X_{\text{max}}$	400 $\mu\text{m}$
Hamaker constant	$-8 \times 10^{-21}$ J

**Figure 3.12** shows the comparison of the measured film profiles with the predictions from both models at different measurement times of 68, 119, 183 and 301 s. The results in this figure indicate that the prediction of the film profiles from the NSRYL model using the system parameters in **Table 3.7** is in good agreement with the experimental data. In contrast to the good agreement between measured and predicted film profiles with the NSRYL model, **Figure 3.12b** indicates a large difference between the experimental data and the prediction of the LSRYL model. Due to the lack of time dependent force data, it is difficult to find the uncertainty in controlling of the overlap (which is the difference between the tube displacement and initial separation) in the experiment. The error in the overlap is artificially compensated by considering the initial thickness as an adjustable parameter by comparison of the position where the interaction force between an air bubble and solid surface is detectable in both the measured and predicted force profiles. This uncertainty in the measurement is due to the fact that the lower

solid flat surface in the experiment is not fixed in its position, which led to the uncertainty in the overlap measurement. However to decrease the error in the film profile measurement with TFFA, a very thick flat solid surface was used for this measurement and at the same time we used the minimum possible overlap for this measurement. Consequently, the error in the film profile measurement is not expected to be very large, however it is not negligible.

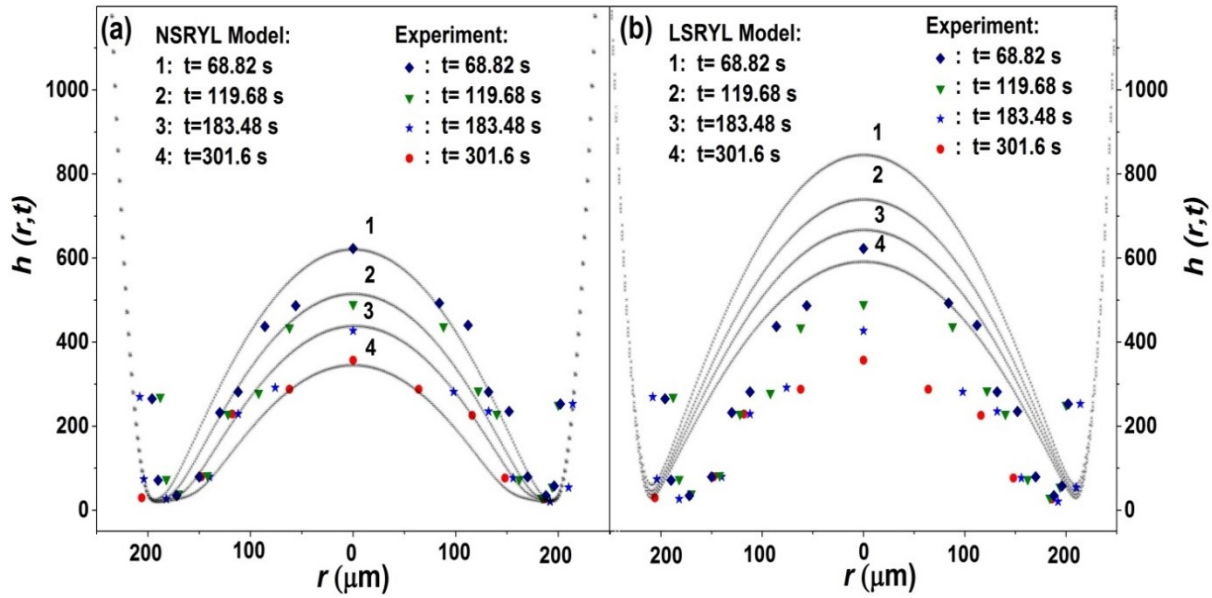


**Fig. 3.12.** Profile of the aqueous film,  $h(r,t)$  between the bubble and the flat glass surface at different measurement times during the holding phase (in which the bubble approach velocity is zero) predicted with (a) the NSRYL model and (b) the LSRYL model. Experiments are denoted by symbols and models by solid lines. The electrolyte concentration is 100 mM KCl and bubble approach velocity of 1000  $\mu\text{m/s}$  corresponds to a capillary number of  $1.36 \times 10^{-5}$ . The immobile boundary condition at bubble surface was used in the two models.

To model this experimental data with both the NSRYL and LSRYL model, the  $r_{max}^*$  is considered as adjustable parameter which is set as 14.3 and 26 (correspond to  $r_{max}$  of  $\sim 1050$   $\mu\text{m}$  and  $\sim 1921$   $\mu\text{m}$ ) for the NSRYL and LSRYL models, respectively. The selected adjustable parameter for the NSRYL model is in the order of bubble radius (1200  $\mu\text{m}$ ) and is more reasonable. It is necessary to mention that the LSRYL model is also able to fit with this

experimental data but by considering the  $r_{max}$  much larger than 1921  $\mu\text{m}$ . Compared with the bubble radius (1200  $\mu\text{m}$ ) this adjustable parameter is not acceptable. As a result, this comparison confirms that only the NSRYL model can better predict the behavior of bubble in the intermediate capillary number region.<sup>2</sup>

### 3.8. Discussion

In this study we compared the NSRYL model with the LSRYL model for a wide range of  $Ca$  numbers from  $10^{-8}$  to  $10^{-3}$ . **Figures 3.13a** and **3.13b** show the normalized hydrodynamic repulsive forces predicted with the NSRYL and LSRYL models, respectively. **Figure 3.13b** shows that the scaled hydrodynamic repulsive force predicted with the LSRYL model (shown in the inset of **Figures 3.3c, 3.6c, 3.7c** and **3.8c**) behaves in a universal way and all collapse into one single curve. This result is not surprising since the governing equations of the LSRYL model (**eqns. 3.14** and **3.15**) contain no other physical parameters apart from the scaled disjoining pressure which is negligible in this study. Only the boundary condition at  $r^* = r_{max}^*$  has a weak logarithmic dependence on the capillary number, **eqn. 3.12**.

---

<sup>2</sup> Another way to model this experimental data is that the  $r_{max}$  is considered the same as the bubble radius ( $r_{bubble}$ ) for both the NSRYL and LSRYL models and then by changing (or adjusting) the initial thickness and so the overlap, try to fit the models with the experimental data and then compare the adjusted initial thickness predicted from the two models.

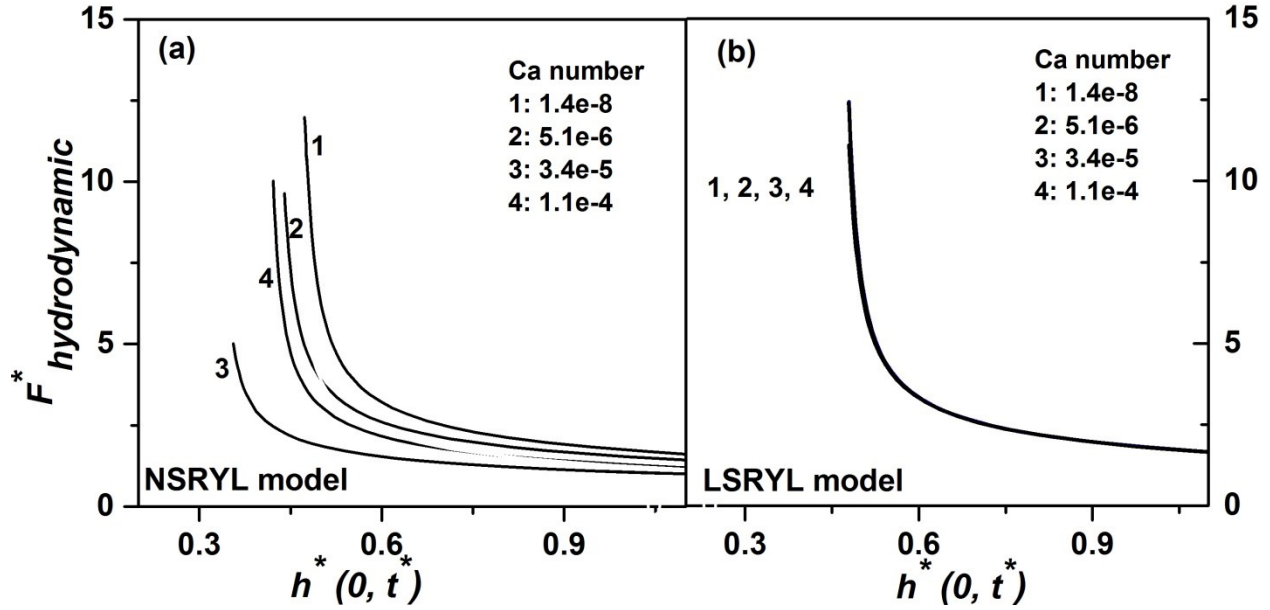


**Fig. 3.13.** Variation of the scaled hydrodynamic force with the scaled film thickness at the axis of symmetry with (a) the NSRYL model and (b) the LSRYL model at a wide range of  $Ca$  numbers.

**Figure 3.13a** demonstrates the scaled hydrodynamic repulsive forces predicted with the NSRYL model (shown in inset of **Figures 3.3c, 3.6c, 3.7c and 3.8c**) depend on the  $Ca$  number and do not behave in a universal way. This observation is due to the appearance of capillary number in the Young Laplace equation used in the NSRYL model, as shown in **eqn. 3.10**. **Figure 3.13a** shows that at a  $Ca$  number of  $\sim 1.4 \times 10^{-8}$  both models give the same prediction for the scaled hydrodynamic force. At larger  $Ca$  numbers the NSRYL model gives a lower prediction of hydrodynamic repulsive force than that predicted by the LSRYL model. **Figure 3.13a** also indicates that the maximum deviation between the two models to calculate the scaled hydrodynamic force occurs at  $Ca$  number of  $\sim 3.4 \times 10^{-5}$ .

The normalized results of time dependent force predicted with the NSRYL model and the LSRYL model over a wide range of  $Ca$  numbers are shown in **Figures 3.14a and 3.14b**,

respectively. In all of the normalized results, the bubble initially is at the scaled separation of 150 from the solid surface. The air bubble is driven toward the solid surface for the scaled approaching time of 180 before it is retracted. Again **Figure 3.14b** shows that the normalized time dependent force profiles with the LSRYL model (shown in **Figures 3.3a, 3.6a, 3.7a and 3.8a**) behave in a universal way for different  $Ca$  numbers. In contrast, **Figure 3.14a** shows that the normalized time dependent force profiles predicted with the NSRYL model (shown in **Figures 3.3a, 3.6a, 3.7a and 3.8a**) depend on the  $Ca$  numbers and do not collapse into one single curve. The results in **Figure 3.14a** indicate that at  $Ca$  number of  $\sim 1.4 \times 10^{-8}$  both models give the same prediction for the scaled force profile. However with increasing the capillary numbers, the scaled force decreases first, and reaches to its minimum value at  $Ca$  number of  $\sim 3.4 \times 10^{-5}$  and increases thereafter at higher  $Ca$  numbers.

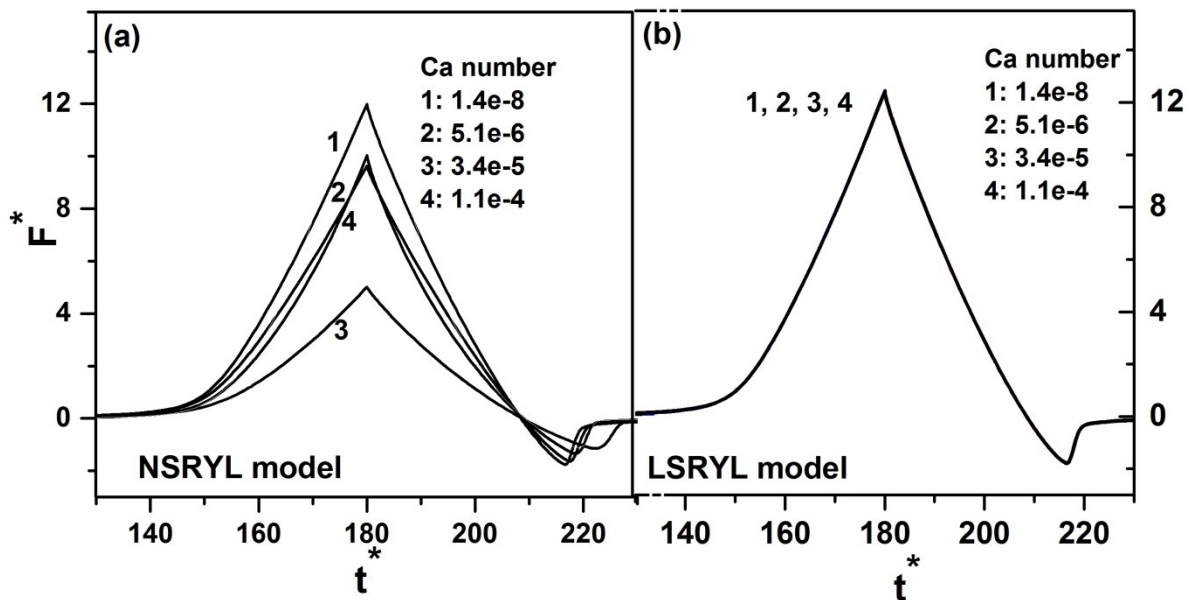


**Fig. 3.14.** Variation of the scaled force with the scaled time with the NSRYL model (a) and the LSRYL model (b) at a wide range of  $Ca$  numbers.

The normalized results for the spatial evolution of film profile with the two models (shown in the inset of **Figures 3.3d, 3.6d, 3.7d and 3.8d**) have been summarized in **Figure 3.15**. From **Figures 3.15b and 3.15d**, the bubble deformations predicted with the LSRYL model over this wide range of  $Ca$  number all collapse into one single curve, i.e., behave in a universal way. As mentioned earlier, this is due to the universal nature of the governing equations in this model. **Figures 3.15a and 3.15b** show the critical film profiles where the dimple initially forms predicted with the NSRYL model and the LSRYL model, respectively. The film profiles at the end of the approach phase with the NSRYL model and LSRYL model are presented in **Figures 3.15c and 3.15d**, respectively.

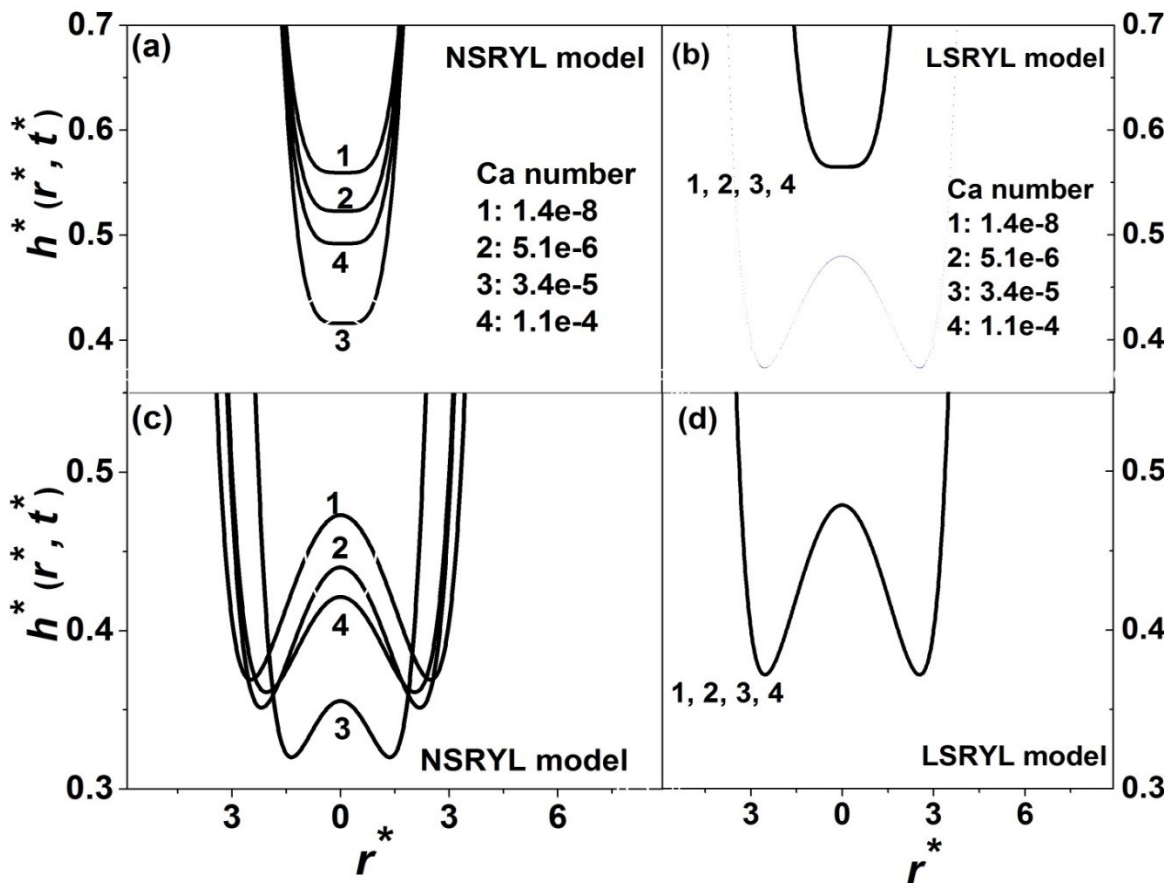


**Fig. 3.15.** Variation of the scaled film profile with the scaled bubble radius using the NSRYL model (a): film profile where bubble initially forms and c: film profile at the end of approach) and the LSRYL model (b): film profile where bubble initially forms and d: film profile at the end of approach).

**Figure 3.15** shows that at low  $Ca$  number of  $\sim 1.4 \times 10^{-8}$  both models provide the same prediction for the bubble deformation. This is because at  $Ca$  number of  $\sim 10^{-8}$  and lower both models provide the same estimation of the hydrodynamic repulsive force, **Figure 3.13**. Therefore, both models predict the same bubble deformation since drop deformation is determined by overall force exerted on bubble which is in balance with the hydrodynamic pressure, disjoining pressure and capillary forces (Chan et al. 2011). By increasing the capillary numbers, the LSRYL model predicts the formation of dimple at larger film thickness, as shown in **Figure 3.15b**. Furthermore these two models give different predictions for the film profile at the end of the approach, as shown in **Figure 3.15c** and **d**. These differences can be attributed to the different estimation of the hydrodynamic repulsive force by these two models, **Figure 3.13**.

### 3.9. Conclusions

The NSRYL model was presented to describe thin film drainage and non-equilibrium interactions between an air bubble and flat solid surface. In the NSRYL model the augmented Young Laplace equation is not linearized within the interaction zone. Therefore, the governing equations of the NSRYL model depend on the physical parameters of the system via  $Ca$  number. This model was compared with the LSRYL model over a wide range of  $Ca$  number from  $10^{-8}$  to  $10^{-3}$ .

The simulation results indicate that at  $Ca$  number of  $\sim 10^{-8}$  or smaller, both the NSRYL model and LSRYL model provide the same prediction for bubble deformation, time dependent

force and hydrodynamic force. Consequently, both models can be confidently used to infer the spatial and temporal evolutions of the film profile as these models are shown to be able to give an accurate account of the non-equilibrium forces measured by AFM.

At  $Ca > 10^{-8}$ , the LSRYL model led to over estimation of hydrodynamic repulsive force. The maximum difference between the two models was observed at the  $Ca$  number of  $\sim 3.4 \times 10^{-5}$ . The over estimation of hydrodynamic repulsive force by the LSRYL model in turn led to inaccurate estimation of bubble deformation and time dependent force profiles.

At  $Ca > 10^{-8}$ , the simulation results indicate that changing the initial separation (i.e., the overlap) could provide the same prediction on the time dependent force profiles by these two models. However, adjusting the initial separation could not provide the same prediction of bubble shape and hydrodynamic repulsive force. Therefore at the  $Ca$  numbers larger than  $10^{-8}$ , even though the LSRYL model is shown to give an accurate account of time dependent force profiles, we cannot confidently use the LSRYL model to infer the spatial and temporal evolution of the shape of the liquid film trapped between the interacting interfaces. At very high capillary numbers the NSRYL model predicts that the bubble behaves like a solid sphere and does not deform during the approach phase. In contrast the LSRYL model predicts bubble deformation at all capillary numbers tested.

Validation of simulation results by thin film profile measurement using TFFA, conclude that the NSRYL model is more accurate for high  $Ca$  number systems. With the NSRYL model, we can numerically predict the critical bubble approach velocity where bubble behaves like a solid sphere. The NSRYL model provides new opportunities to study the effect of individual physical parameters of a system such as bubble size, interfacial tension and bulk viscosity on bubble deformation.

This study reveals that there is limitation for choosing the  $r_{max}$  in the NSRYL model. Approximately, the NSRYL model cannot be solved with  $r_{max}$  larger than the bubble radius. The maximum selected  $r_{max}$  in this model is around or the same with the bubble radius.

# Chapter 4

## Measurement and modeling on hydrodynamic forces and deformation of an air bubble approaching a solid sphere in liquids with the Integrated thin film drainage apparatus (ITFDA)

### 4.1. Introduction

#### 4.1.1 Background and motivations

Interaction between bubbles and solid surfaces in aqueous solutions plays a crucial role in various industrial processes, most notably in froth flotation which is widely used in the separation of mineral particles, treatment of wastewater, recycling of fibers from waste paper, removal of toxic components from industrial effluent and separation of biological cells (Fuerstenau and Herrera-Urbina *Surfactant Science Series* 1989; Ødegaard 2001). Since the selective attachment of air bubbles and particles determines the separation between hydrophobic and hydrophilic particles in a flotation cell, understanding bubble-particle interactions in froth flotation is of great importance (Luttrell and Yoon 1992; Yoon 1992). An important feature of bubble-particle interaction is drainage of aqueous liquid films between air bubbles and solid surfaces under the influence of hydrodynamic and surface forces, compounded by bubble deformation. Accounting for such deformations under the hydrodynamic forces makes analysis of liquid film drainage dynamics much more challenging. Derjaguin and Kussakov (Derjaguin and Kussakov Reprinted in *Prog Surface Sci* 1992) are among the first who analyzed non-equilibrium interactions between an air

bubble and a flat mica plate. They showed for the first time dimple formation on the bubble surface.

A number of different experimental techniques have been used to study film drainage and time dependent interactions between an air bubble and a solid surface immersed in a liquid (Chan et al. 2011). One of the earliest methods to study the drainage dynamics of the liquid film involving deformable interfaces was based on the Scheludko cell. In this technique, the captive air bubble was pressed against a flat silica surface through a capillary tube, (Platikanov 1964; Ivanov 1988; Blake and Kitchener 1972; Schulze 1975) or by pulling out the liquid between two approaching surfaces (Pan and Yoon 2010). The film thickness between the two surfaces was measured using an interferometric method which was based on multiple reflection and interference of a monochromatic light. Using this method, the time evolution of the central liquid film thickness,  $h(t)$ , was obtained. Although the Scheludko thin liquid film apparatus allowed the thickness of center film to be measured accurately, it was not capable of measuring the interaction force between an air bubble and a solid surface.

The atomic force microscope (AFM), on the other hand, has been widely and effectively used to measure both static and dynamic interaction forces of deformable bubbles (Ducker et al. 1994; Butt 1994; Fielden et al. 1996; Preuss and Butt 1998) or oil drops (Basu and Sharma 1996; Mulvaney et al. 1996; Snyder et al. 1997; Hartley et al. 1999; Aston and Berg 2001; Bhatt et al. 2001; Chan et al. 2001; Nespolo et al. 2003; Dagastine et al. 2004; Gillies and Prestidge 2004) approaching solid probe particles in aqueous solutions. In dynamic forces measurements between an air bubble and a solid surface using the AFM probe technique, a small air bubble ( $\sim 500 \mu\text{m}$ ) is placed on a hydrophobic substrate and a spherical probe particle is attached to one of AFM cantilevers (Aston and Berg 2002; Dagastine et al.

2005; Dagastine et al. 2004). In most of the measurements, the air bubble is moved up and down by a piezoelectric transducer to approach and retract from the probe particle (Butt et al. 1995; Ducker et al. 1994; Fielden et al. 1996). In a few cases, the cantilever is driven to approach and retract from the lower air bubble/droplet surface (Butt 1994). Alternatively, smaller bubbles or oil drops ( $\sim 100 \mu\text{m}$ ) can also be attached on the cantilever to measure their dynamic interactions with solid surfaces. In all the cases, the interaction force as a function of bubble displacement is obtained by monitoring the deflection of the cantilever. The AFM colloidal or bubble probe technique allowed direct measurement of interaction forces, but provided no direct information on bubble deformation.

Neither the Scheludko thin liquid film apparatus nor the AFM colloid/bubble probe technique is capable of determining simultaneously the deformation of air bubbles and colloidal forces. Moreover, the experiments conducted by the thin liquid film apparatus and AFM probe technique are mostly in the low Reynolds number regime. For example, the reported maximum bubble approach velocity towards a particle in AFM measurement was  $\sim 100 \mu\text{m/s}$ , (Nguyen et al. 2003) corresponding to a bubble Reynolds number of  $\sim 0.02$  which is much lower than the Reynolds number of particles-bubble encounters in a flotation cell.

To better understand interactions between air bubbles and solid particles in aqueous media as encountered in flotation practice, it is important to develop a device that measures both forces and bubble deformation in systems of higher Reynolds numbers as encountered in mineral flotation practice. For this purpose, an integrated thin film drainage apparatus (ITFDA) was developed recently to measure the bubble-particle interactions over a wide range of dynamic conditions (Wang et al. 2012; Wang 2013). The ITFDA is capable of measuring simultaneously the dynamic forces and the geometric properties of the bubble

interacting with solid particles. Using the diaphragm of a high frequency speaker as the drive of the bubble, the approach velocity of the bubble to a solid particle can be as high as 5000  $\mu\text{m/s}$ , which gives a bubble Reynolds number of 10, making the ITFDA an ideal device to study the bubble-particle interactions under dynamic conditions.

#### **4.1.2 Coverage and scope**

Historically, the systematic investigation of bubble-particle interactions in the context of colloid and interface science began in late 1930's, with Derjaguin and Kussakov (Derjaguin and Kussakov Reprinted in Prog Surface Sci 1992) as the pioneers who studied the behavior of a bubble in water rising under buoyancy towards a mica plate. The experiment was intended to measure surfaces forces that were the foundation of the Derjaguin-Landau-Verwey-Overbeek theory of colloidal stability (Derjaguin and Landau 1941; Verwey and Overbeek 1948). The short-ranged nature of such forces required measurement using molecularly smooth surfaces such as a bubble-mica system. In a typical force measurement experiment, one either varies the separation between surfaces and measures the force, or imposes a known force and observes how the intervening liquid film thins. In the Derjaguin and Kussakov experiments, the buoyancy force was known. However, being a time-dependent dynamic experiment, it was necessary to track the position of the bubble and the separation between the bubble surface and the mica plate as a function of time. Furthermore for deformable bubbles, it is also necessary to measure the position and interfacial deformation of the bubble as a function of time during the experiment. These technical and theoretical challenges were perhaps too overwhelming at the time for quantitative measurements. Nonetheless, Derjaguin and Kussakov were able to infer that the hydrodynamic repulsion that arose as the bubble approached the mica plate caused the

bubble surface to form a dimple whose shape changed over the time. The work by Derjaguin and Kussakov demonstrated that any attempt to measure dynamic forces involving deformable bubbles has to be able to: i) control and/or measure the force as a function of time; ii) measure the spatial and temporal profile of the bubble or the film thickness between the bubble and the solid surface; and iii) control and/or measure the position of the moving bubble. Missing any of these elements in an experiment or a theoretical model to interpret the experimental results would limit the value of the work.

Due to technical constraints in instrumentation and allowable size of samples, it is not easy to incorporate all the above key elements in every experimental approach. As a consequence, many papers that appeared in the past that attempted to study bubble-particle interactions, unfortunately only provided partial or in some cases even omitted such information. Nevertheless the experimental research coupled with a theoretical framework that includes all the afore mentioned key information of dynamic force measurements, has provided a good understanding of rather complex systems. This overview on the use of the integrated thin film drainage apparatus (ITFDA) should be placed into that context with other complementary methods of studying the dynamic interactions between deformable bubbles and solid surfaces.

#### **4.2. Dynamic experimental methods**

In this section, we review complementary methods of studying dynamic bubble-solid interactions. Although no single approach was capable of including all key elements of dynamic experiments discussed in Section 4.1.2, each concentrated on certain key aspects of the system that taken together, will form a complete picture and foster an in-depth understanding of a rather complex problem.

#### **4.2.1 Free bubble rise method**

There have been a number of experiments that considered the rise of mm-size bubbles in water impinging on a horizontal solid surface (Tsao and Koch 1997; Klaseboer et al. 2001; Krzan and Malysa 2002; Malysa et al. 2005). These studies focused on the trajectories of the bubbles that collided with and bounced from the surface. The bubbles in these studies were in the millimeter to hundreds of micron size range, with Reynolds number between 200 and 600, calculated based on the bubble terminal velocity. The initial bubble-solid surface encounter was determined to be dominated by inertia effect. The interaction forces in this regime were modeled successfully (Klaseboer et al. 2001). Recently, high-speed interferometry has been used to provide information on the film deformation and thin liquid film drainage mechanisms in this high Reynolds number regime (Hendrix et al. 2012).

Using smaller bubbles in the tens of micron size range allowed study of colloidal forces between rising bubbles and solid surfaces (Parkinson and Ralston 2010). Under such conditions the role of surface forces were shown to play an important role in determining thin liquid film drainage dynamics between the bubble and the solid surface (Manica et al. 2010)

#### **4.2.2 Bubble expansion methods**

With the bubble rise method, the buoyancy force can be controlled by changing bubble size. But in order to measure the bubble deformation and film drainage, a larger interaction area between the bubble and the solid surface is needed. Detailed measurements of the spatial and temporal evolution of a draining aqueous film between a bubble and a smooth hydrophilic quartz plate were made in early 1990's by Fisher et al. (Fisher et al. 1992). Their

study concluded that comparing the results from different laboratories was very difficult if not impossible, since the method of forming the draining film profoundly affected its shape and the kinetics of the evolution of that shape. They pointed out that not all the authors publishing in the field were aware of these limitations. They noted a “scarcity of data where the initial conditions for film formation have been reliably and reproducibly controlled”.

In the bubble expansion method, (Fisher et al. 1992; Fisher et al. 1991; Hewitt et al. 1993) a bubble is forced to emerge rapidly (in less than 1 s) out of a (1 mm inner diameter) glass capillary tube held perpendicularly to a quartz plate placed 610  $\mu\text{m}$  away. The evolution of the trapped water film between the bubble and the plate was measured by interferometry from 5 s after the bubble expansion for over 200 s as the film drainage proceeded. This was a constant force experiment where the applied force on the bubble was estimated to be  $\sim 40 \mu\text{N}$ . The detailed sets of experimental data were only analyzed quantitatively some 20 years later (Manica and Chan 2011) using the model discussed in Section 4.4.

### **4.2.3 Surface forces apparatus**

The surface force apparatus, using fringes of equal chromatic order, has provided accurate measurement of film thickness at sub-nanometer resolution in elucidating the drainage dynamics of water films trapped between a molecular smooth mica plate and a mercury drop (Connor and Horn 2003; Manica et al. 2008). Although the apparatus could have been used to measure the force, the early experiments mainly focused on the measurement of film drainage process. Such studies provided valuable insights into the role of hydrodynamic forces along with repulsive and attractive surface forces in determining the

film drainage dynamics that led to either a stable equilibrium film or rupture of the film, leading to three phase contact.

The same experimental technique has been used to study the interaction between a bubble and a mica plate in a range of monovalent electrolyte solutions of mM concentration range (Pushkarova and Horn 2005; Pushkarova and Horn 2008). From these studies, the surface potential of the bubbles was found to be negative, with magnitude being less than 10 mV. However, the observed force displacement behavior remained unexplained (Pushkarova and Horn 2008). This is an area worth further investigation, as it is likely to yield some extremely interesting results.

#### **4.2.4 Atomic force microscope**

Complementary to film drainage measurements using the bubble expansion method or the surface force apparatus, the atomic force microscope (AFM) has been adapted to measure bubble-particle interactions. The earliest attempts used the colloid-probe technique to measure the equilibrium force between a colloid particle and sessile bubble on a substrate in electrolyte solutions (Butt 1994; Ducker et al. 1994). With the development of the technique to attach small, ultrasonically generated bubbles (~100  $\mu\text{m}$  diameter) in water onto the force-sensing cantilever, (Vakarelski et al. 2008) the time-dependent force between the bubble and a solid surface as the cantilever moved towards and away from the solid surface, was measured and modeled. The deformation of the bubble and film drainage between a bubble and various substrate materials have been studied using this approach (Manor et al. 2008; Manor et al. 2008; Tabor et al. 2011). Unfortunately, the flexibility of the AFM in undertaking such measurements was offset by the fact that there was no method to measure directly the bubble-surface separation or to determine the extent of bubble deformation

during the measurement. Such information had to be inferred from theoretical modeling of the drainage process.

#### **4.2.5 An important but less explored domain**

Due to the experimental design, each of the experimental methods described above to study bubble-particle interactions has its own strengths, but also suffers some inherent limitations. The free bubble rise method is capable of monitoring the motion, collision and bounce of the bubble to and from a solid plate surface over a high Reynolds number regime. However, to quantify experimentally the effects of bubble deformation and film drainage during the course of collision and bounces between the bubble and the solid surface, significant technical challenges remain because of the disconnect between the temporal and spatial scales involved.

Studies of bubble-solid interactions using the bubble expansion method or the surface force apparatus yielded accurate and valuable information on bubble deformation and film drainage. The inherent design of the apparatus limited the experiments to a low Reynolds number regime. While it is possible in principle to measure the time dependent force using this approach, this has yet to be attempted.

In contrast, experiments using the AFM are capable of direct measurement of colloidal forces at the nN sensitivity. There is also considerable flexibility and controls in bubble approach/retract velocities. However, since only bubbles or particles of sizes  $\sim 100 \mu\text{m}$  or less can be used in the AFM experiments, direct and precise measurements of bubble deformation is difficult if not impossible. Furthermore in common with SFA studies, experiments with AFM are typically confined to the low Reynolds number regime.

Therefore a relatively unexplored domain, defined by small to intermediate Reynolds numbers, the ability to control the bubble-particle collision trajectory, to measure the extent of bubble deformation and the drainage of the trapped film between the deformed bubble and the particle, presents fertile opportunities for a different experimental approach. The integrated thin film drainage apparatus, in its current stage of the development with potential extensions, has the promise of adding to this important knowledge domain.

#### **4.3. Integrated thin film drainage apparatus (ITFDA)**

The current version of the integrated thin film drainage apparatus (ITFDA) is designed to measure the force between a solid glass sphere, as a model particle, and a bubble in different liquids. The design principle of the ITFDA is similar to that of an atomic force microscope (AFM) and the surface forces apparatus (SFA). It operates in the millimeter size range of bubbles and particles – intermediate between that of the AFM and SFA, and allow measurement of interaction forces over a wider range of Reynolds numbers. The ITFDA incorporates the strength of both SFA and AFM that features the flexibility of measuring the time-dependent forces between the bubble and the particle under controlled variations in their relative displacement. The radii of the bubble and particle, the initial bubble-particle separation and bubble deformation that occur during the interaction are measured from the images of real time videos. Another important attribute of the ITFDA is the ability to modify the surface properties of the bubble and the glass sphere in situ during the measurement. This capability offers the opportunity to study the effect of surfactants on the liquid-air interface, the wetting properties of solid surface and the additives in solution on stability and thin film drainage dynamics. All of the experiments used in this chapter are conducted by Louxiang Wang in 1 mM KCl solutions of pH 5.6 (Wang 2013).

### 4.3.1 Design features

A schematic diagram of the key components of the ITFDA and a photo of the bubble-glass sphere configuration is given in **Figure 4.1**. The apparatus is housed in a stainless liquid chamber with two optical grade transparent windows placed perpendicular to each other to permit the view and recording of the bubble approaching the sphere particle during the measurement for subsequent analysis.

A bubble is generated at the end of a vertical glass capillary tube that is immersed in the test liquid. It is sealed when the bubble attains the required size to be used for force measurements. The glass capillary tube, with the bubble attached is positioned above the glass sphere. They are aligned in an axisymmetric configuration with the help of two perpendicularly positioned cameras in the plane perpendicular to the axis of symmetry, to provide views in orthogonal directions. The axisymmetric alignment facilitates theoretical analysis.

The time-dependent interaction between the bubble and the glass sphere is studied as the capillary tube drives the bubble to approach or retract away from the solid sphere in a well-controlled manner in terms of the extend of bubble-particle overlap and the bubble-particle approach/retract velocities.

### 4.3.2 Force sensing bimorph

The glass sphere is attached to the free end of a bimorph cantilever that is used as a force sensor. A piezo ceramic actuator with a dimension of 20 mm × 3 mm × 0.3 mm and a capacitance of 20 nF (Fuji Ceramics Corp.), is used to fabricate the force sensor. The actuator is enclosed in a fluorinated ethylene propylene sheath and mounted on a small

stainless steel chamber. The piezoelectric property of the bimorph material generates an electrical potential in response to deformation under an external force,  $F$  exerted on the glass sphere by the approaching bubble. The deformation of bimorph cantilever is determined by measuring the voltage. The bimorph force sensor is calibrated by placing small pieces of platinum wire of known mass on the cantilever and determining the voltage generated. The cantilever used in this study has a force sensitivity in the  $\mu\text{N}$  range.

The ITFDA measures the interaction force in terms of the calibrated output voltage of the bimorph sensor. In contrast, the force measurement in AFM is accomplished by determining the deflection of a force sensing cantilever using the optical lever technique and a position-sensitive photo diode system. After determining the effective spring constant of the cantilever, the force is obtained from the product of deflection and the effective spring constant of the cantilever.

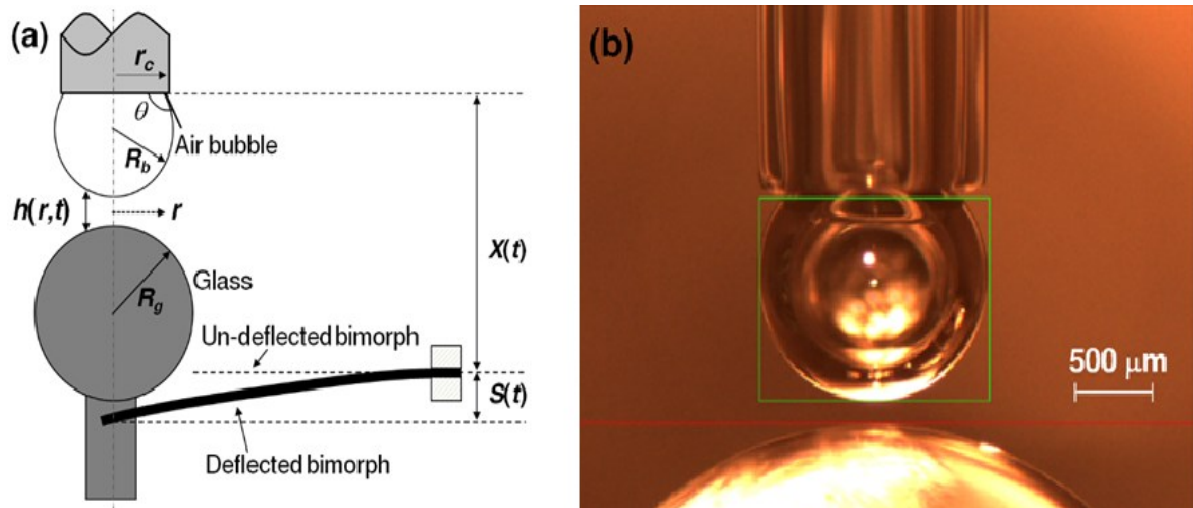


**Fig. 4.1** (a) Schematic diagram of the key components and characteristic parameters of the ITFDA: the time-dependent separation distance between the lower surface of the bubble and the top surface of the glass sphere at a distance  $r$  from the axis of symmetry,  $h(r,t)$ ; inner radius of the glass capillary tube,  $r_c$ ; angle of the bubble on the bottom of the capillary tube,  $\theta$ ; bubble

radius,  $R_b$ ; glass sphere radius,  $R_g$ ; the position of the glass capillary tube relative to the fixed end of the cantilever,  $X(t)$ ; and the deflection of the bimorph cantilever,  $S(t)$ . (b) Photograph of the bubble at the end of the glass capillary tube above the glass sphere. The red line and green square are drawn to confirm the symmetry of the bubble.

### 4.3.3 The glass sphere

The glass sphere attached to the bimorph used in the current study is obtained by melting a  $1.5 \pm 0.1$  mm diameter Pyrex rod under a butane-oxygen flame until the surface tension of the melting Pyrex produces nearly a spherical surface with a diameter of  $4.5 \pm 0.2$  mm. The spheres prepared this way are molecularly smooth with a peak-to-peak roughness determined by AFM imaging to be less than 1.2 nm.

### 4.3.4 Bubble generation and displacement control

The air bubble is generated using a micro-syringe at the end of the glass capillary tube of  $1.10 \pm 0.01$  mm inner diameter (Fisher Scientific). The end of the glass tube is placed under a butane flame to create a smooth end appropriate for bubble generation and force measurements. Extreme caution is taken to avoid overheating of the tube to ensure a uniform geometric symmetry at the end of the capillary tube. The bubble generation process and its size are monitored by real-time video observations. This arrangement allows reproducible generation of bubbles with desired diameters of  $1.46 \pm 0.01$  mm. The other end of the capillary is attached to the diaphragm of a speaker that is used to control the vertical displacement of the capillary tube. A computer-generated waveform is used to control the patterns of the diaphragm displacement that in turn drives the attached air bubble towards or away from the lower glass sphere in the desired manner.

### 4.3.5 Force measurement protocol

For a typical force measurement, a fresh air bubble was generated at the end of the glass capillary tube. The bubble size and the gap between the bubble and the glass sphere were precisely controlled with the aid of two CCD cameras positioned perpendicular to each other. The glass capillary tube, with the attached air bubble, was driven towards and then away from the lower glass sphere by the diaphragm of the speaker. A typical approach-retract cycle that records variations of the capillary tube position with time,  $t$ , is shown in **Figure 4.2**. The capillary tube with the bubble attached is first driven towards the lower glass sphere by decreasing the distance  $X(t)$  between the capillary tube and the fixed end of the cantilever (**Figure 4.1**) in the approach part of the cycle. The voltage to the speaker is then reversed to move upward the air bubble away from the glass surface in retraction phase. The time-dependent voltage applied to the speaker, the actual displacement recorded with a position sensitive displacement sensor and bimorph output are recorded for the approach-retract cycle and synchronized with the video recording the bubble shape using two CCD cameras placed in orthogonal orientations in the plane normal to the direction of bubble displacement.

Change in the position of glass tube,  $\Delta X(t)$ , is measured by a displacement sensor with a detection sensitivity of 5  $\mu\text{m}$ , mounted on the speaker diaphragm. The measured  $\Delta X(t)$  (dotted line) in **Figure 4.2a** was fitted with a polynomial function to obtain a smooth curve (solid line) and hence facilitate the determination of capillary displacement velocity. The instantaneous velocity  $dX(t)/dt$  was obtained by differentiating this polynomial function as shown in **Figure 4.2b**. The instantaneous values of  $\Delta X(t)$  and  $dX(t)/dt$  were used in all data analysis and modeling.

The initial distance of the closest approach between the bubble and the glass spheres is

set to  $h_0 = 120 \pm 10 \mu\text{m}$  and the maximum displacement of the capillary tube is set to  $160 \pm 5 \mu\text{m}$  (see **Figure 4.2**). Such a combination of settings translates to an overlap of the bubble and the solid sphere by  $40 \mu\text{m}$ . The ability to measure or specify the initial separation and the maximum displacement between the bubble and the sphere, and hence the bubble-particle overlap in the ITFDA is one of the advantages of the ITFDA over the AFM.

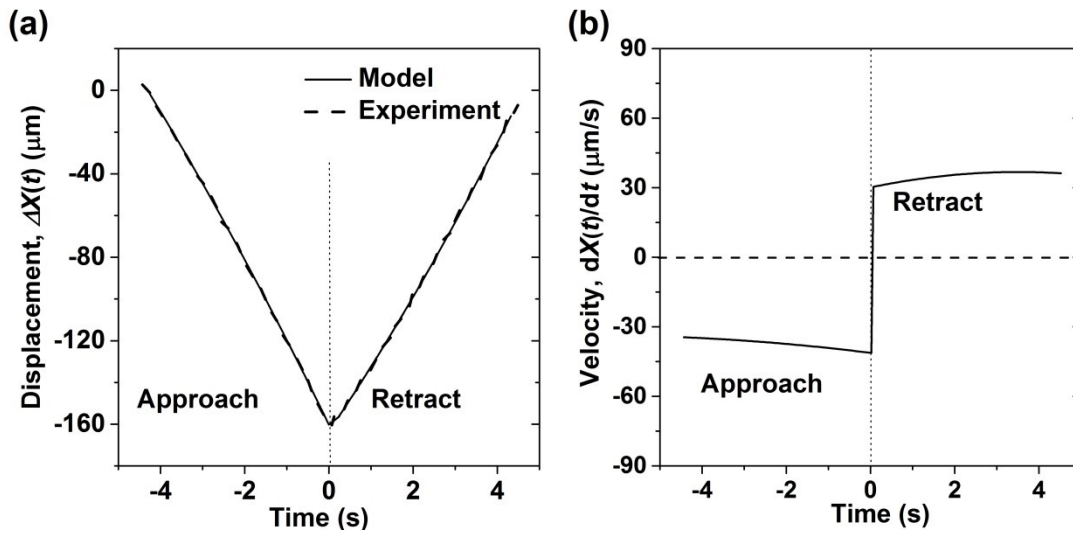


**Fig. 4.2** (a) The measured (points) displacement of the capillary tube  $\Delta X(t)$  and the corresponding polynomial fit (line); and (b) the instantaneous velocity  $dX(t)/dt$  (see **Figure 4.1**) obtained by differentiating the polynomial, as a function of measurement time. The nominal velocity of the approach-retract cycle is  $33.4 \mu\text{m/s}$ . The maximum displacement is  $160 \mu\text{m}$ .

By varying the approach and retract time of the capillary tube for a given displacement, the bubble can be driven with nominal velocity from around  $30 \mu\text{m/s}$  to  $140 \mu\text{m/s}$ . In the experiment, at least 10 measurements were conducted for each set of conditions. For noise reduction, the force signal was processed through a low pass filter with a cut-off frequency of 10 Hz.

The initial separation between the bubble and the glass sphere,  $h_0$ , the radius of the

bubble,  $R_b$ , the radius of the glass sphere,  $R_g$ , as well as the angle subtended by the bubble at the end of the capillary tube,  $\theta$  (**Figure 4.1**) can all be determined from the recorded images, using the image analysis program interfaced with LabVIEW 8.0.

#### **4.3.6 Cantilever deflection**

Quantitative modeling of the experimentally measured forces requires to know the value of the instantaneous cantilever deflection,  $S(t)$ . With the linear-dependence of  $F$  on the deflection  $S$  as verified independently, the measured deflection,  $S(t)$  of the force sensing bimorph allows the calculation of the applied force,  $F(t)$  by  $F(t) = K S(t)$ , if the cantilever spring constant,  $K$  is available. The bimorph cantilever used in this study has a spring constant  $K$  in the range of 60 - 70 N/m. To determine  $S(t)$  from the measured voltage, the relation between the charge (or voltage) developed in the bimorph and the displacement of the bimorph,  $S(t)$  is first established by placing the glass capillary tube in the direct contact with the bimorph cantilever and measure the output voltage of the bimorph due to the change in the capillary tube displacement,  $\Delta X(t)$  that is now equal to the change in the cantilever deflection  $\Delta S(t)$  (see **Figure 4.1**).

#### **4.4. Theoretical model**

The theoretical framework that we used to model the measurements of the hydrodynamic interaction between a deformable bubble and a glass sphere was established in the third chapter of this thesis. Readers are referred to the third chapter of this thesis for a more detailed description of the theoretical model. In brief, drainage of the liquid film between the bubble and the sphere is described by the Reynolds lubrication theory under Stokes flow. This theory relates the evolution of the position- and time-dependent separation,  $h(r,t)$  to the

hydrodynamic pressure,  $p(r,t)$  and the disjoining pressure,  $\Pi(h(r,t))$  arisen from the surface forces in the film. The deformation of the liquid-air interface of the bubble is described by the non-linearized Young-Laplace equation. The approach is known as the non-linearized Stokes-Reynolds-Young-Laplace (NSRYL) model. In the experiments with the ITFDA, the displacement function,  $X(t)$  of the glass capillary tube drives the space-time evolution of these equations.

#### 4.4.1 Governing equations

The Stokes-Reynolds equation for film evolution is given by

$$\frac{\partial h}{\partial t} = \frac{1}{12\mu} \frac{1}{r} \frac{\partial}{\partial r} \left[ r h^3 \left( \frac{\partial P}{\partial r} \right) \right] \quad (4.1)$$

where  $\mu$  is the shear viscosity of the Newtonian liquid. Implicit in **eqn. 4.1** is that the hydrodynamic boundary condition at the bubble surface is the same as the tangentially immobile condition that holds at the glass surface. The usual assumption of a zero tangential stress condition at the bubble surface was found to result in a drainage rate that is too fast as compared to the observations with the ITFDA. Trace surface impurities are suggested as being responsible for the observed immobile boundary condition at the bubble surface.

The liquid-air interface of the film deforms as a result of the hydrodynamic pressure in the film. According to the Young-Laplace model, the film thickness is governed by the equation:

$$\frac{\gamma}{r} \frac{\partial}{\partial r} \left( \frac{r \partial h / \partial r}{(1 + (\partial h / \partial r)^2)^{1/2}} \right) = \frac{\gamma}{r} \left[ \frac{\partial h / \partial r + r \partial^2 h / \partial r^2 + (\partial h / \partial r)^3}{(1 + (\partial h / \partial r)^2)^{3/2}} \right] \quad (4.2)$$

$$= \frac{2\gamma}{R} - \Pi(h(r, t)) - p(r, t)$$

where  $\gamma$  is the surface tension of liquid (Chan et al. 2011). The mean radius,  $R$  is defined as a characteristic value of the pressure: ( $\gamma/R$ ) in this problem.

The Laplace pressure, that is the pressure difference between the interior and the exterior of a spherical bubble of radius  $R_b$ , is given by ( $2\gamma/R_b$ ). If the bubble at the end of the capillary tube is deformed as a result of interaction, its Laplace pressure will change to ( $2\gamma/R_L$ ). If the deformation is small then the approximation:  $R_L \approx R_b$  would hold. We can then approximate  $R$  in **eqn. 4.2** by

$$\frac{1}{R} \equiv \frac{1}{R_L} + \frac{1}{R_g} \approx \frac{1}{R_b} + \frac{1}{R_g} \quad (4.3)$$

With the initial parabolic profile

$$h(r, t) = h_0 + \frac{r^2}{2R} \quad (4.4)$$

**Eqns. 4.1** and **4.2** are solved in the domain of  $0 \leq r \leq r_{\max}$  where the motion of the glass capillary tube enters in the boundary condition at  $r = r_{\max}$

$$\frac{\partial h(r_{\max}, t)}{\partial t} = V - \frac{1}{2\pi\gamma} \frac{dF(t)}{dt} \left\{ \log \left( \frac{r_{\max}}{2R} \right) + B(\theta) \right\} \quad (4.5)$$

with  $D(t) \equiv S(t) + X(t) = F(t)/K + X(t)$ ,

$$B(\theta) = 1 + \frac{1}{2} \log \left( \frac{1 + \cos\theta}{1 - \cos\theta} \right) \quad (4.6)$$

and the force  $F(t)$  is given by

$$F(t) = 2\pi \int_0^{\infty} [p(r', t') + \Pi(h(r', t'))] r' dr' \quad (4.7)$$

In the current study of hydrodynamic interactions using the ITFDA, the effect of the disjoining pressure,  $\Pi(h(r,t))$  due to surface forces is negligible because the liquid film between the bubble and the glass sphere remains much thicker than the operative range of  $\Pi$ , which was confirmed experimentally by observing a negligible effect of changing aqueous solution pH and electrolyte concentration on the measured force profiles in the current study.

#### 4.4.2 Scaling and universality of the governing equations

The non-linearized Stokes-Reynolds-Young-Laplace equations can be cast into a universal form with the following scaling in which the dimensionless variables are denoted by asterisks: <sup>36</sup>

$$\begin{aligned} \text{film thickness: } h &\equiv [Ca^{1/2}R] h^* \\ \text{radial coordinate: } r &\equiv [Ca^{1/4}R] r^* \\ \text{time: } t &\equiv [Ca^{1/2}R/V] t^* \\ \text{pressure: } p &\equiv [\gamma/R] p^* \\ \text{disjoining pressure: } \Pi &\equiv [\gamma/R] \Pi^* \\ \text{force: } F &\equiv [(\gamma/R) (Ca^{1/4}R)^2] F^* \equiv [Ca^{1/2} \gamma R] F^*. \end{aligned} \quad (4.8)$$

where  $V \sim dX(t)/dt$  is a characteristic velocity and  $Ca \equiv \mu V/\gamma$  is the capillary number that measures the ratio of viscous forces to capillary forces. In the present ITFDA experiments, the capillary number is small:  $Ca \sim 10^{-6}$ .

In terms of the scaled variables, the Stokes-Reynolds equation that describes film drainage between a bubble and a solid sphere, **eqn. 4.1**, becomes

$$\frac{\partial h^*}{\partial t^*} = \frac{1}{12r^*} \frac{\partial}{\partial r^*} \left( r^* h^{*3} \frac{\partial p^*}{\partial r^*} \right) \quad (4.9)$$

and **eqn. 4.2** for film thickness becomes

$$\frac{1}{r^*} \left[ \frac{\partial h^* / \partial r^* + r^* \partial^2 h^* / \partial r^{*2} + Ca^{0.5} (\partial h^* / \partial r^*)^3}{(1 + Ca^{0.5} (\partial h^* / \partial r^*)^2)^{3/2}} \right] = 2 - p^* - \Pi^* \quad (4.10)$$

The initial condition, **eqn. 4.4** now has the form

$$h^*(r^*, 0) = h_o^* + (r^*)^2 \quad (4.11)$$

A remarkable observation is that these scaled equations depend on the physical parameters system via capillary number and disjoining pressure in **eqn. 4.10**. The boundary condition at  $r^*_{max}$ , **eqn. 4.5**, with  $dX(t)/dt \sim -V$ , also has a weak logarithmic dependence on the capillary number  $Ca$ :

$$\frac{\partial h^*(r^*_{max}, t^*)}{\partial t^*} = -1 + \frac{1}{2\pi} \frac{dF^*}{dt^*} \left\{ \frac{2\pi\gamma}{K} - \log\left(\frac{1}{2} Ca^{1/4} r^*_{max}\right) - B(\theta) \right\} \quad (4.12)$$

**Eqn. 4.12** provides the dependence of film drainage on the interfacial tension and the fluid viscosity. The left hand side of **eqn. 4.10** represents the small deformation approximation of mean curvature of  $h^*$ . If the disjoining pressure is negligible, that is  $\Pi \ll (\gamma/R)$ , then this curvature changes sign when the scaled pressure  $p^* \equiv (R/\gamma) p$  has the numerical value of 2.

The governing equations, **eqns. 4.9** and **4.10** together constitute a differential algebraic equation system and can be solved numerically to find the temporal evolution of the drainage, deformation of air/liquid interface, and the time dependent forces between interacting air bubble and glass sphere. The NSRYL model provides a consistency check on results obtained with the ITFDA using fluids of different interfacial tensions and fluid viscosities. We will see a demonstration of this application in Section 4.5.

#### **4.5. Experiments with hydrophilic glass**

Now we present results of force measurements between a bubble and a glass sphere in aqueous electrolyte solutions, ethanol and silicone oil using the ITFDA. These fluids are chosen to demonstrate the flexibility of the ITFDA: being able to measure hydrodynamic interaction in a fluid over a wide range of surface tension, fluid viscosity and driving speed. The results will be compared with the non-linearized Stokes-Reynolds-Young-Laplace (NSRYL) model outlined in Section 4.4.

To facilitate comparison across the three liquids, the glass sphere is rendered hydrophilic to avoid any possible hydrophobic attraction between the bubble and the glass that might rupture the intervening liquid film. A summary of material properties and characteristics of the ITFDA is given in **Table 4.1**. Aqueous KCl electrolyte solution and ethanol have nearly identical viscosities but with surface tensions that differ by a factor of 3, whereas ethanol and silicone oil have nearly identical surface tensions but have viscosities that differ by a factor of 55. Thus measurements using this triplet of fluids allow us to delineate the effects of interfacial tension and fluid viscosity on thin liquid film drainage dynamics and validate the applicability of NSRYL model over a wider range of fluids and Reynolds numbers.

**Table 4.1** Material constants and ITFDA parameters.

Bubble radius, $R_b$	$730 \pm 5 \mu\text{m}$
Particle radius, $R_p$	$2200 \pm 50 \mu\text{m}$
Geometric mean radius, $R$	$550 \mu\text{m}$
Bubble angle at capillary tube, $\theta$	$132^\circ$
Surface tension, $\gamma$ – KCl solution	71 mN/m
– ethanol	22 mN/m
– silicone oil	22 mN/m
Viscosity, $\mu$ – KCl solution	1 mPa s
– ethanol	1 mPa s
– silicone oil	55 mPa s
Bimorph cantilever constant, $K$	$64 \pm 4 \text{ N/m}$
Initial separation, $h(0,0)$	$123 \pm 3 \mu\text{m}$
Maximum displacement, $\Delta X_{\text{max}}$	$160 \mu\text{m}$
KCl	1mM
pH	5.6
Zeta potential of air bubble	-30 mV
Zeta potential of glass sphere	-50 mV
Hamaker constant	$-8 \times 10^{-21} \text{ J}$

#### 4.5.1 Surface treatment

The capillary tube and the glass sphere were treated in freshly prepared piranha solutions (3:1 v/v  $\text{H}_2\text{SO}_4:\text{H}_2\text{O}_2$ ) at  $80^\circ\text{C} - 90^\circ\text{C}$  for 30 min, rinsed thoroughly with Milli-Q water and blow-dried using an ultra-pure nitrogen stream. The surfaces prepared in this manner were free of contamination and completely water wettable. The sample chamber was cleaned in the anhydrous ethyl alcohol (Commercial Alcohols Inc.) under ultrasonication for half an hour, rinsed with de-ionized water and then blow-dried with ultrapure nitrogen. The bimorph beam was mounted on to the chamber wall. A glass sphere was clamped at the free end of the bimorph in a dust-free laminar flow environment. The chamber was then filled with test

solutions and placed on a three-dimensional translation stage. The capillary tube was filled with fresh air before being immersed into the solution. The system was then left for two hours to equilibrate the interfaces and to stabilize the bimorph signal before any measurement.

#### **4.5.2 Interaction in aqueous electrolyte solutions**

An example of the time-dependent force profile between an air bubble and a hydrophilic glass sphere in 1 mM KCl aqueous electrolyte solution of pH 5.6, measured using the ITFDA, is shown in **Figure 4.3a**. The bubble, initially at a separation of 120  $\mu\text{m}$  from the glass sphere, is first driven towards the sphere by moving the capillary tube at a nominal velocity of 33  $\mu\text{m/s}$  for 160  $\mu\text{m}$  and is then retracted at the same velocity. The repulsive force, rising towards the maximum during the approach phase is solely due to hydrodynamic repulsion, counterbalanced by the Laplace pressure force from the bubble. The force then decreases at the commencement of the retraction phase. The attractive (negative) force minimum is attributed to hydrodynamic suction as the bubble separates from the glass sphere. Using the system parameters in **Table 4.1**, the prediction of the time dependent force from the non-linearized Stokes-Reynolds-Young-Laplace model is in good agreement with the experimental data.

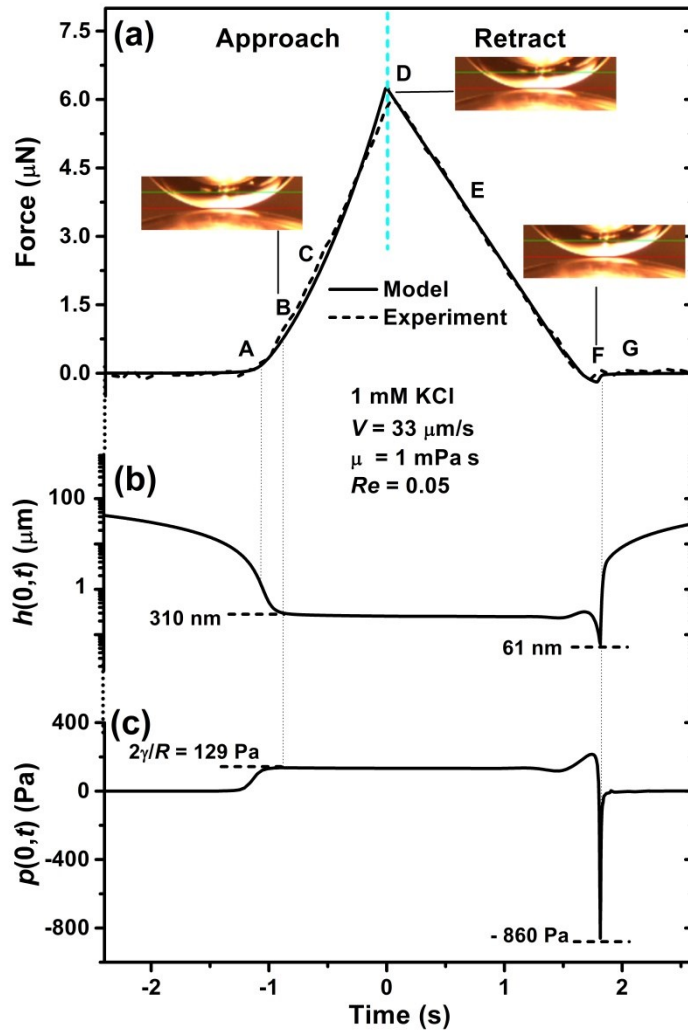


**Fig. 4.3** Variation of the force  $F(t)$  – experiment (dashed line) and model (solid line), calculated central film thickness  $h(0,t)$  and central pressure  $p(0,t)$  as a function of measurement time for an air bubble approaching a solid sphere in aqueous electrolyte solution of 1 mM KCl and pH = 5.6 at nominal velocity of  $33 \mu\text{m/s}$ , corresponding to a Reynolds number  $Re = 0.05$  and capillary number of  $\sim 4.6 \times 10^{-7}$ . Insets of (a): photographs of the bubble and the glass sphere at times corresponding to point B, D and F on the force curve.

In **Figure 4.3b**, we show the predicted film thickness at the axis of symmetry,  $h(0,t)$  as a function of measurement time. When the force is repulsive,  $h(0,t)$  remains approximately constant at 310 nm, but briefly attains a minimum value of around 61 nm at the attractive

force minimum. In **Figure 4.3c**, we show the hydrodynamic pressure,  $p(0,t)$  at the same position. When the force is repulsive,  $p(0,t)$  has the constant value of 129 Pa. The force minimum is the consequence of the hydrodynamic suction at the negative pressure minimum of  $-860$  Pa and  $h(0,t) \sim 61$  nm.

However, both the variation of the film thickness profile,  $h(r,t)$  and the pressure profile,  $p(r,t)$  within the film are more complex and interesting. In **Figures 4.4a** and **4.4b**, we show the film profile,  $h(r,t)$  at various times along the force profile,  $F(t)$  indicated in **Figure 4.3a**. One key feature is the initial development of a dimple at point B, when the film thickness is  $\sim 310$  nm. The dimple grows to a maximum size at the force maximum (point D) with a dimple rim radius of  $\sim 110$   $\mu\text{m}$ . The minimum film thickness of  $\sim 170$  nm occurs at the dimple rim.

As discussed in Section 4.4.2, the initial formation of the dimple at a film thickness  $\sim 310$  nm is due to hydrodynamic repulsion, as the disjoining pressure arising from surface forces at such large separations is negligible. Indeed, turning now to **Figure 4.4c** for the hydrodynamic pressure, we see that at point B, the hydrodynamic pressure  $p$  reaches  $(2\gamma/R)$ , scaled Laplace pressure  $p^* \equiv (2\gamma/R) p = 2$  of the bubble, when the dimple begins to develop.

During the retraction phase (points D to G in **Figure 4.4b**), the thickness of most parts of the film increases with retraction from D to G, except around the axis of symmetry  $r = 0$ . In fact, we see in **Figures 4.3b** and **4.4b** that  $h(0,t)$  actually decreases to a minimum value  $\sim 61$  nm at point F, corresponding to the force minimum, before increasing with further retraction. This negative pressure is the hydrodynamic suction that gives rise to an attractive retraction minimum in the force profile.

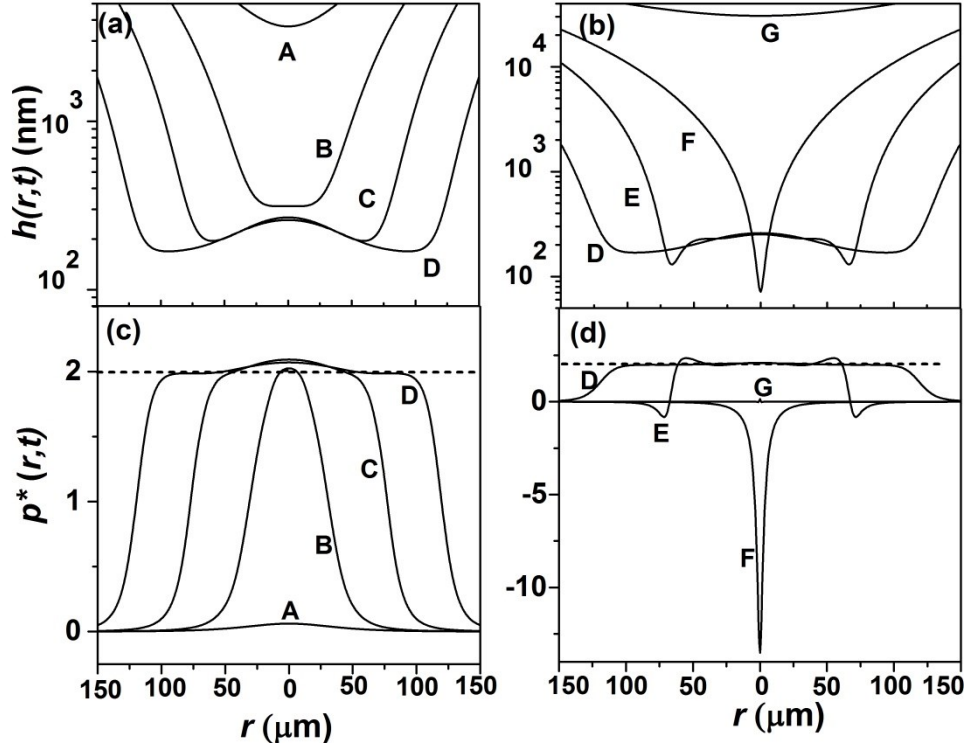


**Fig. 4.4** Thickness of the aqueous film,  $h(r,t)$  between the bubble and the glass sphere at different measurement times during (a) approach and (b) retraction; and the hydrodynamic pressure profile,  $p(r,t)$  scaled by  $(\gamma/R) = 64.5$  Pa in the water film during (c) approach and (d) retraction. As in **Figure 4.3**, the electrolyte concentration is 1 mM KCl and the nominal velocity,  $33 \mu\text{m/s}$ .

The experiment in **Figure 4.3** corresponds to a Reynolds number,  $Re = 2R\rho V/\mu = 0.05$ . In **Figure 4.5** we compare the experimental and theoretical results taken at  $Re = 0.2$ , corresponding to a nominal bubble velocity of  $134 \mu\text{m/s}$  which is 4 times larger than that for the experiment in **Figure 4.3**, with all other experimental parameters such as bubble size, initial separation and total displacement being the same as used in the experiment described in **Figure 4.3**. Qualitatively the results in **Figures 4.3** and **4.5** are similar. However, we note that the force maximum under higher approach velocity shown in **Figure 4.5a** is smaller than that shown in **Figure 4.3a**. The result can be understood by investigating bubble deformation shown in **Figures 4.5d** and **4.5e**.

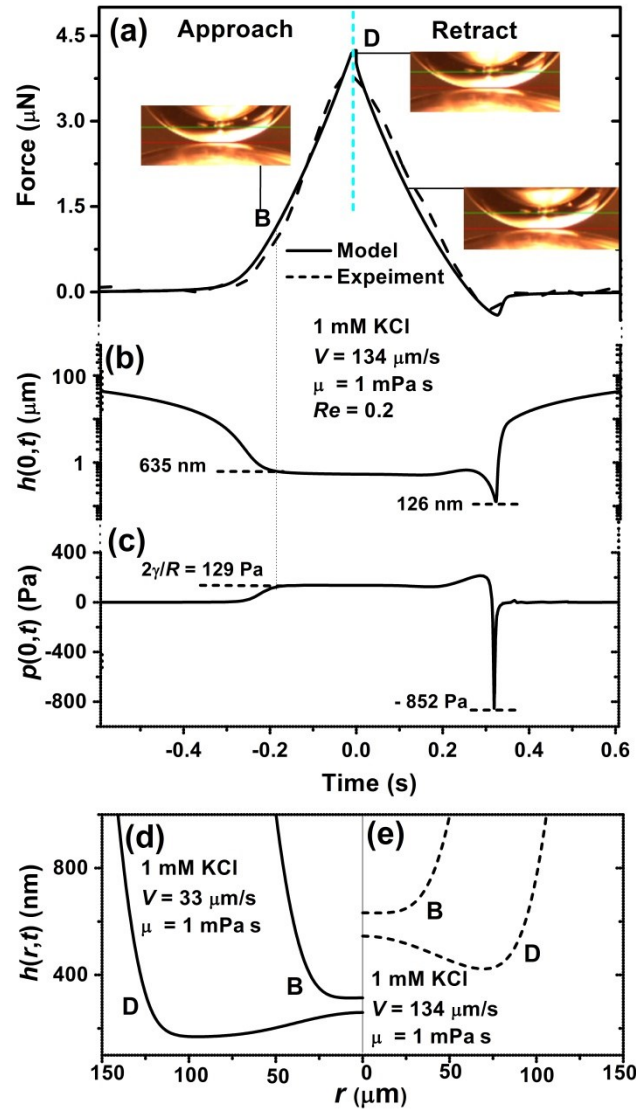


**Fig. 4.5** Variation of the force  $F(t)$  – experiment (points) and model (line), calculated central film thickness  $h(0,t)$  and central pressure  $p(0,t)$  as a function of measurement time for an air bubble approaching a solid sphere in aqueous electrolyte (1 mM KCl, pH = 5.6) at nominal velocity of  $134 \mu\text{m/s}$ , corresponding to a Reynolds number  $Re = 0.2$  and capillary number of  $\sim 1.8 \times 10^{-6}$ . Insets: photographs of the bubble and the glass sphere at times indicated on the force curve.

Since the bubbles have identical radii in both experiments, they have the same Laplace pressure:  $2\gamma/R = 129 \text{ Pa}$ . As the hydrodynamic pressure in the water film due to the approach

of the bubble increases to  $2\gamma/R$ , the bubble surface will flatten, resulting in an increase in the intervening film (interaction) area. At higher approach velocity of  $134\ \mu\text{m/s}$  or higher  $Re$  of 0.2 (**Figure 4.5**), the hydrodynamic pressure reaches the Laplace pressure at a larger bubble-particle separation of  $635\ \text{nm}$ , as compared to the separation of  $310\ \text{nm}$  for bubble approaching at  $33\ \mu\text{m/s}$  or  $Re = 0.05$  (**Figure 4.3**), see curve B in **Figures 4.5d** and **4.5e**. The radial extent of the dimple at  $134\ \mu\text{m/s}$  or  $Re = 0.2$  is smaller, expanding to around  $75\ \mu\text{m}$  (curve D in **Figure 4.5e**) in comparison to around  $110\ \mu\text{m}$  for the case of bubble approach velocity of  $33\ \mu\text{m/s}$  or  $Re = 0.05$  (curve D in **Figure 4.5d**). Since the force is approximately the product of the Laplace pressure and the flattened film area, the smaller flattened area (or radius) at higher bubble approach velocity of  $134\ \mu\text{m/s}$  or  $Re = 0.2$  is responsible for the observed smaller force maximum.

It is interesting to note that the minimum film thickness reached before retraction is 50% thinner at  $61\ \text{nm}$  for the lower bubble approach velocity case, as compared to  $126\ \text{nm}$  for the higher bubble approach velocity case. In the context of interactions involving deformable surfaces, an important finding from this study is that with all other things being equal, slower bubble approach velocity will result in the formation of thinner liquid films. This is in contrast to rigid bodies in which a faster drive velocity will lead to smaller separations.

### 4.5.3 Interaction in ethanol and silicone oil

In **Figure 4.6** we show the effects of varying the surface tension of liquid by using ethanol with a surface tension about one third of the surface tension of water. The effect of liquid viscosity is shown in **Figure 4.7** by conducting the measurements in silicone oil which has a viscosity 54 times higher than the viscosity of ethanol but the same surface tension as ethanol (see **Table 4.1**).

The essential difference between the results obtained in water and in ethanol can be understood in terms of the difference in Laplace pressure,  $2\gamma/R$ , for the two liquids. For the same size of air bubble, the Laplace pressure of air bubble in ethanol is 40 Pa, in comparison to 129 Pa for the air bubble in water. Such a difference in the Laplace pressure of the air bubble means that with all other things being equal, bubble deformation in ethanol will occur at smaller hydrodynamic forces, translating to larger separation distances as shown in **Figures 4.6d** and **4.6e**. By the same reasoning developed to account for the decreased maximum repulsive forces with increasing bubble approach velocity in water, the maximum repulsive force in ethanol at the same bubble approach velocity is found to be only about one-thirds of the value obtained for water.

For an air bubble approaching a solid sphere at 33.4  $\mu\text{m/s}$  in the silicone oil having a viscosity 54 times higher than the viscosity of water or ethanol, although the Reynolds number is small  $\sim 10^{-4}$ , the hydrodynamic pressure on the solid sphere from the motion of the bubble is much higher. As a result, a larger repulsive force (**Figure 4.7a**) and a stronger hydrodynamic pull-off adhesion (**Figure 4.7c**) are measured in the silicon oil than in the ethanol, although both have the same surface tension of the liquid. Such differences are again accounted for by the deformation and flattening of the bubble, now occurring at a much larger separation distance of about 4,125 nm in silicon oil, as compared to 600 nm for the bubble approaching the solid sphere at the same bubble velocity in the ethanol that has the same Laplace pressure of 40 Pa.

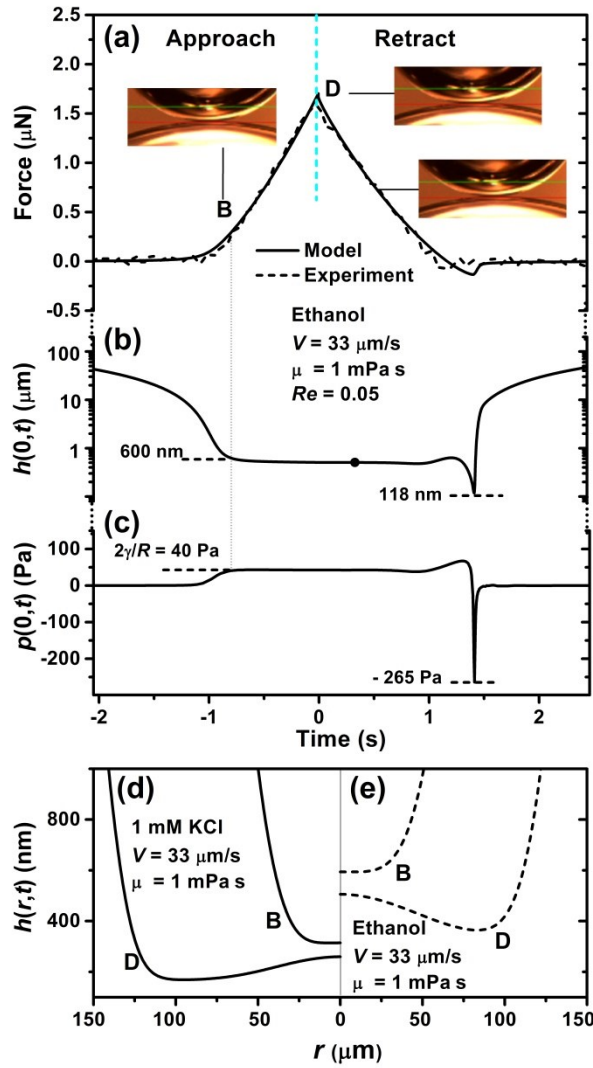


**Fig. 4.6** Variation of the force  $F(t)$  – experiment (points) and model (line) along with the calculated central film thickness  $h(0,t)$  and central pressure  $p(0,t)$  as a function of measurement time of an air bubble approaching a solid sphere in ethanol at the nominal velocity of  $33.4 \mu\text{m/s}$ , corresponding to a Reynolds number  $Re = 0.05$  and capillary number of  $\sim 1.4 \times 10^{-6}$ . Insets: photographs of the bubble and the glass sphere at the times indicated on the force curve.

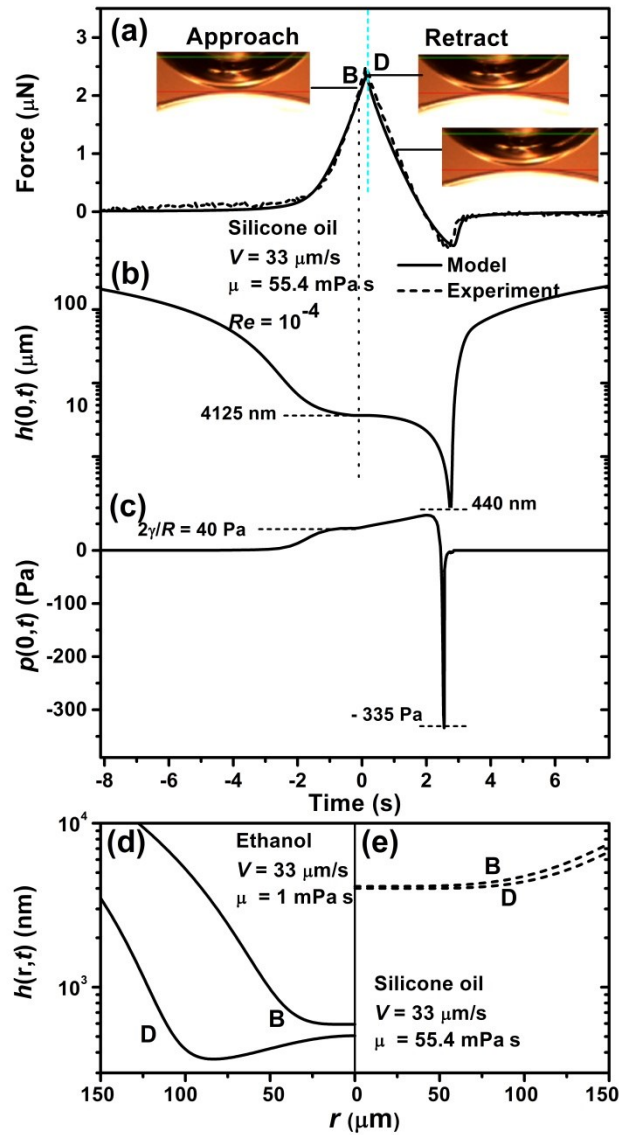


**Fig. 4.7** Variation of the force  $F(t)$  – experiment (points) and model (line) along with the calculated central film thickness  $h(0,t)$  and central pressure  $p(0,t)$  as a function of measurement time of an air bubble approaching a solid sphere in silicone oil at nominal velocity of  $33.4 \mu\text{m/s}$ , corresponding to a Reynolds number  $Re = 10^{-4}$  and capillary number of  $9.1 \times 10^{-5}$ . Insets: photos of the bubble and the glass sphere at the times indicated on the force curve.

#### 4.5.4 Scaling of experimental results

The above experiments of measuring the hydrodynamic forces between bubbles and

solid glass spheres in water, ethanol and silicone oil of different surface tensions and viscosities are conducted using the ITFDA at small Reynolds number,  $Re (< 0.2)$  and small capillary number,  $Ca (\sim 10^{-6})$ , which allows us to compare the experimental results and theoretical predictions. In **Figure 4.8**, the measured contact diameters between the bubble and the glass sphere from the side view cameras for all the systems studied are compared with the predicted contact diameter or twice the dimple radius,  $R_f$ . Considering such a wide range of experimental conditions, the agreement is considered remarkably good, demonstrating not only the excellent capability of the newly designed ITFDA for studying hydrodynamic interactions between deformable surfaces, but also the wider range applicability of non-linearized Stokes-Reynolds-Young-Laplace model.

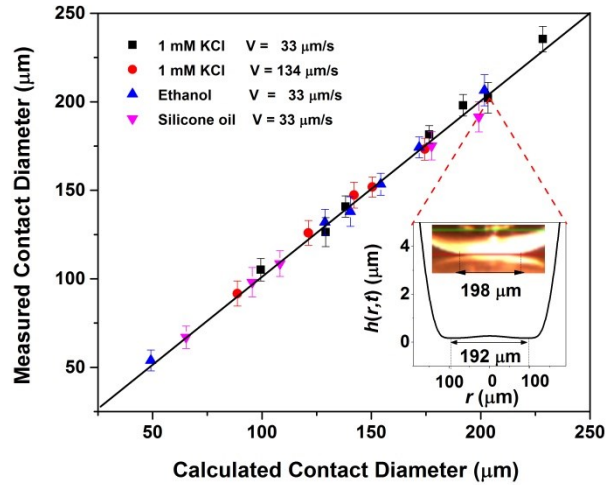


**Fig. 4.8** A comparison between the measured and the calculated contact diameter between the bubble and the glass sphere in water, ethanol and silicone oil under different approach velocities in the repulsive part of the force profiles given in **Figures 4.3, 4.5- 4.7**.

To further understand the measured variation of repulsive forces with bubble approach velocity, liquid surface tension and viscosity, the measured repulsive forces scaled by

Laplace pressure of bubble ( $2\gamma/R_b$ ) are plotted as a function of film area in **Figure 4.9**. The good correlation between the two parameters suggests that in the absence of surface forces (i.e., when the disjoining pressure is very small or negligible), the Laplace pressure of bubble during interaction counterbalances the hydrodynamic force which drives bubble deformation. Even at relatively high hydrodynamic forces or large deformations, the measured repulsive force can be estimated from the product of the Laplace pressure of the undeformed bubble and the observed film area.

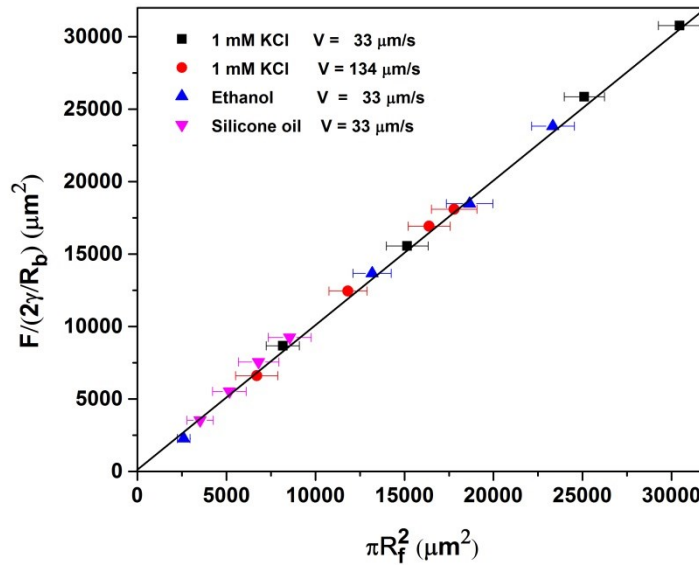


**Fig. 4.9** Correlation between the measured repulsive forces normalized by capillary pressure ( $2\gamma/R_b$ ) and the film area between the bubble and the glass sphere in water, ethanol and silicone oil under different drive conditions.

#### 4.6. Conclusions and future perspectives

With the ability to measure forces and deformations simultaneously, the development of the ITFDA makes it possible to delineate details of the system physics. The ITFDA offers the flexibility to vary parameters such as displacement velocity, interfacial tension and viscosity

of the fluids and the chemistry to modify the solid surface to variable wettabilities. The excellent agreement between the measured in the three fluids of very distinct physicochemical properties (viscosity, surface tension and polarity) and the predicted interaction forces demonstrates that the NSRYL model can be applied to the systems of a wider range of bubble approach velocity, liquid interfacial tension and viscosity. The excellent agreement also makes it possible to use the model to infer quantitative information about film profiles during the bubble approach-retraction. The simulation results indicate that the minimum film thickness in approach phase is thinner for the system of low bubble approach velocity, and/or low viscosity and high surface tension of the liquids. The agreement between the measured and predicted contact diameter shows the capability of ITFDA to accurately measure bubble deformation. The linear relationship between the normalized repulsive force by Laplace pressure and bubble deformation confirms the interdependence between bubble deformation and the strength of the hydrodynamic interaction forces. The results from this study also suggest that even under the relatively high hydrodynamic forces or large deformations, the force can be estimated from the product of the Laplace pressure of the un-deformed bubble and the film areas. It is our intention to further measure the bubble profile with similar experimental systems to fill the gap of confirming theoretical prediction with experimental results. In principle, the film thickness profile between the glass sphere and the deforming bubble can be measured by interferometry. This is an obvious direction for further development of this apparatus.

# Chapter 5

## Effect of hydrophobicity and bubble approach velocity on stability of wetting films between bubble and glass surfaces studied by non-linearized SRYL (NSRYL) model

### 5.1. Introduction

Wetting films form when bubbles and oil droplets approach a solid in an immiscible liquid (often water). Studying stability of wetting films is a major subject of surface and colloidal science. Many industrial processes such as foaming, emulsification, flotation and oil recovery operations depend on the stability of the intervening liquid films within these dispersion systems. In flotation, for example, the success of air bubble-particle attachment depends largely on the stability and drainage rate of thin liquid film between a solid particle and an air bubble (Yoon 2000; Nguyen and Schulze 2004; Nguyen et al. 1997). If the intervening aqueous film is unstable, the particles can attach to the bubble and float, otherwise no flotation would be possible. Thus, control of the stability of thin liquid film is of critical importance in flotation. Furthermore flotation of valuable particles is achieved through their selective attachment to air bubbles. According to the classical DLVO theory, the key parameter controlling the thin liquid film stability is the balance between the electrostatic and van der Waals forces. The concept of the classical DLVO theory proposed by Derjaguin-Landau (Deryagin and Khim 1940) and Verwey-Overbeek, (Verwey and Overbeek 1948) served as a basis for studying the stability of the wetting films and colloidal suspensions. However subsequent investigations showed that for many systems the classical DLVO theory fails to predict the stability of thin liquid films

(Lyklema and Mysels 1965; Tchaliowska et al. 1994; Yoon and Aksoy 1999). This discrepancy arises from hydrodynamic fluctuations (Ruckenstein and Churaev 1991) and/or the presence of other colloidal forces such as hydrophobic forces (Yoon and Aksoy 1999; Wang and Yoon 2004; Angarska et al. 2004). To resolve this controversy, an extended DLVO theory was proposed to include the hydrophobic attractive force in the classical DLVO theory (Yoon and Mao 1996; Mao and Yoon 1997). Furthermore in dynamic system, the hydrodynamic resistance force plays a crucial role in determining the drainage of thin liquid films. The complex interaction of hydrodynamic and surface forces (components of extended DLVO theory) ultimately controls the stability of wetting films between an air bubble and a solid particle in a liquid (water).

Early fundamental studies of thin films were conducted in specially designed capillary cells, referred to as Scheludko-Exerowa cells (Platikanov 1964; Ivanov 1988; Blake and Kitchener 1972). The technique has been used to indirectly examine the surface forces. In this technique a captive bubble was pressed against a flat silica surface to observe the time dependent drainage and stability of thin liquid films using an optical interferometer. A stable aqueous film was formed between an air bubble and a hydrophilic flat silica surface as a result of repulsive van der Waals and electrostatic double layer forces. The adsorption of cationic surfactants made the negatively charged silica surface hydrophobic. As a result the intervening liquid film became meta-stable and susceptible to spontaneous rupture (Schulze et al. 2001; Aronson and Princen 1978). It was observed that the rate of film drainage increased by increasing surface hydrophobicity (Pan and Yoon 2010; Pan et al. 2011). Numerous researches have been carried out with the colloidal probe technique in AFM invented by Binnig et al. (Binnig et al. 1986) to study the stability of thin liquid wetting films. One of the common applications of AFM is direct force measurement to investigate hydrodynamic and surface forces involved in stabilizing thin

liquid films. The interaction force between an air bubble and a solid was measured with AFM first by Butt (Butt 1994) and Ducker et al. (Ducker et al. 1991; Ducker et al. 1994). The AFM technique was further refined by Fielden et al. (Fielden et al. 1996). In their experiments, an air bubble was placed on a hydrophobic surface. A spherical particle was attached to the cantilever of AFM, which functioned as the probe of interaction forces. The net interaction force was measured by recording the cantilever deflection in response to the interactions between the probe and bubble surface using a split photodiode detector. Using this technique, it was observed that for hydrophobic particles there is a “jump to contact” into the air bubble at a critical distance. The jump-to-contact distance was found to be related to surface hydrophobicity and to be much larger for strongly hydrophobic surfaces (Preuss and Butt 1998; Preuss and Butt 1998). In fact the jump-to-contact distance of the particle into the air bubble is a strong indicator of the solid hydrophobicity. The hydrophobic attractive force is related to contact angle of particles. The hydrophobic force becomes stronger and accelerates film drainage for surfaces of larger contact angles (Fielden et al. 1996; Nguyen et al. 2003; Ishida 2007). The AFM has also been used for study of hydrodynamic interactions between a mineral particle and an air bubble. However, the force measurements were mainly carried out at low approach speed (up to  $\sim 100 \mu\text{m/s}$ ) so that the hydrodynamic force of the system was not comparable with the hydrodynamic forces of real systems, such as in flotation cells. The range and magnitude of the hydrodynamic force were found to increase significantly with increasing approach speed (Nguyen et al. 2003; Ishida 2007). As a result, the spontaneous rupture of the intervening liquid film was observed at very low approaching velocity (Butt 1994; Ducker et al. 1994; Fielden et al. 1996; Preuss and Butt 1998). Another technique to directly measure the interaction forces between two approaching interfaces is the integrated thin film drainage apparatus (Wang et al. 2012; Wang et al. 2013). The design

principle of the ITFDA is similar to the atomic force microscope (AFM). The ITFDA incorporates the strength of AFM in having the flexibility to measure the time-dependent forces between the bubble and particle under well-controlled relative displacement. This technique is able to operate at much greater approaching velocity (up to  $\sim 5000 \mu\text{m/s}$ ) which makes this technique capable of studying hydrodynamic conditions closer to the real system such as encountered in flotation. Under flotation conditions, hydrodynamic resistance force dominates the total force until the separation between the two surfaces reduces to approximately “jump to contact” distance. This is where the attractive hydrophobic force prevails the film drainage resistance, which results in a spontaneous film rupture and leads to the formation of three phase contact (TPC). The energy barrier between two interacting surfaces is mainly the result of counterbalance between hydrophobic, hydrodynamic, electrostatic and van der Waals forces (Yoon and Mao 1996). The external energy of an air bubble approaching a particle must be larger than the energy barrier to reach a thermodynamically stable state of TPC after a spontaneous film rupture.

The time needed for the film drainage, i.e., the thinning of intervening liquid film to a critical thickness (jump to contact distance) where rupture occurs, is known as the induction time (Yoon and Yordan 1991; Ye et al. 1989). Induction time between an air bubble and mineral particles has received extensive attention by researchers (Yoon and Yordan 1991; Ye et al. 1989; Gu et al. 2003; Nguyen et al. 1997; Nguyen et al. 1997). The induction time is a critical parameter needed to model bubble-particle attachment in flotation. A shorter induction time corresponds to a higher probability of bubble-particle attachment (Yoon and Yordan 1991; Laskowski et al. 1992; Coons et al. 2003).

The critical thickness, where the film rupture occurs, has been the subject of several theoretical and experimental investigations during the past four decades (Vrij 1966; Radoev et al. 1983; Valkovska et al. 2002; Scheludko and Manev 1968; Ivanov et al. 1970; Manev et al. 1974; Sharma and Ruckenstein 1987; Angarska and Manev 2001; Coons et al. 2003). In these early studies to estimate the critical film thickness, the approximate equations describing film drainage (Manev et al. 1997; Coons et al. 2003) and corrugation growth rate derived from linear stability studies (Vrij 1966; Sharma and Ruckenstein 1987; Coons et al. 2003) have been used. However, the experimental verification of the theories for the critical film thickness has been carried out using systems of varying conditions, which makes the comparison of the theories and verification of their validity difficult. In spite of comprehensive review by Coons et al. (Coons et al. 2003) that summarized the previously available data, there is still lack of direct comparison of the experimentally measured and theoretically predicted critical film thickness obtained under the same and well defined conditions. Despite the numerous efforts, there are significant confusions and uncertainties to predict critical film thickness from physiochemical properties of the system.

In this study we use the Young-Laplace equation to model bubble deformation and the Reynolds lubrication theory to account for hydrodynamic interactions with both no-slip and full slip boundary conditions at the bubble surface. The complete non-linear form of the governing equations was used with no simplifications. This model was developed to account for the effect of hydrophobic attractive force. More detailed description on the NSRYL model can be found in Section 5.2. The numerical results of the NSRYL model for time dependent force profiles are compared with the experimental data obtained using the integrated thin film drainage apparatus (ITFDA). The objective of the current study is to evaluate the hydrophobic force which is

considered as a driving force for destabilizing water films on hydrophobic surfaces. The effect of bubble approaching velocity and solid hydrophobicity on film drainage rate is investigated. This work also focuses on the prediction of induction time and force barriers, which are the minimum applied force needed to overcome the energy barrier between two surfaces before TPC. Furthermore, the current study will investigate the critical film thickness over a wide range of solid hydrophobicity and hydrodynamic conditions.

Theoretical model is developed in Section 5.2. Details of force measurements on bubble-solid in water using ITFDA are presented in Section 5.3. Measured dynamic forces are compared with theory in Section 5.4 and the results are discussed in Section 5.5.

## 5.2. Formulation of the problem (model)

The relative motion between the interacting drops or between the drop and solid particle will generate hydrodynamic interactions that arise from the flow of the continuous phase. The flow of the thin liquid film trapped by the deformable drop can be described by the Reynolds lubrication theory under Stokes flow. This theory relates the evolution of the position- and time-dependent separation,  $h(r,t)$  to the hydrodynamic pressure,  $p(r,t)$ . The Stokes-Reynolds equation for film evolution is given by:

$$\frac{dh(r,t)}{dt} = \frac{1}{12\mu} \frac{1}{r} \frac{\partial}{\partial r} \left[ rh^3 \left( \frac{\partial P(r,t)}{\partial r} \right) \right] \quad (5.1)$$

where  $\mu$  is the shear viscosity of the Newtonian liquid. Implicit in **eqn. 5.1** is that the hydrodynamic boundary condition at the bubble surface is the same as the tangentially immobile condition that holds at the glass surface. Trace surface active impurities are suggested as being responsible for the observed immobile boundary condition at the bubble surface.

The liquid-air interface of the film deforms as a result of the hydrodynamic and disjoining pressures in the film according to the Young-Laplace model. The film thickness then obeys the equation:

$$\frac{\gamma}{r} \frac{\partial}{\partial r} \left( \frac{r \partial h / \partial r}{(1 + (\partial h / \partial r)^2)^{1/2}} \right) = \frac{\gamma}{r} \left[ \frac{\partial h / \partial r + r \partial^2 h / \partial r^2 + (\partial h / \partial r)^3}{(1 + (\partial h / \partial r)^2)^{3/2}} \right] \quad (5.2)$$

$$= \frac{2\gamma}{R} - \Pi(h(r, t)) - p(r, t)$$

where  $\gamma$  is the surface tension of liquid. The mean radius,  $R$  is defined as a characteristic value of the pressure:  $(\gamma/R)$  in this problem. The Laplace pressure, that is the pressure difference between the interior and the exterior of a spherical bubble of radius  $R_b$ , is given by  $(2\gamma/R_b)$ . If the bubble at the end of the capillary tube is deformed as a result of interaction, its Laplace pressure will change to  $(2\gamma/R_L)$ . If the deformation is small, then the approximation:  $R_L \approx R_b$  would hold. We can then approximate  $R$  in **eqn. 5.2** by:

$$\frac{1}{R} \equiv \frac{1}{R_L} + \frac{1}{R_g} \approx \frac{1}{R_b} + \frac{1}{R_g} \quad (5.3)$$

with the initial parabolic profile of:

$$h(r, t) = h_0 + \frac{r^2}{R} \quad (5.3a)$$

By imposing appropriate initial conditions, **eqns. 5.1** and **5.2** are solved in the finite domain of  $0 \leq r \leq r_{max}$ , together with the boundary conditions at  $r = 0$  and  $r_{max}$ . Because of axisymmetry the boundary conditions at  $r = 0$  are  $\frac{\partial h}{\partial r} = 0$ ,  $\frac{\partial p}{\partial r} = 0$ . At  $r = r_{max}$  the boundary condition is:  $r \left( \frac{\partial p}{\partial r} \right) + 4p = 0$ . Another boundary condition at  $r = r_{max}$ , which takes into account the drop deformation during the approach, is:

$$\frac{\partial h(r_{max}, t)}{\partial t} = V - \frac{1}{2\pi\gamma} \frac{dF(t)}{dt} \left\{ \log\left(\frac{r_{max}}{2R}\right) + B(\theta) \right\} \quad (5.4)$$

$$B(\theta) = 1 + \frac{1}{2} \log\left(\frac{1 + \cos\theta}{1 - \cos\theta}\right) \quad (5.5)$$

and the force  $F(t)$  is given by:

$$F(t) = F_{Hydrodynamic} + F_{Surface} = 2\pi \int_0^\infty p(r', t') r' dr' + 2\pi \int_0^\infty \Pi(h(r', t')) r' dr' \quad (5.6)$$

The force,  $F(t)$  acts on the bubble due to the hydrodynamic and disjoining pressures, respectively. In this study the hydrodynamic resistance force is calculated by:

$$F_{Hydrodynamic} = 2\pi \int_0^\infty p(r', t') r' dr' \quad (5.7)$$

In **eqn. 5.2**,  $\Pi(h(r, t))$  is disjoining pressure due to surface forces. The classical DLVO theory recognizes two surface forces, i.e., a double-layer force and a van der Waals dispersion force. The van der Waals dispersion force is repulsive in wetting films. The double-layer force can also be repulsive in alkaline pH where both the solid/water and air/water interfaces are usually charged negatively. The rupture of wetting films formed on hydrophobic surfaces can be attributed to the presence of an attractive hydrophobic force. We, therefore, use the extended DLVO theory instead of classical DLVO theory in this study:

$$\Pi_t = \Pi_d + \Pi_e + \Pi_h \quad (5.8)$$

which includes disjoining pressures due to the van der Waals-dispersion force ( $\Pi_d$ ), electrical double-layer force ( $\Pi_e$ ), and hydrophobic force ( $\Pi_h$ ). The electrical double layer force is calculated by a numerical solution of the nonlinear Poisson-Boltzmann equation using the algorithm of Chan et al. (Chan 2002; McCormack et al. 1995). Hydrophobic forces measured in

experiments are usually represented by the exponential functions (Kékicheff et al. 1989; Herder 1990; Pashley et al. 1985):

$$\Pi_h = K \exp\left(-\frac{h}{\lambda}\right) \quad (5.9)$$

where  $\lambda$  is the decay length (unit of length) and  $K$  is a negative constant (unit of pressure). In this study we also use a power law of the following form to describe the hydrophobic force (Yoon et al. 1997; Claesson et al. 1986):

$$\Pi_h = -\frac{K_{132}}{6\pi h^3} \quad (5.10)$$

where  $K_{132}$  is a constant (unit of energy) representing the magnitude of the hydrophobic force in a wetting film.

Furthermore, the experimental data are re-solved by considering the full mobile hydrodynamic boundary condition at the bubble surface in which **eqn. 5.1** is replaced by the following equation:

$$\frac{dh}{dt} = \frac{1}{3\mu} \frac{1}{r} \frac{\partial}{\partial r} \left[ r h^3 \left( \frac{\partial P}{\partial r} \right) \right] \quad (5.11)$$

**Eqns. 5.1** and **5.11** (the Stokes-Reynolds equation for immobile and full mobile hydrodynamic boundary condition, respectively) only differ by a factor of 4. In the case of full mobile interfaces, the drainage rate of the intervening aqueous film increases as a result of lower hydrodynamic resistance arising from the full-slip boundary condition at the bubble surface.

### 5.2.1 Scaling of governing equations

The NSRYL equations can be non-dimensionalized with the following scaling parameters, in which the dimensionless variables are denoted by asterisk (Klaseboer et al.

2001):

film thickness:  $h \equiv [Ca^{1/2}R] h^*$

radial coordinate:  $r \equiv [Ca^{1/4}R] r^*$

time:  $t \equiv [Ca^{1/2}R/V] t^*$

pressure:  $p \equiv [\gamma/R] p^*$  (5.12)

disjoining pressure:  $\Pi \equiv [\gamma/R] \Pi^*$

force:  $F \equiv [(\gamma/R) (Ca^{1/4}R)^2] F^* \equiv [Ca^{1/2} \gamma R] F^*$

where  $V \sim dX(t)/dt$  is a characteristic velocity and  $Ca \equiv \mu V/\sigma$  is the capillary number which measures the ratio of viscous forces to capillary forces. In terms of the scaled variables, the Stokes-Reynolds equation that describes film drainage between a bubble and a solid sphere, i.e., **eqns. 5.1** and **5.11**, becomes:

$$\frac{\partial h^*}{\partial t^*} = \frac{1}{12r^*} \frac{\partial}{\partial r^*} \left( r^* h^{*3} \frac{\partial p^*}{\partial r^*} \right) \quad (5.13)$$

$$\frac{\partial h^*}{\partial t^*} = \frac{1}{3r^*} \frac{\partial}{\partial r^*} \left( r^* h^{*3} \frac{\partial p^*}{\partial r^*} \right) \quad (5.14)$$

and **eqn. 5.2** for film thickness becomes

$$\frac{1}{r^*} \left[ \frac{\partial h^*/\partial r^* + r^* \partial^2 h^*/\partial r^{*2} + Ca^{0.5} (\partial h^*/\partial r^*)^3}{(1 + Ca^{0.5} (\partial h^*/\partial r^*)^2)^{\frac{3}{2}}} \right] = 2 - p^* - \Pi^{**} h_0 + \frac{r^2}{2R} \quad (5.15)$$

The initial condition, **eqn. 5.3** now has the form

$$h^*(r^*, 0) = h_o^* + \frac{(r^*)^2}{2} \quad (5.16)$$

A remarkable observation of these equations is that the scaled Young Laplace equation contains the capillary number. Therefore, the governing equations of NSRYL model (**eqns.**

**5.13** and **5.15**) depend on the capillary number. Moreover the boundary condition at  $r_{max}^*$  (**eqn. 5.4**) has a weak logarithmic dependence on the capillary number (Ca):

$$\frac{\partial h^*(r_{max}^*, t^*)}{\partial t^*} = -1 + \frac{1}{2\pi} \frac{dF^*}{dt^*} \left\{ \frac{2\pi\gamma}{K} - \log\left(\frac{1}{2} Ca^{1/4} r_{max}^*\right) - B(\theta) \right\} \quad (5.17)$$

The scaled non-linearized Stokes–Reynolds–Young–Laplace equations, **eqns. 5.13** and **5.15**, for immobile hydrodynamic boundary condition, or **eqns. 5.14** and **5.15**, for full mobile boundary condition constitute a partial differential algebraic equation system. The equations can be solved numerically to determine the drainage dynamics of the intervening liquid films, the deformation (profile) of the air/liquid interface, and the time dependent forces between interacting air bubble and glass sphere.

### 5.3. Experimental methods

The integrated thin film drainage apparatus (ITFDA) is designed to measure the force between a bubble or oil droplet and a solid surface in a liquid. More details on this apparatus were given in Section 4.2 of Chapter 4. A photo of the bubble-glass sphere configuration of the ITFDA is given in **Figure 5.1**. The testing surface is housed in a transparent liquid chamber that permits the bubble-sphere approaching/attachment process to be viewed by video recording for subsequent analysis. A bubble is generated at one end of a vertical glass capillary tube that is immersed in the liquid. It is sealed when the bubble attains the required size to be used for the force measurement. The glass capillary tube with the bubble attached is positioned above the glass sphere. They are aligned in an axisymmetric configuration with the aid of two video cameras positioned perpendicularly in the plane perpendicular to the axis of symmetry to provide views in orthogonal directions. The axisymmetric alignment facilitates theoretical analysis. The

time-dependent interaction between the bubble and the glass sphere is determined as the capillary-sphere separation is varied in a controlled manner of prescribed function of time.

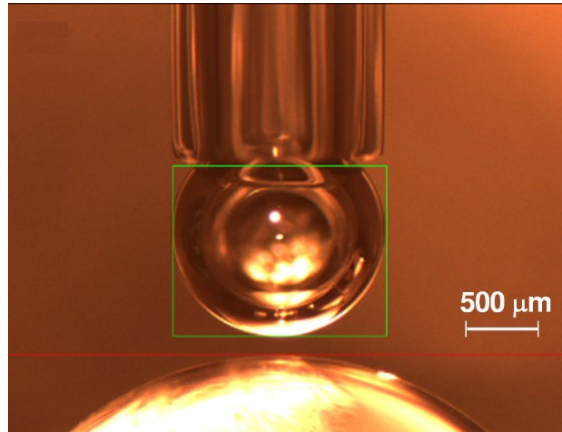


**Fig. 5.1.** A photograph of the bubble-glass sphere configuration in the ITFDA. The horizontal red line and green square are drawn to confirm the symmetry of the bubble (Wang 2013).

The glass sphere is attached to the free end of a bimorph cantilever that is used as a force sensor. The piezoelectric property of the bimorph material generates an electrical charge in response to the deformation of the bimorph. The force,  $F$  exerted on the glass sphere that deforms the bimorph cantilever can be obtained by measuring the voltage after the bimorph cantilever voltage-force characteristic is calibrated by placing small pieces of platinum wire of known mass on the cantilever. The cantilever used in this study has a force sensitivity in the  $\mu\text{N}$  range. The ITFDA measures independently the interaction force in terms of the calibrated output voltage of the bimorph sensor (Wang 2013).

### 5.3.1 The glass sphere

The glass spheres attached to the bimorph used in the current study is obtained by melting a  $1.5 \pm 0.1$  mm diameter Pyrex rod under a butane-oxygen flame until the surface tension of the melting Pyrex produces a spherical surface with a diameter of  $4.3 \pm 0.2$  mm. The glass spheres

prepared this way are molecularly smooth with a peak-to-valley roughness of less than 1.2 nm. The glass sphere and capillary tube were treated in freshly prepared piranha solution (3 H<sub>2</sub>SO<sub>4</sub>:1 H<sub>2</sub>O<sub>2</sub>, by volume) at 80 - 90 °C for half an hour, and rinsed with Mili-Q water. The surfaces prepared in this manner were free of contamination and completely water-wet with a contact angle value of zero. Octadecyltrichlorosilane (OTS), purchased from Sigma-Aldrich, was used to prepare 1 mM OTS in toluene (Fisher Scientific) solutions which were used to treat the hydrophilic glass spheres. To change the hydrophobicity of the hydrophilic silica surfaces, OTS molecules are often used to react with the hydroxyl groups on solid substrate surface, a reaction called silanation. It has been reported that different hydrophobicity can be achieved by varying the reaction time of silanation. In this study, the hydrophilic glass spheres were treated with 1 mM OTS in toluene solutions for 5 s, 10 s, 10 min and 10 hours to obtain different hydrophobicity of the glass spheres. Potassium chloride (KCl), purchased from Sigma-Aldrich, was used as supporting electrolyte, and stock solutions of NaOH and HCl were used as pH modifiers. More details about treatment of glass sphere can be found in Wang's thesis (Wang 2013).

### **5.3.2 Bubble generation and motion control**

The air bubble is inflated at the end of a glass capillary (inner diameter of  $1.10 \pm 0.01$  mm, Fisher Scientific) using a micro-syringe. The end of the glass tube is placed under a butane flame to create a smooth end appropriate for bubble generation and force measurements. Extreme caution is taken to avoid overheating and ensure uniform geometric symmetry of the end of the capillary tube. The bubble generation process and bubble size are monitored by direct video observations. This arrangement gives a reproducible bubble diameter of  $1.46 \pm 0.01$  mm. The other end of the capillary tube is attached to a speaker diaphragm that is used to control the

vertical motion of the capillary tube. A computer-generated waveform is used to vary the movement of the speaker diaphragm that in turn moves the attached air bubble towards or away from the lower glass sphere in the required manner.

### 5.3.3 Force measurement

For force measurements, a fresh air bubble was generated at the end of the glass tube. The bubble size as well as the gap between the bubble and glass sphere were precisely controlled with the aid of two CCD cameras positioned perpendicular to each other in a horizontal plane. The glass capillary tube, with the attached air bubble, was driven towards and then away from the lower glass sphere by the speaker diaphragm. **Figure 5.2** shows a representative capillary tube position (top) and bimorph signal profile (bottom) as a function of measurement time, obtained from a single measurement between an air bubble and a hydrophobic glass sphere of  $\theta_a = 38^\circ$  in 1 mM KCl solutions of pH 5.6. In this measurement, the initial separation distance between the air bubble and the glass sphere,  $h_0$ , was set at 120  $\mu\text{m}$ . A trapezoidal wave was generated to produce a movement of glass tube holding the air bubble. As a result, the glass tube firstly approached the solid sphere at the constant velocity of 240  $\mu\text{m/s}$  for 1 second, from points A to C in **Figure 5.2a**. Then the air bubble was held in contact with the glass sphere for 2 seconds with zero velocity of glass tube, from points C to F. From points F to J, the glass tube was retracted from the glass sphere at the same velocity of 240  $\mu\text{m/s}$  for more than 1 second. The reason to choose 1 second of retraction is that when the glass tube retracted from the glass sphere for 1 second, the glass tube reached its original position (point G) while the air bubble remained attaching to the glass sphere. Therefore the glass tube was further moved back, up to point J to separate the air bubble from the glass sphere and measure the adhesion force. Finally from point J to K, the glass tube returned to its

original position, point K, at the end of the measurement.

In **Figure 5.2b**, points A to C show the bimorph signal during the approach cycle. At large separation between the air bubble and glass sphere, i.e., from points A to B, there are only noise signals with no detectable interaction forces as indicated by a zero average bimorph signal. By further moving the air bubble toward the glass sphere, the separation between the two interfaces reduces. At small separation, the hydrodynamic repulsive force and/or surface forces become significant. The repulsive force between these two surfaces is first detected at point B, as indicated by an increase in bimorph signal at this point. The repulsive force continues to increase as the bubble is further driven toward the glass sphere and reaches the maximum at point C. During the “holding” phase the bimorph signal remains constant initially (from points C to D) and drops from 0.34 V at point D to 0.09 V at point E, indicating the rupture of the intervening liquid film and the formation of TPC. The interfacial tension force at the TPC line pulls the glass sphere up, exhibiting a “jump in” of the glass sphere at point D. From point E to F the signal remains almost constant and at point F, a sharp drop in the signal is observed, reflecting the retracting of the bubble on the glass tube from the glass sphere, and hence an increase of attractive capillary force from the bubble without significant displacement of TPC line. Eventually, the capillary force reaches the restoring force of the bimorph and the bubble detaches from the glass sphere at point H, where the bimorph signal returns to zero as indicated at point I. Depending on the stability of the thin liquid film, the rupture of the film can happen at any time during the measurement, i.e., approach, hold or retract period. From this force profile, the induction time or film drainage time can be accurately measured as the time from point B to point D. For example, the induction time for the system in **Figure 5.2b** is determined to be 0.59 s. This reading

represents the most accurate measurement of true induction time as it can accurately detect thin film rupture. This definition of the induction time is used in this study (Wang 2013).

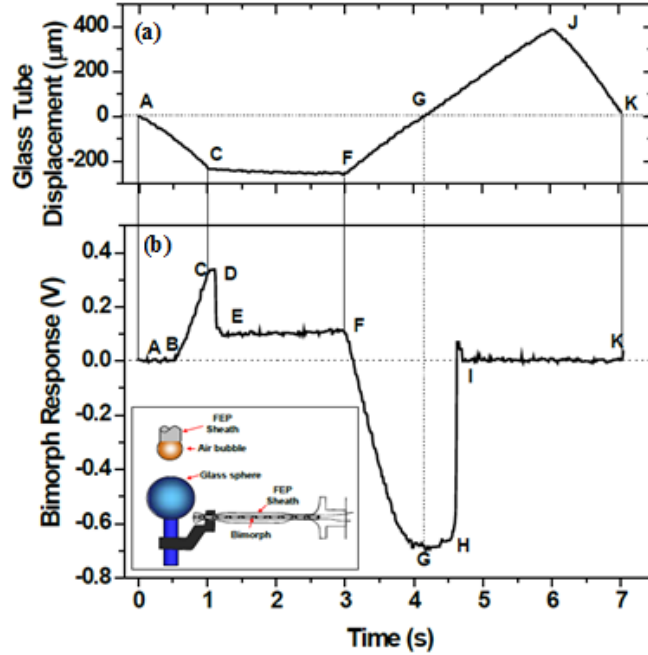


**Fig. 5.2** A representative capillary tube position (a) and bimorph signal (b) as a function of measurement time between an air bubble and a hydrophobic glass sphere ( $\theta_a = 38^\circ$ ) in 1 mM KCl solutions of pH 5.6. The bubble approach velocity was set at 240  $\mu\text{m/s}$ . The inset shows a schematic configuration of the integrated thin film drainage apparatus (Wang 2013).

### 5.3.4 Bimorph cantilever

Quantitative modeling of experimental force measurements requires to know the value of the instantaneous bimorph cantilever deflection,  $S(t)$ . Assuming linear behavior that can be verified independently, the deflection,  $S(t)$  of the force sensing bimorph can be deduced from the force,  $F(t)$  if the cantilever spring constant,  $\kappa$  is known:  $S(t) = F(t)/\kappa$ . The latter can be obtained by placing a known weight at the end of the bimorph cantilever and measure the output voltage of the bimorph due to the weight. The bimorph cantilever used in this study has a spring constant  $\kappa$  in the range of 60 - 70 N/m.

## 5.4. Results

The non-equilibrium interactions between an air bubble and a hydrophobic glass sphere are studied using the NSRYL model. In this study, the diameter of the air bubbles and glass sphere were controlled at  $1.5\pm 0.1$  mm and  $4.3\pm 0.1$  mm, respectively. The initial separation ( $h_0$ ) between the air bubble and glass sphere was set at 120  $\mu\text{m}$ . The maximum displacement of glass tube was set at 240  $\mu\text{m}$ . Water is used as liquid fluid with the viscosity and surface tension of 0.001 Pa.s and 0.072 N/m, respectively. For a given hydrophobicity (contact angle), the hydrophobic force is evaluated with the best fit of the NSRYL model to the experimental data. The effect of solid hydrophobicity and bubble approach velocities on the force barrier and induction time is studied. The NSRYL model is also used to predict the critical film thickness of the intervening liquid film. All of the experiments used in this chapter are conducted by Louxiang Wang and Xurui Zhang in 1 mM KCl solutions of pH 5.6 (Wang 2013). In this study, the NSRYL model is solved with different models for hydrophobic force (i.e., the power law and exponential form) and by considering both immobile and full mobile boundary conditions at bubble surface. To validate the model, the simulation results are first compared with the experimental data obtained from ITFDA and thin film force apparatus at contact angle of  $52^\circ$  and velocity of 24  $\mu\text{m/s}$ . Details on thin film force apparatus can be found in Chapter 3. Comparison of the interaction force profile obtained from ITFDA and critical film thickness obtained from thin film force apparatus with the simulation result allows us to select the model more suitable to describe hydrophobic forces for current experimental systems. Then we use this model to study the effect of bubble approach velocity and solid surface hydrophobicity (contact angles of  $38^\circ$ ,  $52^\circ$ ,  $84^\circ$  and  $103^\circ$ ) on the interactions between bubble and solid sphere. The experimental parameters used in this study are summarized in Table 5.1.

**Table 5.1.** Material constants used in the experiments with ITFDA (Israelachvili. J. 1991; Hough and White 1980).

Bubble diameter	1.5±0.1 mm
Glass sphere diameter	4.3±0.1 mm
Surface tension, $\gamma$	72.8 mN/m
Viscosity, $\mu$	1 mPa s
KCl	1 mM
pH	5.6
Zeta potential of air bubble	-30 mV
Zeta potential of glass sphere	-50 mV
Initial separation, $h(0,0)$	120 $\mu\text{m}$
Maximum displacement, $\Delta X_{\text{max}}$	240 $\mu\text{m}$
Hamaker constant	- $8 \times 10^{-21}$ J

#### 5.4.1 Evaluation of hydrophobic force

In this section we examine the applicability and accuracy of the NSRYL model with different hydrophobic models to predict time dependent force profile and critical film thickness at which the thin liquid film ruptures. The power law (eqn. 5.10) and exponential (eqn. 5.9) forms of hydrophobic force are used in this study. Both immobile and full mobile boundary conditions are considered at bubble surface. For each model, the hydrophobic force constant is evaluated with the best fit between the measured and the predicted time dependent force profile using a single approach velocity of 24  $\mu\text{m/s}$  for a given contact angle of 52°. **Figure 5.3** shows a reasonable fit between the measured and the predicted time dependent force profile using hydrophobic force constants summarized in **Table 5.2**. It is evident that with these hydrophobic force constants, all the models are able to accurately predict the force barrier of 1  $\mu\text{N}$ . Further from the time dependent force profile, the induction time or film drainage time can be accurately

determined as the time from point 4, when the hydrodynamic force and/or surface forces become significant or detectable, to point 3, when the thin liquid film ruptures, as shown in **Figure 5.3a**. This figure shows that with proper hydrophobic force constants, all the models are able to accurately predict the induction time of  $t_3-t_4= 0.24$  s. The most important characteristic in regard to the occurrence of coalescence is the time evolution of the film thickness at rim,  $h_{rim}$ . The time dependent film thickness at rim predicted with the different models are shown in the insets of **Figure 5.3**. This figure shows that the different models have different prediction for the critical film thickness. The predicted critical film thickness,  $h_{cr}$ , from these models is summarized in **Table 5.2**.

**Table 5.2** The best fitted hydrophobic force constants of various models and air bubble surface boundary conditions.

Power law model ( <b>eqn. 5.10</b> )	$K_{132}$ (J)		Predicted $h_{cr}$ (nm)	$\Delta h_{cr} = h_{cr} - 122.8$ (nm)
<b>Immobile boundary condition</b>	$2 \times 10^{-17}$		<b>103</b>	<b>-19.8</b>
Full mobile boundary condition	$2.1 \times 10^{-18}$		40	-82.8
Exponential model ( <b>eqn. 5.9</b> )	$K$ (Pa)	$\lambda$ (nm)		
Immobile boundary condition	79925.33	39	198	+75.2
Full mobile boundary condition	88736	13.8	70	-52.8

**Figure 5.3** shows that the predicted critical film thicknesses are  $\sim 103$  nm and  $\sim 40$  nm using power law form of hydrophobic force and immobile and full mobile bubble surface boundary conditions, respectively. For the exponential form of hydrophobic force and immobile and full mobile boundary conditions, the predicted critical film thicknesses are  $\sim 198$  nm and  $\sim 70$  nm, respectively. Now we compare these simulation results with the critical film thickness of  $122.8 \pm 16.3$  nm measured with thin film force apparatus at contact angle of  $50^\circ$  and velocity of

24 $\mu\text{m/s}$ . The experimental parameters used to measure the critical film thickness with the thin film force apparatus are the same as parameters summarized in **Table 5.1**. The deviations of the simulation results from the measured critical film thickness denoted as  $\Delta h_{cr}$  ( $\Delta h_{cr} = h_{cr} - 122.8$ ), are also given in **Table 5.2**. The results demonstrate that the NSRYL model with power law form of hydrophobic force and immobile boundary condition at the bubble surface has the lowest deviation from the experimental data. This model is therefore considered as a more appropriate model and used in this study. The results for hydrophobic force constant and critical film thickness are comparable with the results determined by Pan et al. (2010). They reported that the hydrophobic force constant,  $K_{132}$ , changes from 0 to  $2 \times 10^{-17} \text{ J}$  for contact angles in the range of  $17^\circ$  to  $82^\circ$ . Although it should be noted that the prediction of hydrophobic force constant depends on the accuracy of theoretical model and in the literature, researchers used approximate equations for the prediction of hydrophobic constants. For instance, Pan et al.(2010) used the flat film model to determine the hydrophobic force constant. In the rest of this chapter, we will use the power law form of hydrophobic force and immobile bubble surface boundary condition in the NSRYL model to investigate the effect of bubble approach velocity and hydrophobicity of solid surface on the interactions between bubble and hydrophobic glass sphere.

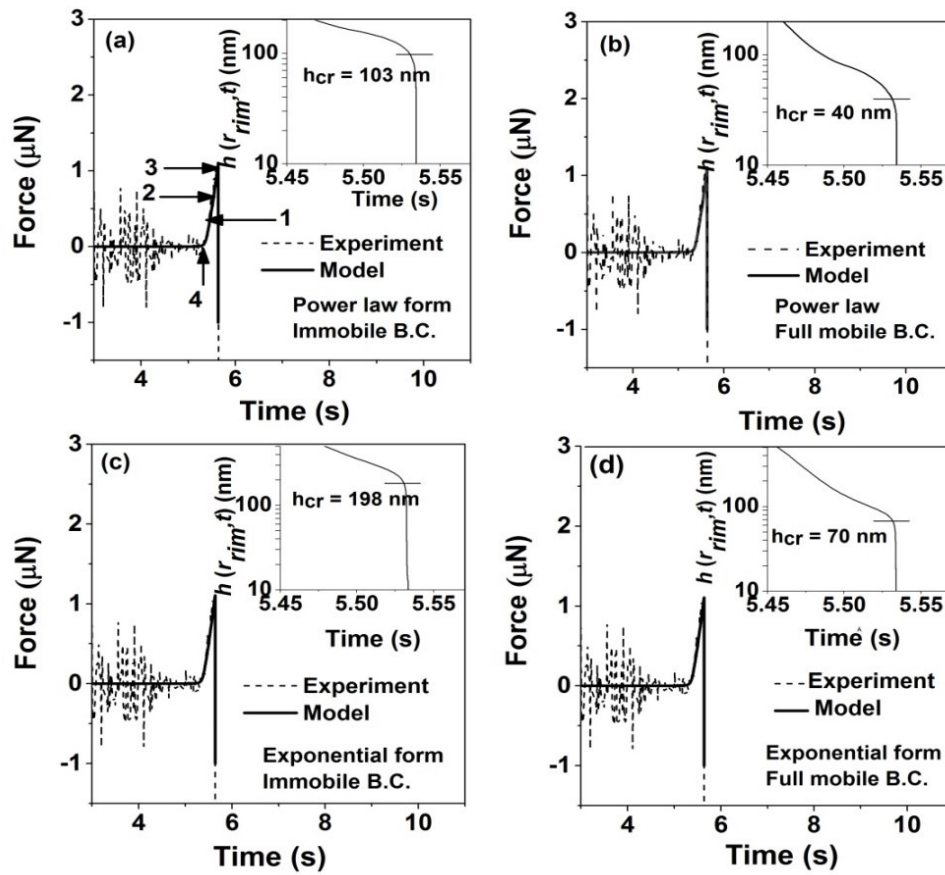


**Fig. 5.3** Variation of the force  $F(t)$  – experiment (dashed line) and model (solid line) for an air bubble approaching a hydrophobized solid sphere of  $\theta_a=52^\circ$  in aqueous electrolyte solution of 1 mM KCl and pH = 5.6 at bubble approach velocity of  $24\mu\text{m/s}$ . Insets show the calculated film thickness at rim  $h(r_{rim},t)$  as a function of time. The NSRYL model (solid line) is solved with (a) power law form of hydrophobic force and immobile B.C.; (b) power law form of hydrophobic force and full mobile B.C.; (c) exponential form of hydrophobic force and immobile B.C. and (d) exponential form of hydrophobic force and full mobile B.C. at bubble surface. The best fitted hydrophobic force constants determined with these models are summarized in **Table 5.2**.

In **Figure 5.4a** we show the spatial evolution of film profile,  $h(r,t)$  at various time (1, 2 and 3) along the force profile,  $F(t)$  indicated in **Figure 5.3a** for bubble approach velocity of  $24\mu\text{m/s}$ . One key feature is an initial development of a dimple at point 1 corresponding to bubble approach time of 5.42 s, and a minimum film thickness of  $\sim 239\text{ nm}$ . As bubble continues to

approach the dimple grows to a maximum size at the force maximum (point 3, corresponding to bubble approach time of 5.56 s) with a dimple rim radius of  $\sim 28 \mu\text{m}$ . As shown in **Figure 5.3a** the intervening aqueous film ruptures at point 3. At the moment of rupture (point 3) in **Figure 5.4a** the film thickness is  $\sim 103 \text{ nm}$  at the dimple rim. It is interesting to note that as the bubble approaches from points 1 to 2, the central film thickness decreases from 239 nm to 214 nm. Further approach of bubble from points 2 to 3 increases the central film thickness from 214 nm to 250 nm. The observed variation of central film thickness with bubble approaching time can be attributed to a sharp increase in the hydrodynamic resistance force from points 2 to 3, as shown in **Figure 5.4b** with the hydrodynamic resistance force being calculated using **eqn. 5.7**. This figure shows that from points 1 to 2 ( $t_2-t_1=0.07 \text{ s}$ ), the hydrodynamic force increases from  $0.77 \mu\text{N}$  to  $1.41 \mu\text{N}$ , while from points 2 to 3 ( $t_3-t_2=0.07 \text{ s}$ ), the hydrodynamic force increases from  $1.41 \mu\text{N}$  to  $3.34 \mu\text{N}$ . In other words, the sharp increase in the hydrodynamic resistance force is responsible for the increase in the bubble deformation and surface concavity.

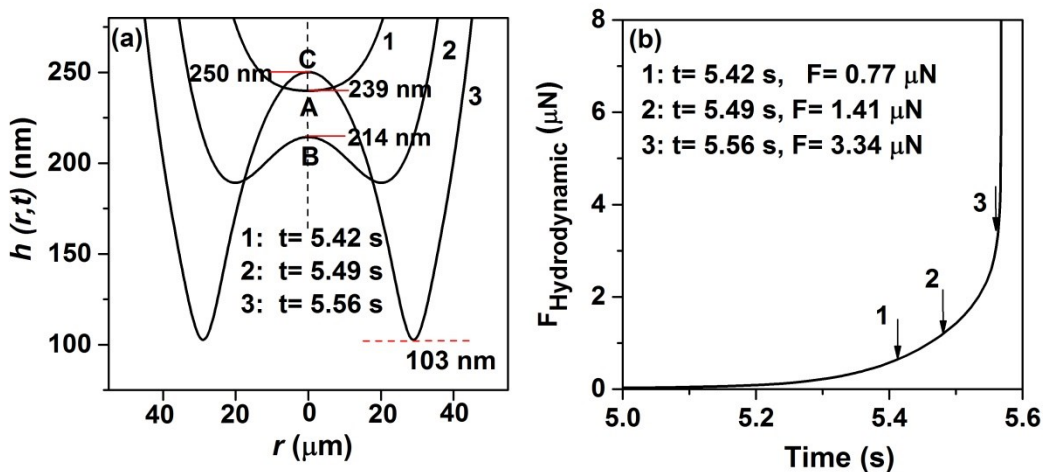


**Fig. 5.4** Thickness of the aqueous film,  $h(r,t)$  between the bubble and hydrophobic glass sphere at different measurement times (a) and corresponding variation of the hydrodynamic resistance force (b). As in Figure 5.3a, the contact angle is  $52^\circ$  and the electrolyte

concentration is 1 mM KCl at bubble approach velocity of 24  $\mu\text{m/s}$ . The NSRYL model is solved with  $K_{132}$  being set of  $2 \times 10^{-17} J$  for immobile bubble surface boundary condition.

In **Figure 5.5** we show the distribution of the film pressure, hydrodynamic pressure, hydrophobic pressure and classical disjoining pressure ( $\Pi_{classical}^* = \Pi_{el}^* + \Pi_{vW}^*$ ) at various times of 1, 2 and 3 indicated in **Figure 5.3a** for bubble approach velocity of 24  $\mu\text{m/s}$ . All of these pressures are scaled values, denoted by asterisks. The pressure drop  $\Delta p(r,t)$  across the liquid/air interface is obtained from:

$$\Delta p(r,t) = p_c \left( 2 - p_{film}^*(r,t) \right) = p_c [2 - p_{hydrodynamic}^*(r,t) - \Pi_{classical}^*(r,t) - p_{hydrophobic}^*(r,t)] \quad (5.18)$$

in which  $p_c = \gamma/R$ . **Eqn. 5.18** indicates that for  $p_{film}^*(0,t) < 2$  the bubble interface will remain a convex shape with the film thickness at the center being smaller than the rest of the film due to a positive  $\Delta p$ . When  $\Delta p(r=0,t) = 0$  or  $p_{film}^*(0,t)=2$ , dimple starts to form and bubble begins to deform. When  $p_{film}^*(0,t) > 2$  or  $\Delta p(0,t) < 0$ , dimple develops and the thickness of the film at the center is larger than that at the rim of the film, i.e.,  $h(rim,t) < h(0,t)$ . In this case the bubble interface has a concave shape. **Figure 5.4b** shows the formation of the dimple at point 1 where the film thickness is around 239 nm. At this point, the classical disjoining pressure at such large separations is negligible, while the hydrophobic pressure at the moment of dimple formation is at play as shown in **Figures 5.5b and d**, respectively. **Figures 5.5c and d** show that at point 1 the hydrodynamic and hydrophobic pressures in the center [ $p_{hydrodynamic}^*(0,5.42)$  and  $p_{hydrophobic}^*(0,5.42)$ ] are  $\sim 2.18$  and  $-0.18$ , respectively. Clearly in the absence of surface forces (i.e., when the disjoining pressure is very small or negligible), the formation of dimple at point 1 is due to hydrodynamic force counter-balanced by hydrophobic force. At this point as

shown in **Figure 5.5a** the film pressure  $p$  reaches  $(2\gamma/R)$ , the scaled Laplace pressure of the bubble  $p_{film}^* \equiv (R/\gamma) p = 2$ , when the dimple starts to form. **Eqn. 5.18** also confirms that at point 1, the pressure drop at center,  $\Delta p(r = 0, t)$ , is zero. As the bubble continues to approach to the silica sphere from points 1 to 2, the minimum film thickness reaches  $\sim 189$  nm at point 2 (see **Figure 5.4a**). **Figure 5.5b** shows that the classical disjoining pressure remains negligible at these large separations while **Figures 5.5c** and **d** show a gradual increase in hydrodynamic and hydrophobic pressures from points 1 to 2. Meanwhile after point 1, pressure drop at the centre of the film has a negative value, corresponding to a concave shape of bubble as shown in **Figure 5.4a**. From points 2 to 3, all the pressures sharply increase around dimple rim of radius  $\sim 28$   $\mu\text{m}$ , lines E.

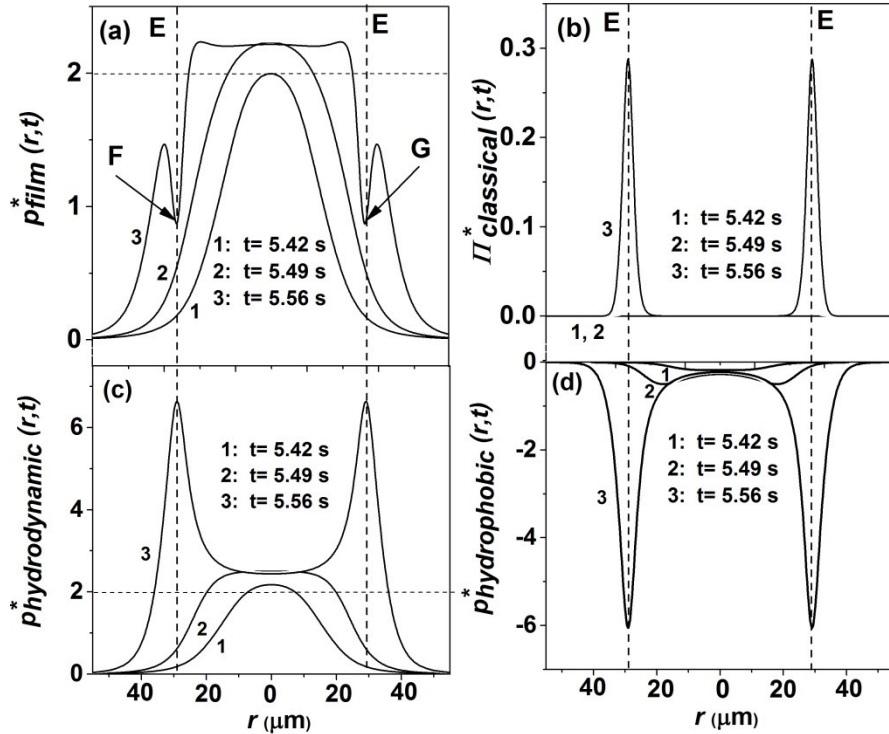


**Fig. 5.5** The film pressure (a), classical disjoining pressure (b), hydrodynamic (c) and hydrophobic pressures (d) scaled by  $(\gamma/R)$  in the water film. As in **Figure 5.3a**, the contact angle is  $52^\circ$  and the electrolyte concentration is 1 mM KCl at bubble approach velocity of 24  $\mu\text{m/s}$ .

The NSRYL model is solved with  $K_{132}$  being set at  $2 \times 10^{-17} J$  for immobile bubble surface boundary condition.

It is interesting to note that at point 3 i.e., at the moment of film rupture with the minimum film thickness at the dimple rim of  $\sim 103$  nm, the film pressure drops as denoted by points F and G in **Figure 5.5a**. In other words for bubble approach velocity of  $24 \mu\text{m/s}$  at point 3, the film pressure at dimple rim suddenly drops towards less repulsive and becomes minus (or attractive) which leads to spontaneous film rupture at the dimple rim. During the entire film drainage process, the hydrodynamic and hydrophobic forces dominate the process. **Figure 5.6** shows that by decreasing the bubble approach velocity, the film rupture occurs much closer to the center.<sup>3</sup>

**Figure 5.6a** is the same as **Figure 5.4a**.

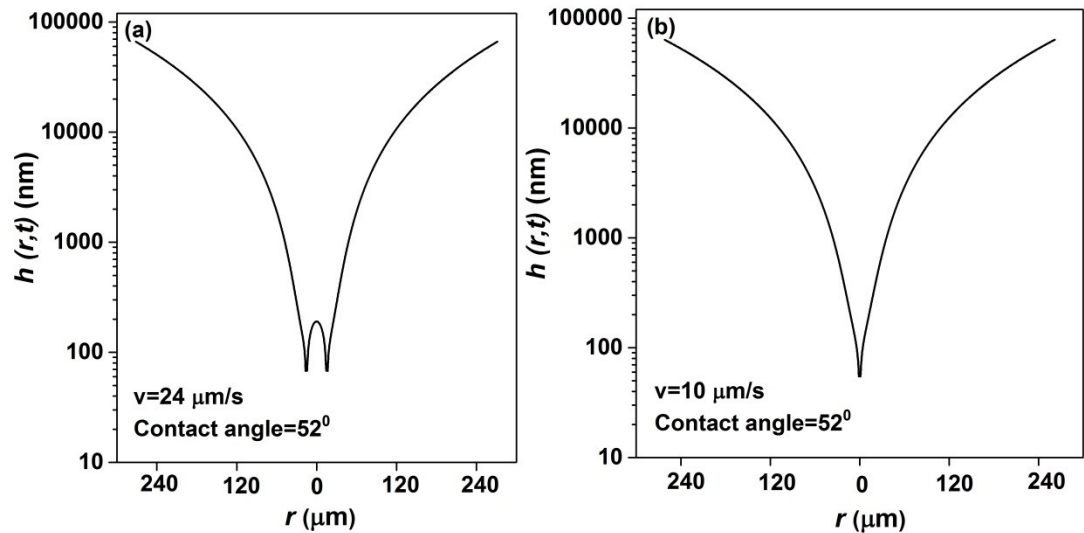


**Fig. 5.6** Thickness of the aqueous film,  $h(r,t)$  between the bubble and hydrophobic glass sphere at (a) bubble approach velocity of  $24 \mu\text{m/s}$ , which is the same as **Figure 5.4a** and (b) bubble approach velocity of  $10 \mu\text{m/s}$  (b). The contact angle is  $52^\circ$  and the electrolyte concentration is 1 mM KCl. The NSRYL model is solved with  $K_{132}$  being set at  $2 \times 10^{-17} J$  for immobile bubble

<sup>3</sup> The simulation results indicate that by decreasing the bubble approach velocity or increasing the surface hydrophobicity, the dimple rim radius decreases. As a result the film rupture occurs closer to centre with decreasing bubble approach velocity or increasing the surface hydrophobicity.

surface boundary condition. The modeling parameters used in this study is the same as the experimental parameters summarized in **Table 5.1**.

#### **5.4.2 Contact angle of 52°**

After establishing the form of hydrophobic force and corresponding hydrophobic force constant  $K_{132}$  to be  $2 \times 10^{-17} J$ , the time dependent force profile and film thickness at the rim can now be calculated using the NSRYL model. The results are shown in **Figure 5.7**. For comparison, the results for bubble approach velocity of  $24 \mu\text{m/s}$  are shown in **Figure 5.7a**. The results in **Figures 5.7b** and **5.7c** show a good agreement between the predicted and measured force profiles for bubble approach velocities of  $120$  and  $240 \mu\text{m/s}$ , respectively.

As shown in **Figure 5.7** increasing the bubble approach velocity increases the force barrier between the approaching air bubble and the hydrophobic glass sphere, indicating an increase in film drainage resistance. For example, the force barrier increases from  $\sim 1 \mu\text{N}$  to  $\sim 21.6 \mu\text{N}$  prior to film rupture when the bubble approach velocity increases from  $24$  to  $240 \mu\text{m/s}$ . This result is consistent with the data reported in the literature (Wang 2013). The simulation and experimental results of induction time are summarized in **Figure 5.7d**. As shown in this figure the induction time increases with increasing bubble approach velocity. However from this figure, the slope of increase becomes less with increasing bubble approach velocity. This observation arises from two opposite effects of increasing bubble approach velocity on the film drainage rate. Higher approach velocity increases both the film radius and hydrodynamic repulsive force which in turn retards the film drainage rate. On the other hand, at higher bubble approach velocity the dimple initially forms at larger film thickness, which accelerates film drainage rate. These two opposite effects cause the film drainage rate and hence the induction times to remain almost constant at high bubble approach velocity (Wang 2013).

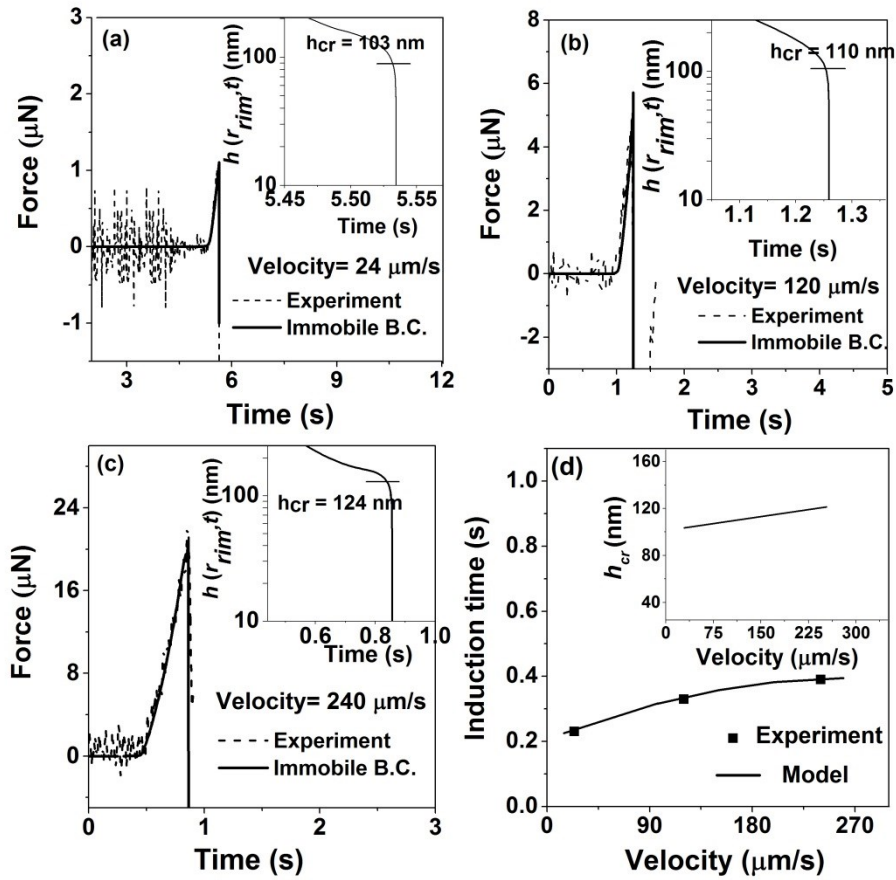


**Fig. 5.7** (a), (b) and (c): Variation of the – measured (dashed line) and predicted (solid line) – force  $F(t)$  and (d): the effect of bubble approach velocity on the induction time, for an air bubble approaching a hydrophobized solid sphere of  $\theta_a=52^\circ$  in aqueous electrolyte solution of 1 mM KCl and pH = 5.6 at bubble approach velocities of 24, 120 and 240  $\mu\text{m/s}$ . Insets of (a), (b) and (c): the predicted film thickness at rim  $h(r_{rim}, t)$  as a function of time; inset of (d): the effect of bubble approach velocity on the critical film thickness. The NSRYL model (solid line) is solved with  $K_{132}$  being set at  $2 \times 10^{-17} \text{ J}$  for the immobile bubble surface boundary condition.

The inset of **Figure 5.7d** shows the results of NSRYL model for the critical thickness at various bubble approach velocities predicted using power law form of hydrophobic force and immobile bubble surface boundary condition. This figure shows that the critical thickness of film rupture at the rim increases slightly from 103 to 124 nm by increasing the bubble approach velocity from 24 to 240  $\mu\text{m/s}$ .

### 5.4.3 Contact angle of 38°, 84° and 103°

For the immobile boundary condition and using power law form of hydrophobic force, the NSRYL model is solved to determine the time dependent force profile between an approaching air bubble and hydrophobic glass sphere of various contact angles of 38°, 84° and 103°. The results are shown in **Figures 5.8, 5.9** and **5.10**, respectively. These figures show an excellent fit between the measured and the predicted time dependent force profile, with the best fitted hydrophobic force constant  $K_{132}$  to be  $4.5 \times 10^{-18}$  J,  $8.6 \times 10^{-17}$  J and  $4 \times 10^{-16}$  J for contact angles of 38°, 84° and 103°, respectively. The results demonstrate that  $K_{132}$  increases with increasing contact angle, thereby a stronger and longer range of hydrophobic force increases the surface hydrophobicity and is responsible for film rupture (Pan et al. 2011; Pan and Yoon 2010). As shown in these figures, increasing the bubble approach velocity increases the force barrier dramatically. For instance, the force barrier for solid of contact angle 38° increases from  $\sim 2.2$   $\mu\text{N}$  to  $\sim 46.4$   $\mu\text{N}$  when the bubble approach velocity increases from 48 to 240  $\mu\text{m/s}$  (see **Figures 5.8**). The insets of these figures show the time dependent film thickness at rim. The results show that the critical film thickness increases slightly with increasing bubble approach velocity. For example the critical film thickness increases from  $\sim 165$  nm to  $\sim 188$  nm by increasing bubble approach velocity from 120  $\mu\text{m/s}$  to 480  $\mu\text{m/s}$  for particle of contact angle 84° (see **Figure 5.9**). The simulation and experimental results of induction time are summarized in **Figure 5.8d, 5.9d** and **5.10d**. As shown in these figures the induction time increases initially with increasing bubble approach velocity. At high bubble approach velocity, the film drainage rate and hence the induction time remains almost constant.

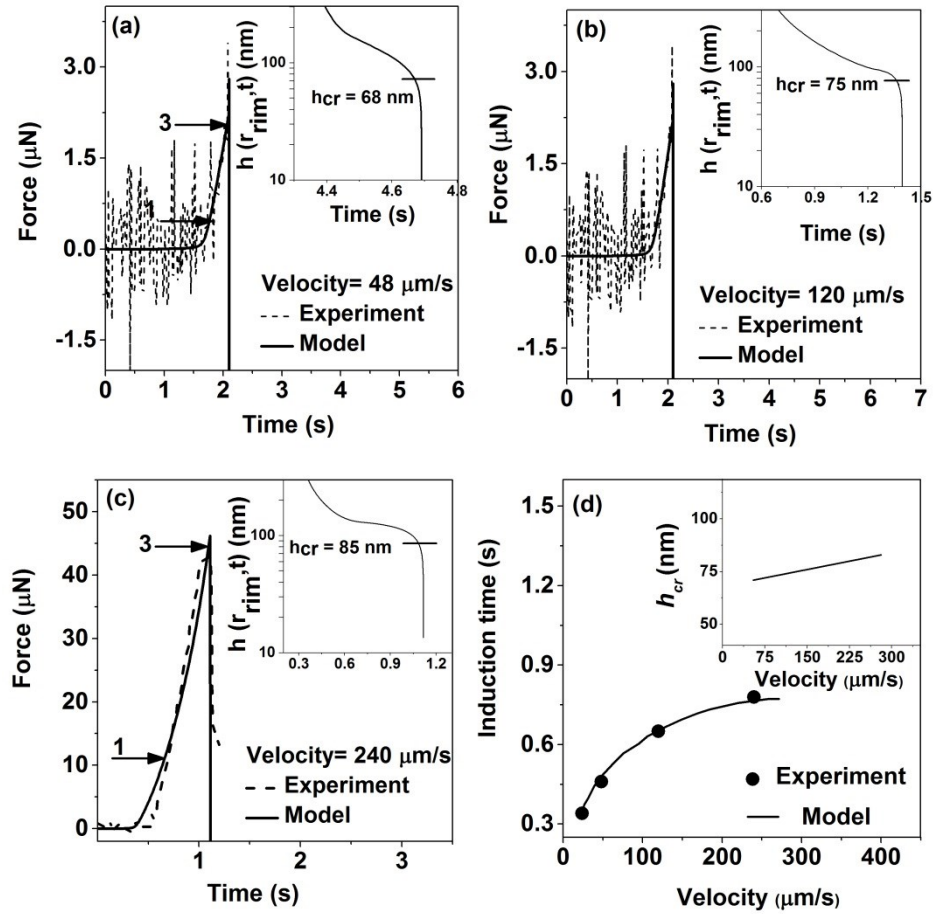


**Fig. 5.8** (a), (b) and (c): Variation of the – measured (dashed line) and predicted (solid line) – force  $F(t)$  and (d): the effect of bubble approach velocity on the induction time, for an air bubble approaching a hydrophobized solid sphere of  $\theta_a=38^\circ$  in aqueous electrolyte solution of 1 mM KCl and  $\text{pH} = 5.6$  at bubble approach velocities of 48, 120 and  $240 \mu\text{m/s}$ . Insets of (a), (b) and (c): the predicted film thickness at rim  $h(r_{rim}, t)$  as a function of time; inset of (d): the effect of bubble approach velocity on the critical film thickness. The NSRYL model (solid line) is solved with  $K_{132}$  being set at  $4.5 \times 10^{-18} \text{ J}$  for the immobile bubble surface boundary condition.

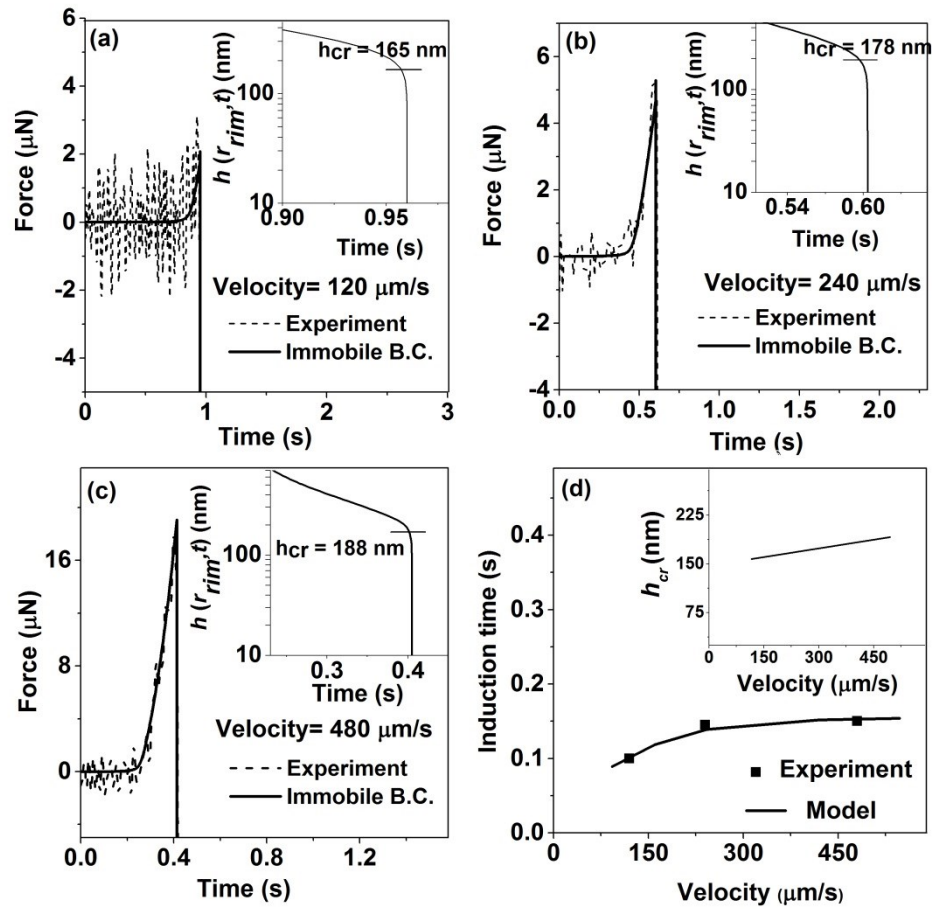


**Fig. 5.9** (a), (b) and (c): Variation of the – measured (dashed line) and predicted (solid line) – force  $F(t)$  and (d): the effect of bubble approach velocity on the induction time, for an air bubble approaching a hydrophobized solid sphere of  $\theta_a = 84^\circ$  in aqueous electrolyte solution of 1 mM KCl and  $\text{pH} = 5.6$  at bubble approach velocities of 120, 240 and 480  $\mu\text{m/s}$ . Insets of (a), (b) and (c): the predicted film thickness at rim  $h(r_{rim}, t)$  as a function of time; inset of (d): the effect of bubble approach velocity on the critical film thickness. The NSRYL model (solid line) is solved with  $K_{132}$  being set at  $8.6 \times 10^{-17} \text{ J}$  for the immobile bubble surface boundary condition.

The predicted critical film thicknesses are summarized in the inset of **Figures 5.8d, 5.9d and 5.10d**. It is found for bubble approach velocity of 240  $\mu\text{m/s}$ , the critical film thicknesses are  $\sim 85$ ,  $\sim 178$  and  $\sim 300 \text{ nm}$  for contact angles of  $38^\circ$ ,  $84^\circ$  and  $103^\circ$ , respectively. In other words, the critical film thickness increases dramatically with increasing surface hydrophobicity. The

comparison of **Figures 5.8, 5.9** and **5.10** reveals that increasing the surface hydrophobicity, dramatically reduces the force barrier suggesting a stronger and longer range hydrophobic force. For example for bubble approach velocity of  $240\mu\text{m/s}$ , the force barrier reduces from  $\sim 5.2\ \mu\text{N}$  to  $\sim 2.8\ \mu\text{N}$  by increasing contact angle from  $84^\circ$  to  $103^\circ$  (**Figures 5.9** and **5.10**). In the next section these results will be discussed in more detail.

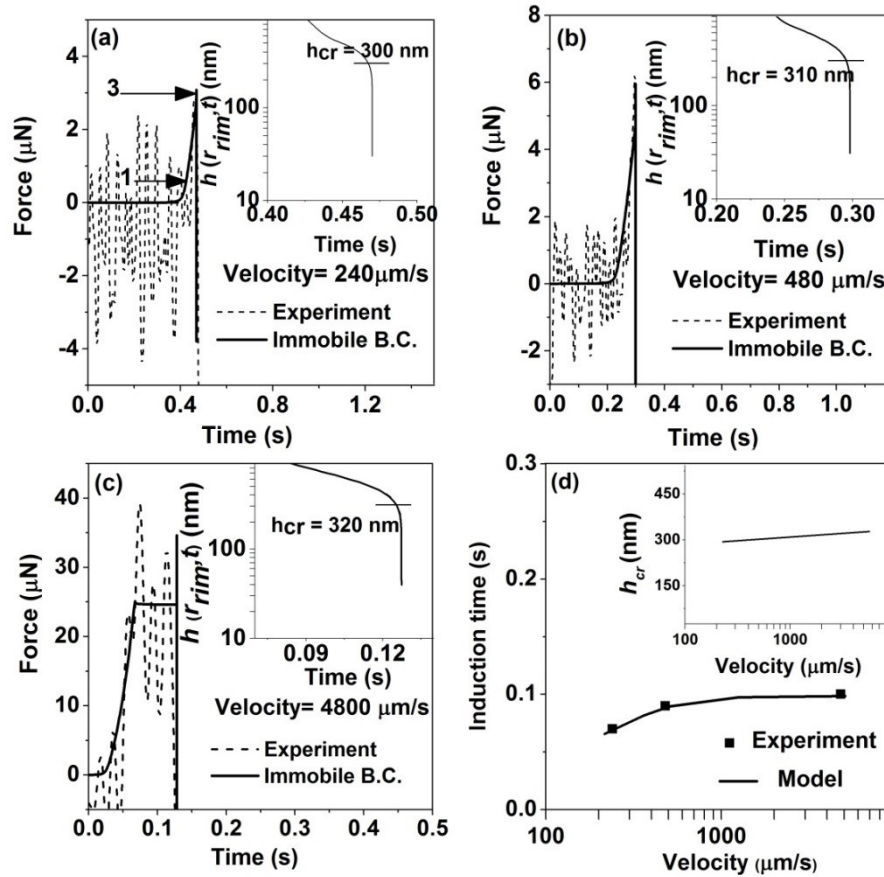


**Fig. 5.10** (a), (b) and (c): Variation of the – measured (dashed line) and predicted (solid line) – force  $F(t)$  and (d): the effect of bubble approach velocity on the induction time, for an air bubble approaching a hydrophobized solid sphere of  $\theta_a = 103^\circ$  in aqueous electrolyte solution of 1 mM KCl and  $\text{pH} = 5.6$  at bubble approach velocities of 240, 480 and  $4800\ \mu\text{m/s}$ . Insets of (a), (b) and (c): the predicted film thickness at rim  $h(r_{rim}, t)$  as a function of time; inset of (d): the effect of bubble approach velocity on the critical film thickness. The NSRYL model (solid line) is solved with  $K_{132}$  being set at  $4 \times 10^{-16}\ \text{J}$  for the immobile bubble surface boundary condition.

## 5.5. Discussion

In this study we developed the NSRYL model to study the effect of surface hydrophobicity and bubble approach velocity on hydrophobic force, bubble deformation, critical film thickness and induction time of bubble-particle attachment. The time dependent force profiles measured with the integrated thin film drainage apparatus (ITFDA) and the critical film thickness measured with thin film force apparatus (TFFA), were used to validate the model and calibrate the hydrophobic force constant. With the best fit between the measured and the predicted time dependent force profile, the hydrophobic force constants for solids of different contact angles are determined, which are summarized in **Table 5.3**. This study shows that the developed NSRYL model is able to provide valuable information on film profiles, pressure profiles and critical film thicknesses.

**Table 5.3** The best fitted of hydrophobic force constant,  $K_{132}$  (J), in eqn. 5.10 using immobile bubble surface boundary condition.

Contact angle (°C)	$K_{132}$ (J)
38	$4.5 \times 10^{-18}$
52	$2 \times 10^{-17}$
84	$8.6 \times 10^{-17}$
103	$4 \times 10^{-16}$

The simulation results of the NSRYL model for the force barriers and induction times for different contact angles are summarized in **Figure 5.11**.<sup>4</sup> As shown in **Figure 5.11a**, increasing the bubble approach velocity increased the force barrier between the air bubble and the

---

<sup>4</sup> The hydrophobic force constants for the power law form with full mobile boundary condition and also for the exponential form with both immobile and full mobile boundary conditions can be found in the Appendix C.

hydrophobic glass sphere, indicating an increase of film drainage resistance. For example for contact angle of  $38^\circ$ , the force barrier increased significantly from  $2.2 \mu\text{N}$  to  $45 \mu\text{N}$  when the bubble approach velocity increased from  $48$  to  $240 \mu\text{m/s}$ . As illustrated in **Figures 5.11a**, surface hydrophobicity has a significant impact on the force barrier. In this figure, the force barrier is shown to decrease significantly with increasing surface hydrophobicity. For example for bubble approach velocity of  $240 \mu\text{m/s}$ , the force barrier decreases from  $45$  to  $21.6$ ,  $5.2$  and  $2.8 \mu\text{N}$  when the contact angle increases from  $38^\circ$  to  $52^\circ$ ,  $84^\circ$  and  $103^\circ$ , respectively. The reduced force barrier or film drainage resistance suggests the presence of strong and long-range attractive force which depresses the repulsive forces between the bubble and solid of increasing hydrophobicity even at high bubble approach velocity. The simulation results show that the attractive hydrophobic force predicted with the NSRYL model becomes stronger as the contact angle or surface hydrophobicity increases (**Table 5.3**). The induction time of an air bubble-glass sphere attachment is measured and predicted as a function of bubble approach velocity and surface hydrophobicity. The results presented in **Figure 5.11b** show that at the same velocity, the induction time decreases with increasing surface hydrophobicity, which demonstrates the important role of surface hydrophobicity in the film drainage. The film drainage rate increases with increasing the surface hydrophobicity, which is consistent with the results obtained by the thin film pressure balance apparatus (Pan et al. 2011; Pan and Yoon 2010).

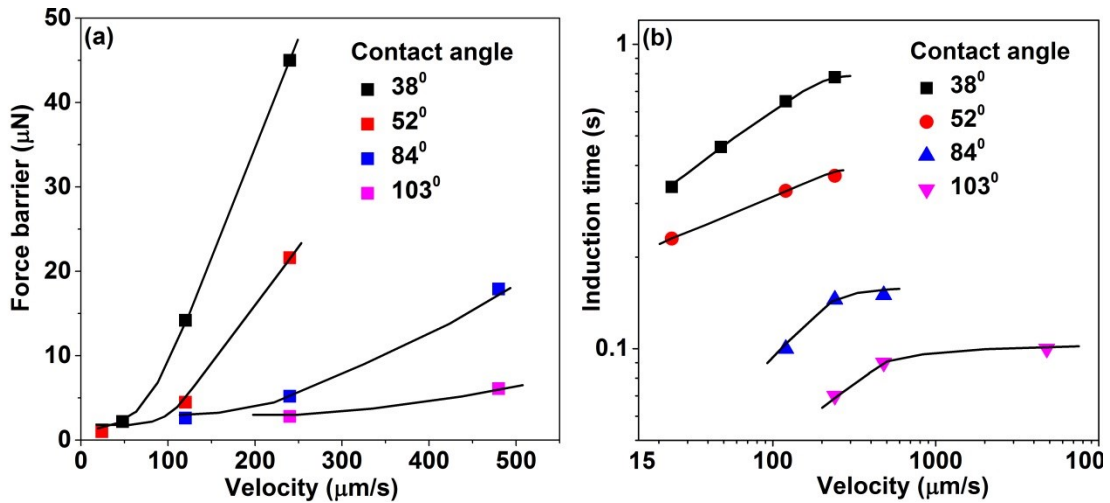


**Fig. 5.11** Effect of bubble approach velocity on the force barrier (a), and induction time (b) for an air bubble to approach a hydrophobized solid sphere in aqueous electrolyte solution of 1 mM KCl and pH = 5.6. Experimental results are given by symbols and model prediction by solid line. The NSRYL model is solved with the best fitted hydrophobic force constant  $K_{132}$  to be  $4.5 \times 10^{-18}$  J,  $2 \times 10^{-17}$  J,  $8.6 \times 10^{-17}$  J and  $4 \times 10^{-16}$  J for contact angles of  $38^\circ$ ,  $52^\circ$ ,  $84^\circ$  and  $103^\circ$ , respectively.

At the same surface hydrophobicity, the induction time increases with increasing bubble approach velocity (**Figure 5.11b**). However the slope of induction time increase becomes slower with increasing bubble approach velocity. This observation can be attributed to two opposite effects of increasing bubble approach velocity. Firstly, increasing bubble approach velocity increases both the film radius and hydrodynamic repulsive force, leading to a decrease in film drainage rate. At the same time, the dimple starts to form at larger film thickness at higher bubble approach velocity which accelerates the film drainage. These two opposite effects cause the film drainage rate and hence the induction times to remain almost constant at high bubble approach velocity.

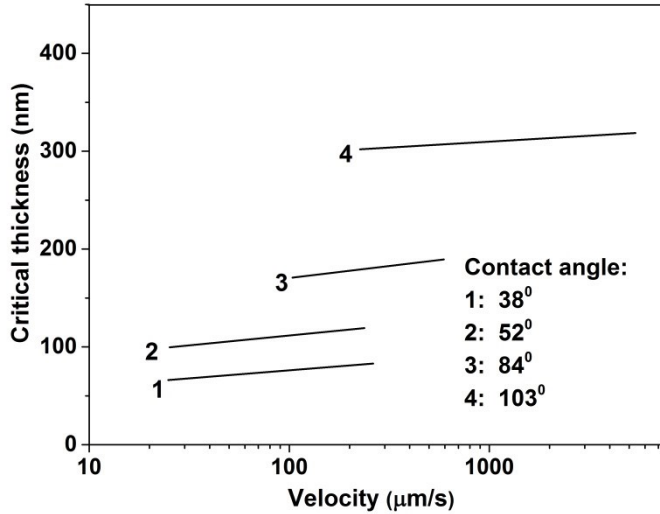


**Fig. 5.12** Effects of bubble approach velocity and surface hydrophobicity on the predicted critical film thickness. The NSRYL model is solved with the best fitted hydrophobic force constant  $K_{132}$  to be  $4.5 \times 10^{-18}$  J,  $2 \times 10^{-17}$  J,  $8.6 \times 10^{-17}$  J and  $4 \times 10^{-16}$  J for contact angles of  $38^\circ$ ,  $52^\circ$ ,  $84^\circ$  and  $103^\circ$ , respectively.<sup>5</sup>

**Figures 5.12** shows that the critical film thickness increases significantly with increasing glass sphere hydrophobicity. For example, for bubble approach velocity of  $240 \mu\text{m/s}$ , the critical film thicknesses are  $\sim 85$ ,  $\sim 124$ ,  $\sim 178$  and  $\sim 300$  nm for contact angles of  $38^\circ$ ,  $52^\circ$ ,  $84^\circ$  and  $103^\circ$ , respectively. **Figure 5.12** also shows that for a specific surface hydrophobicity, the critical film thickness increases slightly with increasing bubble approach velocity. In the next two sections, i.e., Sections 5.5.1 and 5.5.2 we will investigate in more details the effect of bubble approach velocity and surface hydrophobicity on the film profiles and hence the critical film thickness.

### 5.5.1 Effect of approach velocity

To better understand the effect of bubble approach velocity on bubble deformation and film drainage, we compare the film profiles at points 1 (where dimple starts to form) and 3 (at the

---

<sup>5</sup> The predicted critical film for the exponential form with both immobile and full mobile boundary conditions can be found in the Appendix C.

moment of film rupture) of **Figure 5.8a** at bubble approach velocity of  $48\mu\text{m/s}$  with **Figure 5.8c** at bubble approach velocity of  $240\mu\text{m/s}$ . The surface hydrophobicity or contact angle is the same ( $38^\circ$ ). This comparison is presented in **Figure 5.13**. One key feature of this figure is that for higher bubble approach velocity, the dimple forms at larger film thickness, which accelerate liquid film drainage (**Figure 5.13a and b**). This result is expected as at higher bubble approach velocity, the hydrodynamic resistance force increases, which causes the pressure drop across the liquid/air interface,  $\Delta p(r,t)$ , to become zero at larger film thickness. As indicated in **eqn. 5.19** the dimple starts to form when  $\Delta p(r,t)=0$ . **Figure 5.13** shows that the film thickness where dimple starts to form increases from  $\sim 218\text{ nm}$  to  $\sim 349\text{ nm}$  when the bubble approach velocity increases from  $48\mu\text{m/s}$  to  $240\mu\text{m/s}$ . Another important feature of higher bubble approach velocity is more complex film profile in the interaction zone and larger film radius (**Figure 5.13**). As shown in this figure the film radius increases from  $\sim 80\mu\text{m}$  to  $\sim 250\mu\text{m}$  when the bubble approach velocity increases from  $48\mu\text{m/s}$  to  $240\mu\text{m/s}$ . In other words, decreasing bubble approach velocity makes the film rupture to occur at locations much closer to the centre. The intervening aqueous film ruptures at points A ( $h_{cr} = \sim 68\text{ nm}$ ) and B ( $h_{cr} = \sim 85\text{ nm}$ ) for bubble approach velocity of  $48\mu\text{m/s}$  and  $240\mu\text{m/s}$ , respectively. As a result, the hydrophobic force at point B is smaller than at point A. As shown in **Figures 5.13c and d**, the hydrodynamic resistance force which is in the balance by the hydrophobic force (the disjoining pressure is almost negligible at these separations), at point B is smaller than at point A. As a result at higher bubble approach velocity, smaller hydrophobic force (smaller hydrodynamic repulsive force) at rim is needed to make film rupture at larger film thickness.

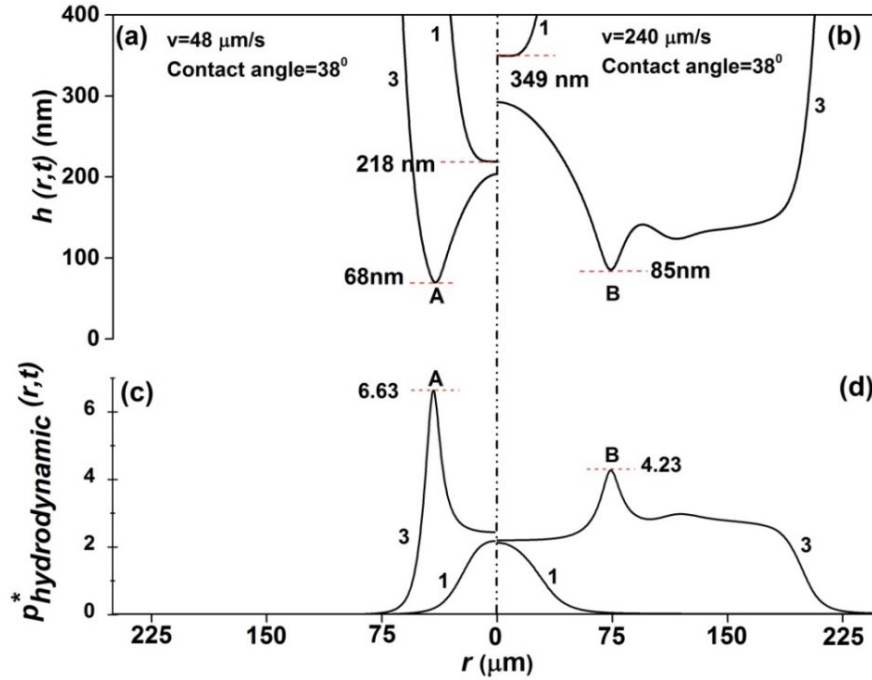


**Fig. 5.13** Thickness of the aqueous film,  $h(r,t)$  between the bubble and hydrophobized glass sphere of  $\theta_a=38^\circ$  at point 1 where dimple starts to form and point 3 at the moment of film rupture for (a) bubble approach velocity of  $48 \mu\text{m/s}$  and (b) bubble approach velocity of  $240 \mu\text{m/s}$ . The corresponding hydrodynamic pressure profile,  $p^*_{hydrodynamic}(r,t)$  scaled by  $(\gamma/R) = 125.9 \text{ Pa}$  for (c) bubble approach velocity of  $48 \mu\text{m/s}$  and (d) velocity of  $240 \mu\text{m/s}$ . As in **Figure 5.7**, the electrolyte concentration is  $1 \text{ mM KCl}$  and  $\text{pH} = 5.6$ . The NSRYL model is solved with  $K_{I32}$  being set at  $4.5 \times 10^{-18} \text{ J}$ .

### 5.5.2 Effect of surface hydrophobicity

To study the effect of surface hydrophobicity on film rupture and critical film thickness at the same bubble approaching velocity of  $240 \mu\text{m/s}$ , we compare the film profiles at points 1 and 3 of **Figure 5.8c** of  $\theta_a=38^\circ$  with **Figure 5.10a** of  $\theta_a=103^\circ$ . This comparison is presented in **Figure 5.14**. As shown in this figure, higher surface hydrophobicity makes the dimple to form at larger film thickness, which accelerates liquid film drainage. The film thickness, where dimple initially forms, increases from  $\sim 349 \text{ nm}$  to  $\sim 520 \text{ nm}$  when the contact angle increases from  $38^\circ$

to  $103^\circ$  (Figure 5.14a and b). Another important feature of Figure 5.14 is the reduction of the film radius with increasing surface hydrophobicity. For example the film radius decreases from  $\sim 250 \mu\text{m}$  to  $\sim 100 \mu\text{m}$  when the contact angle increases from  $38^\circ$  to  $103^\circ$ . As shown in this figure, increasing surface hydrophobicity makes the film rupture to occur at locations closer to the center.

Figure 5.14a and b show that the intervening aqueous film ruptures at points A ( $h_{cr} = \sim 300 \text{ nm}$ ) and B ( $h_{cr} = \sim 85 \text{ nm}$ ). As the hydrophobic force constant,  $K_{132}$  being set at  $4.5 \times 10^{-18} \text{ J}$  and  $4 \times 10^{-16} \text{ J}$  for contact angle of  $38^\circ$  and  $103^\circ$  respectively, the hydrophobic force predicted from eqn. 5.10 at point B is smaller than at point A. Figure 5.14c and d indicate that the hydrodynamic resistance force which is in the balance with the hydrophobic force (the disjoining pressure is almost negligible at these separation), at point B is smaller than at point A. As a result larger hydrophobic force (larger hydrodynamic repulsive force) at rim is responsible for film rupture at larger film thickness for higher surface hydrophobicity.

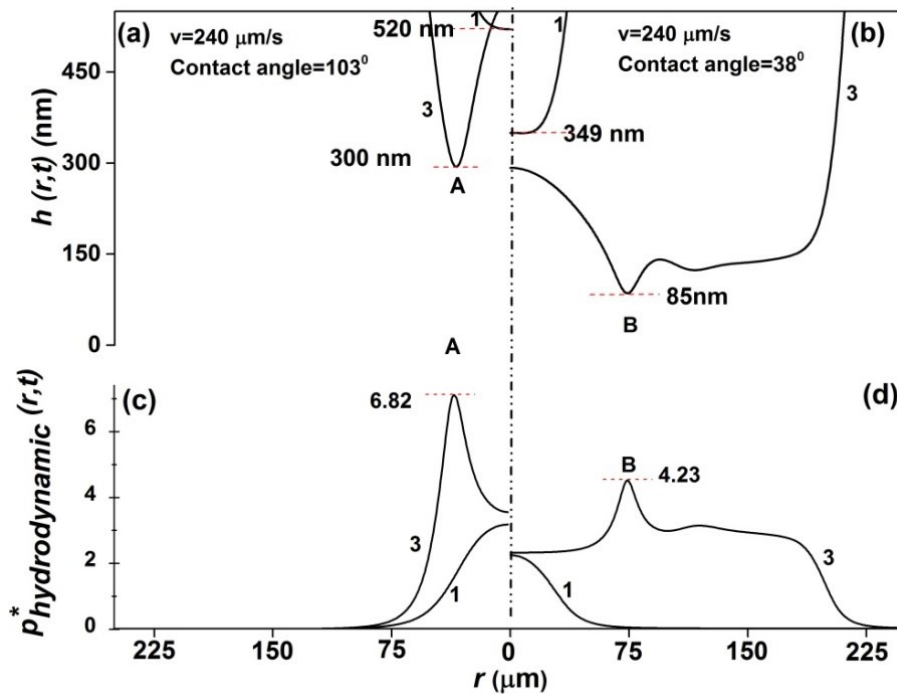


**Fig. 5.14** Thickness of the aqueous film,  $h(r,t)$  between the bubble and the hydrophobized glass sphere with bubble approach velocity of  $240 \mu\text{m/s}$  at point 1 where dimple initially forms and point 3 where the film ruptures for (a)  $\theta_a=103^\circ$  and (b)  $\theta_a=38^\circ$ . The hydrodynamic pressure profile,  $p_{hydrodynamic}^*(r,t)$  scaled by  $(\gamma/R) = 125.9 \text{ Pa}$  for (c)  $\theta_a=103^\circ$  and (d)  $\theta_a=38^\circ$ . The electrolyte concentration is  $1 \text{ mM KCl}$  and  $\text{pH} = 5.6$ . The NSRYL model is solved with  $K_{132}$  being set at  $4.5 \times 10^{-18} \text{ J}$  and  $4 \times 10^{-16} \text{ J}$  for contact angle of  $38^\circ$  and  $103^\circ$ , respectively.

## 5.6. Conclusion

In this study, the NSRYL model was developed to determine the non-equilibrium interaction forces exerted by the moving air bubble on hydrophobic glass spheres while providing the spatial and temporal evolution of the intervening aqueous film. The experimental data quantified with the integrated thin film drainage apparatus (ITFDA) and the thin film force apparatus (TFFA) was used to validate the model. The hydrophobic force which was considered as the driving force for destabilizing water films on hydrophobic surface was evaluated with the best fit between the measured and predicted time evolution forces. The numerical results showed that the longer-range hydrophobic force by increasing the surface hydrophobicity was responsible for film rupture (Pan and Yoon 2010). The effect of hydrophobicity and bubble approach velocity on the drainage rate of intervening liquid film was studied. The results showed that the wetting films formed on hydrophobic glass sphere thin much faster with increasing the surface hydrophobicity. It was found that film drainage resistance or force barrier was reduced greatly by increasing the solid surface hydrophobicity. Moreover the film drainage resistance or force barrier was found to increase with increasing bubble approach velocity. By decreasing bubble approach velocity or/and increasing surface hydrophobicity, the film radius decreased and the film rupture occurred at locations closer to the center of the film.

This model is able to numerically predict the critical film thickness at the moment of film rupture. The prediction of film thickness is achieved by solving non-linear equations with no simplifications. The simulation results indicate that the critical film thickness increases with increasing surface hydrophobicity and bubble approach velocity.

This study reveals that for higher bubble approach velocity, dimple starts to form at larger film thickness which accelerates film drainage. Increasing bubble approach velocity increases both the film radius and hydrodynamic resistance force, which retards film drainage. These two opposite effects of higher bubble approach velocity cause the film drainage rate and hence the induction times to remain almost constant at higher bubble approach velocity. For higher surface hydrophobicity, dimple starts to form at larger film thickness, which accelerates the film drainage. This factor along with the stronger and longer-range hydrophobic force accelerates the film drainage dramatically and leads to a much larger critical film thickness.

# Chapter 6

## Conclusions and future perspectives

The main conclusions of this thesis and the suggestions for the future research are summarized in this chapter.

### 6.1. Major conclusions

In contrast to the linearized SRYL model, the augmented Young Laplace equation is used without linearization within the interaction zone for the non-linearized SRYL model. As a result, the scaled governing equations of the non-linearized SRYL model do not exhibit the universal nature; instead they depend on the physical parameters of system via capillary number. The numerical results of non-linearized and linearized SRYL model at a broad range of capillary number from  $10^{-8}$  to  $10^{-3}$  show that at low  $Ca$  number of  $10^{-8}$  and smaller, both the non-linearized and the linearized SRYL models lead to the same prediction for bubble deformation, time dependent force and hydrodynamic force. Therefore, over this range of  $Ca$  number both NSRYL and LSRYL models can be confidently used to obtain the spatial and temporal evolutions of the film profile, once these models are shown to be able to give an accurate prediction of time dependent force profiles.

For systems of  $Ca$  number larger than  $10^{-8}$ , the LSRYL model predicts a stronger hydrodynamic repulsive force, and the maximum difference in prediction between the two models occurs at the  $Ca$  number around  $\sim 3.4 \times 10^{-5}$ . The over prediction of hydrodynamic repulsive force by the LSRYL model in turn influences the estimation of bubble deformation and time dependent force profiles. However, over this high  $Ca$  number range, both the LSRYL and

the NSRYL models can predict the same time dependent force profiles with different overlaps, while there are differences in the prediction of bubble shape and hydrodynamic repulsive force. Therefore, even if the LSRYL model is shown to be able to give an accurate account for time variations of the interaction forces over this range of  $Ca$  numbers, we cannot confidently use the LSRYL model to predict the spatial and temporal evolutions of the shape of the film trapped between interacting interfaces. For a system of very high capillary numbers the NSRYL model predicts a solid-like bubble that does not deform in the approach phase. In contrast, the LSRYL model is unable to show the bubble rigidity at high capillary numbers. In fact the LSRYL model predicts bubble deformation at all capillary numbers studied. Validation of simulation results by thin film profile measurement using TFFA, conclude that the NSRYL model is more accurate for high  $Ca$  number systems.

Furthermore the NSRYL model is able to predict the critical bubble approach velocity above which the bubble behaves like a solid sphere. This study shows that the NSRYL model is needed to study the effect of individual parameters of system such as bubble size, interfacial tension and liquid viscosity on the critical bubble approach velocity at which bubble behaves like a solid sphere.

Interaction forces between an air bubble and a hydrophilic glass sphere were predicted with the NSRYL model, and the results were compared with the data obtained using the ITFDA under dynamic conditions. Excellent agreement was observed between the predicted and the measured interaction forces in three liquids of very distinct physicochemical properties, demonstrating that the NSRYL model can be applied to the systems of a wider range of bubble approach velocity, and liquid interfacial tension and viscosity. The excellent agreement suggests that the NSRYL model can be used to obtain quantitative information on film profiles during the bubble

approach-retract cycle. The simulation results show that the minimum film thickness reached over a given approach period is thinner for the system of low bubble approach velocity, and/or low viscosity and high surface tension of the liquids. The agreement between the measured and predicted contact diameter confirms the capability of the NSRYL to accurately predict bubble deformation. Furthermore the linear relationship between the normalized repulsive force by Laplace pressure and bubble deformation confirms the interdependence between bubble deformation and the strength of the hydrodynamic interaction forces. The results also show that even under the relatively high hydrodynamic forces or large bubble deformations, the total force between the bubble and hydrophilic glass sphere can be estimated from the product of the Laplace pressure of the un-deformed bubble and the radius of the areas of the flattened film.

In this study, the NSRYL model was developed to determine the dynamic interaction forces exerted by the moving air bubble on hydrophobic glass spheres; while providing the spatial and temporal evolution of the intervening aqueous film. The experimental data quantified with the integrated thin film drainage apparatus (ITFDA) and the thin film force apparatus (TFFA) was used to validate the model. The hydrophobic force which was considered as the driving force for destabilizing water films on hydrophobic surface was evaluated with the best fit between the measured and predicted time evolution forces. The numerical results showed that the longer-range hydrophobic force with increasing the surface hydrophobicity was responsible for film rupture (Pan and Yoon 2010). The effect of surface hydrophobicity and bubble approach velocity on the drainage rate of intervening liquid film was studied. The results showed that the wetting films formed on hydrophobic glass sphere of increasing surface hydrophobicity thin much faster. It was found that film drainage resistance or force barrier was reduced greatly by increasing the solid surface hydrophobicity. Moreover the film drainage resistance or force

barrier was found to increase with increasing bubble approach velocity. Decreasing bubble approach velocity or/and increasing surface hydrophobicity were found to decrease the film radius. As a result the film ruptures at locations closer to the center of the film.

The extended NSRYL model incorporating proper form of hydrophobic force is able to predict the critical film thickness where the film ruptures. The prediction of the critical film thickness is achieved by solving nonlinear SRYL equations without simplifications. The simulation results indicate that the critical film thickness increases with increasing surface hydrophobicity and bubble approach velocity.

This study reveals that for higher bubble approach velocity, dimple starts to form at larger film thickness, which accelerates film drainage. Increasing bubble approach velocity increases both the film radius and hydrodynamic resistance force, which retards film drainage. These two opposite effects of higher bubble approach velocity cause the film drainage rate and hence the induction times to remain almost constant at higher bubble approach velocity. For solids of higher surface hydrophobicity, dimple starts to form at larger film thickness, which accelerates the film drainage. This factor along with the stronger and longer-range hydrophobic force accelerates the film drainage dramatically and lead to a much larger critical film thickness.

## **6.2. Suggestions for future research**

✓ The presence of surfactant in solution, which decreases the surface tension, decreases the hydrophobicity of both the glass and bubble surfaces and making the thin liquid film more stable (Wang 2013). This observation, i.e., decreasing the film drainage with decreasing the surface tension can be theoretically investigated with the NSRYL model.

✓ In addition to the reduction of the surface charge, the thin aqueous film becomes more stable with increasing solution pH and electrolyte concentration due to a reduced solid

hydrophobicity and/or structure breaking of water molecules (Wang 2013). The effects of solution pH and electrolyte concentration can be theoretically explored with the NSRYL model.

✓ The induction time depends on both the sizes of mineral particles and air bubbles (Ye et al. 1989; Yoon and Yordan 1991). The effect of bubble and particle size on the film drainage can be theoretically explored with the NSRYL model.

✓ Study the interactions of bubbles and solid particles with off-center alignment to illustrate the role of shear in bubble-particle attachment.

✓ Study the behavior of bubble or bouncing phenomena at high capillary numbers with the NSRYL model.

✓ Study the effect of individual physicochemical parameters of system on the critical bubble approach velocity above which bubble behaves like a solid sphere.

✓ Develop the NSRYL model to predict the terminal velocity of rising bubble which is also subject to the buoyancy force.

## References

- Angarska, J. K., Dimitrova, B. S., Danov, K. D., Kralchevsky, P. A., Ananthapadmanabhan, K. P., and Lips, A. (2004). "Detection of the hydrophobic surface force in foam films by measurements of the critical thickness of the film rupture." *Langmuir*, 20(5), 1799-1806.
- Angarska, J. K., and Manev, E. D. (2001). "Effect of surface forces and surfactant adsorption on the thinning and critical thickness of foam films." *Colloids Surf.Physicochem.Eng.Aspects*, 190(1-2), 117-127.
- Aronson, M. P., and Princen, H. M. (1978). "Aqueous films on silica in the presence of cationic surfactants." *Colloid and Polymer Science Kolloid-Zeitschrift & Zeitschrift Für Polymere*, 256(2), 140-149.
- Ashbaugh, H. S., Garde, S., Hummer, G., Kaler, E. W., and Paulaitis, M. E. (1999). "Conformational Equilibria of Alkanes in Aqueous Solution: Relationship to Water Structure Near Hydrophobic Solutes." *Biophys.J.*, 77(2), 645-654.
- Aston, D. E., and Berg, J. C. (2002). "Thin-film hydrodynamics in fluid interface-atomic force microscopy." *Industrial and Engineering Chemistry Research*, 41(3), 389-396.
- Aston, D. E., and Berg, J. C. (2001). "Quantitative analysis of fluid interface-atomic force microscopy." *J.Colloid Interface Sci.*, 235(1), 162-169.
- Baldessari, F., and Leal, L. G. (2006). "Effect of overall drop deformation on flow-induced coalescence at low capillary numbers." *Phys.Fluids*, 18(1),.
- Basu, S., and Sharma, M. M. (1996). "Measurement of critical disjoining pressure for dewetting of solid surfaces." *J.Colloid Interface Sci.*, 181(2), 443-455.
- Batchelor, G. K. (1968). "Erratum: An introduction to fluid dynamics (Nature (1968) 217 (199))." *Nature*, 217(5126), 394.
- Bhatt, D., Newman, J., and Radke, C. J. (2001). "Equilibrium force isotherms of a deformable bubble/drop interacting with a solid particle across a thin liquid film." *Langmuir*, 17(1), 116-130.
- Binnig, G., Quate, C. F., and Gerber, C. (1986). "Atomic Force Microscope." *Phys. Rev. Lett.*, 56 930-933.
- Blake, T. D., and Kitchener, J. A. (1972). "Stability of aqueous films on hydrophobic methylated silica." *Journal of the Chemical Society, Faraday Transactions 1: Physical Chemistry in Condensed Phases*, 68 1435-1442.
- Brochard-Wyart, F., Di Meglio, J. -, Quéré, D., and De Gennes, P. -. (1991). "Spreading of nonvolatile liquids in a continuum picture." *Langmuir*, 7(2), 335-338.

Burrill, K. A., and Woods, D. R. (1973). "Film shapes for deformable drops at liquid-liquid interfaces. II. The mechanisms of film drainage." *J. Colloid Interface Sci.*, 42(1), 15-34.

Butt, H. J. (1994). "A Technique for Measuring the Force between a Colloidal Particle in Water and a Bubble." *J. Colloid Interface Sci.*, 166(1), 109-117.

Butt, H. J., Graf, K., and Kappl, M. (2013). "Physics and Chemistry of Interfaces." 3rd Edition. Wiley.

Butt, H. J., Jaschke, M., and Ducker, W. (1995). "Measuring surface forces in aqueous electrolyte solution with the atomic force microscope." *Bioelectrochem. Bioenerget.*, 38(1), 191-201.

Carnie, S. L., Chan, D. Y. C., Lewis, C., and Manica, R. and Dagastine, R. R. (2005). "Measurement of dynamical forces between deformable drops using the Atomic Force Microscope I. Theory." *Langmuir*, 21 2912-2922.

Carnie, S. L., Chan, D. Y. C. and Manica, R. (2005). "Modelling drop-drop interactions in an atomic force microscope." *Anziam J*, 46 (E) pp C805-C819.

Chan, D. Y. C. (2002). "A simple algorithm for calculating electrical double layer interactions in asymmetric electrolytes - Poisson-Boltzmann theory." *J. Colloid Interface Sci.*, 245(2), 307-310.

Chan, D. Y. C., Dagastine, R. R., and White, L. R. (2001). "Forces between a rigid probe particle and a liquid interface. I. The repulsive case." *J. Colloid Interface Sci.*, 236(1), 141-154.

Chan, D. Y. C., Klaseboer, E., and Manica, R. (2011). "Film drainage and coalescence between deformable drops and bubbles." *Soft Matter*, 7(6), 2235-2264.

Chan, D. Y. C., Klaseboer, E., and Manica, R. (2011). "Film drainage and coalescence between deformable drops and bubbles." *Soft Matter*, 7(6), 2235-2264.

Chan, D. Y. C., Klaseboer, E., and Manica, R. (2011). "Theory of non-equilibrium force measurements involving deformable drops and bubbles." *Adv. Colloid Interface Sci.*, 165(2), 70-90.

Chan, D. Y. C., Klaseboer, E., and Manica, R. (2009). "Dynamic deformations and forces in soft matter." *Soft Matter*, 5(15), 2858-2861.

Chandler, D. (2005). "Interfaces and the driving force of hydrophobic assembly." *Nature*, 437 640-647.

Cheng Y.K., and Rosky, P. J. (1998). "Surface Topography Dependence of Biomolecular Hydrophobic Hydration " *Nature*, 392 696-699.

Christenson, H. K., and Claesson, P. M. (2001). "Direct measurements of the force between hydrophobic surfaces in water." *Adv. Colloid Interface Sci.*, 91(3), 391-436.

Claesson, P. M., and Christenson, H. K. (1988). "Very long range attractive forces between uncharged hydrocarbon and fluorocarbon surfaces in water " *J. Chem. Phys.*, 92 1650-1655.

Claesson, P. M., Blom, C. E., Herder, P. C., and Ninham, B. W. (1986). "Interactions between water—stable hydrophobic Langmuir—Blodgett monolayers on mica." *J. Colloid Interface Sci.*, 114(1), 234-242.

Clift, R., Grace, J. R., Weber, M. E. (1978) "Bubbles, Drops and Particles", Academic press, NY.

Connor, J. N., and Horn, R. G. (2003). "The influence of surface forces on thin film drainage between a fluid drop and a flat solid." *Faraday Discuss.*, 123 193-206.

Coons, J. E., Halley, P. J., McGlashan, S. A., and Tran-Cong, T. (2005). "Bounding film drainage in common thin films." *Colloids Surf. Physicochem. Eng. Aspects*, 263(1-3 SPEC. ISS.), 197-204.

Coons, J. E., Halley, P. J., McGlashan, S. A., and Tran-Cong, T. (2005). "Scaling laws for the critical rupture thickness of common thin films." *Colloids Surf. Physicochem. Eng. Aspects*, 263(1-3 SPEC. ISS.), 258-266.

Coons, J. E., Halley, P. J., McGlashan, S. A., and Tran-Cong, T. (2003). "A review of drainage and spontaneous rupture in free standing thin films with tangentially immobile interfaces." *Adv. Colloid Interface Sci.*, 105(1-3), 3-62.

Dagastine, R. R., Chau, T. T., Chan, D. Y. C., Stevens, G. W., and Grieser, F. (2005). "Interaction forces between oil-water particle interfaces - Non-DLVO forces." *Faraday Discuss.*, 129 111-124.

Dagastine, R. R., Manica, R., Carnie, S. L., Chan, D. Y. C., Stevens, G. W., and Grieser, F. (2006). "Dynamic forces between two deformable oil droplets in water." *Science*, 313(5784), 210-213.

Dagastine, R. R., Prieve, D. C., and White, L. R. (2004). "Forces between a rigid probe particle and a liquid interface: III. Extraction of the planar half-space interaction energy  $E(D)$ ." *J. Colloid Interface Sci.*, 269(1), 84-96.

Dagastine, R. R., Stevens, G. W., Chan, D. Y. C., and Grieser, F. (2004). "Forces between two oil drops in aqueous solution measured by AFM." *J. Colloid Interface Sci.*, 273(1), 339-342.

Dagastine, R. R., Stevens, G. W., Chan, D. Y. C., and Grieser, F. (2004). "Forces between two oil drops in aqueous solution measured by AFM." *J. Colloid Interface Sci.*, 273(1), 339-342.

De Gennes, P. G. (1985). "Wetting: Statics and dynamics." *Reviews of Modern Physics*, 57(3), 827-863.

Derjaguin, B. V., and Landau, L. (1941). *Acta Physicochim URSS*, (14), 633. Reprinted in *Prog Surface Sci* 1993;43:30.

Derjaguin, B., Kussakov, M., and Lebedeva, L. (1939). *Compt. Rend. Acad. Sci.*, URSS 23(7), 671.

Derjaguin, B. V. (1955). 17 207.

Derjaguin, B. V., and Kussakov, M. (Reprinted in *Prog Surface Sci* 1992). *Acta Physicochim URSS*, 1939;10:25., 40 26.

Derjaguin, B., and Kussakov, M. (1992). "An experimental investigation of polymolecular solvate (adsorbed) films as applied to the development of a mathematical theory of the stability of colloids." *Prog Surf Sci*, 40(1-4), 26-45.

Deryagin, B. V., and Khim, Z. F. (1940). 14 137.

Ducker, W. A., Senden, T. J., and Pashley, R. M. (1991). "Direct Measurement of Colloidal Forces using an Atomic Force Microscope." *Nature*, 353 239-241.

Ducker, W. A., Xu, Z., and Isrealachvili, J. N. (1994). "Measurements of hydrophobic and DLVO forces in bubble-surface interactions in aqueous solutions." *Langmuir*, 10(9), 3279-3289.

Eigeles, M. A., and Volova, M. L. (1960). "Kinetic Investigation of Effect of Contact-Time, Temperature and Surface Condition on the Adhesion of Bubbles to Mineral Surfaces." *5th Int. Miner. Process. Congr., London, Trans*, 271-284.

Eriksson, J. C., and Toshev, B. V. (1982). "Disjoining Pressure in Soap Film Thermodynamics." *Colloids and Surfaces*, 5 241-264.

Ferrari, M., Liggieri, L., and Miller, R. (2012). "Drops and Bubbles in Contact with Solid Surfaces." .

Fielden, M. L., Hayes, R. A., and Ralston, J. (1996). "Surface and Capillary Forces Affecting Air Bubble-Particle Interactions in Aqueous Electrolyte." *Langmuir*, 12 3721-3727.

Fisher, L. R., Hewitt, D., Mitchell, E. E., Ralston, J., and Wolfe, J. (1992). "The drainage of an aqueous film between a solid plane and an air bubble." *Adv. Colloid Interface Sci.*, 39(0), 397-416.

Fisher, L. R., Mitchell, E. E., Hewitt, D., Ralston, J., and Wolfe, J. (1991). "The drainage of a thin aqueous film between a solid surface and an approaching gas bubble." *Colloids and Surfaces*, 52(0), 163-174.

Frumkin, A. (1933). *Uspekhi Khimii (Adv Chem)*, 2 27–35.

Frumkin, A. N., and Khim, Z. F. (1938). 12 337.

Fuerstenau, D. W., and Herrera-Urbina, R. (Surfactant Science Series 1989). "Mineral Separation by Froth Flotation." 33 259-320.

Gauss, C. F. (1830). "Principia generalia theoriae figurae fluidorum in statu aequilibrii." *Dieterichs*, .

Gillies, G., and Prestidge, C. A. (2004). "Interaction forces, deformation and nano-rheology of emulsion droplets as determined by colloid probe AFM." *Adv.Colloid Interface Sci.*, 108-109 197-205.

Glembotsky, V. A. (1953). *Izv. Akad. Nauk SSSR (OTN)*, 1524-1531.

Gu, G., Xu, Z., Nandakumar, K., and Masliyah, J. (2003). "Effects of physical environment on induction time of air-bitumen attachment." *Int.J.Miner.Process.*, 69(1-4), 235-250.

Gu, G., Sean Sanders, R., Nandakumar, K., Xu, Z., and Masliyah, J. H. (2004). "A novel experimental technique to study single bubble-bitumen attachment in flotation." *Int.J.Miner.Process.*, 74(1–4), 15-29.

Gu, G., Xu, Z., Nandakumar, K., and Masliyah, J. (2003). "Effects of physical environment on induction time of air-bitumen attachment." *Int.J.Miner.Process.*, 69(1–4), 235-250.

Gunning, A. P., Mackie, A. R., Wilde, P. J., and Morris, V. J. (2004). "Atomic Force Microscopy of Emulsion Droplets: Probing Droplet-Droplet Interactions." *Langmuir*, 20 116-122.

Haberman, W. L., Morton, R. K. (1953). "An Experimental Investigation of the Drag and Shape of Air Bubble Rising in Various Liquids." Report 802, Navy Dept., David W. Taylor Model Basin, Washington. DC, 68.

Hartley, P. G., Grieser, F., Mulvaney, P., and Stevens, G. W. (1999). "Surface forces and deformation at the oil-water interface probed using AFM force measurement." *Langmuir*, 15(21), 7282-7289.

Hendrix, M. H. W., Manica, R., Klaseboer, E., Chan, D. Y. C., and Ohl, C.D. (2012). "Spatiotemporal evolution of thin liquid films during impact of water bubbles on glass on a micrometer to nanometer scale." *Phys.Rev.Lett.*, 108(24),.

Herder, P. C. (1990). "Interactions between mica surfaces in dodecyl- and octylammonium chloride solutions." *J.Colloid Interface Sci.*, 134(2), 346-356.

Hewitt, D., Fornasiero, D., Ralston, J., and Fisher, L. R. (1993). "Aqueous film drainage at the quartz/water/air interface." *Journal of the Chemical Society, Faraday Transactions*, 89(5), 817-822.

Hough, D. B., and White, L. R. (1980). "The calculation of hamaker constants from liftshitz theory with applications to wetting phenomena." *Adv.Colloid Interface Sci.*, 14(1), 3-41.

Ishida, N. (2007). "Direct measurement of hydrophobic particle-bubble interactions in aqueous solutions by atomic force microscopy: Effect of particle hydrophobicity." *Colloids Surf.Physicochem.Eng.Aspects*, 300(3 SPEC. ISS.), 293-299.

Israelachvili, J. and Pashley, R. (1982). "The hydrophobic interaction is long range, decaying exponentially with distance." *Nature (London)*, 300(5890), 341-342.

Israelachvili, J. N., and Tabor, D. (1972). "Measurement of Van Der Waals Dispersion Forces in the Range 1.5 to 130 Nm." *Proc. Roy. Soc. London, Ser. A*, 331 19-38.

Israelachvili, J. N., and Pashley, R. M. (1984). "Measurement of the hydrophobic interaction between two hydrophobic surfaces in aqueous electrolyte solutions." *J.Colloid Interface Sci.*, 98(2), 500-514.

Israelachvili, J. (1991). "Intermolecular and Surface Forces." *2nd Ed., Academic Press, San Diego*, .

Ivanov, I. B. (1988). "Thin Liquid Films." .

Ivanov, I. B., Dimitrov, D. S., Somasundaran, P., and Jain, R. K. (1985). "Thinning of films with deformable surfaces: Diffusion-controlled surfactant transfer." *Chemical Engineering Science*, 40(1), 137-150.

Ivanov, I. B., Radoev, B., Manev, E., and Scheludko, A. (1970). "Theory of the critical thickness of rupture of thin liquid films." *Transactions of the Faraday Society*, 66 1262-1273.

Kékicheff, P., Christenson, H. K., and Ninham, B. W. (1989). "Adsorption of cetyltrimethylammonium bromide to mica surfaces below the critical micellar concentration." *Colloids and Surfaces*, 40(C), 31-41.

Klaseboer, E., Chevaillier, J. -, Mate, A., Masbernat, O., and Gourdon, C. (2001). "Model and experiments of a drop impinging on an immersed wall." *Phys.Fluids*, 13(1), 45-57.

Klaseboer, E., Chevaillier, J. P., Gourdon, C., and Masbernat, O. (2000). "Film drainage between colliding drops at constant approach velocity: Experiments and modeling." *J.Colloid Interface Sci.*, 229(1), 274-285.

Krasowska, M., and Malysa, K. (2007). "Wetting films in attachment of the colliding bubble." *Adv.Colloid Interface Sci.*, 134-135(0), 138-150.

Krzan, M., and Malysa, K. (2002). "Profiles of local velocities of bubbles in n-butanol, n-hexanol and n-nonanol solutions." *Colloids Surf.Physicochem.Eng.Aspects*, 207(1-3), 279-291.

Lai, A., and Bremond, N. and Stone, H. A. (2009). "Separation-driven coalescence of droplets: an analytical criterion for the approach to contact." *Journal of Fluid Mechanics*, 632 97-107.

Laskowski, J., and Iskra, J. "Role of Capillary Effects in Bubble-Particle Collision in Flotation. Transactions of the Institution of Mining and Metallurgy, Section C: Mineral Processing and Extractive Metallurgy. 1970; 79." .

Laskowski, J. S., Xu, Z., and Yoon, R. H. (1992). "Energy barrier in particle-to-bubble attachment on flotation kinetics." *Mines & Carrieres.Les Techniques*, 95-100.

Leal, L. G. (2007). *Advanced transport phenomena: fluid mechanics and convective transport processes*. Cambridge University Press, New York.

Luttrell, G. H., and Yoon, R. H. (1992). "A hydrodynamic model for bubble-particle attachment." *J.Colloid Interface Sci.*, 154(1), 129-137.

Lyklema, J., and Mysels, K. J. (1965). "A study of double layer repulsion and van der Waals attraction in soap films." *J.Am.Chem.Soc.*, 87(12), 2539-2546.

Mahanty, J. H. and Ninham, B. W. (1977). *Dispersion Forces*. Academic Press, London.

Malysa, K., Krasowska, M., and Krzan, M. (2005). "Influence of surface active substances on bubble motion and collision with various interfaces." *Adv.Colloid Interface Sci.*, 114–115(0), 205-225.

Manev, E., and Pugh, R. J. (1997). "The Influence of Tetraalkylammonium Counterions on the Drainage and Stability of Thin Films and Foams Stabilized by Dilute Aqueous Solutions of Sodium Dodecyl Sulfate." *J.Colloid Interface Sci.*, 186(2), 493-497.

Manev, E., Scheludko, A., and Exerowa, D. (1974). "Effect of surfactant concentration on the critical thicknesses of liquid films." *Colloid and Polymer Science Kolloid Zeitschrift & Zeitschrift Für Polymere*, 252(7-8), 586-593.

Manev, E., Tsekov, R., and Radoev, B. (1997). "Effect of thickness non-homogeneity on the kinetic behavior of microscopic foam films." *Journal of Dispersion Science and Technology*, 18(6-7), 769-788.

Manev, E. D., and Nguyen, A. V. (2005). "Critical thickness of microscopic thin liquid films." *Adv.Colloid Interface Sci.*, 114–115(0), 133-146.

Manev, E. D., and Nguyen, A. V. (2005). "Effects of surfactant adsorption and surface forces on thinning and rupture of foam liquid films." *Int.J.Miner.Process.*, 77(1), 1-45.

Manica, R., and Chan, D. Y. C. (2011). "Drainage of the air-water-quartz film: Experiments and theory." *Physical Chemistry Chemical Physics*, 13(4), 1434-1439.

Manica, R., Connor, J. N., Carnie, S. L., Horn, R. G., and Chan, D. Y. C. (2007). "Dynamics of interactions involving deformable drops: Hydrodynamic dimpling under attractive and repulsive electrical double layer interactions." *Langmuir*, 23(2), 626-637.

Manica, R., Connor, J. N., Clasohm, L. Y., Carnie, S. L., Horn, R. G., and Chan, D. Y. C. (2008). "Transient responses of a wetting film to mechanical and electrical perturbations." *Langmuir*, 24(4), 1381-1390.

Manica, R., Klaseboer, E., and Chan, D. Y. C. (2008). "Dynamic interactions between drops - A critical assessment." *Soft Matter*, 4(8), 1613-1616.

Manica, R., Parkinson, L., Ralston, J., and Chan, D. Y. C. (2010). "Interpreting the dynamic interaction between a very small rising bubble and a hydrophilic titania surface." *Journal of Physical Chemistry C*, 114(4), 1942-1946.

Manica, R., Hendrix, M., Gupta, R., Klaseboer, E., Ohl, C.D., and Chan, D. Y. C. (2013). "Effects of hydrodynamic film boundary conditions on bubble-wall impact." *Soft Matter*, 9, 9755-9758.

Manor, O., Vakarelski, I. U., Stevens, G. W., Grieser, F., Dagastine, R. R., and Chan, D. Y. C. (2008). "Dynamic forces between bubbles and surfaces and hydrodynamic boundary conditions." *Langmuir*, 24(20), 11533-11543.

Manor, O., Vakarelski, I. U., Tang, X., O'Shea, S. J., Stevens, G. W., Grieser, F., Dagastine, R. R., and Chan, D. Y. C. (2008). "Hydrodynamic boundary conditions and dynamic forces between bubbles and surfaces." *Phys.Rev.Lett.*, 101(2),.

Mao, L., and Yoon, R. H. (1997). "Predicting flotation rates using a rate equation derived from first principles." *Int.J.Miner.Process.*, 51(1-4), 171-181.

McCormack, D., Carnie, S. L., and Chan, D. Y. C. (1995). "Calculations of Electric Double-Layer Force and Interaction Free Energy between Dissimilar Surfaces." *J.Colloid Interface Sci.*, 169(1), 177-196.

Motomura, K., Iwanaga, S., Hayami, Y., Uryu, S., and Matuura, R. (1981). "Thermodynamic studies on adsorption at interfaces: IV. Dodecylammonium chloride at water/air interface." *J.Colloid Interface Sci.*, 80(1), 32-38.

Mulvaney, P., Perera, J. M., Biggs, S., Grieser, F., and Stevens, G. W. (1996). "The Direct Measurement of the Forces of Interaction between a Colloid Particle and an Oil Droplet." *J.Colloid Interface Sci.*, 183(2), 614-616.

Nedyalkov, M., Alexandrova, L., Platikanov, D., Leveck, B., and Tadros, T. (2007). "Wetting films on a hydrophilic silica surface obtained from aqueous solutions of hydrophobically modified inulin polymeric surfactant." *Colloid Polym.Sci.*, 285(15), 1713-1717.

Nespolo, S. A., Chan, D. Y. C., Grieser, F., Hartley, P. G., and Stevens, G. W. (2003). "Forces between a rigid probe particle and a liquid interface: Comparison between experiment and theory." *Langmuir*, 19(6), 2124-2133.

Newman, J. S. (1991). "Electrochemical systems." *Prentice Hall, Englewood Cliffs, N. J.*, .

Nguyen, A. V., Stechemesser, H., Schulze, H. J., and Zobel, G. (1997). "Contact time during impact of aspherical particle against a plane gas-liquid interface: Theory." *Int. J. Miner Process*, 50 97-111.

Nguyen, A. V., and Schulze, H. J. (2004). "Colloidal science of flotation." .

Nguyen, A. V., Nalaskowski, J., and Miller, J. D. (2003). "A study of bubble-particle interaction using atomic force microscopy." *Minerals Eng*, 16(11), 1173-1181.

Nguyen, A. V., Schulze, H. J., and Ralston, J. (1997). "Elementary steps in particle-bubble attachment." *Int.J.Miner.Process.*, 51(1-4), 183-195.

Ødegaard, H. (2001). "The use of dissolved air flotation in municipal wastewater treatment." *Water Science and Technology*, 43(8), 75-81.

Pan, L., Jung, S., and Yoon, R.H. (2011). "Effect of hydrophobicity on the stability of the wetting films of water formed on gold surfaces." *J. Colloid Interface Sci.*, 361 321-330.

Pan, L., and Yoon, R. H. (2010). "Hydrophobic forces in the wetting films of water formed on xanthate-coated gold surfaces." *Faraday Discuss.*, 146 325-340.

Parker, J. L., Claesson, P. M., Wang, J. H., and Yasuda, H. K. (1994). "Surface forces between plasma polymer films." *Langmuir*, 10(8), 2766-2773.

Parker, J. L. (1992). "A novel method for measuring the force between two surfaces in a surface force apparatus." *Langmuir*, 8(2), 551-556.

Parker, J. L., and Attard, P. (1992). "Deformation of surfaces due to surface forces." *J.Phys.Chem.*, 96(25), 10398-10405.

Parkinson, L., and Ralston, J. (2010). "The interaction between a very small rising bubble and a hydrophilic titania surface." *Journal of Physical Chemistry C*, 114(5), 2273-2281.

Pashley, R. M., McGuiggan, P. M., Ninham, B. W., and Evens, D. F. (1985). "Attractive forces between uncharged hydrophobic surfaces: direct measurements in aqueous solution." *Science*, 229 1088.

- Platikanov, D. (1964). "Experimental investigation on the "dimpling" of thin liquid films." *J.Phys.Chem.*, 68(12), 3619-3624.
- Preuss, M., and Butt, H. J. (1998). "Direct measurement of particle-bubble interactions in aqueous electrolyte: Dependence on surfactant." *Langmuir*, 14(12), 3164-3174.
- Preuss, M., and Butt, H. J. (1998). "Measuring the contact angle of individual colloidal particles." *J.Colloid Interface Sci.*, 208(2), 468-477.
- Pugh, R. J., and Yoon, R. H. (1994). "Hydrophobicity and Rupture of Thin Aqueous Films." *J.Colloid Interface Sci.*, 163(1), 169-176.
- Pushkarova, R. A., and Horn, R. G. (2008). "Bubble-solid interactions in water and electrolyte solutions." *Langmuir*, 24(16), 8726-8734.
- Pushkarova, R. A., and Horn, R. G. (2005). "Surface forces measured between an air bubble and a solid surface in water." *Colloids Surf.Physicochem.Eng.Aspects*, 261(1-3), 147-152.
- Radoev, B. P., Scheludko, A. D., and Manev, E. D. (1983). "Critical thickness of thin liquid films: Theory and experiment." *J.Colloid Interface Sci.*, 95(1), 254-265.
- Read, A. D., and Kitchener, J. A. (1969). "Wetting films on silica." *J.Colloid Interface Sci.*, 30(3), 391-398.
- Reynolds, O. (1886). *Philos. Trans. R. Soc. London, Ser. A*, 177 157.
- Ruckenstein, E., and Churaev, N. (1991). "A possible hydrodynamic origin of the forces of hydrophobic attraction." *J.Colloid Interface Sci.*, 147(2), 535-538.
- Scheludko, A. (1967). *Adv. Colloid Interface Sci.*, 1 391.
- Scheludko, A., and Manev, E. (1968). "Critical thickness of rupture of chlorbenzene and aniline films." *Transactions of the Faraday Society*, 64 1123-1134.
- Schulze, H. J. (1984). "Physicochemical elementary processes in flotation. An analysis from the point of view of colloid science including process engineering considerations." *Amsterdam Elsevier*, .
- Schulze, H. J. "Rupturing of Thin Liquid Films on Solid Surfaces. (1975)." *Colloid and Polymer Science*, 253 730-737.
- Schulze, H. J., Stöckelhuber, K. W., and Wenger, A. (2001). "The influence of acting forces on the rupture mechanism of wetting films - Nucleation or capillary waves." *Colloids Surf.Physicochem.Eng.Aspects*, 192(1-3), 61-72.

Shahalami, M., Zhang, X., Tchoukov, P., Masliyah, J., Xu, Z. (manuscript in preparation). "Study of non-equilibrium interactions between an air bubble and a solid surface using Stokes-Reynolds-Young-Laplace model." .

Sharma, A., and Ruckenstein, E. (1987). "Critical thickness and lifetimes of foams and emulsions: Role of surface wave-induced thinning." *J.Colloid Interface Sci.*, 119(1), 14-29.

Sharma, A., and Ruckenstein, E. (1987). "Stability, critical thickness, and the time of rupture of thinning foam and emulsion films." *Langmuir*, 3(5), 760-768.

Snyder, B. A., Aston, D. E., and Berg, J. C. (1997). "Particle-Drop Interactions Examined with an Atomic Force Microscope." *Langmuir*, 13 590-593.

Stefan J. (1874). *Sitzber Akad Wiss Wien. Math-Naturw Kl*, 69 713.

Sven-Nilsson, I. (1934). *Kolloid-Zeitschrift*, 69(2), 230-232.

Tabor, D., and Winterton, R. H. S. (1969). "Direct Measurement of Normal and Retarded Van Der Waals Forces." *Proc. Roy. Soc. , Ser. A*, 312 435-450.

Tabor, R. F., Manica, R., Chan, D. Y. C., Grieser, F., and Dagastine, R. R. (2011). "Repulsive Van der Waals forces in soft matter: Why bubbles do not stick to walls." *Phys.Rev.Lett.*, 106(6),.

Tchaliovska, S., Manev, E., Radoev, B., Eriksson, J. C., and Claesson, P. M. (1994). "Interactions in Equilibrium Free Films of Aqueous Dodecylammonium Chloride Solutions." *J.Colloid Interface Sci.*, 168(1), 190-197.

Tsao, Y. H., Evans, D. F., and Wennerstroem, H. (1993). " Long-range attraction between a hydrophobic surface and a polar surface is stronger than that between two hydrophobic surfaces " *Langmuir*, 9 779-785.

Tsao, Y. H., Evans, D. F., and Wennerstroem, H. (1993). "Long-range attractive force between hydrophobic surfaces observed by atomic force microscopy." *Science (Washington, D.C.)*, 262 547.

Tsao, H. -, and Koch, D. L. (1997). "Observations of high Reynolds number bubbles interacting with a rigid wall." *Phys.Fluids*, 9(1), 44-56.

Tsekov, R., and Evstatieva, E. (2004). "A fractal classification of the drainage dynamics in thin liquid films." *Progress in Colloid and Polymer Science*, 126 93-96.

Tsekov, R. (1998). "The R4/5-problem in the drainage of dimpled thin liquid films." *Colloids Surf.Physicochem.Eng.Aspects*, 141(2), 161-164.

- Vakarelski, I. U., Lee, J., Dagastine, R. R., Chan, D. Y. C., Stevens, G. W., and Grieser, F. (2008). "Bubble colloidal AFM probes formed from ultrasonically generated bubbles." *Langmuir*, 24(3), 603-605.
- Vakarelski, I. U., Manica, R., Tang, X., O'Shea, S. J., Stevens, G. W., Grieser, F., Dagastine, R. R., and Chan, D. Y. C. (2010). "Dynamic interactions between microbubbles in water." *Proc.Natl.Acad.Sci.U.S.A.*, 107(25), 11177-11182.
- Valkovska, D. S., Danov, K. D., and Ivanov, I. B. (2002). "Stability of draining plane-parallel films containing surfactants." *Adv.Colloid Interface Sci.*, 96(1-3), 101-129.
- Verwey, E. J. W., and Overbeek, J. T. G. (1948). "Theory of the stability of Lyophobic colloids." *Elsevier, Amsterdam*, 216.
- Verwey, E. J. W., and Overbeek, J. T. G. (1955). "Theory of the stability of lyophobic colloids." *J.Colloid Sci.*, 10(2), 224-225.
- Vinogradova, O. I. (1996). "Hydrodynamic interaction of curved bodies allowing slip on their surfaces." *Langmuir*, 12(24), 5963-5968.
- Vinogradova, O. I. (1995). "Drainage of a thin liquid film confined between hydrophobic surfaces." *Langmuir*, 11 2213-2220.
- Vrij, A. (1966). "Possible mechanism for the spontaneous rupture of thin, free liquid films." *Discuss.Faraday Soc.*, 42 23-33.
- Wang, L., Sharp, D., Masliyah, J., and Xu, Z. (2013). "Measurement of interactions between solid particles, liquid droplets, and/or gas bubbles in a liquid using an integrated thin film drainage apparatus." *Langmuir*, 29(11), 3594-3603.
- Wang, L., Sharp, D., Xu, Z., and Masliyah, J. (2012). "A novel induction timer to study interactions between an air bubble and a bitumen surface." *Separation Technologies for Minerals, Coal, and Earth Resources*, 47-55.
- Wang, L., and Yoon, R. H. (2004). "Hydrophobic forces in the foam films stabilized by sodium dodecyl sulfate: Effect of electrolyte." *Langmuir*, 20(26), 11457-11464.
- Wang, L. (2013). "A study of interactions between an air bubble and a solid surface in a liquid." *ProQuest Dissertations and Theses*, .
- Webber, G. B., Edwards, S. A., Stevens, G. W., Grieser, F., Dagastine, R. R., and Chan, D. Y. C. (2008). "Measurements of dynamic forces between drops with the AFM: Novel considerations in comparisons between experiment and theory." *Soft Matter*, 4(6), 1270-1278.

Webber, G. B., Manica, R., Edwards, S. A., Carnie, S. L., Stevens, G. W., Grieser, F., Dagastine, R. R., and Chan, D. Y. C. (2008). "Dynamic forces between a moving particle and a deformable drop." *Journal of Physical Chemistry C*, 112(2), 567-574.

Wills, B. A. (1988). *Mineral processing technology*, Pergamon Press, 457-595.

Ye, Y., and Miller, J. D. (1988). "bubble/particle contact time in the analysis of coal flotation " *Coal Prep*, 5 147-166.

Ye, Y., Khandrika, S. M., and Miller, J. D. (1989). "Induction-time measurements at a particle bed." *Int.J.Miner.Process.*, 25(3-4), 221-240.

Yeh, E. K., Newman, J., and Radke, C. J. (1999). "Equilibrium configurations of liquid droplets on solid surfaces under the influence of thin-film forces. Part I. Thermodynamics." *Colloids Surf.Physicochem.Eng.Aspects*, 156(1-3), 137-144.

Yoon, R. H., Flinn, D. H., and Rabinovich, Y. I. (1997). "Hydrophobic Interactions between Dissimilar Surfaces." *J Colloid Interface Sci.*, 185(2), 363-370.

Yoon, R. H. (2000). "The role of hydrodynamic and surface forces in bubble-particle interaction." *Int.J.Miner.Process.*, 58(1-4), 129-143.

Yoon, R. H. (1992). "Hydrodynamic and surface forces in bubble-particle interactions." *Mines & Carrieres.Les Techniques*, 74-79.

Yoon, R. H., and Aksoy, B. S. (1999). "Hydrophobic forces in thin water films stabilized by dodecylammonium chloride." *J.Colloid Interface Sci.*, 211(1), 1-10.

Yoon, R.H., and Mao, L. (1996). "Application of extended DLVO theory, IV: Derivation of flotation rate equation from first principles." *J.Colloid Interface Sci.*, 181(2), 613-626.

Yoon, R.H., and Ravishankar, S. A. (1996). "Long-Range Hydrophobic Forces between Mica Surfaces in Alkaline Dodecylammonium Chloride Solutions." *J.Colloid Interface Sci.*, 179(2), 403-411.

Yoon, R.H., and Yordan, J. L. (1991). "Induction time measurements for the quartz—amine flotation system." *J.Colloid Interface Sci.*, 141(2), 374-383.

Yoon, Y., Baldessari, F., Cenicerros, H. D., and Leal, L. G. (2007). "Coalescence of two equal-sized deformable drops in an axisymmetric flow." *Phys.Fluids*, 19(10),.

Young, T. (1805). *Philos. Trans. R. Soc. London*, 95 65.

## Appendix

### Appendix A

Augmented Young Laplace equation:

$$\frac{\gamma}{r} \frac{\partial}{\partial r} \left( \frac{r \partial h / \partial r}{(1 + (\partial h / \partial r)^2)^{1/2}} \right) = \frac{2\gamma}{R} - \Pi(h(r, t)) - p(r, t) \quad (1)$$

Left hand side of **eqn.1**:

$$\begin{aligned} & \frac{\gamma}{r} \frac{\partial}{\partial r} \left( \frac{r \partial h / \partial r}{(1 + (\partial h / \partial r)^2)^{1/2}} \right) \\ &= \frac{\gamma}{r} \left[ \frac{(\partial h / \partial r + r \partial^2 h / \partial r^2)(1 + (\partial h / \partial r)^2)^{1/2} - r(\partial h / \partial r)^2 \partial^2 h / \partial r^2 / ((1 + (\partial h / \partial r)^2)^{1/2})}{(1 + (\partial h / \partial r)^2)} \right] \\ &= \frac{\gamma}{r} \left[ \frac{(\partial h / \partial r + r \partial^2 h / \partial r^2)(1 + (\partial h / \partial r)^2) - r(\partial h / \partial r)^2 \partial^2 h / \partial r^2}{(1 + (\partial h / \partial r)^2)^{3/2}} \right] \\ &= \frac{\gamma}{r} \left[ \frac{\partial h / \partial r + r \partial^2 h / \partial r^2 + (\partial h / \partial r)^3 + r \partial^2 h / \partial r^2 (\partial h / \partial r)^2 - r(\partial h / \partial r)^2 \partial^2 h / \partial r^2}{(1 + (\partial h / \partial r)^2)^{3/2}} \right] \\ &= \frac{\gamma}{r} \left[ \frac{\partial h / \partial r + r \partial^2 h / \partial r^2 + (\partial h / \partial r)^3}{(1 + (\partial h / \partial r)^2)^{3/2}} \right] \end{aligned}$$

As a result **eqn.1** becomes:

$$\frac{\gamma}{r} \left[ \frac{\partial h / \partial r + r \partial^2 h / \partial r^2 + (\partial h / \partial r)^3}{(1 + (\partial h / \partial r)^2)^{3/2}} \right] = \frac{2\gamma}{R} - \Pi(h(r, t)) - p(r, t) \quad (2)$$

With using dimensionless variables (**eqn. 3.8**) the left hand side of **eqn. 2** becomes:

$$\begin{aligned}
& \frac{\gamma}{r} \left[ \frac{\partial h / \partial r + r \partial^2 h / \partial r^2 + (\partial h / \partial r)^3}{(1 + (\partial h / \partial r)^2)^{\frac{3}{2}}} \right] \\
&= \frac{\gamma}{r^* Ca^{1/4} R} \left[ \frac{Ca^{1/4} \partial h^* / \partial r^* + r^* Ca^{1/4} \partial^2 h^* / \partial r^{*2} + Ca^{3/4} (\partial h^* / \partial r^*)^3}{(1 + Ca^{1/2} (\partial h^* / \partial r^*)^2)^{\frac{3}{2}}} \right] \\
&= \frac{\gamma}{r^* R} \left[ \frac{\partial h^* / \partial r^* + r^* \partial^2 h^* / \partial r^{*2} + Ca^{1/2} (\partial h^* / \partial r^*)^3}{(1 + Ca^{1/2} (\partial h^* / \partial r^*)^2)^{\frac{3}{2}}} \right]
\end{aligned}$$

Now the **eqn. 2** becomes:

$$\begin{aligned}
& \frac{\gamma}{r^* R} \left[ \frac{\partial h^* / \partial r^* + r^* \partial^2 h^* / \partial r^{*2} + Ca^{1/2} (\partial h^* / \partial r^*)^3}{(1 + Ca^{1/2} (\partial h^* / \partial r^*)^2)^{\frac{3}{2}}} \right] \tag{3} \\
&= \frac{2\gamma}{R} - \Pi(h(r, t)) - p(r, t)
\end{aligned}$$

$$\begin{aligned}
& \frac{1}{r^*} \left[ \frac{\partial h^* / \partial r^* + r^* \partial^2 h^* / \partial r^{*2} + Ca^{1/2} (\partial h^* / \partial r^*)^3}{(1 + Ca^{1/2} (\partial h^* / \partial r^*)^2)^{\frac{3}{2}}} \right] \tag{4} \\
&= 2 - \Pi(h(r, t)) \times \frac{R}{\gamma} - p(r, t) \times \frac{R}{\gamma}
\end{aligned}$$

$$\frac{1}{r^*} \left[ \frac{\partial h^* / \partial r^* + r^* \partial^2 h^* / \partial r^{*2} + Ca^{1/2} (\partial h^* / \partial r^*)^3}{(1 + Ca^{1/2} (\partial h^* / \partial r^*)^2)^{\frac{3}{2}}} \right] = 2 - \Pi^* - p^* \tag{5}$$

## Appendix B1

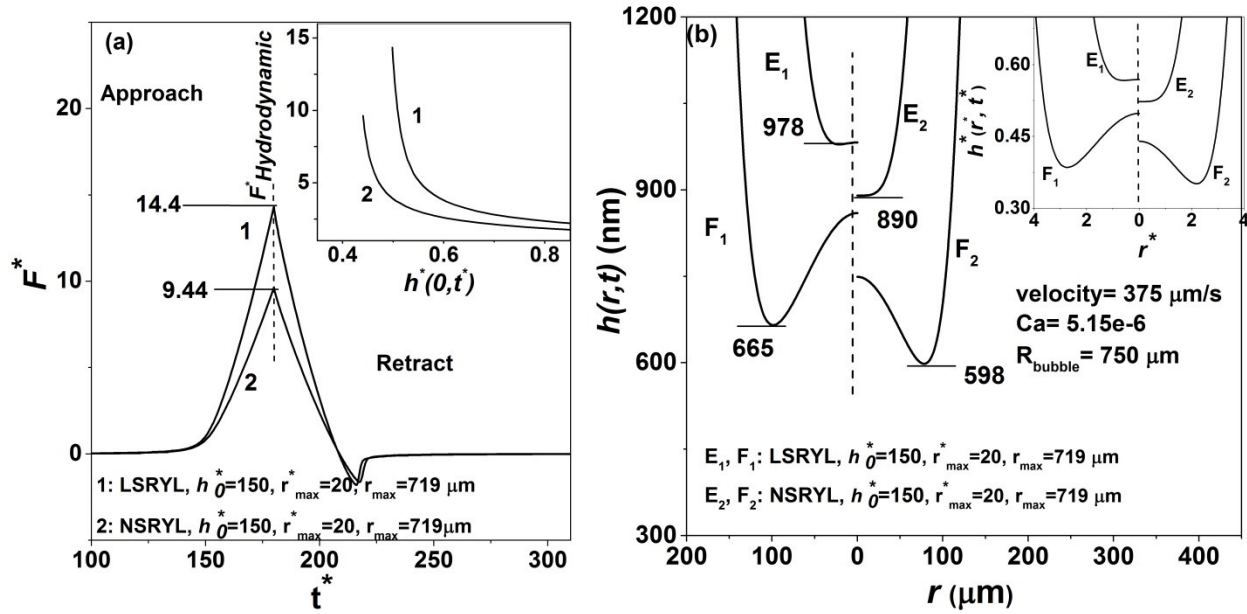


**Fig. B1.** (a) Variation of scaled force with scaled time, (b) variation of film thickness with film radius in aqueous electrolyte (100 mM KCl, pH = 5.6) at a bubble approach velocity of 375  $\mu\text{m/s}$ , corresponding to a capillary number of  $5.15 \times 10^{-6}$ - the LSRYL model results are denoted with 1 and the NSRYL model results are denoted with 2. Insets: (a) Variation of scaled hydrodynamic force with scaled film thickness at the axis of symmetry, and (b) variation of scaled film thickness with scaled film radius. In this run, the  $r_{\text{max}}^*$  is 20 (correspond to  $r_{\text{max}}$  of 719  $\mu\text{m}$ ). The physical parameters used in the NSRYL and LSRYL models summarized in **Table 3.1 and 3.3**.

## Appendix B2

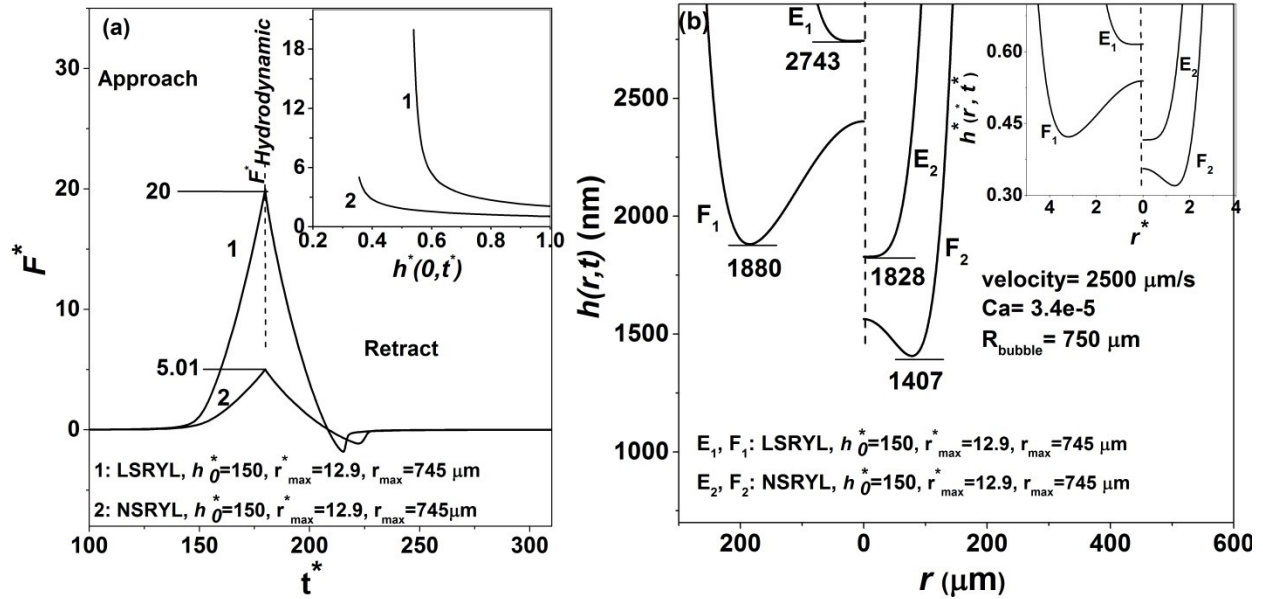


**Fig. B2.** (a) Variation of scaled force with scaled time, (b) variation of film thickness with film radius in aqueous electrolyte (100 mM KCl, pH = 5.6) at a bubble approach velocity of 2500  $\mu\text{m/s}$ , corresponding to a capillary number of  $3.4 \times 10^{-5}$  - the LSRYL model results are denoted with 1 and the NSRYL model results are denoted with 2. Insets: (a) Variation of scaled hydrodynamic force with scaled film thickness at the axis of symmetry, and (b) variation of scaled film thickness with scaled film radius. In this run, the  $r_{max}^*$  is 12.9 (correspond to  $r_{max}$  of 745  $\mu\text{m}$ ). The physical parameters used in the NSRYL and LSRYL models summarized in **Table 3.1 and 3.4**.

## Appendix B3

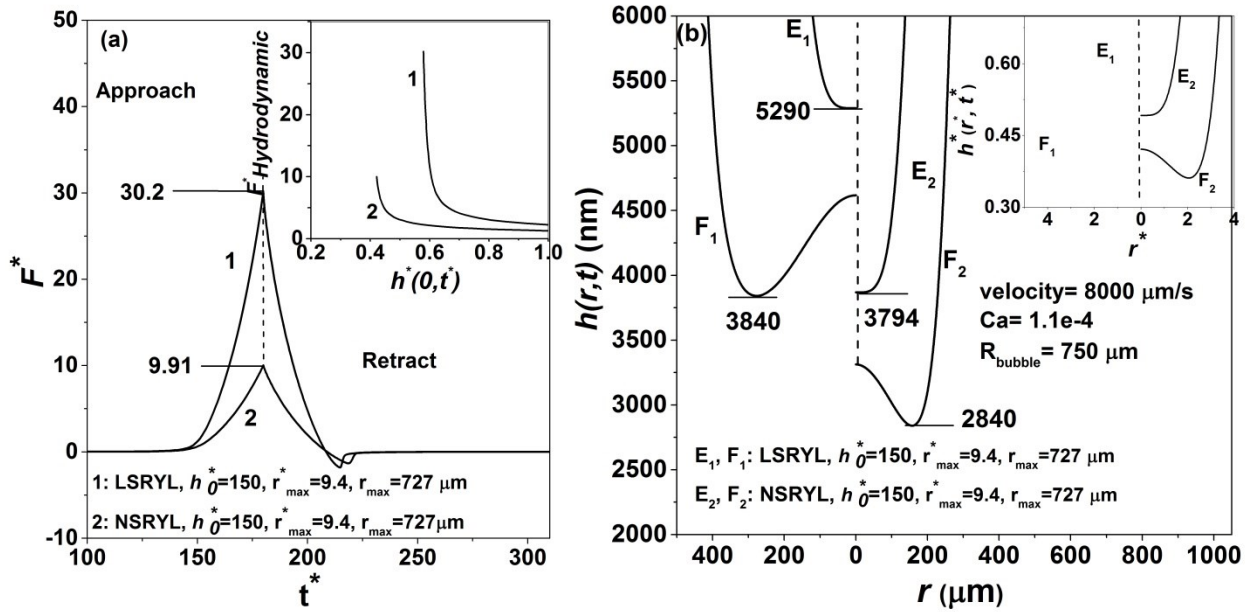


**Fig. B3.** (a) Variation of scaled force with scaled time, (b) variation of film thickness with film radius in aqueous electrolyte (100 mM KCl, pH = 5.6) at a bubble approach velocity of 8000  $\mu\text{m/s}$ , corresponding to a capillary number of  $1.09 \times 10^{-4}$ - the LSRYL model results are denoted with 1 and the NSRYL model results are denoted with 2. Insets: (a) Variation of scaled hydrodynamic force with scaled film thickness at the axis of symmetry, and (b) variation of scaled film thickness with scaled film radius. In this run, the  $r_{max}^*$  is 9.4 (correspond to  $r_{max}$  of 727  $\mu\text{m}$ ). The physical parameters used in the NSRYL and LSRYL models summarized in **Table 3.1 and 3.5**.

## Appendix B4

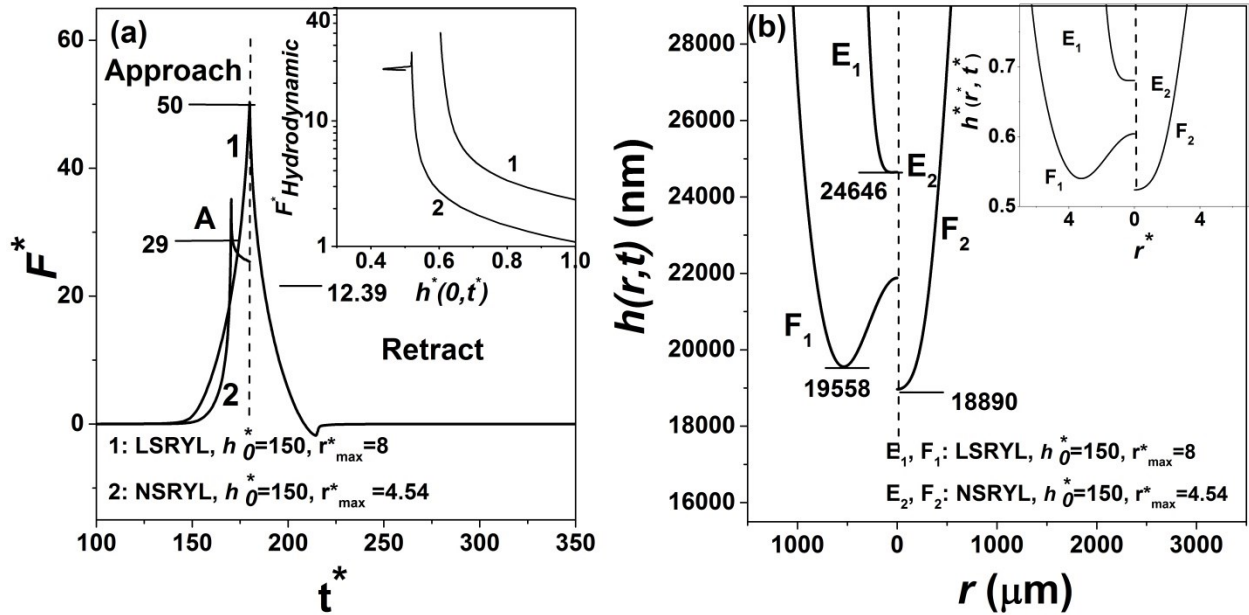


**Fig. B4.** (a) Variation of scaled force with scaled time, (b) variation of film thickness with film radius in aqueous electrolyte (100 mM KCl, pH = 5.6) at a bubble approach velocity of  $165000 \mu\text{m/s}$ , corresponding to a capillary number of  $2.3 \times 10^{-3}$ - the LSRYL model results are denoted with 1 and the NSRYL model results are denoted with 2. Insets: (a) Variation of scaled hydrodynamic force with scaled film thickness at the axis of symmetry, and (b) variation of scaled film thickness with scaled film radius. In this run, the  $r_{\text{max}}^*$  is 4.54 and 8 (correspond to  $r_{\text{max}}$  of  $727 \mu\text{m}$  and  $1318 \mu\text{m}$ ) for the NSRYL and LSRYL model, respectively. The physical parameters used in the NSRYL and LSRYL models summarized in **Table 3.1 and 3.6**.

## Appendix C

With the best fit between the measured and the predicted time dependent force profile, the hydrophobic force constants for solids of different contact angles are determined using the SRYL model with power law form for hydrophobic force, given in **Table C.1**.

**Table C.1.** The best fitted of hydrophobic force constant,  $K_{132}$  (J), in **eqn. 5.10** using full mobile bubble surface boundary condition

Contact angle (°C)	$K_{132}$ (J)
38	$1.1 \times 10^{-18}$
52	$2.1 \times 10^{-18}$
84	$7 \times 10^{-18}$
103	$2 \times 10^{-17}$

With the best fit between the measured and the predicted time dependent force profile, the hydrophobic force constants for solids of different contact angles are determined using the SRYL model with exponential form for hydrophobic force (**eqn. 5.9**). The results are summarized in **Tables C.2** and **C.3**.

**Figure C.1** shows the effects of bubble approach velocity and surface hydrophobicity on the predicted critical film thickness. In this figure the SRYL model is solved with power law form of hydrophobic force with full mobile bubble surface boundary condition. **Figure C.1** shows that the critical film thickness increases significantly with increasing glass sphere hydrophobicity. This figure also shows that for a specific surface hydrophobicity, the critical film thickness increases slightly with increasing bubble approach velocity.

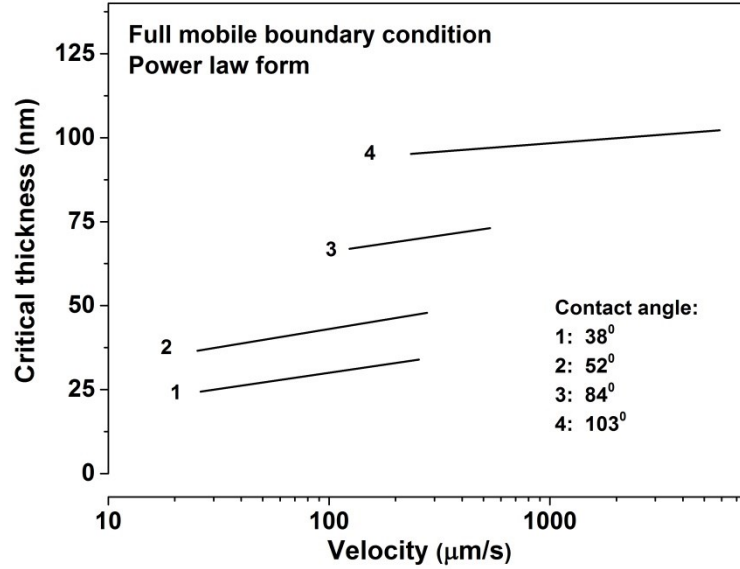


**Fig. C.1.** Effects of bubble approach velocity and surface hydrophobicity on the predicted critical film thickness. The SRYL model is solved with the best fitted hydrophobic force constant  $K_{132}$  (J) [in **eqn. 5.10**] to be  $1.1 \times 10^{-18}$  J,  $2.1 \times 10^{-18}$  J,  $7 \times 10^{-18}$  J and  $2 \times 10^{-17}$  J for contact angles of  $38^\circ$ ,  $52^\circ$ ,  $84^\circ$  and  $103^\circ$ , respectively for full mobile bubble surface boundary condition.

**Table C.2.** The best fitted of hydrophobic force constant (decay length,  $\lambda(\text{nm})$ ), in **eqn. 5.9** using both immobile and full mobile bubble surface boundary condition

	Immobile B.C.	Full mobile B.C.
Contact angle $38^\circ$	30	11
Contact angle $52^\circ$	39	13.8
Contact angle $84^\circ$	58	20
Contact angle $103^\circ$	70	24

**Table C.3.** The best fitted of hydrophobic force constant,  $K(\text{pa})$ , in **eqn. 5.9** using both immobile and full mobile bubble surface boundary condition

	Immobile B.C.	Full mobile B.C.
Contact angle $38^\circ$	69227	85125
Contact angle $52^\circ$	79925	88736

Contact angle 84°	106987	93771
Contact angle 103°	132160	97894

**Figure C.2** shows the effects of bubble approach velocity and surface hydrophobicity on the predicted critical film thickness. In this figure the SRYL model is solved with exponential form of hydrophobic force with both immobile and full mobile bubble surface boundary conditions.

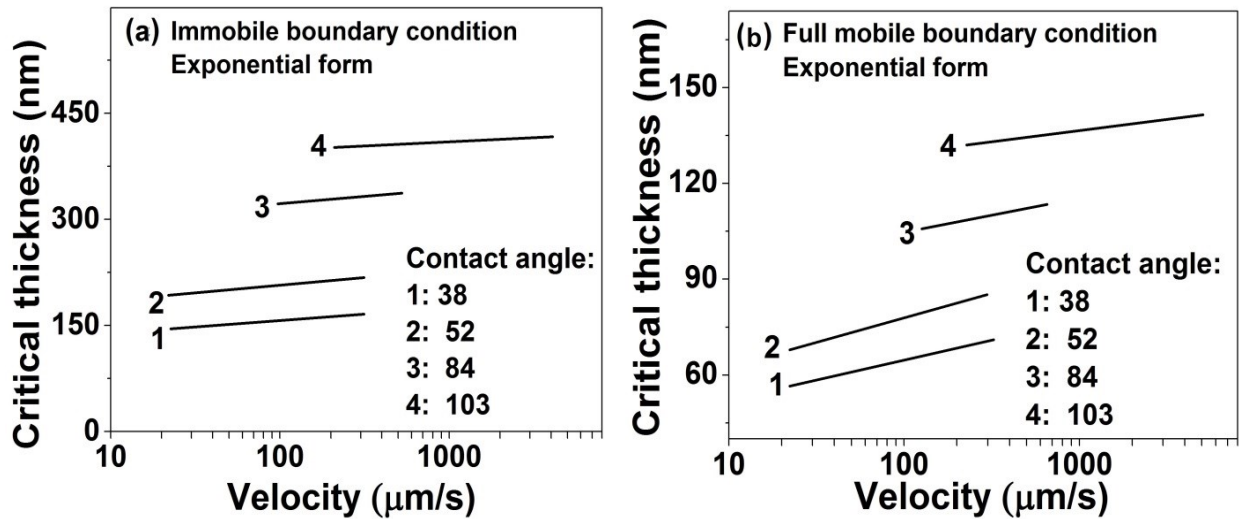


**Fig. C.2.** Effects of bubble approach velocity and surface hydrophobicity on the predicted critical film thickness. (a) The SRYL model is solved with the best fitted hydrophobic force constant  $\lambda$  (nm) [in **eqn. 5.9**] to be 30 nm, 39 nm, 58 nm and 70 nm for contact angles of 38°, 52°, 84° and 103°, respectively for immobile bubble surface boundary condition. (b) The SRYL model is solved with the best fitted hydrophobic force constant  $\lambda$  (nm) [in **eqn. 5.9**] to be 11 nm, 13.8 nm, 20 nm and 24 nm for contact angles of 38°, 52°, 84° and 103°, respectively for full mobile bubble surface boundary condition.

**Figures C.2 (a)** and **(b)** show that the critical film thickness increases significantly with increasing glass sphere hydrophobicity. These figures also show that for a specific surface hydrophobicity, the critical film thickness increases slightly with increasing bubble approach velocity.